ADVANCED ONE-DIMENSIONAL NANOSTRUCTURES FOR HIGH PERFORMANCE CATALYST ELECTRODES IN POLYMER ELECTROLYTE FUEL CELLS

By

Yaxiang Lu

A thesis submitted to the

University of Birmingham

for the degree of

DOCTOR OF PHILOSOPHY

Centre for Fuel Cell and Hydrogen Research

School of Chemical Engineering

College of Engineering and Physical Sciences

University of Birmingham

October 2015

ABSTRACT

In the past decades, the study of nanotechnology has brought in tremendous progress to the development of polymer electrolyte fuel cells (PEFC) and many advanced catalyst approaches have been developed. However, many of these still remain at 'test-tube' level and have not been implemented in practical fuel cells. The concerns about the gap between the pure material research and fuel cells are increasing, and a study focusing on the electrode structures is required to help address this issue.

The Centre for Fuel Cell and Hydrogen Research at the University of Birmingham has been working in the area of Pt nanowires for several years. Based on previous results, the aim of this PhD thesis is to investigate integrated gas diffusion electrodes (GDEs) with in-situ grown Pt nanowires (Pt NWs) to achieve further understanding of the structure-property relationship for PEFC electrodes. A comprehensive study is carried out for various electrode structures by controlling the morphology, crystal structure and distribution of Pt nanowires in catalyst layers through tuning the in-situ growing process. Considering the performance of the corresponding GDEs as cathodes in single fuel cells, the influence mechanisms of the in-situ growing process on Pt nucleation, growth and distribution of single crystal Pt NWs are examined to understand the electrode structure.

First, the electrode structure is optimised by varying the in-situ growing temperature between 5 and 50 ^{o}C. A vital role of the temperature is demonstrated with its influence on the wettability of the super hydrophobic GDL surface and its effect on the crystal

nucleation and growth rates of Pt NWs. An optimal temperature is found at 40 °C, and higher power performance and better durability are achieved as compared with electrodes made from state-of-the-art commercial TKK Pt/C catalysts. A possible mechanism for the influence of temperature on Pt nanowire growth is suggested.

Second, Pd is introduced to control the electrode structure through its hybrid effect with Pt to direct the nucleation and growth processes to form different PdPt nanostructures on the GDL surface. The mechanisms of the effect of Pd on the growth and performance of the PdPt nanostructures are inspected. The atomic content of Pd is adjusted between 0.5% to 50% to tune the morphology and distribution of PdPt nanostructures. The results demonstrate that Pd not only can be an efficient tool in regulating the morphology and distribution of bimetallic PdPt nanostructures throughout the large-area GDL substrate to achieve a high performance GDE, but also manipulates the durability of nanostructures. At an optimal Pd content of 5%, a GDE with uniform PdPt nanodendrites (NDs) is achieved. The power performance and durability together with the intrinsic mass and specific area activity of PdPtND GDEs are compared with pure PtNW GDE to examine the effect of Pd on the electrode structure.

Finally, Pt NW GDEs with different structures are studied combined with various GDL structures. A systematic study is conducted to investigate the effects of carbon loading, carbon composition, carbon treatment and polytetrafluoroethylene (PTFE) amount in the microporous layer (MPL), as well as PTFE loading in the carbon fibre substrate. Sigracet® standard GDLs are used to study the PTFE loading in the substrate. GDLs with self-painted MPLs on standard 35BA substrates are employed to investigate the features of the

MPL. Experimental results indicate that the GDL, in particular the MPL features, plays a significant role in the distribution of Pt NWs thus transforming the electrode structure and its performance in PEFCs, while the substrate shows very little effect.

This work demonstrates that besides the intrinsic catalytic activities of the catalysts themselves, their optimal implementation in electrodes, i.e. the electrode structure, plays an important role in the power performance of PEFCs than we initially expected.

ACKNOWLEDGMENTS

This thesis marks the end of my journey in pursuing my PhD. Looking back from September 2012, it is impossible for me to complete this journey without the excellent guidance of my supervisors, the unreserved assistance of my colleagues, the continuous encouragement of my friends and the endless care from my family members.

I would like to express my deepest acknowledgement to my primary supervisor **Dr. Shangfeng Du** for his outstanding guidance and insightful advice throughout my PhD. Thanks to his foresight and sagacity, this PhD project is well directed and could be finished on time. Whenever I meet difficulties in the research work he is always there to discuss with and provide inspiring suggestions with his expertise. No matter I send him the weekly summary, monthly report, manuscript draft or thesis chapter, he always patiently revises and gives me valuable feedbacks to help improve my work. Besides the research work, he also pays attention to the development of my other skills to help me be an independent researcher. He supports me to present my research work at national and international conferences; gives me opportunity to co-supervise Master student; encourages me to participate in the three minute thesis presentation competition, etc., all of which helps improve my presentation, management, leadership skills and benefit for my PhD study as well. I couldn't make so much progress without the remarkable guidance of Dr. Du.

I would also like to express my sincere gratitude to my second supervisor **Professor Robert Steinberger-Wilckens** for his constructive discussion and constant support for my PhD work. As the Chair of the Centre for Fuel Cell & Hydrogen Research, he is busy in supervising PhD students and research fellows of the whole group. However, no matter how busy he is, he always arranges a monthly meeting with me to learn the progress of my research work, helps me resolve difficulties and suggests possible alternative approaches. In addition, I clearly remember that during his absence in office, in order to give me feedbacks timely, he scanned the revised chapters and sent the copies to me via email to make sure I can finish my work within the plan. My PhD study couldn't proceed so smoothly without the enlightening discussion and timely comments of Prof. Steinberger-Wilckens.

Acknowledgment must also go to Dr. Surbhi Sharma and Dr. Aman Dhir for giving me opportunities to participate in Lab Demonstration, Community Day, and Environment Day etc. to make me involved in other activities besides my research work to help improve my teaching and communication skills. I am also thankful to my colleagues Dr. Gaurav Gupta, Dr. Ahmad El-kharouf and Dr. Jong-Eun Hong for their advice on my experiment work and career development. Thanks must also go to Dr. Artur Majewski, Bob Sharpe and Theresa Morris for their technical support. I also would like to take this opportunity to sincerely acknowledge all the members in the Centre for their support in various aspects of the work. My warm appreciation goes to Lynn Draper and John Hopper for their administrative assistance and to other staff in the School of Chemical Engineering at the University of Birmingham for their help and support. My thanks are due to Dr. Zabeada Aslam, Leeds EPSRC Nanoscience and Nanotechnology Research Equipment Facility

(LENNF) for the help in TEM analysis and National EPSRC XPS User's Service (NEXUS) at Newcastle University for the help in XPS analysis.

It's my pleasure to acknowledge my friends Zhen Li, Ju Zhu, Shuai Tian, Rui Wang, Wei Wen, Mingming Du, Lina Troskialina, Carolina Branco, Andrea Masi, Tsang Tsai, Melissa Oum, Kun Zhang, etc. for their help, encouragement and comfort during my stay in UK. Special thanks go to Vikrant Venkataraman for drawing some schematic diagrams and proof reading my thesis.

I owe a great deal of appreciation and gratitude to my dear parents and whole family. Studying outside my hometown since my undergraduate for more than ten years, I have little opportunity to accompany and care for them. However, they always tell me that all I need to do is focus on my study and not worry about other things. They always support the decision I made and encourage me to overcome difficulties. Without their understanding, unfailing support and endless love I wouldn't have managed to get here.

I am also thankful to the sponsorship of the University of Birmingham and the China Scholarship Council for providing the Li Siguang Scholarship for my PhD study.

Finally, I would like to express my sincere acknowledgement to all those who make this thesis possible and contribute to the unforgettable PhD experience for me. Many Thanks!

LIST OF PUBLICATIONS

Peer-reviewed Journal Papers

[1] **Yaxiang Lu**, Shangfeng Du, Robert Steinberger-Wilckens, Evaluation of gas diffusion layer structures for in-situ growing Pt nanowires for PEFC applications, *Under preparation*

[2] **Yaxiang Lu**, Shangfeng Du, Robert Steinberger-Wilckens, One-dimensional nanostructured electrocatalysts for polymer electrolyte fuel cells, *Submitted to Nano Energy*

[3] **Yaxiang Lu**, Shangfeng Du, Robert Steinberger-Wilckens, Three-dimensional catalyst electrodes based on PdPt nanodendrites for oxygen reduction reaction in PEFC applications, *Applied Catalysis B: Environmental* 187 (2016) 108-114. DOI: 10.1016/j.apcatb.2016.01.019

[4] Kaijie Lin**, Yaxiang Lu,** Shangfeng Du, Hanshan Dong, The effect of active screen plasma treatment conditions on the growth and performance of Pt nanowire catalyst layer in DMFCs, *Accepted by International Journal of Hydrogen Energy*

[5] **Yaxiang Lu**, Shangfeng Du, Robert Steinberger-Wilckens, Temperature-controlled growth of single-crystal Pt nanowire arrays for high performance catalyst electrodes in polymer electrolyte fuel cells, *Applied Catalysis B: Environmental* 164 (2015) 389-395. DOI: 10.1016/j.apcatb.2014.09.040

[6] Shangfeng Du, **Yaxiang Lu**, Sairam K. Malladi, Qiang Xu, Robert Steinberger-Wilckens, A simple approach for PtNi-MWCNT hybrid nanostructures as high performance electrocatalysts for the oxygen reduction reaction, *Journal of Materials Chemistry A* 2 (2014) 692-698. DOI: 10.1039/C3TA13608F

[7] Shangfeng Du, **Yaxiang Lu**, Robert Steinberger-Wilckens, PtPd nanowire arrays supported on reduced graphene oxide as advanced electrocatalysts for methanol oxidation, *Carbon* 79 (2014) 346-353. DOI: 10.1016/j.carbon.2014.07.076

[8] Shangfeng Du, Kaijie Lin, Sairam K Malladi, **Yaxiang Lu**, Shuhui Sun, Qiang Xu, Robert Steinberger-Wilckens, Hanshan Dong, Plasma nitriding induced growth of Pt-nanowire arrays as high performance electrocatalyst for fuel cells, *Scientific Reports* 4 (2014) 6439. DOI: 10.1038/srep06439

Peer-reviewed Conference Papers

[1] **Yaxiang Lu**, Shangfeng Du, Robert Steinberger-Wilckens, Three-dimensional catalyst electrodes with PdPt nanodendrites for PEFC applications, 5th European PEFC & H_2 Forum 2015 conference proceedings, Luzern, Switzerland, 30 June-3 July, 2015.

[2] Shangfeng Du, **Yaxiang Lu**, Sairam K. Malladi, Robert Steinberger-Wilckens, Advanced Hybrid nanostructures of single-crystal Pt nanoparticles on Ni-coated MWCNTs as high performance electrocatalysts for oxygen reduction reaction, 4th European PEFC and H_2 Forum 2013 conference proceedings, Luzern, Switzerland, 2-5 July, 2013.

Conference presentations

1. 5th European PEFC & H_2 Forum, Luzern, Switzerland, 30 June-3 July, 2015 (***Oral presentation***)
2. Fuel Cell & Hydrogen Technical Conference, Birmingham, UK, 19-21 May, 2015 (***Oral presentation, Second Prize***)
3. H2FC SUPERGEN 2014 Conference, Birmingham, UK, 15-17 December, 2014 (***Oral presentation***)
4. The CARISMA 2014 conference, Cape Town, South Africa, 1-3 December, 2014 (***Oral presentation***)
5. 15th edition of Trends in Nanotechnology International Conference (TNT2014), Barcelona, Spain, 27-31 October, 2014 (Poster presentation, ***Student Grant***)
6. The Midlands Electrochemistry Group Meeting (MEG 2014), Loughborough, UK, 1 April, 2014 (***Oral presentation***)
7. 10th International Hydrogen & Fuel Cell Technical Conference, Birmingham, UK, 26-27 March, 2014 (Poster presentation)
8. H2FC SUPERGEN 2013 Conference, Birmingham, UK, 16-18 December, 2013 (Poster presentation)
9. 4th European PEFC & H_2 Forum, Luzern, Switzerland, 2-5 July, 2013 (***Oral presentation***)
10. The Midlands Electrochemistry Group Meeting (MEG 2013), Nottingham, UK, 17 April, 2013 (***Oral presentation***)
11. 9th International Hydrogen and Fuel Cell Conference, Birmingham, UK, 20-21 March, 2013 (Poster presentation)

TABLE OF CONTENTS

TABLE OF CONTENTS ..... **IX**
LIST OF FIGURES ..... **XII**
LIST OF TABLES ..... **XIX**
ABBREVIATIONS ..... **XX**

CHAPTER 1. Introduction **2**
1.1 Polymer Electrolyte Fuel Cells (PEFCs) 2
1.2 Challenges and Opportunities for PEFC Electrode 5
1.3 Strategy and Research Objectives 7
1.4 Thesis Overview 9

CHAPTER 2. Literature Review **11**
2.1 Fundamental Aspects of Oxygen Reduction Reaction (ORR) 11
2.2 One-Dimensional (1D) Nanostructures 14
2.3 Advantages of 1D Catalysts for ORR 15
2.4 Preparation of 1D Catalysts for ORR 17
2.5 State-of-the-art 1D Catalysts for ORR 19
2.5.1 1D Pt-based Catalysts for ORR 20
2.5.2 1D Non-Pt based Catalysts for ORR 32
2.6 Electrodes from 1D Pt Nanostructures 34
2.7 Summary and Perspective 38

CHAPTER 3. Materials and Experiments **44**
3.1 Chemicals, Materials and GDE Fabrication 44
3.1.1 In-situ Growth of Catalyst Nanostructures on GDLs 44
3.1.2 Fabrication of Self-made GDLs with Painted MPLs 46
3.2 Physical Characterisations 49
3.2.1 Scanning Electron Microscopy (SEM) 49

3.2.2 Transmission Electron Microscopy (TEM) 49
3.2.3 X-Ray Diffraction (XRD) 50
3.2.4 Thermogravimetric Analysis (TGA) 50
3.2.5 Energy-Dispersive X-ray Spectroscopy (EDS) 50
3.2.6 X-ray Photoelectron Spectroscopy (XPS) 51
3.2.7 Ultraviolet-Visible Spectroscopy (UV-Vis) 51
3.2.8 Drop Shape Analyser 51
3.3 Membrane Electrode Assembly (MEA) Fabrication 52
3.4 Fuel Cell Testing 53
3.4.1 Polarisation Curves 54
3.4.2 Electrochemical Impedance Spectroscopy (EIS) 56
3.4.3 Cyclic Voltammetry (CV) 58
3.4.4 Accelerated Degradation Test (ADT) 59
3.4.5 Catalytic Activity in Oxygen 60

CHAPTER 4. Temperature-Controlled Growth of Pt Nanowires for High Performance Catalyst Electrodes 64
4.1 Introduction 64
4.2 Crystal Structure of Pt Nanostructures at Various Temperatures 66
4.3 Distribution and Morphology of Pt Nanostructures at Various Temperatures 69
4.4 Single Fuel Cell Testing 76
4.4.1 Power Performance in Fuel Cells 76
4.4.2 Electrochemical Impedance Spectroscopy (EIS) 79
4.4.3 Electrochemical Surface Area (ECSA) 81
4.4.4 Durability by Accelerated Degradation Test (ADT) 82
4.4.5 Catalytic Activity in Oxygen 84
4.5 Growth Mechanism 85
4.6 Conclusions 87

CHAPTER 5. Integrated Catalyst Electrodes Based on PdPt Nanodendrites 90
5.1 Introduction 90
5.2 Distribution and Morphology of PdPt Nanostructures 91

5.3 Performance in Single Cell Testing 99
5.3.1 Power Performance in Fuel Cells 99
5.3.2 Electrochemical Impedance Spectroscopy (EIS) 100
5.3.3 Electrochemical Surface Area (ECSA) 103
5.3.4 Stability from the Accelerated Degradation Test (ADT) 104
5.3.5 Catalytic Activity in Oxygen 106
5.4 Structural and Compositional Characterisation of As-Prepared PdPt Nanodendrites 108
5.5 Growth Mechanism of PdPt Nanostructures at Various Pd Amounts 113
5.6 Conclusions 120

CHAPTER 6. Evaluation of Gas Diffusion Layer (GDL) Structures for Pt Nanowire Electrodes 123
6.1 Introduction 123
6.2 Carbon Loadings in Microporous Layers (MPLs) 125
6.3 Carbon Compositions in MPLs 131
6.4 Carbon Treatment for MPLs 139
6.5 PTFE Loading in GDLs 144
6.5.1 PTFE Loading in the Substrate 144
6.5.2 PTFE Loading in the MPL 147
6.6 Conclusions 157

CHAPTER 7. Conclusions and Perspective 160
7.1 Conclusions 160
7.2 Perspective 164

References 166

LIST OF FIGURES

Fig. 1.1 Schematic of an MEA configuration and the basic of a PEFC operating principle 5

Fig. 2.1 Proposed ORR mechanism [11] 12

Fig. 2.2 Volcano plot for ORR activity of (a) pure metal and (b) Pt-based transition metal alloys versus the oxygen binding energy (ΔE_O) [22, 25] 13

Fig. 2.3 A schematic summary of the kinds of quasi-one dimensional nanostructures [32] 15

Fig. 2.4 (a, b) SEM, (c) TEM and (d) high resolution TEM images of SG-PtNW-3 catalyst. Insets in (d) are the Fourier filtered high resolution TEM images of the areas highlighted by the dashed yellow squares [87] 24

Fig. 2.5 (a,b) TEM images showing the morphological evolution of Pd-Pt nanodendrites. High-resolution TEM images of (c) an individual Pd-Pt particle and (d) the small Pt particles shown in (a). In (c), the Pt bumps on the Pd seed are indicated by arrows. (e) High-resolution TEM image of a single Pd-Pt nanodendrite. It can be seen that the lattice fringes are coherently extended from the Pd core to the Pt branches. (f) High-resolution TEM image taken from a Pt branch containing a single twin plane in its structure and the corresponding Fourier transform (FT) pattern (inset). A twin plane is indicated by tw [123] 31

Fig. 2.6 SEM images of the PtCoMn alloy catalyst sputter coating on the microstructured substrate supported whiskers [159]. 36

Fig. 3.1 Fabrication process for in-situ growing nanostructures on GDL. a) GDL; b) in-situ growing nanostructures on GDL; c) GDE with in-situ grown nanostructures (inset is the SEM image of the red square).. 45

Fig. 3.2 Naming rules for GDLs from Sigracet®: AA means a plain substrate; YA indicates different PTFE loadings in the substrate without the MPL; YC indicates different PTFE loadings in the substrate with a standard MPL containing 20% PTFE. 47

Fig. 3.3 The schematic for MEA fabrication. 52

Fig. 3.4 Single fuel cell testing system. 54

Fig. 3.5 Typical polarisation curve of a PEFC. 55

Fig. 3.6 Typical EIS for an MEA at the (a) low and (b) high current density..... 57

Fig. 3.7 Fuel cell impedance equivalent circuit at a high current density 58

Fig. 3.8 Cathode cyclic voltammogram of an MEA. 59

Fig. 3.9 Triangle potential cycling used for the accelerated degradation test..... 60

Fig. 3.10 (a) H_2 crossover current density at 0.6 V and (b) ohmic resistance measured by the EIS at 1kHz. 62

Fig. 4.1 Schematic illustration of the formation and shape evolution of Pt nanostructures corresponding to temperature (H.T.: high temperature; R.T.: room temperature) [68]. 65

Fig. 4.2 TGA plots of the pristine 35BC GDL and PtNW GDE samples grown at 5, 25, 40 and 50 ^{o}C. 68

Fig. 4.3 XRD patterns of (a) 35BC GDL and PtNW GDEs grown at (b) 5; (c) 25; (d) 40; and (e) 50 ^{o}C. 69

Fig. 4.4 SEM images of PtNW GDE grown at 5 ^{o}C. (a, b) and (c-f) show the edge and centre area of the 4cm×4cm GDE piece, respectively with different magnifications..... 70

Fig. 4.5 (a-d) TEM images of PtNW GDE grown at 5 ^{o}C..... 71

Fig. 4.6 SEM images of PtNW GDE grown at 25 ^{o}C. (a, b) and (c-f) show the edge and centre area of the GDE piece, respectively with different magnifications. 72

Fig. 4.7 (a-c) TEM images of PtNW GDE grown at 25 ^{o}C. 73

Fig. 4.8 SEM images of PtNW GDE grown at 40 ^{o}C. (a) and (b-d) show the edge and centre area of the GDE piece, respectively. (b-d) are images for the centre area with different magnifications..... 73

Fig. 4.9 (a-c) TEM images of PtNW GDE grown at 40 ^{o}C. 74

Fig. 4.10 SEM images of PtNW GDE grown at 50 ^{o}C. (a) and (b-d) show the edge and centre area of the GDE piece, respectively. (b-d) are images for the centre area with different magnifications..... 75

Fig. 4.11 (a-d) TEM images of PtNW GDE grown at 50 ^{o}C. 76

Fig. 4.12 (a) Polarisation curves, (b) power density curves and (c) the trend of the power density at 0.6 V for the PtNW GDEs grown at different temperatures and the one with TKK Pt/C catalyst. 78

Fig. 4.13 EIS measured at (a) 0.05, (b) 0.5 and (c) 1.0 A cm^{-2} for PtNW GDEs grown at different temperatures. 80

Fig. 4.14 Cathode CVs of PtNW GDEs grown at different temperatures and the one with TKK Pt/C catalyst. The cathode was fed with fully humidified N_2. 81

Fig. 4.15 (a) CVs and (b) the ECSAs of PtNW GDE 40 ^{o}C and TKK Pt/C before and after the potential cycling. Measurements were taken at T_{cell}=70 ^{o}C with fully humidified H_2 and N_2 at 2 bar (stoichiometry s=1.3/2.4). 83

Fig. 4.16 Original uncorrected (solid square and circular symbols) and corrected (empty square and circular symbols) H_2/O_2 performance of the MEAs with the TKK Pt/C and PtNW GDEs. Measurements were taken at 80 ^{o}C with fully humidified reactants at 1.5 bar (H_2/O_2 stoichiometric flows of s=2/9.5). 84

Fig. 4.17 Schematic diagram for Pt nanostructures grown on carbon paper surface at (a) low, (b) moderate and (c) high temperatures. 87

Fig. 5.1 SEM images at different magnifications for PdPt nanostructures grown on the GDL surface with 50 at% Pd. 92

Fig. 5.2 TEM images at different magnifications for PdPt nanostructures with 50 at% Pd. 93

Fig. 5.3 SEM images at different magnifications for PdPt nanostructures grown on the GDL surface with 25 at% Pd. 93

Fig. 5.4 TEM images at different magnifications for PdPt nanostructures with 25 at% Pd. 94

Fig. 5.5 SEM images at different magnifications for PdPt nanostructures grown on the GDL surface with 10 at% Pd. 95

Fig. 5.6 TEM images at different magnifications for PdPt nanostructures with 10 at% Pd. 95

Fig. 5.7 SEM images at different magnifications for PdPt nanostructures grown on the GDL surface with 5 at% Pd. 96

Fig. 5.8 TEM images at different magnifications for PdPt nanodendrites with 5 at% Pd. Inset in a) and d) shows the SAED pattern and HR-TEM image, respectively.97

Fig. 5.9 SEM images at different magnifications for PdPt nanostructures grown on the GDL surface with 2.5 at% Pd. 98

Fig. 5.10 SEM images at different magnifications for PdPt nanostructures grown on the GDL surface with 0.5 at% Pd. 98

Fig. 5.11 TEM images at different magnifications for PdPt nanostructures with 2.5 at% Pd. 99

Fig. 5.12 (a) Polarisation curves, (b) power density curves and (c) the trend of the power density at 0.6 V for PdPt GDEs with different Pd amounts and the PtNW GDE.. 101

Fig. 5.13 EIS measured at (a) 0.05, (b) 0.5 and (c) 1.0 A cm^{-2} for PdPtND GDEs with various Pd amounts and the PtNW GDE. 102

Fig. 5.14 Cathode CVs for PdPt GDEs with different compositions and the one with Pt nanowire catalysts. Measurements were taken at T_{cell}=25 ^{o}C with fully humidified H_2 and N_2 at 0 bar (stoichiometry s=1.3/2.4). 104

Fig. 5.15 (a) CVs; (b) summary of the ECSAs of PtNW GDE and PdPtND GDE with 5 at% Pd before and after the potential cycling 105

Fig. 5.16 Original uncorrected (solid symbols) and corrected (empty symbols) H_2/O_2 performance of the MEAs with the PtNW and PdPtND 5 at% GDE. 107

Fig. 5.17 XRD patterns of (a) 35BC GDL; (b) pure Pt on GDL; (c) pure Pd on GDL; and (d) PdPt 5 at% NDs on GDL 109

Fig. 5.18 EDS spectrum of PdPt NDs with 5 at% Pd (Cu comes from Cu grid used in TEM analysis)..... 110

Fig. 5.19 (a) TGA curves of the pristine 35BC GDL and PdPt GDE with 5 at% Pd. 111

Fig. 5.20 (a) XPS survey of PdPt NDs with 5 at% Pd and (b) XPS spectra of PdPt nanostructures with different Pd amounts in Pd 3d and Pt 4d3/2 region..... 112

Fig. 5.21 (a) Power performance of PdPt GDEs fabricated by two approaches and (b) UV-Vis spectra of the precursor solution and the mixture of PdPt at different hours. 115

Fig. 5.22 (a-c) TEM images of PdPt nanostructures with 5 at% Pd reacted for 2h and (d) the corresponding EDS spectrum. 116

Fig. 5.23 (a-c) TEM images of PdPt nanostructures with 5 at% Pd reacted for 5h and (d) the corresponding EDS spectrum. 117

Fig. 5.24 (a-c) TEM images of PdPt nanostructures with 5 at% Pd reacted for 10h and (d) the corresponding EDS spectrum. 118

Fig. 5.25 (a-c) TEM images of PdPt nanostructures with 5 at% Pd reacted for 24h and (d) the corresponding EDS spectrum. 119

Fig. 5.26 Schematic diagram for PdPt nanostructures grown on carbon paper surface at (a) high, (b) medium, (c) optimal and (d) very low Pd content. 120

Fig. 6.1 Schematic of the GDL configuration. 124

Fig. 6.2 Optical microscopy images of (a) 35BA substrate and the GDLs with self-painted MPLs at the Vulcan XC-72R CB loading of (b) 1, (c) 3, (d) 4, (e) 4.48 and (f) 5 mg cm^{-2}. 125

Fig. 6.3 SEM images at different magnifications for Pt NWs grown on the self-painted MPL with carbon loading of 1 mg cm^{-2} (20% PTFE in MPLs based on the total MPL weight) 126

Fig. 6.4 SEM images of Pt NWs grown on the self-painted MPL with carbon loading of (a) 3 (b) 4, (c) 4.48 and (d) 5 mg cm^{-2} (20% PTFE in MPLs based on the total MPL weight). 127

Fig. 6.5 (a) Polarisation curves, (b) power density curves and (c) the trend of the power density at 0.6 V for PtNW GDEs with different CB loadings in the painted MPLs. 129

Fig. 6.6 EIS measured at (a) 0.05, (b) 0.5 and (c) 1.0 A cm^{-2} for PtNW GDEs with different CB loadings in the painted MPLs. 130

Fig. 6.7 TEM images of (a, b) carbon black and (c, d) acetylene black. 132

Fig. 6.8 SEM images at different magnifications for Pt NWs grown on the self-painted MPL with pure AB. 133

Fig. 6.9 SEM images at different magnifications for Pt NWs grown on the self-painted MPL with CB 25% and AB 75%. 133

Fig. 6.10 SEM images at different magnifications for Pt NWs grown on the self-painted MPL with CB 50% and AB 50%..... 134

Fig. 6.11 SEM images at different magnifications for Pt NWs grown on the self-painted MPL with CB 75% and AB 25%..... 134

Fig. 6.12 SEM images at different magnifications for Pt NWs grown on the self-painted MPL with pure CB 135

Fig. 6.13 (a) Polarisation curves, (b) power density curves and (c) the trend of the power density at 0.6 V for PtNW GDEs with different carbon compositions in the painted MPLs..... 136

Fig. 6.14 EIS measured at (a) 0.05, (b) 0.5 and (c) 1.0 A cm^{-2} for PtNW GDEs with different carbon compositions in the painted MPLs..... 138

Fig. 6.15 TEM images of nitric acid treated (a, b) carbon black and (c, d) acetylene black. 139

Fig. 6.16 (a) Polarisation curves, (b) power density curves and (c) the trend of the power density at 0.6 V for the PtNW GDEs with different carbon treatment situations in the painted MPLs..... 141

Fig. 6.17 EIS measured at (a) 0.05, (b) 0.5 and (c) 1.0 A cm^{-2} for PtNW GDEs with different carbon treatment situations in the painted MPLs..... 143

Fig. 6.18 Surface images of the commercial (a) 35BC, (b) 35CC and (c) 35DC GDLs.144

Fig. 6.19 (a) Polarisation and power density curves and (b) the trend of the power density at 0.6 V for the PtNW GDEs with different PTFE loadings in the substrate of the commercial GDLs..... 145

Fig. 6.20 EIS measured at (a) 0.05, (b) 0.5 and (c) 1.0 A cm^{-2} for the PtNW GDEs with different PTFE loadings in the substrate of commercial GDLs. 146

Fig. 6.21 SEM images at different magnifications for the centre area of the PtNW GDE with 5% PTFE in the painted MPL. 148

Fig. 6.22 SEM images at different magnifications for the edge area of the PtNW GDE with 5% PTFE in the painted MPL. 149

Fig. 6.23 SEM images at different magnifications for the centre area of the PtNW GDE with 20% PTFE in the painted MPL. 149

Fig. 6.24 SEM images at different magnifications for the edge area of the PtNW GDE with 20% PTFE in the painted MPL. 150

Fig. 6.25 SEM images at different magnifications for the centre area of the PtNW GDE with 40% PTFE in the painted MPL. 150

Fig. 6.26 SEM images at different magnifications for the edge area of the PtNW GDE with 40% PTFE in the painted MPL. 151

Fig. 6.27 (a) Polarisation curves, (b) power density curves and (c) the trend of the power density at 0.6 V for the PtNW GDEs with different PTFE loadings in self-painted MPLs. 152

Fig. 6.28 EIS measured at (a) 0.05, (b) 0.5 and (c) 1.0 A cm^{-2} for the PtNW GDEs with different PTFE loadings in the self-painted MPLs. 153

Fig. 6.29 (a) Cathode CVs and (b) summary of ECSAs for the PtNW GDEs with different PTFE loadings in the MPLs. 155

Fig. 6.30 Continuous operation test at 0.6 V for PtNW GDEs with painted MPLs at the low, medium and high PTFE amounts. Measurements were taken at T_{cell}=70 ^{o}C with fully humidified H_2 and air at 2 bar (stoichiometry s=1.3/2.4). 156

LIST OF TABLES

Table 2.1 Type, preparation method, morphology and performance of one-dimensional catalysts for ORR. 40-42

Table 4.1 Catalytic performance characteristics of the two MEAs with TKK Pt/C and PtNW 40 °C. 85

Table 5.1 Catalytic performance characteristics of the two MEAs with Pt NWs and PdPt 5 at% NDs. 108

Table 6.1 PTFE loading in standard GDLs from Sigracet®. 144

Table 6.2 PTFE loading in the self-made GDLs 147

ABBREVIATIONS

0D	Zero-Dimensional
1D	One-Dimensional
3D	Three-Dimensional
ε_d	d-band centre
ε_F	Fermi Level
AAO	Anodic Aluminum Oxide
AB	Acetylene Black
ADT	Accelerated Degradation Test
ASPN	Active Screen Plasma Nitriding
CB	Carbon Black
CCM	Catalyst Coated Membrane
CHP	Combined Heat and Power
CL	Catalyst Layer
CNFA	Carbon Nanofiber Array
CNT	Carbon Nanotube
CV	Cyclic Voltammetry
DFT	Density Functional Theory
DHE	Dynamic Hydrogen Electrode
DMF	N,N-Dimethyl Formamide
DOE	U.S. Department of Energy
ΔE_O	Oxygen Binding Energy
ECSA	Electrochemical Surface Area

EDS	Energy Dispersive X-ray Spectroscopy
EIS	Electrochemical Impedance Spectroscopy
fcc	face-centred cubic
FFP	Flow Field Plate
ΔG	Gibbs Free Energy
GDE	Gas Diffusion Electrode
GDL	Gas Diffusion Layer
GLAD	Glancing Angle Deposition
HOR	Hydrogen Oxidation Reaction
HR-TEM	High-Resolution Transmission Electron Microscopy
I_m	Mass Activity
I_s	Specific Area Activity
ICR	Interfacial Contact Resistance
IPA	Isopropanol
JM	Johnson Matthey
MEA	Membrane Electrode Assembly
MPL	Microporous Layer
MWCNT	Multi-Walled Carbon Nanotube
NC	Nanochain
ND	Nanodendrite
NF	Nanoflower
NL	Nanolance
NP	Nanoparticle
NPMC	Non-Precious Metal Catalyst

NR	Nanorod
NSTF	Nanostructured Thin Film
NT	Nanotube
NW	Nanowire
OCV	Open Circuit Voltage
ORR	Oxygen Reduction Reaction
PEFC	Polymer Electrolyte Fuel Cell
PEM	Polymer Electrolyte Membrane
PNR	Porous Nanorods
PTFE	Polytetrafluoroethylene
PVP	Poly(vinyl pyrrolidone)
R	Resistance
RDE	Rotating Disk Electrode
rGO	reduced Graphene Oxide
RHE	Reversible Hydrogen Electrode
s	Stoichiometry
SAED	Selected-Area Electron Diffraction
SEM	Scanning Electron Microscopy
SG	Sulfur-doped Graphene
SHE	Standard Hydrogen Electrode
T	Temperature
TEM	Transmission Electron Microscopy
TGA	Thermogravimetric Analysis
TPB	Triple Phase Boundary

UPD	Underpotential Deposition
UTW	Ultra-Thin Window
UV-Vis	Ultraviolet-Visible Spectroscopy
XPS	X-ray Photoelectron Spectroscopy
XRD	X-Ray Diffraction

CHAPTER 1

INTRODUCTION

1. Introduction

1.1 Polymer Electrolyte Fuel Cells (PEFCs)

Since the awareness of the limitation of global resources, the growing of energy consumption and the ever-increasing environmental degradation, more attention has been paid to the development of renewable energy sources and energy conservation measures. Hydrogen fuel cells are widely considered as one of the long-term energy efficiency solutions for the 21st century [1]. They are regarded as promising candidates for the replacement of current combustion-based power generators. Different from the traditional combustion processes, fuel cells possess a high energy efficiency because they can directly convert chemical energy into electrical energy through an electrochemical process without involving any other devices [2]. Besides, without the combustion process, fuel cells are not subjected to the Carnot cycle limitations and have extremely low polluting emissions, which together make fuel cells a very competitive technology for efficient and sustainable energy conversion [3].

The development of fuel cells dates back to two centuries ago when Christian F. Schönbein explained the operational principle of fuel cells in 1838 and Sir Willliam R. Grove demonstrated the first prototype cells on the same principle in 1839 [4, 5]. In the experiment, hydrogen and oxygen displaced the electrolyte at both platinum electrodes and a flow of electrons were indicated by the galvanometer between them. Since then, the discovered fuel cell principle remains unchanged: "*A fuel cell is an electrochemical 'device' that continuously converts chemical energy into electrical energy (and some heat) as long as fuel and oxidant are supplied*" [5]. Since then, many breakthroughs have been achieved step by step and many types of fuel cells have been developed. The whole family

of existing fuel cells can be categorised by the type of electrolytes into alkaline, phosphoric acid, polymer, molten carbonate and solid oxide fuel cells. Each of them determines the materials used in the component and the conditions applied for cell operation.

Of the multitude of fuel cell technologies available, polymer electrolyte fuel cells (PEFCs) are expected to play a significant role due to their low operational temperature, easy start-up and shutdown, and flexible power ranges in applications. PEFCs, invented by Thomas Grubb and refined by Leonard Niedrach at General Electric in the late 1950s, were the first type of fuel cells to find a practical application in NASA's Gemini space programme in mid-1960s [6]. A revolutionary step was made when a perfluorosulfonic acid ionomer membrane named Nafion began to be used in PEFCs [7]. Since then PEFCs attained higher power densities and longer lifetime. Today, with various advantages, PEFCs are expected to find applications in portable electronics, vehicle power systems, and residential combined heat and power (CHP) devices, playing a key role in a sustainable energy supply.

The basic design of a single PEFC consists of three main parts [8]: the proton conducting electrolyte membrane, the porous gas diffusion electrodes (GDEs) at anode and cathode, and the flow field plates (FFPs) for gas distribution. The GDE consists of two layers: a gas diffusion layer (GDL) and a catalyst layer (CL). The assembly of two GDEs and a polymer electrolyte membrane forms the membrane electrode assembly (MEA) which is the core part of a PEFC (Fig. 1.1). The MEA is then sandwiched with two FFPs to construct a single cell. The normal operating temperature for PEFCs ranges between room

temperature to 80 °C while it can be expanded by pressurising the system and utilising special membranes [9, 10]. When such a PEFC is operating, hydrogen and oxygen are fed through channels of the FFP to the anode and cathode, respectively, via diffusion through the GDLs to reach the active CLs. Through electrocatalysis, a hydrogen oxidation reaction (HOR) occurs at the anode side, where hydrogen molecules are oxidised into protons and electrons, while an oxygen reduction reaction (ORR) happens at the cathode side, where oxygen molecules combine with the generated protons and electrons to form water. In order to make this happen, protons travel from the anode across the electrolyte membrane toward the cathode and electrons transfer from the anode through the external electrical circuit to the cathode to form a closed circuit, which provides electrical energy during the process (Fig. 1.1) [11]. The electrochemical reaction equations for each side of the electrode and the overall reaction are as follows:

Anode reaction: $H_2 \rightarrow 2H^+ + 2e^-$ (1.1)

Cathode reaction: $1/2O_2 + 2H^+ + 2e^- \rightarrow H_2O$ (1.2)

Overall reaction: $H_2 + 1/2O_2 \rightarrow H_2O$ (1.3)

From the view of thermodynamics, the overall reaction is spontaneous, and the theoretical electric work generated corresponds to the Gibbs free energy (ΔG), which can be represented by the following equation:

$$\Delta G = -nFE \quad (1.4)$$

where ΔG is the Gibbs free energy, n is the number of electrons involved, F is the Faraday's constant (96485 secAmol^{-1}), and E is the reversible potential. If the reactants and products are in the standard states (T=25 ^{o}C; pressure=1 atm) and water is produced as liquid, the theoretical potential is calculated as follows:

$$E = \frac{-\Delta G}{nF} = \frac{237.340\ \text{J mol}^{-1}}{2 \times 96485\ \text{s A mol}^{-1}} = 1.23\ \text{V} \qquad (1.5)$$

Therefore, under the standard states, the theoretical H_2/O_2 fuel cell potential is 1.23 V.

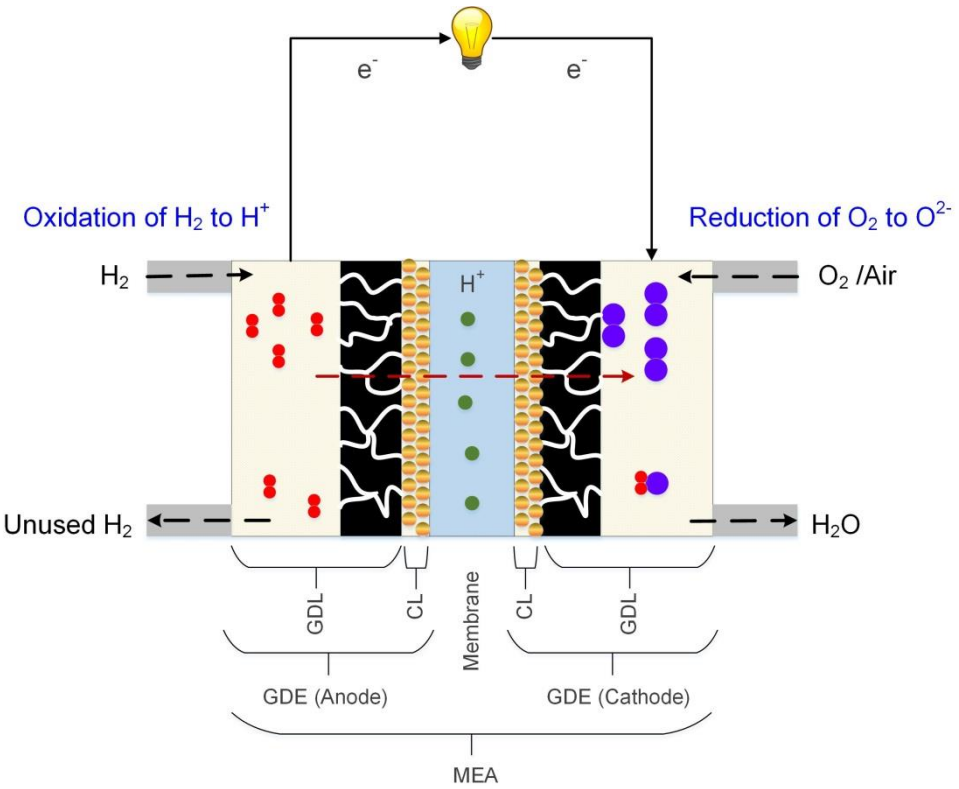

Fig. 1.1 Schematic of an MEA configuration and the basic of a PEFC operating principle.

1.2 Challenges and Opportunities for PEFC Electrode

The great advantages of PEFC technologies have attracted a huge amount of effort with considerable advances in recent years. However, many challenges still need to be overcome before commercialisation can take place. The three major obstacles for a widespread promotion of PEFCs lie in cost, activity and durability.

According to an estimation of the U.S. Department of Energy (DOE), out of the total cost of PEFC components, the electrodes contribute to ca. 50% [12, 13]. The reason is that Pt, a

highly limited natural resource, is required to promote the on-going of anode HOR and cathode ORR and is still regarded as the only viable choice for PEFC catalysts up to today. The second limiting factor is the activity of the electrode, which determines the catalytic efficiency of HOR and ORR occurring on the Pt surface. Because of the slow electrode kinetics and undesired activation overpotential, the cathode ORR is ca. 6 orders of magnitude slower than the anode HOR, which has a decisive impact on the performance of the whole PEFC [14]. The sluggish ORR needs more Pt at the cathode and the typical amount is 0.2–0.6 mg_{Pt} cm^{-2}. Reducing Pt loading to the target of 0.1 mg cm^{-2} and maintaining the catalytic activity is what recent research is concerned with [15]. Another issue that currently needs to be addressed is the high degradation of the state-of-the-art Pt/C catalyst. The decrease in electrochemical surface area (ECSA) and increase in ORR overpotential are the major contributors for PEFC degradation, particularly during fuel cell start-up and shutdown [15, 16]. The generally recognised reasons for the electrode degradation phenomenon are associated with catalyst dissolution, migration, precipitation, coalescence, agglomeration and the corrosion of catalyst supports, which together impact on the long-term operation of PEFCs [17-20]. All of the aforementioned challenges drive researchers to develop inexpensive, highly active and robust electrocatalysts for practical PEFC applications.

Benefitting from the recent development of material science and chemical engineering, the controlled synthesis of novel catalysts and advanced fabrication of electrodes with complex structures can be achieved by innovative approaches, which offer opportunities to address the challenges faced by PEFCs, thus promoting the large-scale deployment of this green technology. Practical measures include optimising Pt catalyst size, shape (e.g. cubic,

tetrahedral, truncated octahedral and high-index tetra-hexahedrons) and structure (e.g. solid, hollow and porous); introducing alloys, core-shell and heterogeneous multi-compositional catalysts; developing advanced support materials (e.g. graphene, macromolecules, new-type oxides and nitrides, and composite supports) with induced synergistic effect between catalysts and supports; controlling the morphology of catalysts (e.g. nanowire, nanotube, nanorod) to display the unique anisotropic nature; or fabricating non-precious metal catalysts (NPMCs) to act as Pt alternatives (See Chapter 2). All of these research directions have shown to be potential solutions to reduce cost as well as improve power performance and durability of PEFCs.

1.3 Strategy and Research Objectives

Today, a lot of new catalyst approaches have been developed. Superior activity and stability have been reported via electrochemical characterisation in liquid electrolytes. However, very few of them have been really tested in-situ in PEFCs. Especially, the NPMC concept seems highly attractive due to avoiding using precious metals to significantly reduce the cost, but the activity and stability is still far below the targets compared with Pt-based catalysts. Hence, for practical applications, Pt-based catalysts are still the focus for the crucial cathodic ORR application. In our Centre for Fuel Cell and Hydrogen Research at the University of Birmingham, an early advance has been achieved on integrated Pt-nanowire (PtNW) GDEs. The whole catalyst layer consists of only a monolayer array of single-crystal Pt nanowires which have an average diameter of ca. 4 nm and a length of 20–200 nm. Compared with the conventional more than 10 μm thick PEFC electrodes with Pt/C catalysts, this extremely thin catalyst layer with regular PtNW arrays dramatically reduce the mass transfer losses and boost the catalyst utilisation ratio,

which has been considered as one big challenge faced by PEFCs for automotive applications. Furthermore, the simple and effective in-situ growth approach in aqueous solution also addresses challenges facing the preparation of catalysts and fabrication of electrodes, e.g. non-scalable approaches and non-green processes.

By taking advantage of PtNW GDEs, the aim of this PhD study was to investigate the structure-property relationship to develop advanced one-dimensional (1D) Pt-based catalyst electrodes for the ORR. Not only considering the properties of catalysts themselves, attention was also paid to the behaviour of Pt NWs on GDLs, which collectively influences the performance of GDEs in PEFCs. The strategies adopted include temperature-controlled growth of Pt NWs on GDLs to obtain high performance GDEs; introduction of Pd to reduce Pt loading as well as improve growth and distribution behaviour to achieve superior PdPt-nanodendrite (PdPtND) GDEs; and optimisation of the GDL structures to facilitate the in-situ growth process of Pt NWs. All of the strategies serve the aim of designing advanced 1D nanostructures for high performance catalyst electrodes in PEFCs. The study involves the following subsidiary scientific and technological objectives:

1) To design and synthesise advanced 1D nanostructures by wet-chemical methods for high performance PEFC electrodes;
2) To study the morphology, structure and composition of the as-prepared GDEs by physical characterisations such as SEM, TEM, XRD, EDS, XPS, TGA, etc.;
3) To identify the effects of reaction temperature, hybridizing metal and GDL structure on the in-situ growth of Pt-based nanostructures;

4) To develop a better understanding of the structure-property relationship of PtNW GDEs;
5) To evaluate the catalytic activity and durability of catalysts as well as electrodes by single cell measurements.

1.4 Thesis Overview

A brief overview of each chapter of this thesis runs as follows: In **Chapter 2** an outline of the ORR features, a brief introduction of 1D nanostructures, as well as the review of recent development efforts on 1D electrocatalysts and electrodes based on 1D Pt nanostructures for ORR will be given. Then the synthesis method and processes for PtNW and PdPtND GDEs employed in this study will be explained in **Chapter 3**, as well as the techniques and principles used for physical characterisation and single cell testing of the as-prepared catalysts and electrodes. After that, in **Chapter 4**, the effects of the reaction temperature on the morphology and distribution of Pt NWs in-situ grown on GDLs are discussed. Possible mechanisms for temperature-controlled growth of PtNW GDEs based on the physical characterisation and single cell testing results are proposed. In **Chapter 5**, the introduction of Pd for controlling the nucleation and growth of PdPt nanostructures on GDLs will be studied by comparing the catalytic performance of PdPt GDEs resulting from various Pd to Pt atomic ratios. The influence of the GDL structure on PtNW GDE performance will be detailed in **Chapter 6**, including the carbon loading, carbon composition and carbon treatment in the microporous layer (MPL) as well as the polytetrafluoroethylene (PTFE) amount in the whole GDL. Finally, the thesis will be concluded in **Chapter 7** by summarising findings obtained from the study and providing recommendations for further work in the field.

CHAPTER 2

LITERATURE REVIEW

2. Literature Review

In this chapter the fundamental aspects of oxygen reduction reaction (ORR) including the possible mechanisms and the descriptors of ORR activity are briefly introduced. Then the definition of one-dimensional (1D) nanostructures and the common morphologies are outlined. A general explanation of the advantages of 1D catalysts for ORR and the development of the preparation methods are provided. Following this, an overview of the recent progress of 1D catalysts as well as electrodes based on 1D Pt nanostructures are summarised, highlighting the obtained novel structures and morphologies to reduce the Pt loading as well as improve the catalytic activity and durability. The chapter is concluded by a summary for the reviewed work and perspectives for the future development of this promising field.

2.1 Fundamental Aspects of Oxygen Reduction Reaction (ORR)

Despite demonstrated applications of polymer electrolyte fuel cells (PEFCs), the successful commercialisation has yet been slowed by the high cost, low catalytic activity and poor durability, in particular with respect to the catalysis of ORR at the cathode. This sluggish reaction has become the bottleneck of the development of PEFCs due to a substantial cathodic overpotential loss of about 300 mV, even on the best Pt catalysts [21]. Many studies have been conducted to find the catalytic mechanism of the multi-electron reaction, which could be helpful for the design of better catalysts to drive the rate-limiting ORR. However, the understanding of the ORR mechanism is not easy owing to the challenges of intermediates in-situ identification, kinetic data unambiguous interpretation as well as electronic structure explicit calculation [11].

The proposed ORR mechanisms such as dissociation, association and peroxo mechanism can be unified in a single scheme and is shown in Fig. 2.1 [11]. Although the detailed process of this complex multistep reaction is still under debate today, the commonly accepted ORR process in acid solution involves steps of O_2 adsorption, protons and electrons transfer, and the O-O bond breaking [22]. It is believed that the binding energies of reactive intermediates such as oxygenated (O*), hydroxyl (OH*) and superhydroxyl (OOH*) species determine the overall ORR process [21, 23]. For catalysts that bind these species too weakly, the rate is limited by proton and electron transfer to dissociate O_2, while for catalysts that bind these intermediates very strongly, the rate is limited by reaction products to desorb from the surface [24]. Therefore, the optimal catalytic activity can be achieved with "moderate" binding energies of reactive intermediates on the catalyst surface.

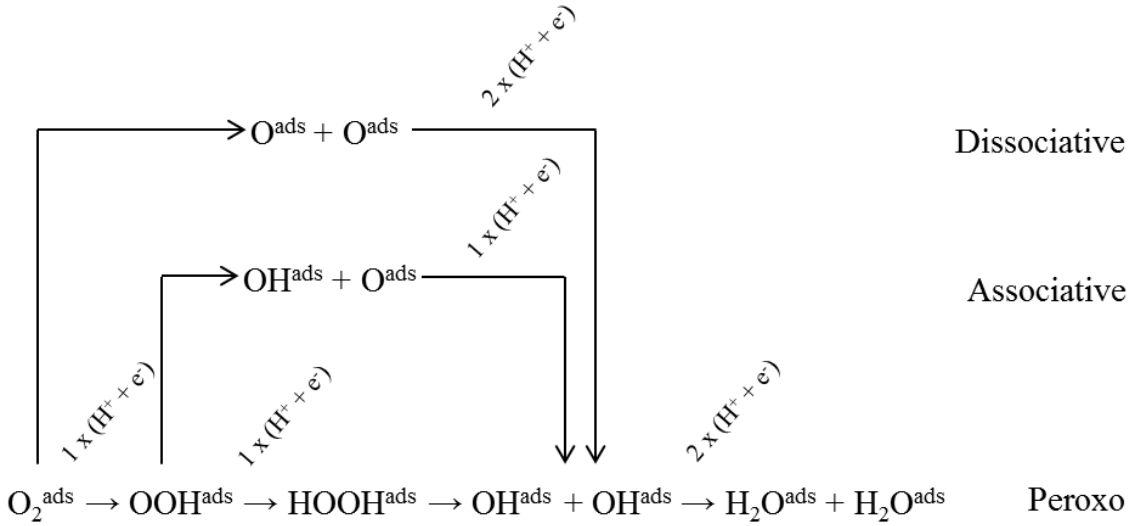

Fig. 2.1 Proposed ORR mechanism [11].

In consideration of this, the oxygen adsorption energy (ΔE_O) is considered as a good descriptor for the catalytic activity. A volcano plot (Fig. 2.2a) has been developed by

Nørskov et al. [25] to describe the relationship between ORR activity and ΔE_O. The metals located on the left side of the volcano peak bind oxygen too strongly while the right side of the metals have a weak oxygen binding ability. Among the pure metals, Pt is the most active one and it locates closest to the volcano peak. Besides pure metals, Pt-based transition metal alloys can possibly provide further enhanced activities, and the trend was explained by Greely et al. [22] with another volcano plot (Fig. 2.2b). It demonstrates that a surface that binds oxygen 0.0–0.4 eV more weakly than Pt (111) will be better, with 0.2 eV weaker than that of Pt as the optimum situation. Therefore, a lot of effort has been made to develop catalysts with ΔE_O around 0.2 eV more positive than that of Pt to improve the ORR kinetics [24].

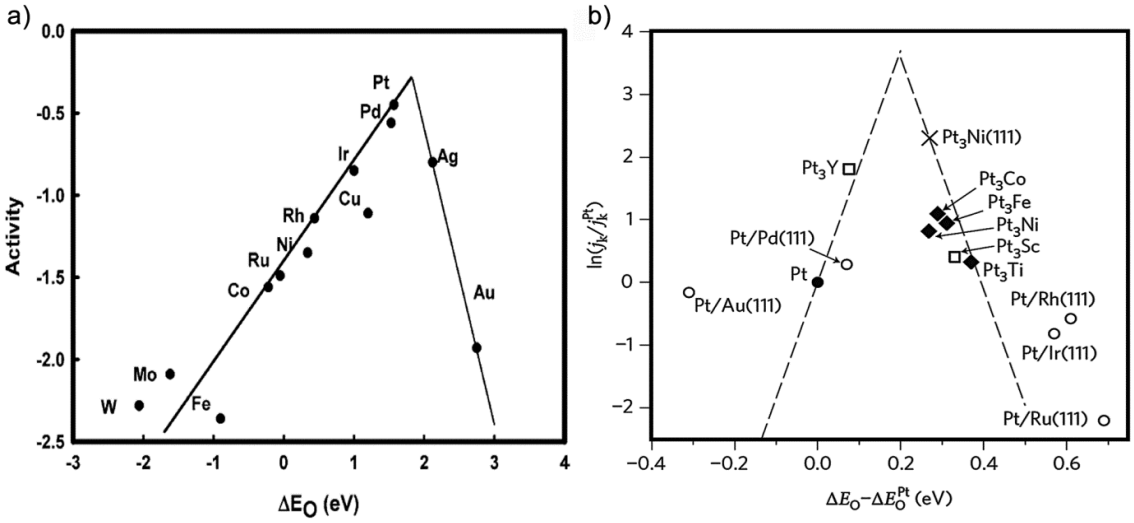

Fig. 2.2 Volcano plot for ORR activity of (a) pure metal and (b) Pt-based transition metal alloys versus the oxygen binding energy (ΔE_O) [22, 25].

Another descriptor to indicate adsorption energy of adsorbates on metal surfaces is the d-band centre (ε_d) model which illustrates the position of ε_d relative to the Fermi Level (ε_F) [26]. Unlike the difficult measurement of ΔE_O, ε_d is experimentally accessible and regarded as the simplest descriptor with good accuracy. The shift of ε_d results from the

variation of electronic structure which is further controlled by the filling state of electrons. Taking oxygen atom adsorption on the Pt surface as an example, the coupling of O 2p state with Pt d electrons causes oxygen resonance to split into two states: a fully filled bonding state below ε_F and a partially filled antibonding state across ε_F. A downward shift of ε_d to ε_F will lead to more filling of antibonding states and thus to a weaker bond, which is favorable to ORR [27]. Hence, the d-band centre is regarded as the ultimate indicator to predict the catalytic activity for ORR. The understandings provide the basis for the design of novel 1D nanostructured materials to catalyse ORR.

2.2 One-Dimensional (1D) Nanostructures

Since Richard Feynman gave his exciting lecture entitled "*There is plenty of room at the bottom*" in 1959, this dream statement has soon been realized with the explosive development of nanoscience and nanotechnology [28]. The products of this new field, nanomaterials, with at least one dimension in the nanometre range and different properties from those of atoms or bulk materials, have captured considerable research interests [29].

Among various nanomaterials, 1D nanostructures with two dimensions less than 100 nm have been synthesised in various configurations such as nanodendrites (NDs), nanowires (NWs), nanotubes (NTs), nanorods (NRs) etc. [30, 31]. Plenty of advanced approaches have been reported to develop 1D nanostructures with well controlled morphologies and compositions in recent years. Xia, Yang and co-workers [32] classified the fabrication of 1D nanostructures into four categories: i) anisotropic growth dictated by solid materials with crystallographic structures; ii) anisotropic growth deliberately directed by various templates; iii) anisotropic growth kinetically controlled by appropriate capping agent or

supersaturation; iv) miscellaneous methods to yield required 1D nanostructures with intriguing properties. A schematic summary of various morphologies of 1D nanostructures is shown in Fig. 2.3. Benefitting from the excellent properties, 1D nanostructures have been investigated in many research fields, such as electronics [33], catalysis [34], sensors [35], medicine [36], and also have captured considerable attention in PEFC applications.

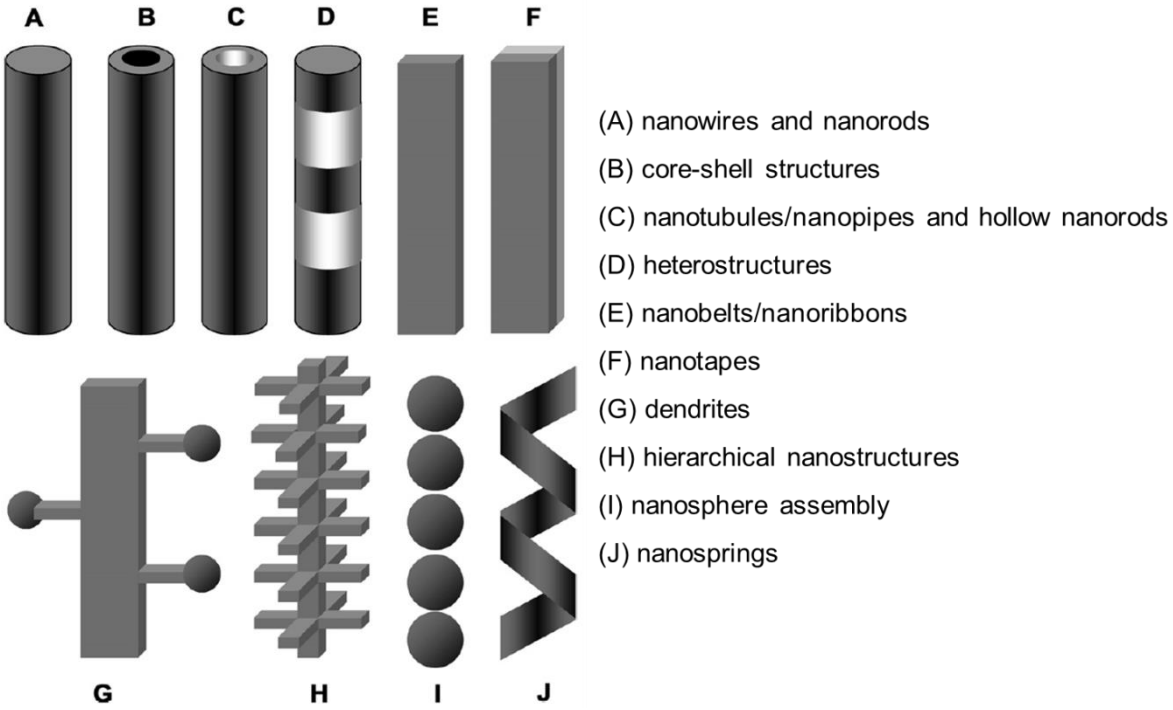

Fig. 2.3 A schematic summary of the kinds of quasi-one dimensional nanostructures [32].

2.3 Advantages of 1D Catalysts for ORR

In the past decades, studies have been intensively conducted for the development of high performance electrocatalysts for ORR with novel nanostructures [37, 38]. Previous results have established that the electrocatalytic activity and durability of electrocatalysts not only depends on the ratio of surface area to volume, but also arrangements of atoms, the surface structures and their morphologies [39]. For example, the high surface energy of extremely small nanoparticles often induces severe aggregation and Ostwald ripening, which are

considered as two of the main contributors to the fast degradation of electrocatalysts [40, 41]. Compared with zero-dimensional (0D) nanoparticles (NPs), 1D geometry is a promising morphology paradigm in the development of PEFC electrocatalysts, which can overcome some inherent drawbacks of 0D nanoparticles.

The 1D motifs, in particular single-crystal nanostructures, allow for the preferential exposure of low energy crystal facets and lattice planes with fewer lattice boundaries [29, 42]. The displayed facet would help reduce the surface energy of the whole system and be highly active for the catalysis. The smooth single-crystalline planes can also minimise the number of undesirable low-coordination defect sites which are less catalytically active and vulnerable to oxidation and decomposition. Besides, 1D nanostructures can facilitate the electron transport by the path directing effects in catalyst electrodes and thus enhancing the reaction kinetics on the catalyst surface [43]. Furthermore, it has also been predicted that when the diameter of 1D nanostructures decreases below a critical value of 2 nm, their electrocatalytic activity will be improved due to a surface contraction effect [44].

In terms of the catalytic stability, due to their asymmetric structure, 1D nanostructures are able to alleviate the dissolution, aggregation and Oswald ripening that the NPs usually suffer from [45]. Benefitting from the relative large scale length and the retained electrical conductivity as compared with NPs, 1D nanostructures are less inclined to require a carbon support for dispersing NPs and conducting electrons, thus can potentially address the support corrosion problem faced by commonly employed Pt/C catalyst [46].

All of these noteworthy advantages of 1D nanostructures provide the potential to reduce the precious metal loading without compromising the electrocatalytic activity but with a better durability. In light of this 1D nanostructures, as a new direction for superior electrocatalysts in PEFC applications, have attracted considerable efforts.

2.4 Preparation of 1D Catalysts for ORR

The earliest approach explored for the synthesis of Pt-based nanowires as fuel cell catalysts is the template preparation method, which starts from the use of mesoporous silica SBA-15 to produce a nanowire network [47]. The diameter and length of the prepared catalysts can be adjusted by controlling the pore diameter and length of templates. This straightforward route has been actively explored and a range of templates such as mesoporous silica [48], anodic aluminum oxide (AAO) [49], ZnO [50], etc. have been applied. Considering the complicated process of template removal, contrary to these hard templates, some soft templates including polymers [51] and viruses [52] have also been used to generate 1D morphology.

Apart from the template method, an electrospinning technique has also been employed to prepare 1D catalysts. With the ability to control the porosity, the fibre diameter and length, the produced 1D nanomaterials exhibit good catalytic performance [53]. However, in order to well disperse the inorganic precursors, surfactants are usually added and needed to be removed in the post-treatment process because the remaining surfactants may cover the catalyst surface, resulting in a low catalytic performance [54].

Although the template and electrospinning techniques could benefit for production of 1D morphologies, both of them require to remove either templates or surfactants to obtain pure products. Moreover, only polycrystalline nanostructures could be obtained during the synthesis process, which limits the further performance improvement [55]. Compared to polycrystalline 1D nanostructures, single-crystalline counterparts possess longer segments of smooth crystal planes, fewer lattice boundaries and a lower number of surface defect sites, which are confirmed to be beneficial for the electrocatalytic reactions [56]. The wet-chemical routes containing both organic solvent and aqueous solution approaches have been demonstrated to successfully synthesise single-crystalline 1D nanostructures for fuel cell catalysts.

In 2004, Xia et al. [57] for the first time demonstrated that the reaction rate is a good control tool for producing 1D Pt nanostructures. They prepared single-crystal Pt nanowires through a polyol process at 110 ^{o}C combined with poly(vinyl pyrrolidone) (PVP) as surfactant and a trace amount of iron species to further slow the reaction rate. After that Bi^{3+} was introduced to decrease the reaction growth rate of Pt-Bi nanowires [58]. However, similar to the electrospinning method, the polyol process also has the problem of removing surfactants. To address this problem, the oleylamine method, without using surfactants or ligands, was adopted to synthesise Pt-Fe nanowires [59]. Nevertheless, the high reaction temperature and the need of protective gas flow also limit the use of this method. Hence, there is a continuous need for the development of facile synthesis techniques which are environmental friendly, surfactant-free, cost-effective, etc. to obtain high-quality single crystalline 1D catalysts.

Based on the improved understanding of the crystal nucleation and growth mechanisms, various synthesis methods based on aqueous solvents have been developed to generate 1D structural motifs, including electrochemical deposition [60], galvanic replacement [61], thermal decomposition [62], seed mediated growth [63], organic-sol [64, 65], hydrothermal synthesis [66], and a combination thereof. In 2007, Sun et al. [67] successfully developed an efficient aqueous approach for the large-scale synthesis of single crystal Pt NWs by using formic acid as the reducing agent. This method is much simpler than the above-mentioned approaches because it doesn't need any templates, surfactants, organic solvents, capping agents or induced growth catalysts and can be directly performed at room temperature with mild formic acid as reductant, which makes it a promising method for the synthesis of 1D Pt nanostructures for fuel cell catalysts. Based on this method, they prepared self-assembled three-dimensional (3D) Pt nanoflowers (NFs) [68], multiarmed starlike Pt NWs [69], and 3D hybrid nanostructures with Pt NWs on Sn@CNT nanocable [70]. The single crystal effect of these 1D Pt nanostructures brought in excellent catalytic activity and durability towards ORR. Taking consideration of these advantages, this formic acid approach was employed throughout this PhD study.

2.5 State-of-the-art 1D Catalysts for ORR

Recent developments in material synthesis methods have enabled the fabrication of many novel highly active and stable 1D nanostructures with precisely controlled shape, composition and structure, bringing them a step forward to fuel cell research and development. Focusing on the very latest efforts on 1D electrocatalysts and concentrating on the rational synthesis of precious metal based elements, alloys, and hybrid structures, as well as non-precious metal catalysts (NPMCs) for ORR, the correlation between the

electrocatalyst structure and electrocatalytic performance is further understood in this PhD study. An overview of all references cited including the 1D nanostructures, the preparation approaches and the achieved results is listed in Table 2.1 at the end of this chapter.

2.5.1 1D Pt-based Catalysts for ORR

On account of the outstanding catalytic and electrical properties, coupled with the excellent corrosion resistance, Pt-based catalysts are still the most efficient electrocatalysts for ORR, especially in acidic medium as they can effectively impede the formation of adsorbed oxygenated intermediates at potentials above 0.8 V and improve ORR kinetics via lower energy pathways [71]. Therefore, to overcome the drawbacks of low intrinsic activity and poor stability of conventional Pt NPs, many efforts have been placed on the combination of the respective advantages of Pt and 1D nanostructures to design novel 1D Pt-based catalysts. Many exciting achievements have been reported in recent years, including pure Pt, Pt-based alloy and Pt-based hybrid catalysts.

2.5.1.1 1D Pt Nanostructured Catalysts for ORR

Ultrathin Pt Nanowires

Ultrathin 1D nanostructures have been explored to increase the surface-area-to-volume ratio for a large electrochemical surface area (ECSA) and thus an enhanced catalytic activity. Unlike either the extremely small nanoparticles or the large bulky volume of Pt NWs, these ultrathin 1D nanostructures don't suffer from the physical ripening and aggregation process or have a mass transport limitation in practical application. Assisted by chromium hexacarbonyl [$Cr(CO)_6$], Xiao et al. [72] synthesised Pt ultrathin NWs with a uniform diameter of 2–3 nm by a pyrolysis approach in oleylamine, showing comparable

mass activity (88 mA mg^{-1}) to that of Pt/C (85 mA mg^{-1}, 45 wt% Pt on Vulcan XC-72 carbon support). Ruan et al. [73] developed ultrathin multiple-twinned Pt NWs with a diameter of about 2 nm by biomimetic synthesis. The material achieved a mass activity of 144 mA mg^{-1}, a 58.2% increase compared with the Johnson Matthey (JM) Pt/C catalyst (20 wt% Pt on Vulcan XC72R carbon support). After a 6000-cycle accelerated degradation test (ADT), they only showed a loss of 14.2% of their initial ECSA, whereas the JM Pt/C catalyst suffered a severe degradation of 56.7%. Koenigsmann et al. [44] synthesised even thinner Pt NWs with a diameter of 1.3 nm through the reduction of H_2PtCl_6 by $NaBH_4$ in the mixture of N,N-dimethyl formamide (DMF) and toluene, followed by a treatment with an acid wash protocol. The as-prepared Pt NWs displayed an outstanding high specific activity of 1.45 mA cm^{-2}, which was nearly 7 times greater than that of Pt/C NPs. It is confirmed that the acid washing exfoliates the nanowires and re-dissolves amorphous platinum deposits so as to expose the active surface area of the wires themselves.

Pt Nanotubes

Another common 1D Pt nanostructure is Pt NTs, which normally show much higher specific surface area than the same size Pt NWs. Pt NTs are usually prepared by either the template method (e.g. AAO template) or the galvanic replacement reaction (e.g. from Ag or Cu nanowires). Through AAO templates [74] the nanotubes obtained are usually large nanoparticulate aggregates composed of small Pt crystallites. Although a higher specific activity can be achieved, the mass activity is usually lower compared with Pt/C. In terms of this, the galvanic replacement approach can partially address the drawback. For example, porous polycrystalline Pt NTs [75] with a wall thickness of 5 nm and an outer diameter of 60 nm were synthesised through galvanic displacement from Ag nanowires

and showed a slightly higher mass activity than Pt/C (Pt NT: 88 mA mg^{-1}; Pt/C: 84 mA mg^{-1}) and a much better durability. A post hydrothermal treatment can evolve the polycrystalline Pt NTs to single crystalline Pt NTs [76], which can further improve the catalytic activity and stability. Single crystal porous Pt dendritic NTs were also reported with Ag dendrites as templates [77]. The unique structure with characteristics of porous, hollow, hierarchical, and single crystallites not only renders a large surface area with high catalyst utilisation, but also improves mass transport and gas diffusion. Instead of using Ag nanowires, more cost-effective Cu nanowire templates have also been employed to prepare Pt NTs [78].

Other 1D Nanostructures

Other 1D nanostructures were also investigated for ORR. For example, vertically-aligned Pt NRs were fabricated on glassy carbon electrodes through the glancing angle deposition (GLAD) technique [79]. Pt nanochains (Pt NCs) were synthesised by a one-pot hydrothermal decomposition method through oriented attachment of spherical Pt nanoparticles [80]. Fu's group [81] prepared polyallylamine (PAH) functionalised single crystal Pt nanolances (Pt NLs) through a hydrothermal reduction route in a two-phase water-complex system. These reported novel 1D nanostructures exhibit a similar activity but a better durability compared to Pt nanoparticle catalysts.

Supported 1D Pt Nanostructures

The reported synergy effect between Pt catalyst and support [82] indicates that the ORR catalytic activity could be further improved by synthesising supported 1D Pt nanostructures. Pt NWs grown on SiO_2 [83] and $Ti_{0.7}Ru_{0.3}O_2$ [84], together with Pt NDs

anchored on bamboo-shaped carbon nanofibre arrays (CNFAs) [85] were synthesised through a hydrogen or formic acid reduction method. Excellent activities and stabilities were achieved, which can be attributed to the uniform dispersion of catalyst and the synergistic effect coupled with the electron donation from the support to Pt. As a class of two-dimensional carbon material, graphene has many advantages such as high electrical conductivity, huge surface area, unique electronic properties and high thermal and chemical stability, owing to the graphitised basal plane structure. Graphene-supported metal nanostructures have emerged as a new class of catalysts due to the metal-support interactions and improved conductivity of the catalysts. Most of them were synthesised via aqueous reduction processes, using either $NaBH_4$ or formic acid as reductant to synchronously reduce the Pt precursor and graphene oxide in one pot. Branched Pt nanostructures on graphene [86], Pt NWs on sulfur doped graphene (SG) [87] and Pt NDs supported on genomic-double-stranded-DNA (gdsDNA) modified reduced-graphene-oxide (rGO) [88] have all been prepared and demonstrated enhanced catalytic performance towards ORR. Compared with pristine graphene support, sulfur doped graphene seems to provide higher density of anchoring sites, which is favourable for Pt nucleation under lower reactant concentrations. The strong metal-support interactions between Pt and SG result in the uniform distributed Pt NWs on the support surface, as shown in Fig. 2.4 [87].

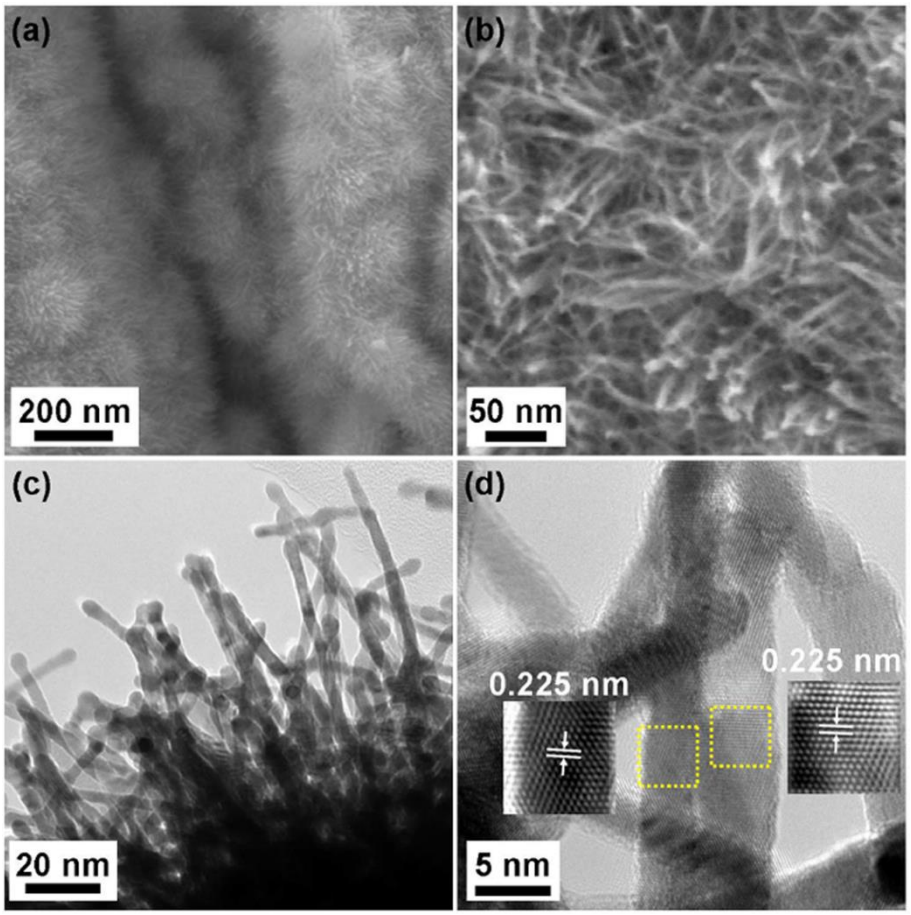

Fig. 2.4 (a, b) SEM, (c) TEM and (d) high resolution TEM images of SG-PtNW-3 catalyst. Insets in (d) are the Fourier filtered high resolution TEM images of the areas highlighted by the dashed yellow squares [87].

2.5.1.2 1D Pt-based Alloy Catalysts for ORR

To reduce the loading of expensive Pt while increasing the ORR activity, another very effective strategy is to introduce less-precious metals into the Pt catalysts to form bi- or multi- metallic alloy catalysts. Compared with Pt, density functional theory (DFT) demonstrated that alloying Pt with other metallic elements can lead to the change of the Pt-Pt interatomic distance, a downshift of the d-band centre, and the increase of d-band vacancy, leading to a more favourable adsorption of oxygen intermediates [89], allowing

the individual element to work synergistically and improving the catalytic performance [90]. 1D Pt-based alloy catalysts, combining both advantages of Pt multimetallic features and the 1D morphology, can mutually and synergistically accelerate the ORR rate.

1D Pt-based Precious Bimetallic Nanostructures

Various precious metals such as Pd, Ag and Au have been introduced in Pt to form alloy catalysts with different morphologies. Among these three precious metals, Pd is a promising candidate as it has a similar valence shell electronic configuration and lattice constant to Pt [91]. The lattice mismatch between Pt and Pd is only 0.77%, which endows the PtPd alloyed nanomaterial similar properties to pure Pt. Additionally, compared to Pt, the cost of Pd is slightly lower and the availability on earth is two hundred times higher [92]. Therefore, it is a good choice to add Pd into Pt to design better ORR catalysts.

By using Te nanowires as templates, PdPt alloy NWs were prepared in wet chemical solution [93]. The NWs have an average diameter of about 10 nm and length up to tens of micrometres. The rotating disk electrode (RDE) testing showed more than double the mass activity over the commercial 20% Pt/C. Starting from Pd nanowires, PtPd porous nanorods (PNR) were synthesised through a bromide-induced galvanic replacement reaction [94]. PtPd PNRs had an average diameter of 35 nm and a length up to 2 μm. The porous structure led to more than 3 times higher ECSA and 40% higher specific activity than Pt/C (40 wt%, from Alfa Aesar). This structure also exhibited an excellent durability with only 5.88% loss of the initial ECSA after the ADT, as compared to 40.4% loss of the commercial Pt/C catalyst. Wang's group [95, 96] prepared carbon supported PtM (M=Au, Pd or Cu) NRs by a formic acid reduction method. The as-prepared NRs have an average

diameter and length of 3.41 and 10–20 nm, respectively. The RDE test showed that the Pt_3Pd NRs had a specific activity of 21.63 μA cm^{-2} at 0.85 V, much higher than 5.66 μA cm^{-2} of Pt NRs, and a good stability with only 17% loss of the specific activity after 1000 cycles of ADT.

1D Pt-transitional Bimetallic Nanostructures

Previous computational and experimental studies pointed out that Pt alloyed with a transition 3d metal such as Fe, Co, Ni and Cu could show dramatic performance enhancement in ORR catalysis [22, 97, 98]. These studies proposed that the transition metals could decrease the absorbed OH species on the active Pt sites and provide kinetic stability against the dissolution of the less precious component, resulting in improved ORR activity and stability.

Nanoporous PtFe alloy NWs [99] with a diameter of 10–20 nm were synthesised by electrospinning and chemical dealloying techniques. The porous long nanowires interweaved to form a self-supporting network, showing 2.3 times higher specific activity and a better stability compared with Pt/C catalysts (40% Pt/C, E-TEK). Ultrathin PtFe and PtCo alloy NWs [100, 101] with diameters around 2–3 nm were prepared via an organic-phase decomposition and reduction process. The experimental results showed that the composition-dependent ORR activity could not be well represented by the PtFe and PtCo NWs owing to the loss of Fe and Co during the acetic acid treatment. If an annealing treatment was introduced, a Pt skin could be formed on the surface of the nanowires, enhancing the ORR activity and stability. Recently, vertically aligned PtNi alloy nanorod arrays were synthesised through a magnetron sputtering GLAD technique and exhibited a

superior mass activity 2.3 folds higher than that of pure Pt nanorods [102]. But the nanorods were also observed to lose activity during potential cycling concomitant with the loss of Ni in spite that a much improved stability was obtained as compared to Pt nanorods and Pt/C.

Since Xia's group [103] reported the preparation of precious metal (Pt, Pd, Au) nanotubes through a galvanic displacement reaction by using Cu nanowires as sacrificial templates, the synthesis of tubular electrocatalysts has received increasing interest, especially the bimetallic PtCu alloy NTs [104, 105]. In the reaction, Cu nanowires were partially replaced by Pt, followed by an acid treatment to remove some Cu, then NTs consist of PtCu alloy would be formed. Cu NWs here not only functioned as templates but also provided alloying of the remaining Cu atoms with Pt. Cui et al. [106] also prepared PtCu tubular catalysts with an AAO template. Thermal annealing was then introduced to increase the surface Pt atomic fraction and lattice ordering, and a potential cycling treatment in acidic electrolyte was used to partially dissolve Cu atoms to obtain a high ECSA. The catalysts displayed an enhanced specific and mass activity of 0.8 mA cm^{-2} and 232 mA mg^{-1} at 0.9 V in RDE measurement, respectively.

1D Pt-based Multimetallic Alloy Nanostructures

Going a step further from bimetallic alloy nanomaterials, multimetallic alloys have been the subject of intensive studies. The multicomponent nature with multimetallic alloys means different elements could work synergistically at a possibly higher efficiency than bimetallic alloys. Ternary PtNiFe NWs [107], PtFeM (M=Cu, Ni) [108] and PtNiCu NRs [109] have been synthesised in organic phase for ORR application. The results showed that

they generally possessed higher mass and specific activities than the binary alloy. Using Cu nanowires as sacrificial templates, Yu's group [110] synthesised PtPdCu nanoparticle nanotubes by galvanic displacement with partially sacrificial Cu nanowire templates, and followed by the electrochemical leaching of the non-noble metal Cu in the acidic electrolyte. Quaternary PtCuCoNi alloy NTs with an ultralow content of Pt have also been synthesised by an AAO template-assisted electrodeposition approach [111]. The multicomponent nature coupled with hollow configuration of NTs enabled an improved ORR activity.

2.5.1.3 1D Pt-based Hybrid Catalysts for ORR

Besides alloys, another efficient way to reduce the content of Pt is to develop Pt-based hybrid catalysts. Unlike alloy nanomaterials which usually have a homogeneous distribution, hybrid nanomaterials with core-shell structure or heterostructure architectures have a heterogeneous atomic arrangement [112]. In this case, the precious metal shell can partially address the leaching problem of transition metals in Pt-based alloy nanostructures under the crucial fuel cell operating conditions, thus slowing the degradation rate of catalysts [113]. Besides, they often offer a variety of parameters such as the composition of the core, the thickness of the shell, the structural morphology etc., which collectively control the catalytic properties towards ORR [114]. Similar to the alloy catalysts, Pt-based 1D hybrid catalysts not only minimise the Pt usage but also offer desired interactions to tune both electronic and surface strain effects, facilitating electron conduction and the stabilisation during the catalysis process as well [90].

1D Pt-based Core-Shell Structure

The unique structure of core-shell architectures captures growing interest in the research community. Pt-based core-shell catalysts are characterised by a thin Pt shell on proper metal cores. In general, the formation involves the growth of an interior core and the further growth of an exterior Pt shell on all faces of the core. The commonly used methods for the controlled synthesis of core-shell structures include the underpotential deposition (UPD) replacement, the structural rearrangement (dealloying or segregation) and the seed-mediated process [115].

By partially galvanic displacing Cu NWs, Pt with a layer thickness of 2 nm coated on Cu NWs were obtained [78]. An alternative catalyst system to using transitional metal cores is to include non-Pt precious metal cores, such as Pd or Au in the 1D structure for long-term stability in acidic media. Through Cu UPD displacement Pd-Pt core-shell NWs [116, 117] could be easily obtained. Without exploiting electrochemical procedures and the contaminating mediators such as Cu, Pd-Pt core-shell NWs were prepared in aqueous solution by a hydrogen sacrificial protective method [118]. Directly through the partial galvanic displacement of Pd NTs, Alia et al. also synthesised Pd-Pt core-shell NTs [119] with a wall thickness of 6 nm.

Core-shell structures with extended bi- or multi- metallic core or shell have also been reported. By kinetically controlling the nucleation and growth process, Pt-Au core-shell NRs with PtAu shell were prepared through a formic acid reduction process [120]. Treating FePtM (M=Cu, Ni) NRs with acetic acid as well as electrochemical etching, Sun's group [108] converted the ternary alloy NRs into core-shell FePtM/Pt NRs.

Recently, this group reported the further synthesis of FePtM/FePt (M=Pd, Au) NWs through a seed-mediated method [121]. The FePt shell with an optimal thickness of 0.8 nm exhibited a mass and specific activity of 1.68 A mg^{-1} and 3.47 mA cm^{-2}, respectively. Based on the outstanding ORR activity of Pt_3Ni, self-supported core-shell Au/Pt_3Ni NWs consisting of small-sized Pt_3Ni nanodendrites on Au nanowires were synthesised in organic phase by using oleylamine [122]. Compared with the Au/Pt core-shell structure, Au/Pt_3Ni displayed more than twice the ORR activity and durability.

1D Pt-based Heterostructure

In addition to the core-shell structure, the heterostructure offers an alternative hybrid catalyst model for the ORR and fuel cell applications. It can partially benefit from the synergistic effect of different metal compositions for accelerated ORR kinetics and at the same time be fabricated through an easier method compared with the core-shell approach. Xia's group [123] synthesised Pd-Pt bimetallic NDs through a seed-mediated approach and investigated the nucleation and growth mechanisms involved in the synthesis. Fig. 2.5 shows the growing process of Pt on Pd nanoseed surface. According to their study results, Pd seed played a crucial role in the formation of open, dendritic structure. Otherwise, only foam-like Pt aggregates were formed under identical conditions. This dendritic nanostructure could also be supported on MWCNTs to provide even higher activities [124]. Pt-on-$Pd_{0.85}Bi_{0.15}$ NWs with a diameter of 8.3 nm were synthesised in an oil phase [125]. The formation of this heterostructure was attributed to the introduction of metal Bi in the synthesis process. The as-prepared catalysts showed superior electrochemical performance, benefitting from the synergistic effect of trimetallic composition and the favouring electron transmission by 1D nanowire structure.

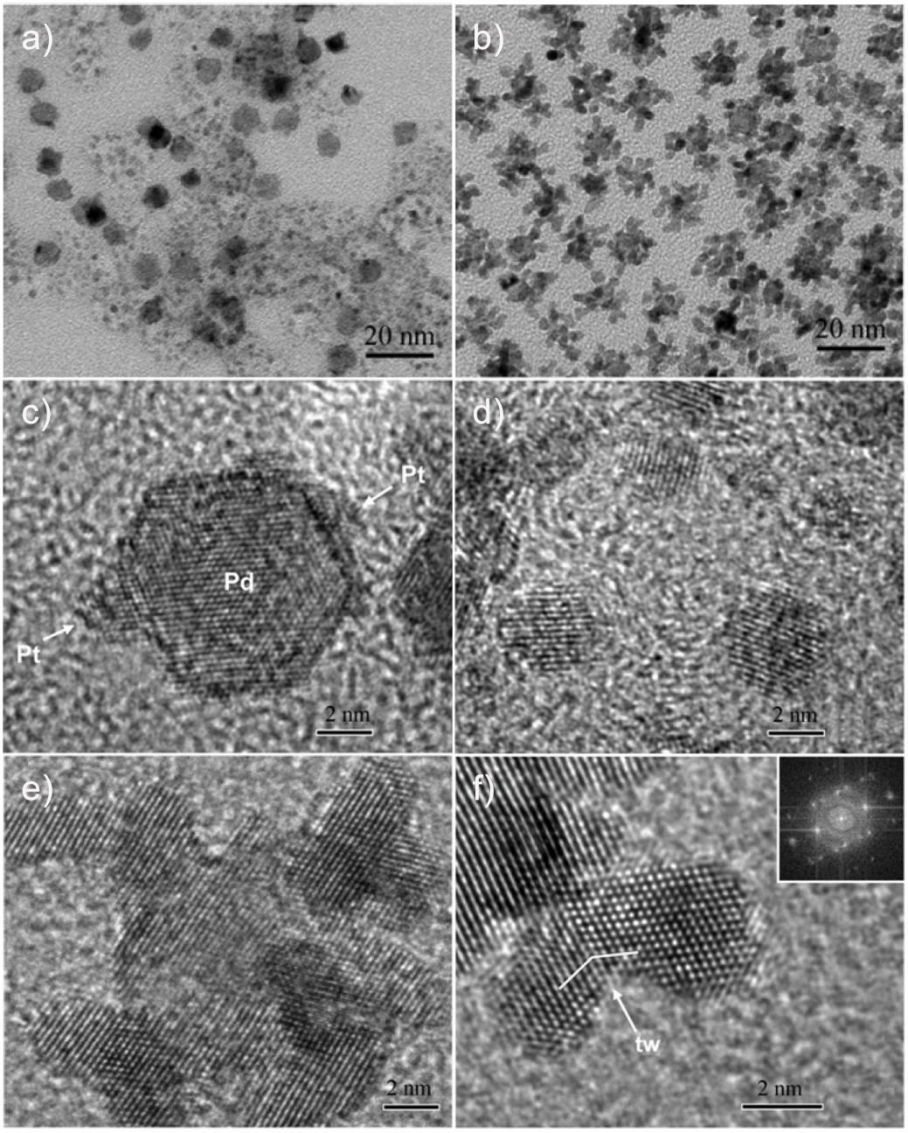

Fig. 2.5 (a,b) TEM images showing the morphological evolution of Pd-Pt nanodendrites. High-resolution TEM images of (c) an individual Pd-Pt particle and (d) the small Pt particles shown in (a). In (c), the Pt bumps on the Pd seed are indicated by arrows. (e) High-resolution TEM image of a single Pd-Pt nanodendrite. It can be seen that the lattice fringes are coherently extended from the Pd core to the Pt branches. (f) High-resolution TEM image taken from a Pt branch containing a single twin plane in its structure and the corresponding Fourier transform (FT) pattern (inset). A twin plane is indicated by tw [123].

2.5.2 1D Non-Pt based Catalysts for ORR

Although Pt-based nanostructures are still the most frequently used catalysts for ORR, the high cost and limited supply can hardly meet the demands for widespread applications of PEFCs. From a long-term point of view, exploring and synthesising non-Pt based catalysts seems to be an emphasis for future research. Due to the unique properties of the 1D morphology, great efforts have also been made to find 1D Pt alternative catalysts for ORR. Recent developments in this field reveal that the relatively cheap and abundant precious metals (Pd, Au and Ag) and their multimetallic alloys, transition metal chalcogenides, metal oxide based nanocrystals and N-doped carbon nanotubes can be potential substitutes for Pt-based electrocatalysts towards ORR in acidic or alkaline media.

2.5.2.1 1D Non-Pt Precious Metal Group Catalysts

1D non-Pt precious metal group catalysts, including Pd, Au, Ag and their alloys have all been reported in recent years, but mainly for ORR in alkaline media. Existing in the same periodic group and possessing similar lattice space, Pd is a potentially ideal alternative to Pt. Pd NWs [126, 127], Pd NTs [128], bimetallic CuPd NWs [129] and PdFe nanoleaves [130], as well as core-shell Pd-coated β-MnO_2 nanorods [131] were prepared and showed comparable or even higher ORR activity in either acidic or alkaline electrolyte. Au is another precious metal which has been extensively studied as electrocatalyst for ORR. Au NDs supported on graphene oxide [132], Au NTs [128], bimetallic PdAu NWs [133, 134], porous Pd shell coated Au nanochain networks [135] and core-shell structure Au@Pd nanothorns [136] were prepared through various synthesis methods and tested in alkaline solution. Besides serving as a template, recently, nanostructured Ag is also directly used in alkaline medium to catalyse ORR. Versatile 1D Ag@POA (poly(o-anisidine)) core-shell

nanostructures such as nanobelts, nanowires and nanocables by rational adjustment of the preparation conditions in water were fabricated [137]. Ag nanorods [138] and Ag nanowires supported on multi-walled carbon nanotube (MWCNT)-incorporated bacterial cellulose [139] and N-doped graphene [140] were also prepared. Besides, incorporating other metals into Ag was also studied to improve catalytic performance. 1D heterostructures such as octopus-tentacle-like Cu nanowire-Ag nanocrystals [141] and 1D Ag/Au/AgCl nanocomposites [142] were synthesised and exhibited enhanced ORR performance, benefitting from the presence of multiple junctions and a strong synergistic effect of their constituents.

2.5.2.2 1D Non-Precious Metal Catalysts (NPMCs)

Since cobalt phthalocyanine was initially reported to show catalytic activity for ORR, many attempts have been carried out to explore a variety of non-precious materials for further cost-cutting [143]. However, due to the large difficulties facing the preparation, the research for 1D NPMCs has only been focused on a few special materials. Transition metal chalcogenide Cu_2Se nanowires [144] with an average diameter of 70 nm have been prepared for ORR applications based on a solid-liquid phase chemical transformation method. Besides the transition metal chalcogenides, manganese oxide (MnO_x) has also been considered to be a good non-precious ORR catalyst due to its low cost, environmental friendliness and high activity. MnO_x doped CNTs [145], amorphous MnO_x nanowires supported on Ketjen carbon black [146] as well as Ni-α-MnO_2 and Cu-α-MnO_2 nanowires [147] were fabricated and evaluated for ORR activity. Spinel phase 1D nanostructures, like marokite $CaMn_2O_4$ nanorods [148] and $NiCo_2O_4$ nanowires [149] were also prepared for ORR applications and a comparable mass and specific activity with Pt/C catalyst has been

reported in alkaline electrolytes. Recently, N-containing carbon materials such as carbon nanotubes (CNTs) have also been intensively studied [150-152] as electrocatalysts for the ORR in acid or alkaline medium. The presence of N influences the O_2 chemisorption/activation as well as the formation of oxygen species on carbon and the surface oxidation, thus facilitating the ultimate O_2 reduction path. However, although all of the above-mentioned 1D NPMCs demonstrated acceptable ORR activity or durability, the mass and specific activity are rarely provided and the performance is still far from the state-of-the-art Pt/C catalysts. Further investigations should be continued to improve the catalytic performance towards ORR.

2.6 Electrodes from 1D Pt Nanostructures

Although the considerable progress has been achieved for catalysts themselves, especially on novel nanostructured catalysts, an increasing gap still exists between the pure material research and practical fuel cell application. Until now, Pt nanowire is still the only 1D nanostructure that has been tested in practical fuel cells. Because of the unusual morphology, nanoscale catalysts are usually very difficult to fabricate into fuel cell electrodes by a conventional process as is used for Pt/C electrodes. This problem also applies to 1D Pt nanostructures.

Carbon supported Pt NWs have been fabricated into PEFC cathodes using the conventional approaches (e.g. painting, printing, screening, etc.) and tested in single cells [153-157], as well as a test conducted with a 1.5 kW PEFC stack with PtNW cathodes under collaboration between Tongji University, University of Waterloo and General Motors [155]. Both power performance and durability test were performed. Although Pt

NWs showed a larger diameter (ca. 4 nm) compared with the conventional Pt nanoparticles, a similar power performance was still achieved benefitting from the unique catalytic activity of Pt NWs and the reduced mass transfer losses in electrodes with enhanced porosity. The characterisation for the catalysts before and after the durability test further indicated the enhanced stability of Pt NWs over Pt/C. However, the large porosity also resulted in a thicker catalyst layer and a loose electrode structure in PEFCs. Although an excellent stability was observed for Pt nanowire catalysts themselves, the poor electrode structure still could not bring a significant improvement to the electrode durability, and finally only a slight improvement was obtained. After a 420 h dynamic drive cycle durability testing, the PEFC stacks exhibited a performance degradation rate of 14.4% and 17.9% for the PtNW/C and commercial PtNP/C based cathodes, respectively [155]. The authors ascribed the majority of performance loss to the degradation of the commercial Pt/C anode materials. However, considering the much easier hydrogen oxidation reaction and the high catalyst loading of 0.2 mg_{Pt} cm^{-2} used in the anode, this performance loss should be mainly ascribed to the degradation of the cathode structure, as pointed out by Holdcroft in his review on fuel cell catalyst layers [158].

One important progress in PEFC electrodes in recent decades is the concept of the thin catalyst layer, which was introduced by the 3M Group in its nanostructured thin film (NSTF) catalyst electrode. The catalyst layer consists of a monolayer array of perylene whiskers (1 μm tall, 30 nm×55 nm in cross-section) with a surface coated 20 nm polycrystalline PtCoMn film, which was achieved by a decal substrate transfer approach [15, 159]. SEM images of the PtCoMn alloy catalyst sputter coating on the microstructured substrate supported whiskers before transferring are shown in Fig. 2.6. This thin catalyst layer with a regular

structure enabled a much higher catalyst utilisation ratio in the electrode to meet the U.S. DOE targets of mass activities. However, the approach is intrinsically limited by challenges facing water management issues in practical operation and the very low ECSA (only 10–15 $m^2\ g_{Pt}^{-1}$), as well as the limitations on the catalyst materials and structures used.

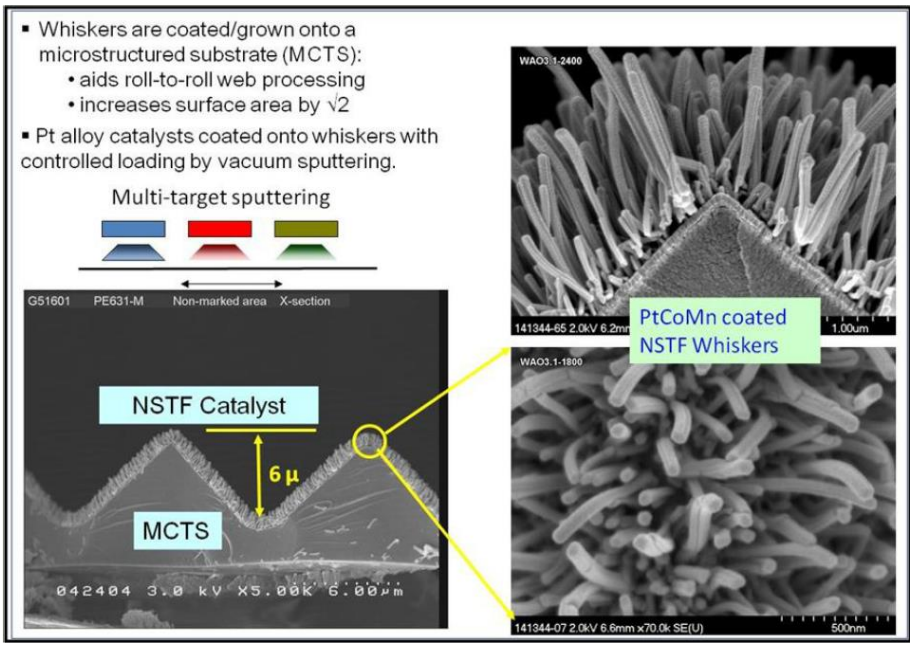

Fig. 2.6 SEM images of the PtCoMn alloy catalyst sputter coating on the microstructured substrate supported whiskers [159].

Another important advance on thin film electrodes was achieved by Du and his colleagues [160] in the Research Centre where this PhD study was undertaken. Integrated gas diffusion electrodes (GDEs) were prepared by in-situ growing single crystal Pt nanowires on gas diffusion layer (GDL) surfaces, taking the advantages of the unique simplicity of the formic acid reduction approach at room temperature [69]. The GDL was directly used as support substrate. The whole catalyst layer contains only a monolayer array of single-crystal Pt nanowires with a diameter of ca. 4 nm and a length of 20–200 nm. The obtained structure could be directly used as fuel cell electrodes. The extremely thin catalyst layer

and the regular structure significantly reduced the mass transfer losses and improved the catalyst utilisation in operation; and the removal of the carbon support in Pt/C potentially contributed to the improvement of the electrode durability, both of which have been considered as the challenges faced by PEFCs in automotive applications [15].

However, due to the hydrophobic surface of Pt nanowires, Nafion ionomer was still required for the catalyst layer to conduct protons within the PtNW electrodes, which has been successfully removed from the NSTF catalyst electrodes due to the hydrophilic pores which led to water flooding, thus facilitating proton transfers [161]. Furthermore, a well-controlled structure of the catalyst layer is also of great importance to control triple phase boundary (TPB) for a higher catalyst utilisation. The results demonstrated that an optimal Pt loading was necessary to achieve a better performance as a low Pt loading could not cover the entire GDL surface while a high loading resulted in little void volume for the gas diffusion [162]. To improve the electrode performance, active screen plasma nitriding (ASPN) was also introduced to the GDL surface before Pt NWs growth [163]. The nitrogen doping on GDL surfaces confined the Pt atoms in reaction to form tiny nuclei and finally produced ultrathin Pt nanowires with a diameter of only 3 nm, offering a larger ECSA for a better catalytic activity. The testing of a PtNW cathode with only half the catalyst loading showed an even better power performance than the electrode with Pt/C nanoparticles. Collaborating with Sui's group, this PtNW catalyst electrode was fabricated by in-situ growing Pt NWs on the carbon coated Nafion membrane or PTFE surface followed by a transfer step to the Nafion membrane surface, which were similar to the catalyst coated membrane (CCM) and decal methods used in fabricating conventional Pt/C electrodes, respectively [164-166]. In this case, a better contact between the catalyst and

the polymer electrolyte membrane (PEM) could be realized to achieve a better power performance. Even though a good performance has been obtained, it is still unclear how to control the growth of Pt NWs on the GDL surface to achieve a uniform distribution for a better electrode structure, which is significant to further improve the power performance and durability. This will be the main topic of this PhD study.

2.7 Summary and Perspective

Impressive progress has been achieved in recent years in the design and synthesis of 1D nanostructured materials as active and durable electrocatalysts for ORR in low temperature PEFC applications. Owing to the inherent properties, 1D nanostructured electrocatalysts have the potential to resolve many issues associated with their 0D counterparts and are regarded as the promising candidates for the replacement of contemporary 0D catalysts.

Among all the 1D catalysts, Pt-based nanocomposites are still the most practical catalysts due to their good electrocatalytic activity and durability. However, the rational design of self-supported, highly active and long-time lasting catalysts is still a challenge, especially when taking the complex reaction mechanism and harsh fuel cell operational conditions into account. Although great efforts have been devoted to fabricate non-Pt or even non-precious metal based catalysts to reduce the production cost, they often suffer from dissolution in acidic electrolyte and most of them can only performed in alkaline medium. At present, numerous work is focused on fabricating advanced catalysts possessing combined merits of 1D morphology, multi-composition as well as novel structures like core-shell, porous, hollow and ultrathin shapes. Nonetheless, it seems there is no in-depth understanding about the function of these factors at molecule reaction level. We also need

to pay attention to that most of the evaluation process for 1D nanostructures is only based on ex-situ electrochemical measurements in liquid electrolyte, and only Pt nanowires have been really tested in fuel cells, which is crucial for the practical application.

In light of these shortfalls, future work should focus on the following aspects: (i) an emphasis must be placed on the validation of catalyst performance in real fuel cell operating conditions; (ii) more in-depth theoretical and experimental studies are demanded to understand the structure-property correlations in electrocatalysis, in particular in practical fuel cell electrodes; (iii) an ongoing pursuit should be performed to develop facile, green and scale-up catalyst synthesis processes to realize high-yield catalyst production; (iv) there is a need for further reducing precious metal loadings to meet the requirement for fuel cell commercialisation; (v) continuous efforts should be made to optimise the geometry, composition and structure of 1D catalysts with characteristics of self-supported, appropriate adsorption for reactant species and favourable electron transfer pathways to further improve the catalytic activity and durability; vi) for the integrated GDE technology, the effects on the distribution of 1D nanostructures and the corresponding impact on the final electrode structure and performance need further investigation. It is believed that with the resolving of these challenges, 1D nanomaterials with novel structural motifs, diverse advantages, multifunctional performance and effective cost will show a high potential in electrocatalysis for low temperature PEFC applications.

Table 2.1 Type, preparation method, morphology and performance of one-dimensional catalysts for ORR.

Catalyst	Preparation	Morphology	Measurement	Activity	Reference
Pt NWs	Wet chemical synthesis	Diameter: 1.3–3 nm; length up to several microns	ORR	88 mA mg^{-1} 0.368–1.45 mA cm^{-2}	[44, 72, 73]
Pt nanowire membrane	Te nanowire template	Diameter: 12 nm; length: hundreds of nanometers	ORR	Comparable with JM Pt/C	[167]
Pt NTs	AAO, Ag or Cu nanowires templates	Wall thickness: 2.5–11 nm	ORR	84.5–240 mA mg^{-1} 0.369–2.39 mA cm^{-2}	[74-78]
Pt NRs	Glancing angle deposition (GLAD) technique	Diameter: 5 up to 100 nm; length: 50–400 nm	ORR in $HClO_4$	Lower mass and higher specific activity than Pt/C	[79]
Pt nanochain or nanolance	Thermal decomposition or Hydrothermal methodology	Diameter: 5–15 nm	ORR	3.24 mA cm^{-2}	[80, 168]
Single Pt NW electrode	UPD or lithography patterning	Radius: 6–130 nm; length: 40 nm.	ORR in KOH and H_2SO_4		[169, 170]
Supported Pt NWs	Spray drying and Formic acid reduction	Diameter: 4–13.9 nm	ORR in acid	33–158 mA mg^{-1} 0.415 mA cm^{-2}	[83-85]
Pt NWs/graphene	$NaBH_4$ or formic acid reduction	Average diameter: 2–5.8 nm	ORR in acid	up to 1010 mA mg^{-1} up to 1.5 mA cm^{-2}	[86-88]
Pt NWs/C	Acid reduction or electrospinning	Diameter: 4.0–85 nm	H_2/air PEFC cathode	max power density: 748.8	[153, 154, 156]
Pt NW arrays	Formic acid reduction	Diameter 4 nm	DMFC cathode	64 mW cm^{-2} with 2 mg cm^{-2} Pt loading	[163]
Pt NW arrays	Formic acid reduction	Diameter: 4 nm	Integrated PEFC cathode	max power density: 340–390 mW cm^{-2}	[160, 164]
Pd-Pt ND, NW and NR	Chemical and template approach	Diameter: 10–35 nm	ORR in $HClO_4$ and KOH	up to 3810 mA cm^{-2}	[93-95, 123, 171]
Pt-Au NRs	Formic acid reduction	Diameter:10–20 nm	ORR in $HClO_4$	48 mA mg^{-1}	[95]
Pt-Fe NWs	Electrospinning / Organic phase reduction	Diameter: 2.5–10nm	ORR in accid	77.1–844 mA mg^{-1} 0.3831.53 mA cm^{-2}	[99-101]
CoPt NWs	Organic phase reduction	Diameter: 2.5 nm;	ORR in $HClO_4$	0.64 mA cm^{-2}	[101]
PtNi NR or NF	Sputtering/template	Diameter: 25–100 nm	ORR in $HClO_4$	440 mA mg^{-1} 1–4.41 mA cm^{-2}	[102, 172]
Pt-Cu NTs	AAO template/ Galvanic replacement	Wall thickness: 30.3 nm	ORR in $HClO_4$	190–232 mA mg^{-1} 0.8–2.57 mA cm^{-2}	[104, 106]

Pt-Cu NRs	Polyol or formic acid reduction	Diameter: 5 nm; length: 6–20 nm	ORR in $HClO_4$	44–48 mA mg^{-1} 0.215 mA cm^{-2}	[95, 109]
PtNiFe NWs or NRs	Organic phase	Diameter: 2 nm; length: 20 nm	ORR in acid	5.32 mA mg^{-1} 0.0077 mA cm^{-2}	[107, 108]
PtCuM NRs, NTs (M=Ni, Fe, Pd)	Wet chemical /template	Diameter: 2–30 nm; length: 20±2 nm	ORR in $HClO_4$	64–103.4 mA mg^{-1} 0.251–1.369 mA cm^{-2}	[108-110]
PtCuCoNi NTs	AAO templates	Wall thickness: 30–10 nm	ORR in $HClO_4$	190 mA mg^{-1} 0.18 mA cm^{-2}	[111]
Pt coated Cu NWs	Galvanic displacement	Outer diameter: 100 nm; Pt layer: 2 nm	ORR in $HClO_4$	82 mA mg^{-1} 1.501 mA cm^{-2}	[78]
Pd-Pt core-shell NWs, NTs	UPD or galvanic displacement	Core diameter: 2.0 nm; wall thickness: less 6 nm	ORR in $HClO_4$	340–1830 mA mg^{-1} 0.58–0.77 mA cm^{-2}	[116, 118, 119, 173]
Au/Pt or PtM (M=Au, Ni) NWs and NRs	Chemical reduction		ORR in acid	41.3–479 mA mg^{-1} 0.308 mA cm^{-2}	[120, 122]
FePtM/Pt or FePt (M=Pd, Au) NWs or NRs	Chemical reduction	Shell thickness: 0.3–1.3 nm	ORR in $HClO_4$	103.4–1680 mA mg^{-1} 1.369–3.47 mA cm^{-2}	[108, 121]
Pt-on-Pd NDs	Ascorbic acid reduction	Branch width: 2–3 nm	ORR in H_2SO_4	36.5 mA mg^{-1} 0.342 mA cm^{-2}	[124]
Pt-on PdBi NW	Oil phase synthesis	Diameter: 8.3 nm;	ORR in $HClO_4$	1160 mA mg^{-1} 1.48 mA cm^{-2}	[125]
Pd NWs	Template method	Diameter: 45 nm,	ORR in $HClO_4$	1.84 mA cm^{-2}	[126]
PdCu NWs	Colloidal method	Width: 18.2 nm	ORR in $HClO_4$		[129]
PdFe nanoleaves	Wet chemical method	Diameter: 2.3 nm	ORR in NaOH	159 mA mg^{-1} 0.305 mA cm^{-2}	[130]
Core-shell MnO_2@Pd-NRs	Electroless deposition	Diameter: 40–50 nm	ORR in KOH	500 mA mg^{-1}	[131]
Au NDs/Graphene	Wet-chemical	Diameter: 35 nm	ORR in KOH		[132]
Pd-Au NTs	Galvanic displacement	Wall thicknesses: 6 nm	ORR in KOH	240 mA mg^{-1} 1.98 mA cm^{-2}	[128]
PdAu NWs	Template or wet-chemical	Diameter: 2–50 nm;	ORR in $HClO_4$	0.4–0.49 mA cm^{-2}	[133, 134]
PdAu nanochain	Template	Diameter: 5.6 nm;	ORR in NaOH		[135]
Au@Pd core-shell nanothorns	Co-chemical reduction	Diameter: 30–50 nm	ORR in KOH		[136]
Ag nanobelt	Hydrothermal method	Thickness: 40–60 nm;	ORR in NaOH		[137]
Ag NRs	Polyol process	Diameter: 83±3 nm	ORR in KOH		[138]

Ag NWs/MWCNTs	Polyol process				[139]
Ag NWs/ N-graphene	Hydrothermal method		ORR in KOH		[140]
Ag/Au/AgCl nanocomposites	Galvanic replacement	Ag nanowire diameter: 500–550 nm	ORR in NaOH		[142]
Cu-Ag NWs	Seed-mediate	Diameter: 16 nm;	ORR in KOH		[141]
Cu_2Se nanowires	solid-liquid phase chemical transformation	Diameter:50–70 nm	ORR in KOH	3.5–12 mA mg^{-1}	[144]
N-CNTs	Wet chemical and annealing		ORR in H_2SO_4 and KOH		[151, 152]
N-Fe/Fe_3C@C	Wet chemical and annealing	Diameter: 20–30 nm;	ORR in PBS		[143]
MnOx-CNTs	Electrochemical deposition		ORR in KOH		[145]
MnOx NWs	Polyol method	Diameter: 10 nm	ORR in KOH		[146]
Graphene-Ni-MnO_2 and Cu-MnO_2 NWs	Hydrothermal method		ORR in alkaline		[147]
$CaMn_2O_4$ NRs	Solvothermal method	Diameter: 150–300 nm;	ORR in KOH	70 mA mg^{-1} 0.0148 mA cm^{-2}	[148]
$NiCo_2O_4$ NWs	Coprecipitation	Diameter: 50 nm	ORR in KOH		[149]
$RuVO_x$ NWs	Vapor–phase transport	Dimension: 182	ORR in PBS		[174]

CHAPTER 3

MATERIALS AND EXPERIMENTS

3. Materials and Experiments

This chapter explains the experimental procedures adopted in this thesis, which are based on bringing together the chemistry of 1D nanostructure synthesis and the engineering of fuel cell test. Detailed experimental processes are introduced for the preparation of gas diffusion electrodes (GDEs) with Pt nanowires (NWs), PdPt nanodendrites (NDs) and self-painted microporous layers (MPLs) with different carbon loadings, carbon compositions, carbon treatment situations and polytetrafluoroethylene (PTFE) loadings, as well as the fabrication of membrane electrode assemblies (MEAs). The physical characterisation techniques for the distribution, morphology, structure and composition of the as-prepared catalysts and corresponding GDEs are discussed, including SEM, TEM, XRD, TGA, EDS and XPS. The detailed testing procedures of the as-prepared GDEs in the single fuel cell are also presented.

3.1 Chemicals, Materials and GDE Fabrication

3.1.1 In-situ Growth of Catalyst Nanostructures on GDLs

Pieces of 4×4 cm^2 Sigracet® 35BC carbon paper were used as the fuel cell GDLs and supports for catalyst nanostructures growth. Before use, the obtained GDLs were rinsed by ultrapure water (18.2 MΩ cm, Millipore water system) and isopropanol (IPA) (C_3H_8O, >99.5%, Fisher Scientific UK), respectively, and treated in IPA solution in ultrasonic bath (U300, Ultrawave, UK) for 30s. For the in-situ growth of catalyst nanostructures on GDLs, a certain amount of metal precursor solution coupled with formic acid was added into the ultrapure water in a 6 cm glass petri dish. Then the carbon paper was immersed in the mixed solution and stored at a fixed temperature for the nanostructure growth.

In-situ Growth of Pt NWs on GDLs at Different Temperatures

Typically, to grow 0.4 mg cm^{-2} Pt NWs on a piece of 16 cm^2 carbon paper, 17 mg hexachloroplatinic acid hexahydrate ($H_2PtCl_6 \cdot 6H_2O$, ≥37.50% Pt basis, Sigma-Aldrich UK) and 0.53 mL formic acid (CH_2O_2, 98%, Sigma-Aldrich UK) were added into 10.6 mL ultrapure water. The carbon paper was immersed in the mixed solution and stored at room temperature for Pt nanowire growth. The reaction took place by the following chemical reaction:

$$H_2PtCl_6 + 2HCOOH \rightarrow Pt + 2CO_2\uparrow + 6HCl \qquad (3.1)$$

The growth of nanostructures was completed when the colour of the solution changed from yellow to colourless. After that, the samples were rinsed using ultrapure water and IPA, followed by drying at 40 ^oC overnight. The as-prepared carbon paper samples with in-situ grown Pt NWs were directly used as GDEs at the cathode side. The whole fabrication process is shown in Fig. 3.1.

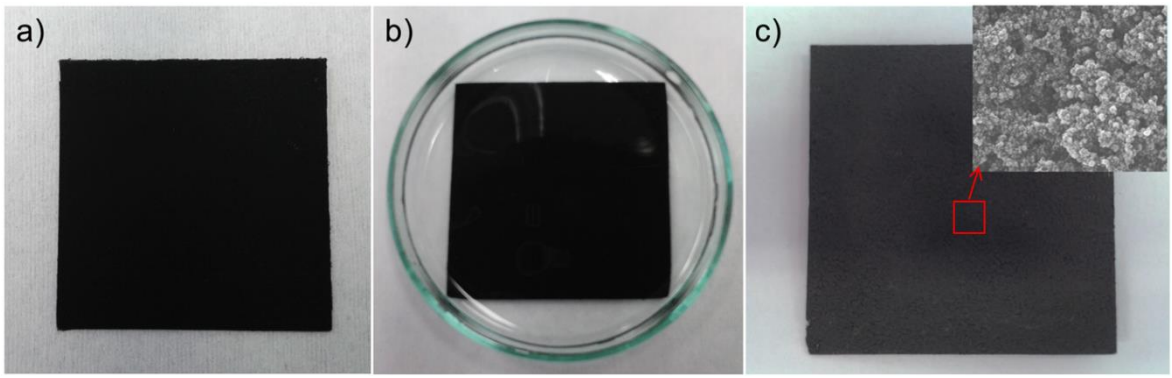

Fig. 3.1 Fabrication process for in-situ growing nanostructures on GDL. a) GDL; b) in-situ growing nanostructures on GDL; c) GDE with in-situ grown nanostructures (inset is the SEM image of the red square).

To understand the influence of the growth temperature on the PtNW GDE performance, the in-situ growing of Pt NWs on GDL surfaces was investigated at various temperatures of 5, 15, 25, 35, 40 and 50 ^{o}C.

In-situ Growth of PdPt Nanostructures with Different Pd Atomic Percentages

The same in-situ growth process as for PtNW GDEs was employed except for the addition of palladium(II) chloride ($PdCl_2$, anhydrous, 60% Pd basis, Sigma-Aldrich UK) in the reaction solution. The PdPt nanostructures with Pd atomic percentages of 50, 25, 10, 5, 2.5 and 0.5% were studied. The reactions took place by chemical reactions according to Equation 3.1 and the following equation:

$$PdCl_2 + HCOOH \rightarrow Pd + CO_2\uparrow + 2HCl \qquad (3.2)$$

3.1.2 Fabrication of Self-made GDLs with Painted MPLs

GDLs usually contain double layers: one is the macroporous substrate layer and the other is MPL coated on the surface of the substrate [175, 176]. The substrate is usually made from porous stacked carbon fibre and treated by a water-proofing agent, e.g. PTFE [177, 178]. The MPL is mainly composed of carbon powder and PTFE as the hydrophobic polymeric binder [179]. The reason for adding PTFE in both layers is to make the GDL surface hydrophobic, thus effectively removing the generated water to avoid water flooding in fuel cell operation [180]. Fig. 3.2 depicts the naming rules of GDLs from Sigracet® used in this work [181]. To evaluate the GDL features for in-situ growing Pt NWs, YC GDLs were directly used as supports to study the effect of PTFE loading in substrates while self-made GDLs with painted MPLs on 35BA substrates were used to

investigate the effect of carbon loading, carbon composition, carbon treatment and PTFE loading in MPLs.

Y	A	B	C	D	E
% PTFE	0	5	10	20	30

Fig. 3.2 Naming rules for GDLs from Sigracet®: AA means a plain substrate; YA indicates different PTFE loadings in the substrate without the MPL; YC indicates different PTFE loadings in the substrate with a standard MPL containing 20% PTFE.

Carbon Loading in MPLs

According to the data of areal weight of 35BA (54 g m^{-2}) and 35BC (110 g m^{-2}) GDLs provided by the Sigracet®, the calculated carbon loading in the standard Sigracet® MPL is 4.48 mg cm^{-2} plus 1.12 mg cm^{-2} PTFE. The carbon loading is much higher than the reported value from literature, which is usually in the range of 0.5–2 mg cm^{-2} [182-184]. To find the optimal amount for in-situ Pt NWs growing, the carbon inks for MPLs were prepared by mixing Vulcan XC-72R carbon black (Fuel cell store, USA) with the loading of 1, 3, 4, 4.48 and 5 mg cm^{-2} and 20% PTFE (60 wt% dispersion in H_2O, Sigma-Aldrich UK) based on the total MPL weight.

Carbon Composition in MPLs

A mixture of Vulcan XC-72R carbon black (CB) and acetylene black (AB) (100% compressed, 99.9+%, Alfa Aesar, USA) were used. The optimal carbon loading obtained from work planned in the above section was employed and the percentage of CB was changed from 0, 10, 25, 40, 50, 60, 75, 90 to 100% in the mixture of CB and AB. Based on the total MPL weight, 20% PTFE was added in all the carbon inks.

Carbon Treatment in MPLs

The as-received CB and AB were immersed in nitric acid (HNO_3, ≥69%, Sigma-Aldrich UK) and treated by ultrasonic bath for 30 min and stirred for 20 h at room temperature [185]. After that the acid treated CB and AB were washed with ultrapure water and dried at 40 ^{o}C overnight. According to the optimal carbon loading, HNO_3 treated pure CB, pure AB and mixtures based on the optimal carbon composition were used to prepare carbon inks.

PTFE Loading in MPLs

With the optimal carbon loading and carbon composition, MPLs were made by using various PTFE loadings of 5, 10, 15, 20, 25, 30 and 40% (to total MPL weight) in carbon inks.

The as-prepared carbon inks were dispersed in a mixture of water and IPA solution and were treated by ultrasonic bath for 15 min and then by ultrasonic horn (130 W, 30% amplitude, VCX 130, SONICS, USA) for 10 min, followed by brush painting on the 35BA substrate. The painted GDLs were dried at 40 ^{o}C in the oven for 1h. After that, they were

treated at 240 ^{o}C for 30 min in air to remove the remaining dispersing agent and then at 350 ^{o}C for 30 min to improve the distribution of PTFE throughout the MPL [186]. The treated GDLs were ready to use for the growth of Pt NWs.

3.2 Characterisations

3.2.1 Scanning Electron Microscopy (SEM)

Scanning electron microscopy (SEM) was used for observing the sample surface. A field emission scanning electron microscope (FE-SEM, JEOL 7000F with Oxford Inca EDS) with a resolution of 1.2 nm at 20 kV and a wide magnification ranges from 25 to 100,000 times was used in the experiment. GDE samples with in-situ grown Pt and PdPt nanostructures were directly cut and pasted on the specimen holder to check the morphology and distribution of catalysts on the GDL surface.

3.2.2 Transmission Electron Microscopy (TEM)

Transmission electron microscopy (TEM) is a very powerful tool for characterising material features. The analysis was performed to provide information about the sample features such as microstructure, crystal structure, and defects. High resolution TEM imaging was conducted to understand the crystal structure of the single nanowires. For preparing TEM samples, Pt and PdPt nanostructures were scratched from the GDE surface and dispersed in ethanol by ultrasonic treating for 30 min. After that, a drop of the solution was pipetted onto an Au or Cu grid with holey carbon film and left to dry in air. TEM images were captured using a high-resolution transmission electron microscope (HR-TEM, Philips CM200 FEG) with an accelerating voltage of 200 kV. Selected-area electron diffraction (SAED) pattern was obtained to confirm the crystallinity of the nanostructures.

3.2.3 X-Ray Diffraction (XRD)

As a non-destructive technique, X-ray diffraction (XRD) was used to identify the general crystal structure of different catalyst nanostructures grown on GDL surfaces. To perform XRD analysis, GDEs were cut to the right size and directly stuck on a customed sample holder. XRD patterns were recorded with a Siemens D5005 powder X-ray diffractometer operated at 40 kV and 30 mA using Cu Kα (λ=0.15418 nm) radiation. The scanning 2θ ranged from 20 to 90° with a step size of 0.0147457°. The holding time was 0.35 second per step.

3.2.4 Thermogravimetric Analysis (TGA)

In this work, thermogravimetric analysis (TGA) was adopted to estimate the amount of catalysts deposited on the GDL surface. The PTFE loading and the carbon decomposition behaviour of GDLs were also interpreted from the TGA curve. The analysis was conducted by a TGA instrument (NETZSCH, TG209F1) under an air flow rate of 40 ml min^{-1} and a heating rate of 10 ^{o}C min^{-1} to 900 ^{o}C.

3.2.5 Energy-Dispersive X-ray Spectroscopy (EDS)

Energy-dispersive X-ray spectroscopy (EDS) integrated with TEM was employed to analyse the chemical elements and composition of GDE samples. In the analysis, EDS spectra were obtained by an Oxford Instruments ultra-thin window (UTW) EDS detector associated with Philips CM200 HR-TEM to detect the existence of PdPt nanostructures on GDLs and determine the relative atomic composition of Pd and Pt.

3.2.6 X-ray Photoelectron Spectroscopy (XPS)

X-ray photoelectron spectroscopy (XPS) was conducted to identify the surface elemental composition of catalysts and to determine the local chemical environment within solid samples. Besides, the peak shift resulting from the variation of atom chemical states was also used to evaluate the oxidation state of elements due to the synergistic effect from alloy and hybrid. In this work, XPS analysis was conducted on an XPS spectrometer (AXIS Nova, Kratos Analytical) by using high power monochromatized Al Kα radiation (1486.6 eV) at the National EPSRC XPS User's Service (NEXUS) at Newcastle University.

3.2.7 Ultraviolet-Visible Spectroscopy (UV-Vis)

Ultraviolet-visible spectroscopy (UV-Vis) was used to determine the absorption peaks of precursor solutions and monitor the reaction evolution with time. Absorption spectra were recorded on an UV-Vis spectrophotometer (Thermo Scientific Evolution 60S, U.S.) with a 1 cm quartz cell.

3.2.8 Drop Shape Analyser

The drop shape analyser (EasyDrop Standard, Kruss) was employed to measure the water contact angle on the self-made GDLs with different PTFE loadings in the MPLs. During the measurement, a 5 μL water droplet was placed on the GDL surface and the analysis was conducted by using the DSA1 software. The water contact angle formed by the intersection of the liquid-solid interface and the liquid-vapour interface was determined as an indication of the hydrophobic degree of the GDL.

3.3 Membrane Electrode Assembly (MEA) Fabrication

Membrane electrode assemblies (MEAs) with an active area of 16 cm^2 were fabricated using commercial Johnson Matthey GDEs (ELE1065-0983, Pt nanoparticle at a loading of 0.4 mg_{Pt} cm^{-2} on Sigracet® 34BC) as anodes and the as-prepared Pt or PdPt GDEs as cathodes. Before being fabricated into MEAs, both of the anode and cathode GDE surface were coated with a thin layer of Nafion ionomer (Nafion loading of ca. 0.6 mg cm^{-2}). The Nafion dispersion was prepared by mixing 90.5 µL Nafion® solution (D1021, 10 wt%, Ion Power Inc.) with 140 µL IPA and treated in an ultrasonic bath for 30 min. The Nafion painted GDEs were dried in the air before assembling. After that, the two GDEs were sandwiched at both sides of a 6×6 cm^2 DuPont Nafion 212 membrane and hot pressed at 125 ^oC under 4.9 MPa pressure for 2 min to obtain the MEA. The detailed fabrication process is shown in Fig. 3.3.

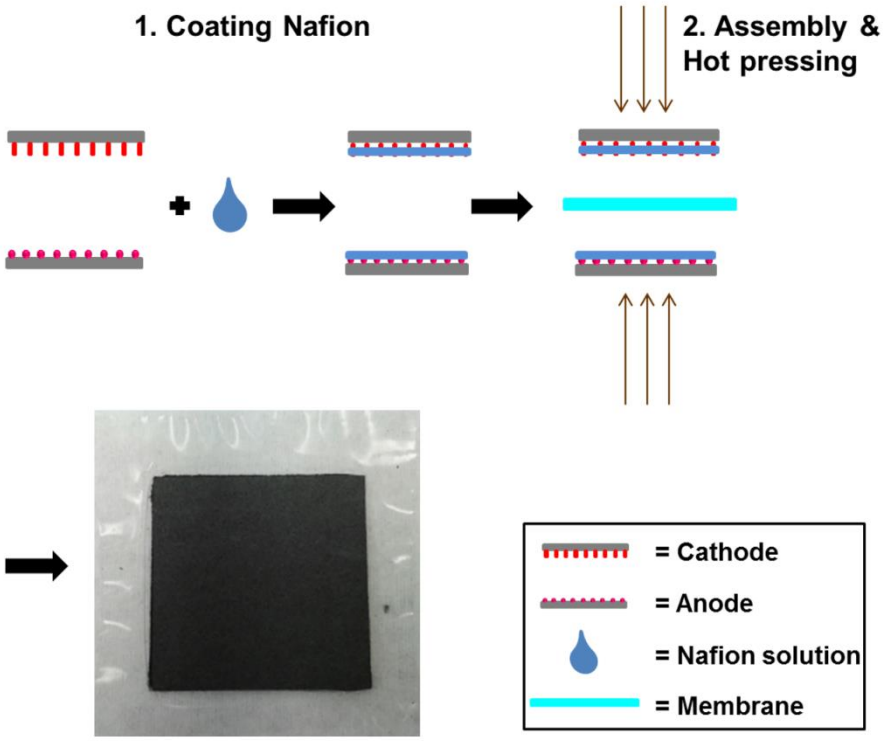

Fig. 3.3 The schematic for MEA fabrication.

For comparison, an MEA was fabricated simultaneously with a cathode of state-of-the-art commercial Pt/C (45.91 wt%) catalyst (TEC10E50E, Tanaka KikinzokuKogyo K. K. (TKK), Japan). The catalyst was mixed with Nafion® solution (10 wt%) and IPA to make catalyst ink, which was treated with ultrasonic horn for 30 min and then hand painted onto the GDL surface at a Pt loading of 0.4 mg_{Pt} cm^{-2}. The as-prepared GDE was dried overnight and used to make the reference MEA.

3.4 Fuel Cell Testing

The fabricated MEAs were tested in a PEFC test stand (PaxiTech-BioLogic FCT-50S) to study the electrode performance, including polarisation curve and electrochemical impedance spectroscopy (EIS). In-situ cathode cyclic voltammetry (CV), accelerated degradation test (ADT), as well as intrinsic mass and specific area activities of catalyst electrodes were also measured by using an EZstat-Pro system (NuVant Systems Inc., U.S.) integrated with the test stand. FC-lab and EZWare software were used to control the testing procedures. Each testing was repeated two or three times and the error bars represent standard deviation of measurements. The gasket used in the fuel cell test was polytetrafluoroethylene (PTFE) sheets with a thickness of 254 μm at both cathode and anode sides. The test system is shown in Fig. 3.4.

Fig. 3.4 Single fuel cell testing system.

3.4.1 Polarisation Curves

After assembly, the MEA was first conditioned by a break-in process kept at 0.6 V until the cell current reached a near stable state, which normally takes ca. 7–10 hours. This process is intended to make sure that the Nafion membrane in the MEA is completely humidified to reach the optimal testing conditions. After this, 100 rapid potential sweep cycles at a rate of 50 mV s^{-1} were conducted from open circuit voltage (OCV) to 0.25 V to further activate the catalysts. Polarisation curves were then recorded at a slow scan rate of 5 mV s^{-1}. The cell activation and testing were conducted at 70 ^{o}C with gases fully humidified before entering the cell. The stoichiometry was 1.3/2.4 for H_2 and air with the gas flow rates kept at least at 120 and 300 mL min^{-1} at a backpressure of 2 bars, respectively.

A typical fuel cell polarisation curve is shown in Fig. 3.5. The actual voltage output is usually obtained from the theoretical ideal value after the activation, ohmic resistance and

concentration losses. The activation loss is caused by the reaction kinetics on the electrode surface. A portion of the lost voltage demonstrates the catalytic activities of Pt nanoparticles or 1D Pt nanostructures in driving the transportation of electrons and protons to complete the electrochemical reactions. The ohmic resistance loss, a linear loss, is related to the electron resistance due to the current flow through different components and ionic resistance owing to the electrolyte membrane used in the MEA. The rapid voltage loss at high current density is the concentration or mass transport loss resulting from the difference between the reactant concentration at the catalyst surface and the bulk area, acting as a good tool to evaluate the electrode structures used in this PhD work. Also, blockage of reaction sites due to the insufficient water removal will also contribute to the concentration overpotential. The corresponding power density curve can be directly plotted by multiplying the cell voltage and the current density.

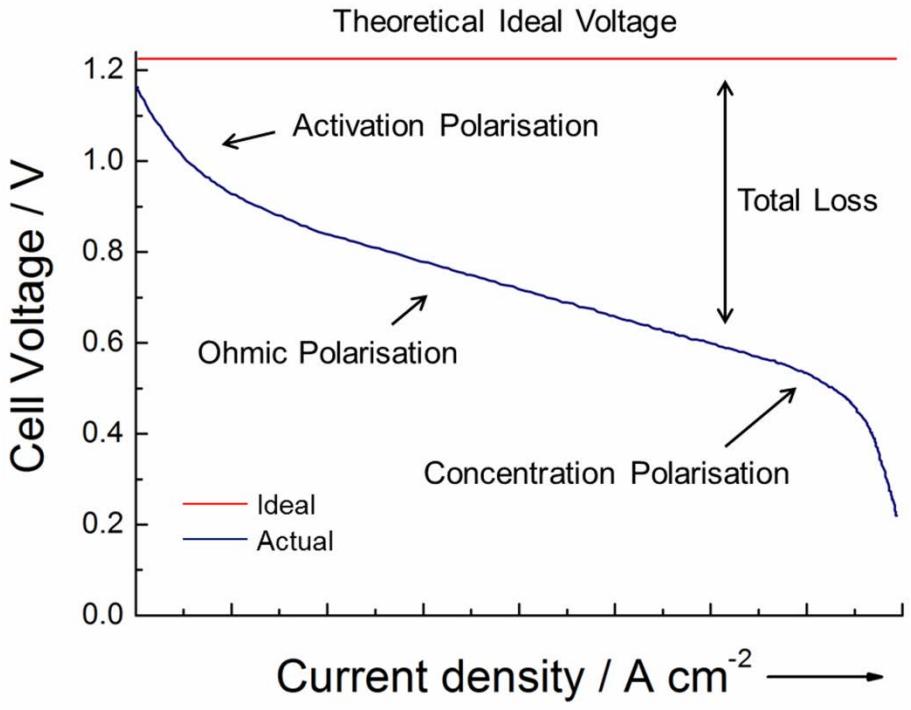

Fig. 3.5 Typical polarisation curve of a PEFC.

3.4.2 Electrochemical Impedance Spectroscopy (EIS)

Electrochemical impedance spectroscopy (EIS) is used as a powerful tool for the analysis of complicated processes in fuel cells. It is employed to determine the electrochemical reaction mechanism and identify the dominant reaction step at a certain frequency. In fuel cell testing, EIS measurements were performed in the frequency range from 10 kHz to 0.1 Hz with amplitudes of 0.05, 1 and 2 A. Three current densities at low, medium and high values, i.e. at 0.05, 0.5 and 1.0 A cm^{-2}, respectively, were chosen for the measurement. At low current densities, the main impedance, usually represented by a single semicircle, is contributed by the charge transfer resistance due to the ORR kinetics of the electrodes. The impedance represented by the intercept with Z_{re} axis at high frequency is the ohmic resistance from the membrane and the interfacial contact resistance (ICR) between different components. With the increase of current density, at a medium or high value, a second semicircle appears at a relative low frequency region (high Z_{re} values), which is mainly caused by the mass transfer losses. Typical EIS at low and high current densities are shown in Fig. 3.6.

The impedance spectrum for fuel cells can be modelled with an equivalent electrical circuit, which usually consists of resistors and capacitors. Fig. 3.7 shows an equivalent impedance circuit for fuel cells at a high current density. R_s is the ohmic resistance of the different components; R_p represents the charge transfer resistance and C_{dl} is the double layer capacitance on the surface of the electrode; the parallel R_d and C_d added to the circuit consider the mass transfer losses through the MEA.

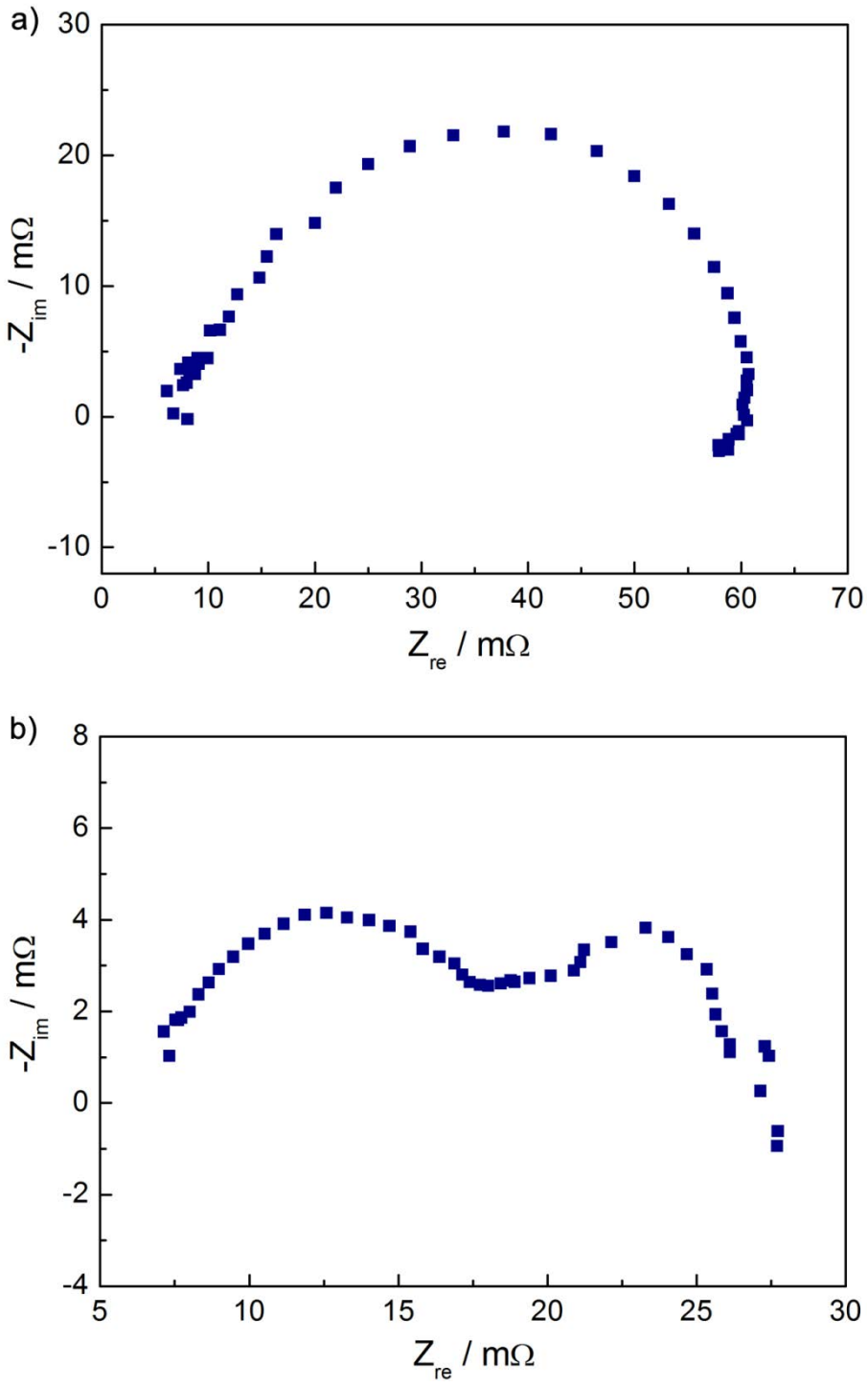

Fig. 3.6 Typical EIS for an MEA at the (a) low and (b) high current density.

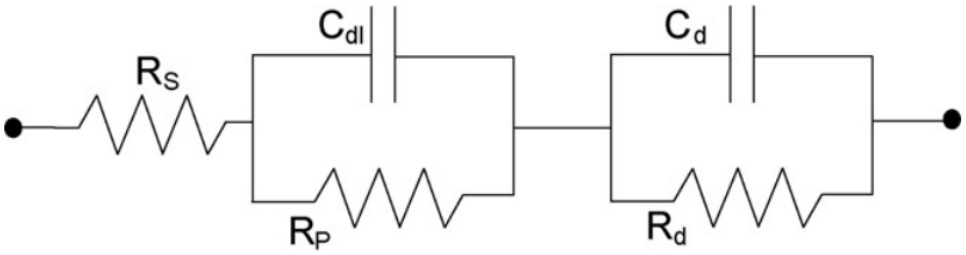

Fig. 3.7 Fuel cell impedance equivalent circuit at a high current density.

3.4.3 Cyclic Voltammetry (CV)

Cathode cyclic voltammograms (CV) were recorded using an EZstat-Pro system integrated with the test stand. The cathode was fed with fully humidified nitrogen at 300 mL min^{-1} as working electrode, and the anode was fed with fully humidified hydrogen at 120 mL min^{-1} as both reference and counter electrode, designated as a dynamic hydrogen electrode (DHE). Then the potential was cycled between 0.05 and 1.2 V versus DHE at 20 mV s^{-1} for 5 cycles, and the fifth cycle was recorded. The electrochemical surface areas (ECSAs) were measured by the electrochemical hydrogen adsorption/desorption method. A typical CV curve with hydrogen desorption area in the positive-going potential scan is illustrated in Fig. 3.8.

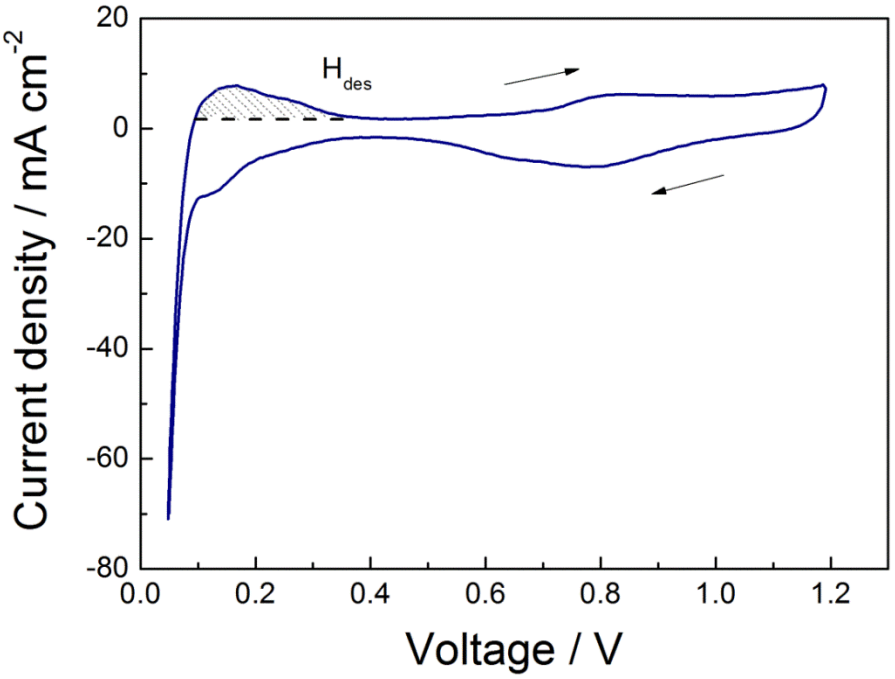

Fig. 3.8 Cathode cyclic voltammogram of an MEA.

The ECSA was calculated by the equation given below:

$$ECSA(m^2/g) = \left[\frac{Q_H(C)}{210\mu C\ cm^{-2} \cdot L(mg\ cm^{-2}) \cdot A_g(cm^2)} \right] \times 10^5 \qquad (3.3)$$

where Q_H is the hydrogen adsorption or desorption charge [187] determined by integrating the current in the hydrogen region (below 0.4 V) after double-layer correction, L is the catalyst loading (e.g. 0.4 mg_{Pt} cm^{-2}) and A_g is the geometric area of the GDE (e.g. 16 cm^2). Q_H = 210 μC cm^{-2} is used as the conversion factor, corresponding to the charge on a polycrystalline Pt surface covered by a monolayer of hydrogen atoms [188, 189].

3.4.4 Accelerated Degradation Test (ADT)

Accelerated degradation tests (ADTs) were used to predict the long-term durability of fuel cells. A representative graph for the cycles of ADT test is shown in Fig. 3.9.

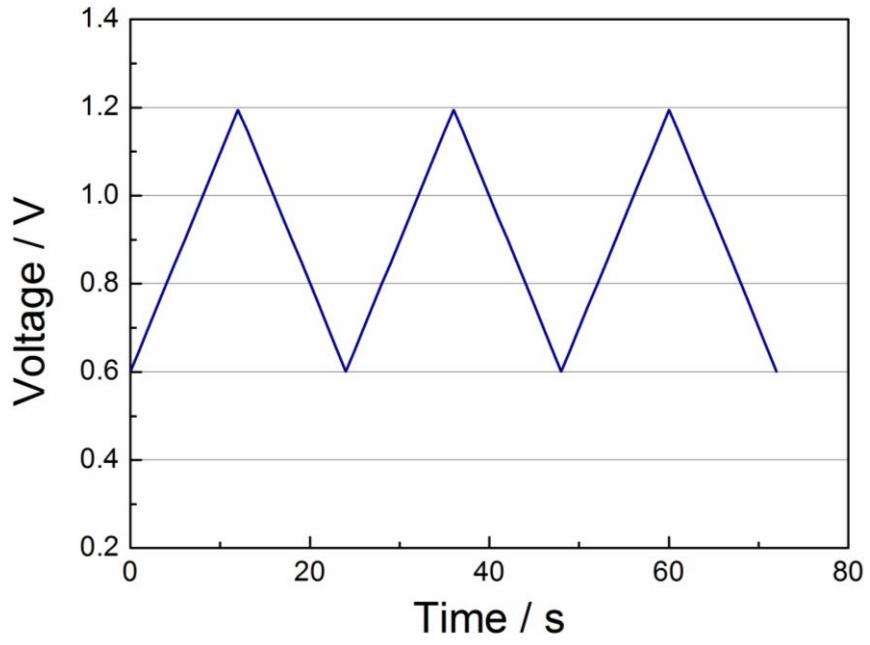

Fig. 3.9 Triangle potential cycling used for the accelerated degradation test.

Triangle potential cycling between 0.6 and 1.2 V at a scan rate of 50 mV s^{-1} was used, showing a much faster degradation compared with the step potential cycling, to shorten the test duration. The cycling potential range of 0.6–1.2 V is employed since this high voltage specially causes a high catalyst degradation ratio at the electrode [190]. During the cycling, the cathode and anode were fed with fully humidified pure N_2 at 300 mL min^{-1} and pure H_2 at 120 mL min^{-1}, respectively. ECSA was measured after the durability test to evaluate the degradation of catalysts.

3.4.5 Catalytic Activity in Oxygen

In addition to the power performance in H_2/air, the intrinsic catalytic activities of catalysts in the as-prepared GDEs were also measured in H_2/O_2 by the standard protocol described in detail by Gasteiger et al. [191] considering the H_2 crossover and ohmic resistance corrections. The testing was conducted on fuel cells at 80 ^oC with fully humidified H_2 and

O_2 to minimise the mass-transfer polarisation in GDEs. Stoichiometric flow rates of H_2 at the anode (s=2) and O_2 at the cathode (s=9.5) were used with minimum flow rates of 120 and 300 mL min^{-1} to meet the requirement of the testing system. The absolute pressure was 1.5 bars on both sides for the entire testing process. The H_2 crossover correction was processed by including the H_2 crossover current densities ($j_{Corrected}$) measured at 0.6 V over a period of 30 min (Fig. 3.10a) under the operating conditions to obtain stable values. The cell resistance (R) was determined by EIS measurement evaluated at 1kHz for iR correction (Fig. 3.10b).

Therefore, the corrected current density is calculated by

$$j_{Corrected} = j_{Original} + j_{H2\text{-}crossover} \tag{3.4}$$

and the corrected voltage is obtained according to

$$E_{Corrected} = j_{Corrected} \times A_{GDE} \times R_{1kHz} + E_{Original} \tag{3.5}$$

where $E_{Original}$ is the measured cell voltage and A_{GDE} is the GDE area. The kinetic catalytic activity, $i_{0.9}$, was determined at 0.9 V from the corrected polarisation curve based on Equation 3.4. The mass and specific area activities of catalysts were calculated by the following equations:

$$i_m(mA\ mg^{-1}) = \frac{i_{0.9}(mA\ cm^{-2})}{L(mg\ cm^{-2})} \tag{3.6}$$

$$i_s(mA\ cm^{-2}) = \left[\frac{i_{0.9}(mA\ cm^{-2})}{ECSA(m^2 g^{-1}) \cdot L(mg\ cm^{-2})}\right] \times 10^{-1} \tag{3.7}$$

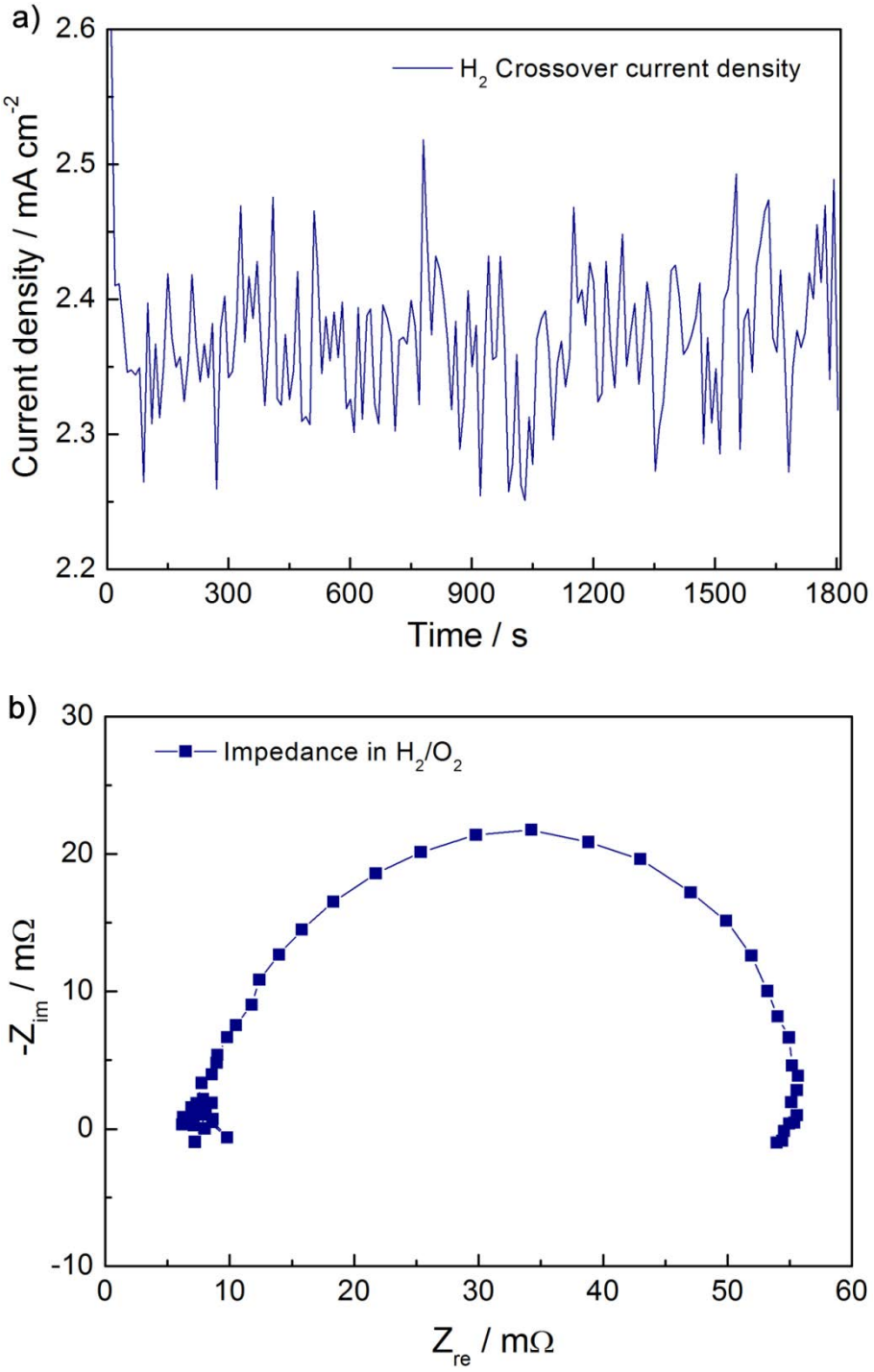

Fig. 3.10 (a) H_2 crossover current density at 0.6 V and (b) ohmic resistance measured by the EIS at 1kHz.

CHAPTER 4

TEMPERATURE-CONTROLLED GROWTH OF Pt NANOWIREs FOR HIGH PERFORMANCE CATALYST ELECTRODES

This chapter is based on the publication

Yaxiang Lu, Shangfeng Du*, Robert Steinberger-Wilckens

Temperature-controlled growth of single-crystal Pt nanowire arrays for high performance catalyst electrodes in polymer electrolyte fuel cells

Applied Catalysis B: Environmental 164 (2015) 389-395.

doi:10.1016/j.apcatb.2014.09.040

4. Temperature-Controlled Growth of Pt Nanowires for High Performance Catalyst Electrodes

This chapter focuses on the investigation of the effect of growth temperature on the in-situ growing of Pt nanowires (Pt NWs) on the gas diffusion layer (GDL) surface to achieve high performance catalyst electrodes for polymer electrolyte fuel cells (PEFCs). Pt-nanowire (PtNW) gas diffusion electrodes (GDEs) fabricated at various temperatures are characterised and tested in a single fuel cell to understand the structure-property relationship.

4.1 Introduction

In the synthesis of nanostructures, reaction temperature has been regarded as an important control factor. Controlling temperature is a tool to tune the phase formation kinetics [192] and the driving force for mass transfer in reaction systems [193], thus changing the morphology and property of the product. A very good example depicted in Fig. 4.1 illustrates how temperature changes the morphology of the product during the reduction of chloroplatinic acid by formic acid [68]. It can be observed that at a high temperature the products are mainly nanoparticles while at room temperature they grow into nanowires and further agglomerate into super structures. The reason for this is temperature affects the crystal nucleation and growth rate. It is usually considered that a relative low reaction temperature is necessary to slow down the reduction rate of Pt ions, favouring the growth of {111} planes and therefore leading to the formation of single-crystal Pt nanowires [41, 194]. For instance, revising from 180 ^{o}C, which is commonly used for synthesising nanoparticles [195], to 110 °C, Xia and co-workers [196] grew Pt nanowires on metal gauzes by reducing H_2PtCl_6 with ethylene glycol. At room temperature, Sun et al. [194]

synthesised single-crystal Pt nanowires on carbon black via the reduction of H_2PtCl_6 by HCOOH. However, in the synthesis of nanostructures, besides morphology, the growth temperature also plays a key role for the behaviour (e.g. the distribution and aggregation) of the synthesised nanostructures. In practical applications, the behaviour of Pt nanowires is as important as Pt nanowires themselves. For example, when Pt nanowires are used as electrocatalysts in fuel cells, they are expected to be optimally distributed in the catalyst layer to achieve a low charge and mass transfer resistance [162], a suitable length to enable self-support [197], and an ultra-thin size to obtain a high electrochemical surface area (ECSA) [87]. This highlights the importance of a finely tuned synthesis temperature for simultaneously controlling the behaviour and structure of Pt nanowires for practical applications.

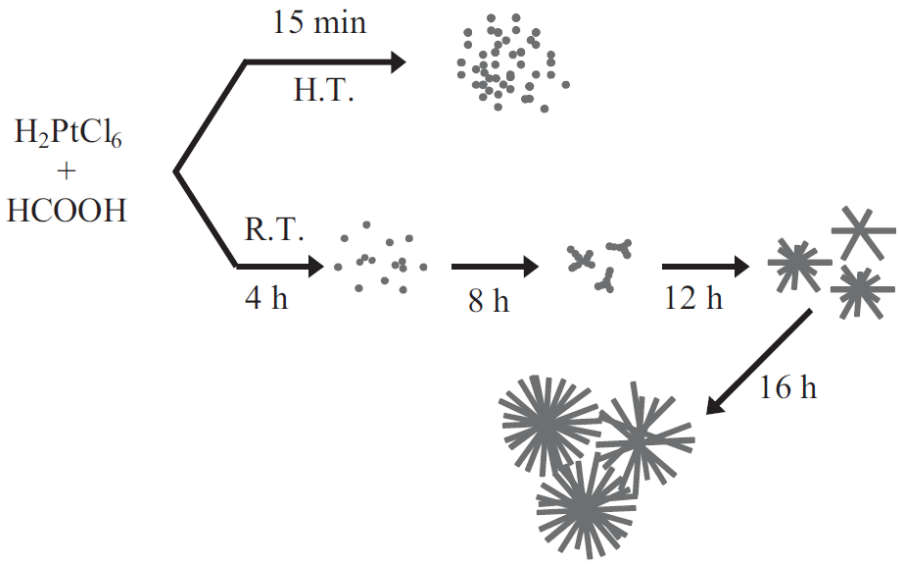

Fig. 4.1 Schematic illustration of the formation and shape evolution of Pt nanostructures corresponding to temperature (H.T.: high temperature; R.T.: room temperature) [68].

Another thing worth noting is that temperature also influences the wetting behaviour of liquids on the solid surface. As PtNW GDEs are fabricated by in-situ growing Pt NWs on

the GDL carbon paper surface through a wet-chemical synthesis process in aqueous solution, the wettability of the GDL should also be taken into consideration. In fuel cells, to prevent the water flooding in operation, the GDL surface is usually treated with PTFE to achieve super hydrophobicity. This feature makes the surface very difficult to be wetted by the aqueous solution. A high temperature can help improve the wettability of the GDL surface, facilitating the growth of Pt nanowires because increase in temperature can reduce the water contact angle, thus making the surface more easily wetted [198].

In this work, Pt nanowires in-situ grown on large-area carbon paper at different growth temperatures are investigated. Various temperatures including 5, 15, 25, 35, 40 and 50 °C are studied. Too high temperatures, e.g. 80 °C [199] will lead to direct formation of Pt nanoparticles in solution by homogeneous nucleation, so the temperature range is chosen to be below 50 °C. Considering the power performance in fuel cells, the role of the reaction temperature in the Pt nanowire growth process is proposed based on their morphology and distribution on the GDL surface.

4.2 Crystal Structure of Pt Nanostructures at Various Temperatures

TGA analysis was implemented to measure the actual Pt loading on the GDL surface, including the pristine 35BC GDL carbon paper and PtNW GDE samples grown at 5, 25, 40 and 50 ^{o}C. The results are shown in Fig. 4.2. It can be seen that at the temperature ranges below 450 ^{o}C and higher than 740 ^{o}C, the plots for all samples are nearly flat and there is no obvious mass change. In the middle range between 450–740 ^{o}C, there is a sharp mass loss. Generally, the TGA curves within this range can be divided into two regions [200]: a relative slow mass loss below 580 ^{o}C and a rapid drop in the range of 580–740 ^{o}C.

The former part between 450–580 ^{o}C can be assigned to the pyrolysis of PTFE in GDLs which corresponds to ca. 20 wt% loss. This is in line with the PTFE loading reported from the company as shown in Chapter 3. The sharp loss between 580–740 ^{o}C is associated with carbon oxidation to form carbon oxides [201]. From Fig. 4.2, we can see that the TGA curves of 35BC GDL and PtNW GDEs overlap well in the PTFE pyrolysis stage, demonstrating no influence from the grown Pt nanowires. However, in the carbon oxidation process, a clear difference is observed between the pristine GDL and PtNW GDEs and a general temperature difference of ca. 50 ^{o}C is observed for the two types of samples. The fast oxidation process of carbon in PtNW GDEs is possibly caused by the catalytic effect from Pt nanowires that accelerate the carbon oxidation. This has also been reported by other researchers in the investigation of thermal stability of PEFC catalyst layers [202]. After this stage, for the PtNW GDEs, there was only Pt left and thus the stable line was used to calculate the Pt loading on the GDL surface. From the figure it can be seen that all PtNW GDEs grown at different temperatures show nearly the same Pt residue, and the calculated average Pt loading is ca. 6.30±0.4 mg on the 16 cm^2 GDL, which is very close to the theoretical 6.4 mg Pt amount, demonstrating that more than 98% Pt NWs have been grown on the GDL support.

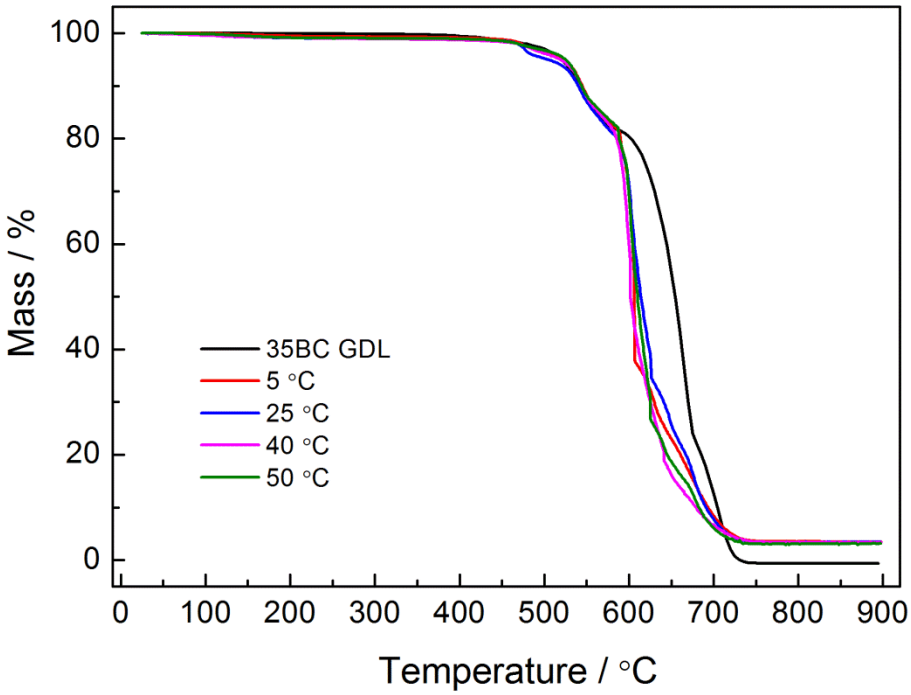

Fig. 4.2 TGA plots of the pristine 35BC GDL and PtNW GDE samples grown at 5, 25, 40 and 50 ^{o}C.

XRD analysis was also conducted to 35BC GDL and PtNW GDEs grown at 5, 25, 40 and 50 ^{o}C to confirm the structure and crystallinity of Pt nanowires. Fig. 4.3 exhibits that 35BC GDL has a lot of peaks within the scan range which correspond to the carbon powder in GDLs. Different from peaks of 35BC GDL, some diffraction peaks observed at 39.5°, 46.8° and 67.6° for PtNW GDEs are assigned to the (111), (200) and (220) planes of the face-centred cubic (fcc) structure of Pt [203], indicating that Pt NWs have a similar crystalline structure to the bulk Pt. Besides, no obvious difference was observed for PtNW GDEs grown at various temperatures, indicating the obtained Pt nanostructures have the same crystallinity.

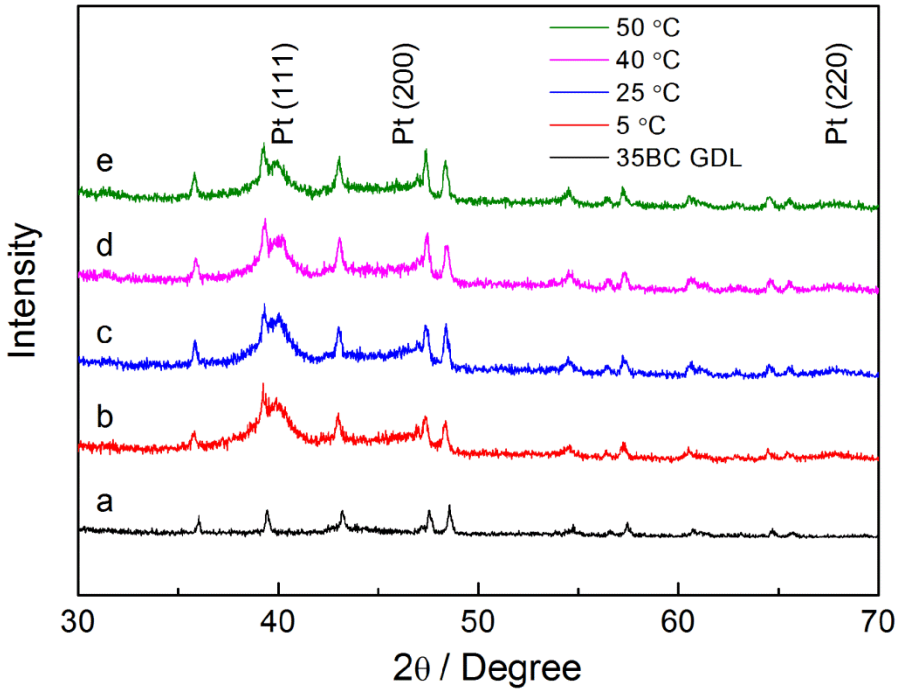

Fig. 4.3 XRD patterns of (a) 35BC GDL and PtNW GDEs grown at (b) 5; (c) 25; (d) 40; and (e) 50 ^{o}C.

4.3 Distribution and Morphology of Pt Nanostructures at Various Temperatures

Pt nanostructures grown at different temperatures on GDLs were directly characterised by SEM. Fig. 4.4 shows SEM images of Pt nanostructures grown at 5 °C. At such a low temperature, a big difference is observed to the morphology and distribution of Pt nanostructures formed between the edge and centre area in a 16 cm^2 GDE. Pt nanostructures have an extremely high density at the edge area (Figs. 4.4a and b) but show a very sparse distribution at the centre area (Figs. 4.4c-f). At the edge, Pt nanostructures agglomerate to form large aggregates with a size of 0.2–0.4 μm or even larger. This structure would significantly reduce the contribution of Pt to the catalytic activity, resulting in a very low catalyst utilisation. At the centre, however, the behaviour of Pt

nanostructures is completely different. Most of the sparse Pt nanostructures assemble together to form small superstructures with a size of ca. 100 nm.

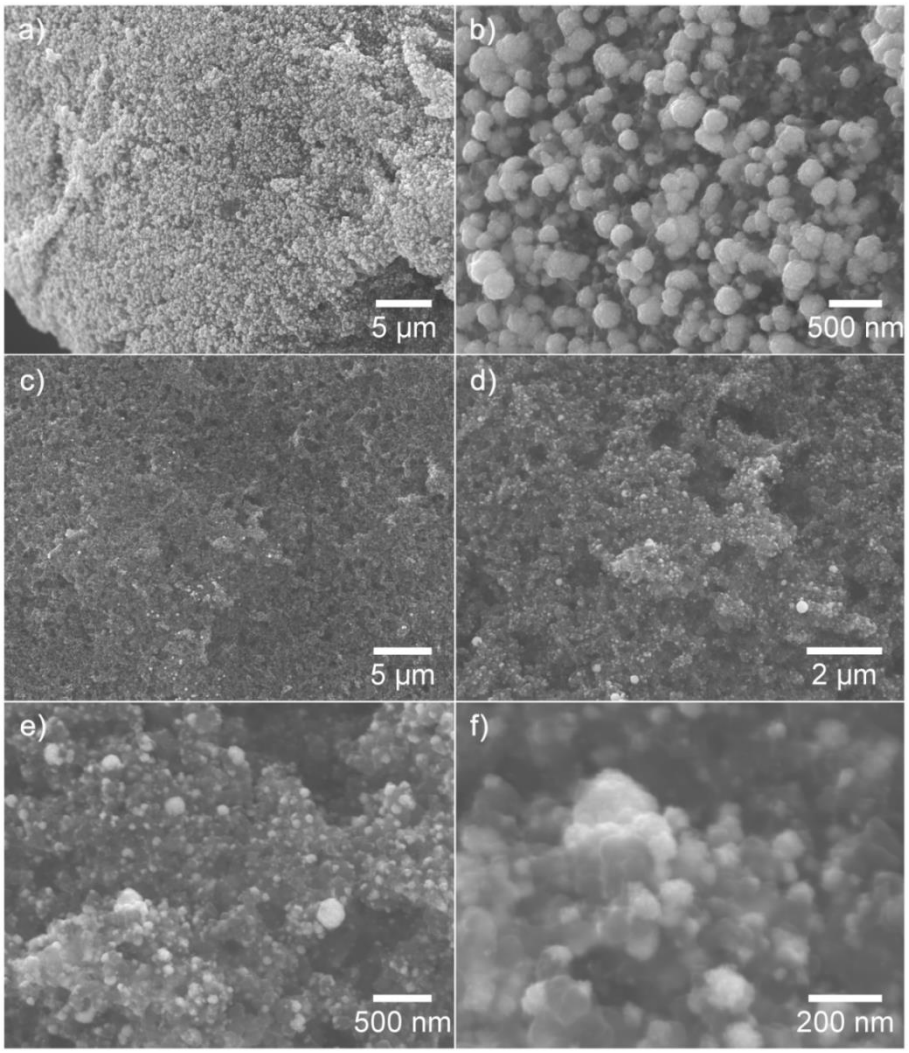

Fig. 4.4 SEM images of PtNW GDE grown at 5 ^{o}C. (a, b) and (c-f) show the edge and centre area of the 4cm×4cm GDE piece, respectively with different magnifications.

Fig. 4.5 shows TEM images of Pt nanostructures grown at 5 ^{o}C. A lot of agglomerates are formed (Fig. 4.5a) and the detailed microstructure can only be recognised at the edge of the agglomeration (Fig. 4.5b). With less aggregated parts, the short nanowire morphology can be observed (Fig. 4.5c) and the lattice space of 0.23 nm between the {111} plane is in agreement with that of the bulk Pt crystal (Fig. 4.5d).

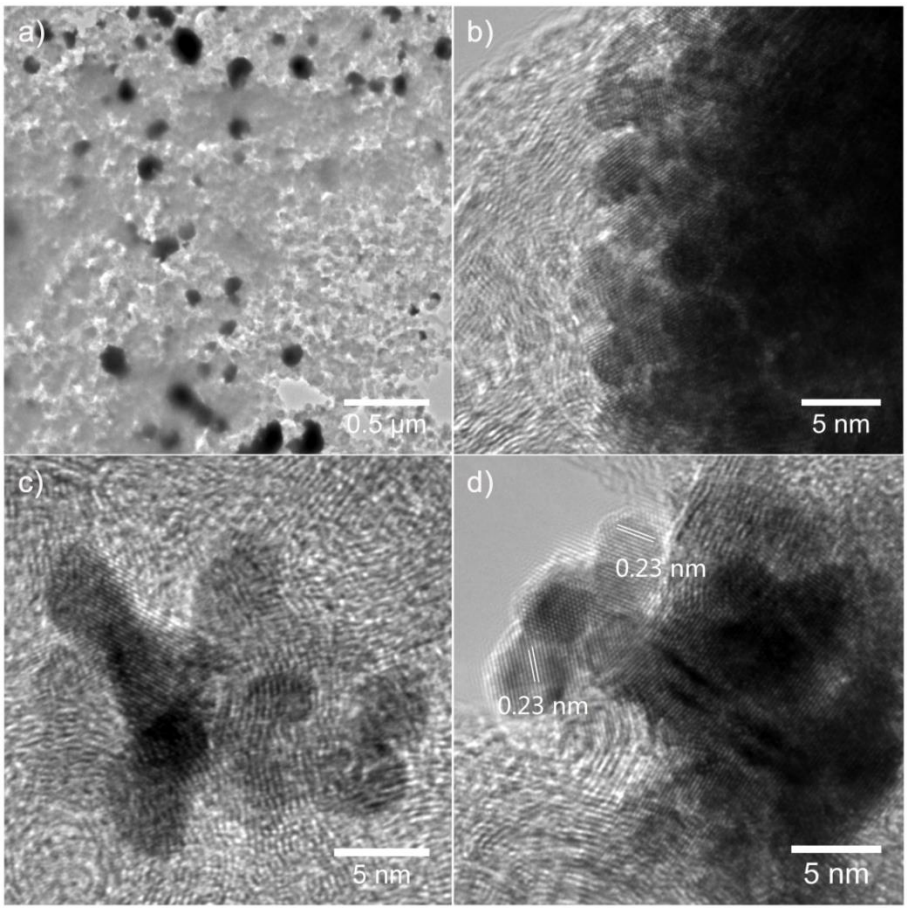

Fig. 4.5 (a-d) TEM images of PtNW GDE grown at 5 ^{o}C.

With the increase of the reaction temperature to 25 ^{o}C, which is a common temperature used for growing Pt nanowires with this formic acid approach [194], even larger Pt nanostructures are formed at the edge area (Fig.4.6a, b). However, Fig. 4.6c-f show that more Pt nanostructures are grown in the centre of the GDE compared with 5 ^{o}C, which means the distribution of Pt nanostructures has been improved with increase in temperature.

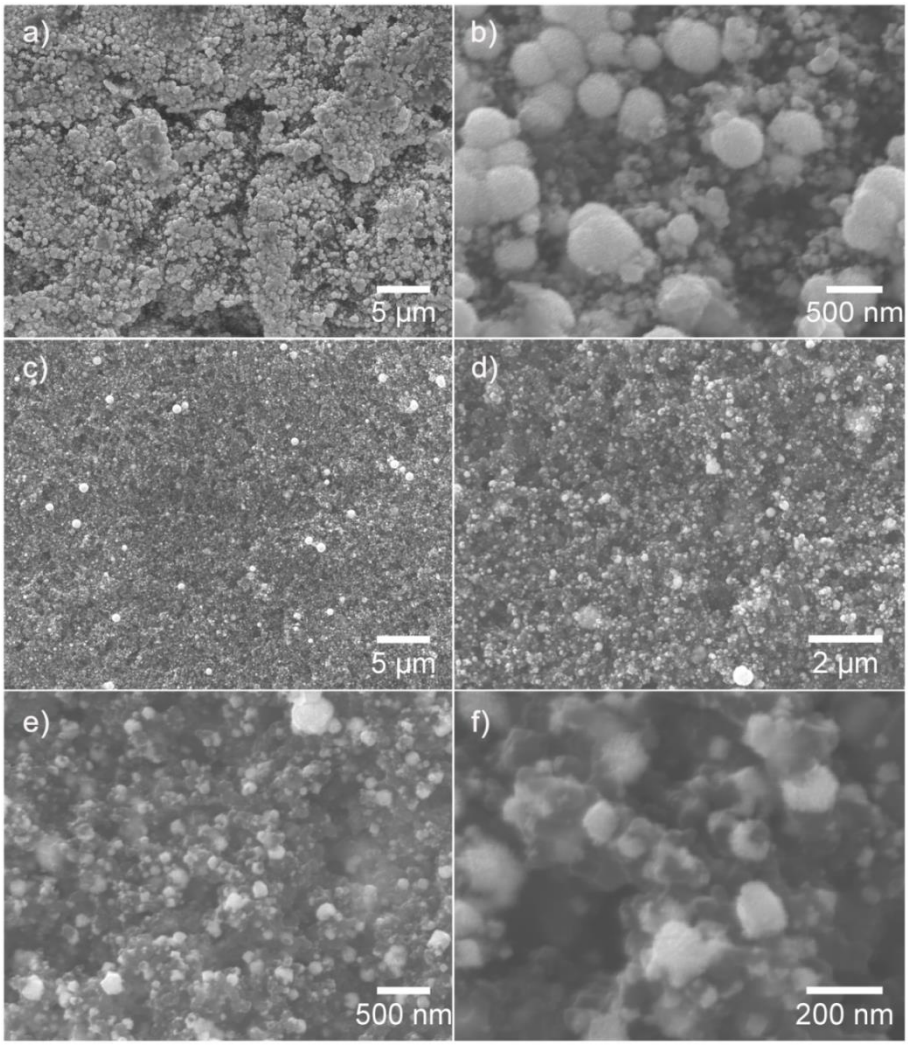

Fig. 4.6 SEM images of PtNW GDE grown at 25 ^{o}C. (a, b) and (c-f) show the edge and centre area of the GDE piece, respectively with different magnifications.

TEM images in Fig. 4.7 indicate that, rather than the nearly spherical Pt nanoparticles at the low temperature of 5 ^{o}C (Fig. 4.5), the nanowire morphology can be observed here. They have a length of ca. 5–20 nm and a diameter of a few nanometers, which is in line with reported work [13]. These nanowires finally form even larger agglomerates (Fig. 4.6b), as mentioned above, and compared to 5 ^{o}C (Fig. 4.4b).

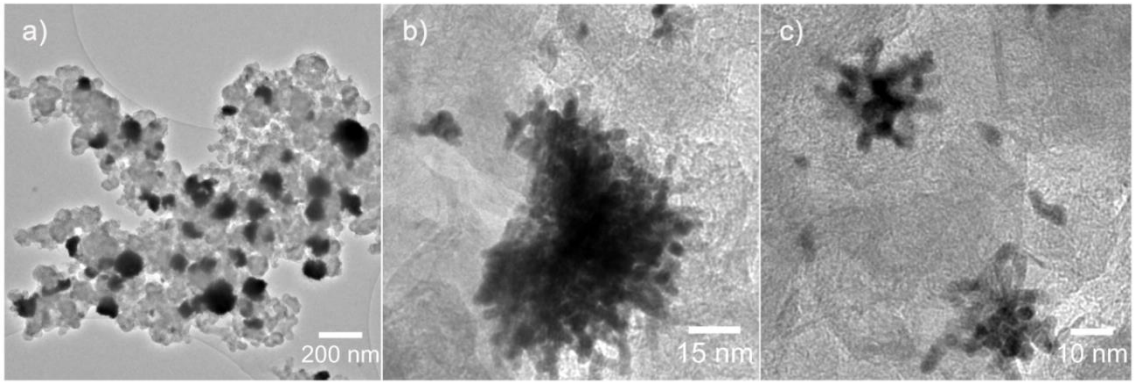

Fig. 4.7 (a-c) TEM images for PtNW GDE grown at 25 ^{o}C.

When the growth temperature increases to 40 ^{o}C, no matter at the edge (Fig. 4.8a) or in the centre (Fig. 4.8b-d) area, uniform Pt nanowire arrays are attained across the entire surface of carbon paper, although growth is still slightly denser at the edge area. The nanowire morphology is clearly displayed from the high magnification image in Fig. 4.8d.

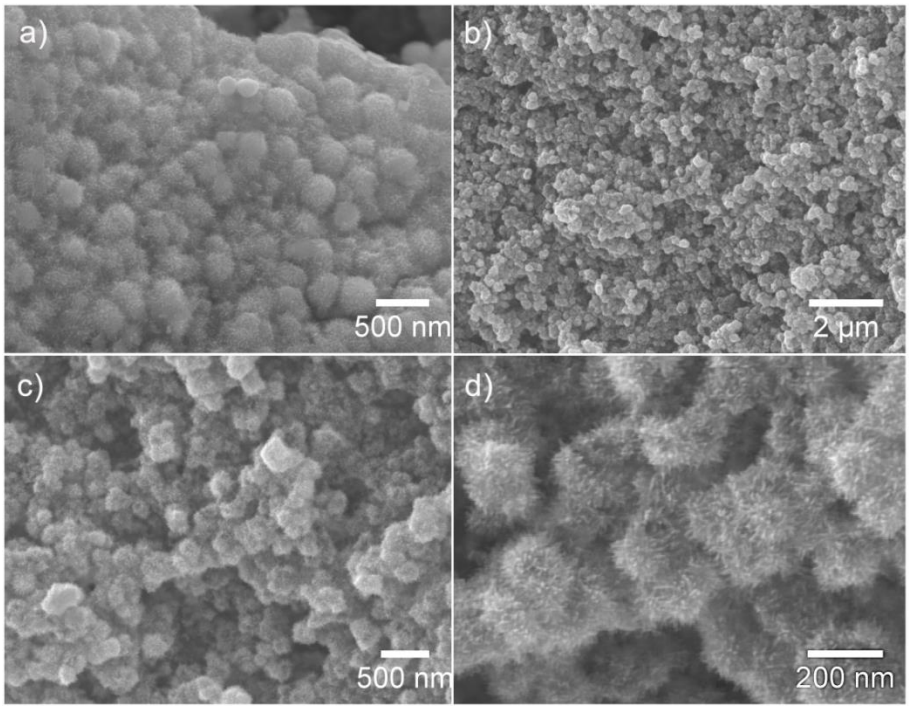

Fig. 4.8 SEM images of PtNW GDE grown at 40 ^{o}C. (a) and (b-d) show the edge and centre area of the GDE piece, respectively. (b-d) are images for the centre area with different magnifications.

TEM images in Fig. 4.9 show less agglomeration and more nanowires can be observed on the carbon surface. The HR-TEM image (Fig. 4.9b) indicates that Pt nanowires have a length of 10–25 nm which is longer than those at lower temperature. A magnified image shown in Fig. 4.9c displays the lattice fringes of Pt nanowires and demonstrates the single crystallinity. In this case, the advantages of the Pt nanowires can be maximised, and an excellent catalytic performance can be expected.

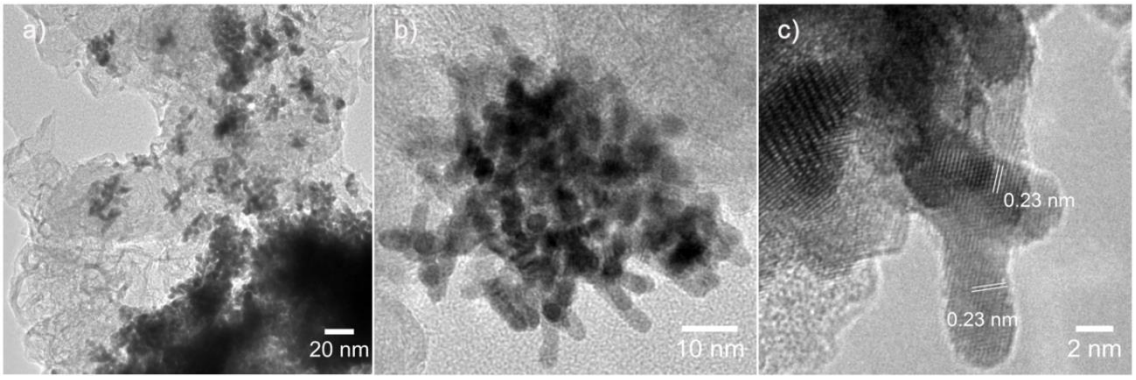

Fig. 4.9 (a-c) TEM images for PtNW GDE grown at 40 ^{o}C.

When the temperature continues to increase, at 50 ^{o}C, the obtained morphology is totally different from that at lower temperatures. As shown in Fig. 4.10, although there is no big difference for Pt NWs grown at the edge (Fig. 4.10a) or in the centre (Fig. 4.10b-d) area, only a mixture of small superstructures and sponge-like morphology can be observed. The high magnification image in Fig. 4.10d shows that a lot of small nanoparticles pile up on the GDL surface, with a particle size of a few nanometres. This thick layer of nanoparticles would significantly reduce the catalyst utilisation, and also partially block the oxygen diffusion in the fuel cell operation, resulting in a large mass transfer resistance. The morphology attained at 50 ^{o}C could be attributed to the high temperature which is enough to overcome the homogenous nucleation energy barrier in solution, thus nanoparticles are produced together with nanowires. TEM images in Fig. 4.11 also show that the

morphology is a mixture of nanowires and nanoparticles, which is consistent with the SEM images shown in Fig. 4.10.

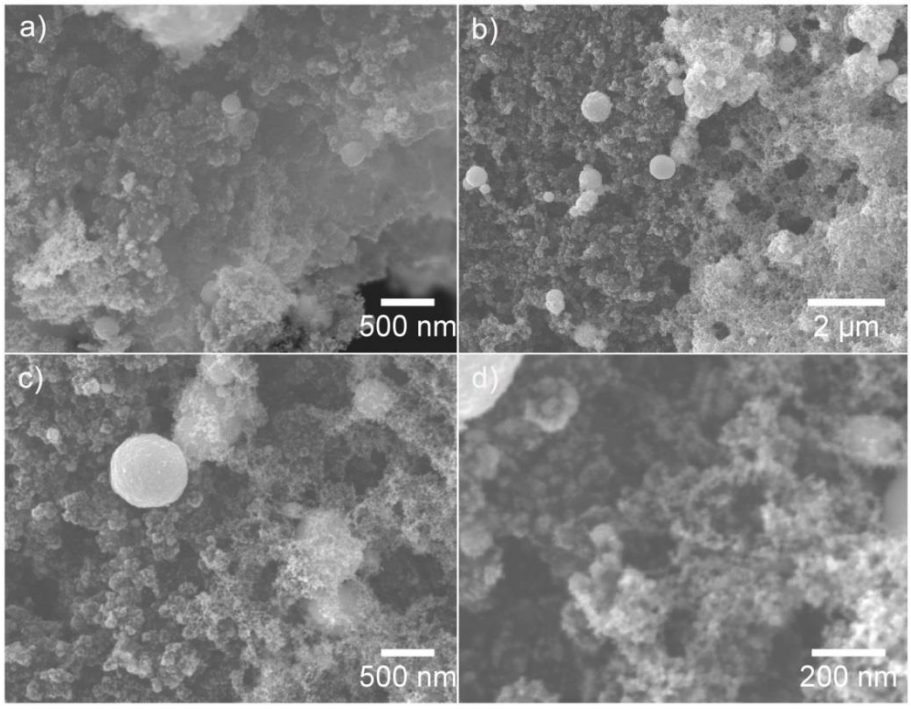

Fig. 4.10 SEM images of PtNW GDE grown at 50 ^{o}C. (a) and (b-d) show the edge and centre area of the GDE piece, respectively. (b-d) are images for the centre area with different magnifications.

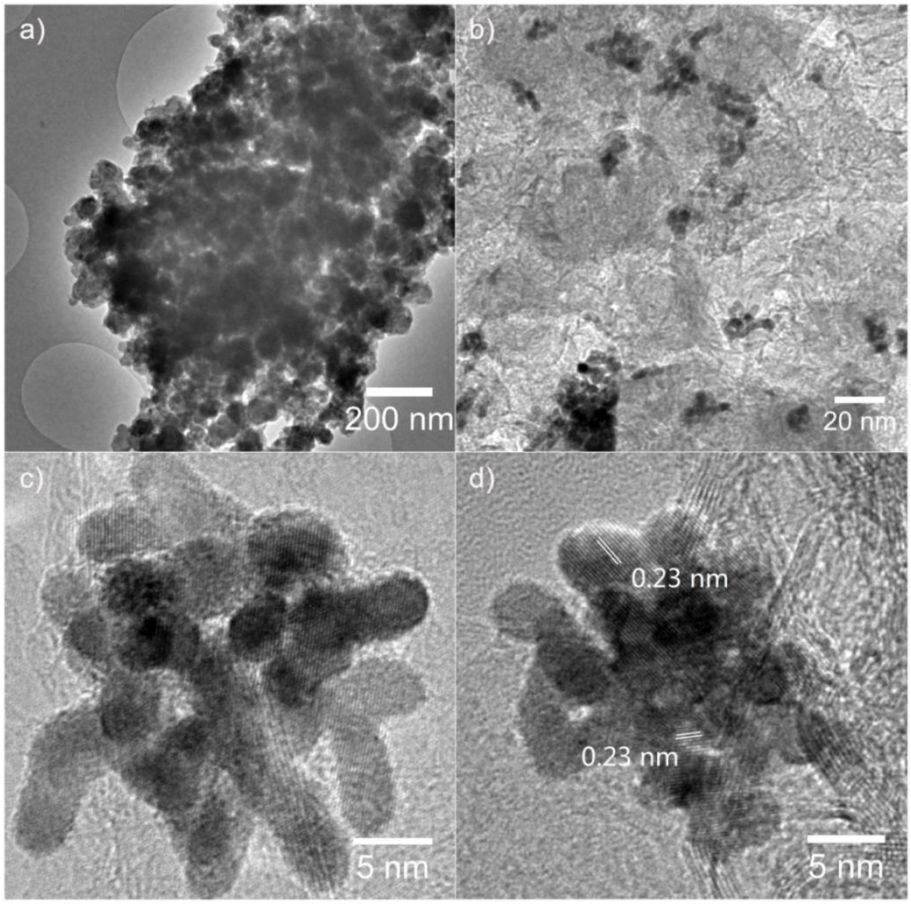

Fig. 4.11 (a-d) TEM images of PtNW GDE grown at 50 ^{o}C.

4.4 Single Fuel Cell Testing

In order to understand the effects of Pt nanowire behaviour on the practical catalytic performance, PtNW GDEs fabricated at various temperatures from 5 to 50 ^{o}C were used directly as cathodes and tested in hydrogen-air PEFCs with an active area of 16 cm^2 to check the catalytic performance and durability. The state-of-the-art commercial TKK Pt/C catalyst was also tested to compare with the Pt nanowire catalyst.

4.4.1 Power Performance in Fuel Cells

Fig. 4.12 shows the power performance of the MEAs with the as-prepared PtNW GDEs. The measurements were taken at T_{cell}=70 ^{o}C with fully humidified H_2 and air at 2 bars

(stoichiometry s=1.3/2.4), which was described in Chapter 3. It can be seen from the figure that the one grown at 5 ^{o}C shows a very poor power performance. With increase in temperature, a better performance is obtained, reaching the maximum value at 40 ^{o}C. The power density at 0.6 V (Fig. 4.12c) increases from 0.505 W cm^{-2} at 5 ^{o}C to 0.822 W cm^{-2} at 40 ^{o}C, respectively. A higher temperature leads to a rapid decrease of the electrode performance, dropping to only 0.54 W cm^{-2} at 50 ^{o}C. It is worth noting that there is no big difference for PtNW GDEs grown in the medium temperature range from 15 to 35 ^{o}C. A comparison of the PtNW GDEs and the one with the state-of-the-art commercial TKK Pt/C catalyst (the same loading of 0.4 mg cm^{-2}) is also included. The commercial catalyst shows a lower power density at 0.6 V, which is 0.74 W cm^{-2}.

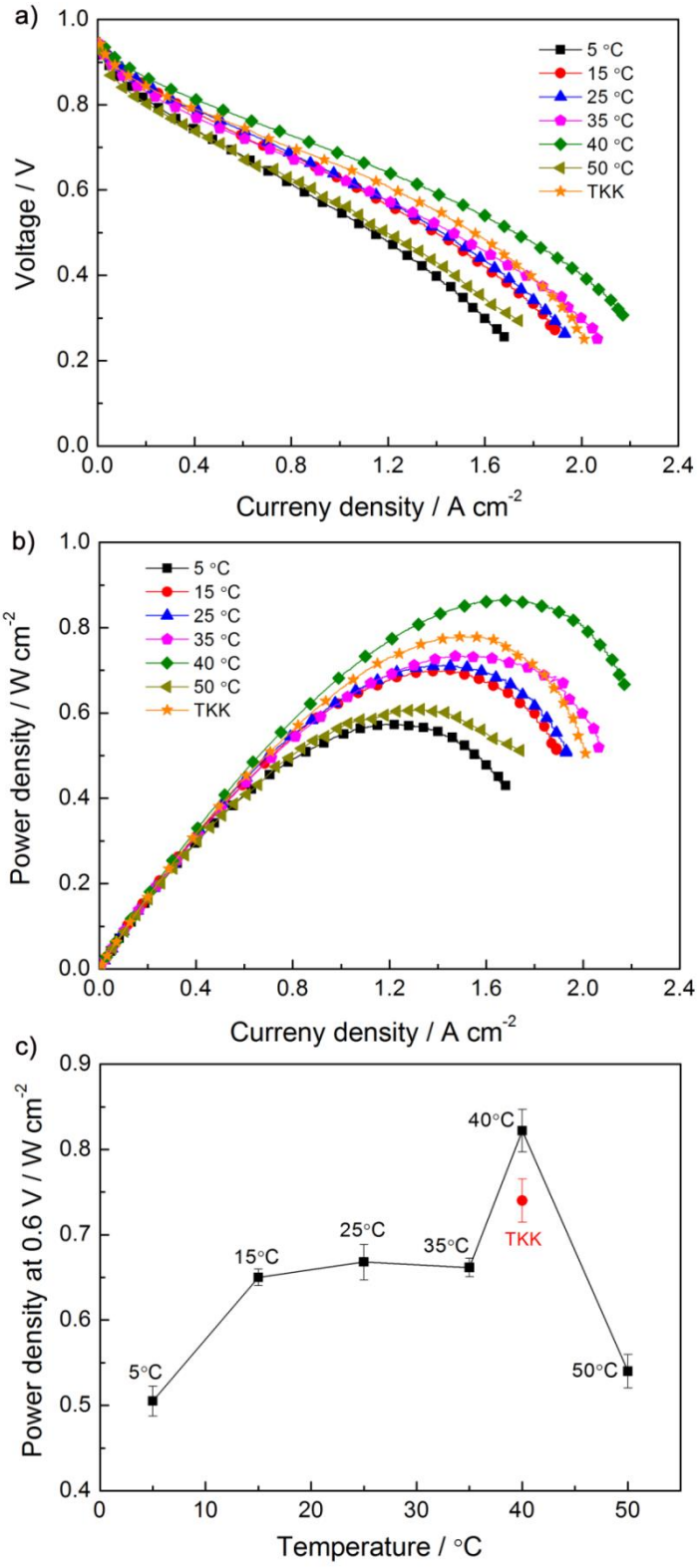

Fig. 4.12 (a) Polarisation curves, (b) power density curves and (c) the trend of the power density at 0.6 V for the PtNW GDEs grown at different temperatures and the one with TKK Pt/C catalyst.

4.4.2 Electrochemical Impedance Spectroscopy (EIS)

To further understand the PtNW behaviour, EIS measurements were conducted for PtNW GDEs grown at 5, 25, 40 and 50 ^{o}C and the results are shown in Fig. 4.13. At a low current density of 0.05 A cm^{-2}, the main impedance is contributed by the charge transfer resistance shown by the diameter of the impedance semi-circle, indicating the catalytic kinetic performance [164, 204]. It can be seen that the PtNW GDE of 40 ^{o}C shows the smallest charge transfer resistance, and the one of 5 ^{o}C exhibits a very large value. At a medium (0.5 A cm^{-2}) or large (1.0 A cm^{-2}) current density, the contribution from mass transfer resistance would dominate the impedance. During this range, the PtNW GDE of 40 ^{o}C still displays the smallest first and second impedance semi-circles, indicating the smallest charge and mass transfer resistances, respectively, benefitting from the regular distribution of Pt nanowire arrays in the catalyst layer. At the high current density, the one of 5 ^{o}C exhibits the largest charge transfer resistance, indicating the poor catalytic performance caused by the large Pt nanowire aggregates; while the one of 50 ^{o}C presents the largest mass transfer resistance, resulting from the thick catalyst layer of the piled up Pt nanoparticles in GDEs. The impedance of TKK Pt/C is also included in Fig. 4.13 and larger values are obtained compared with PtNW GDE of 40 ^{o}C. This is in agreement with the power performance obtained in Fig. 4.12.

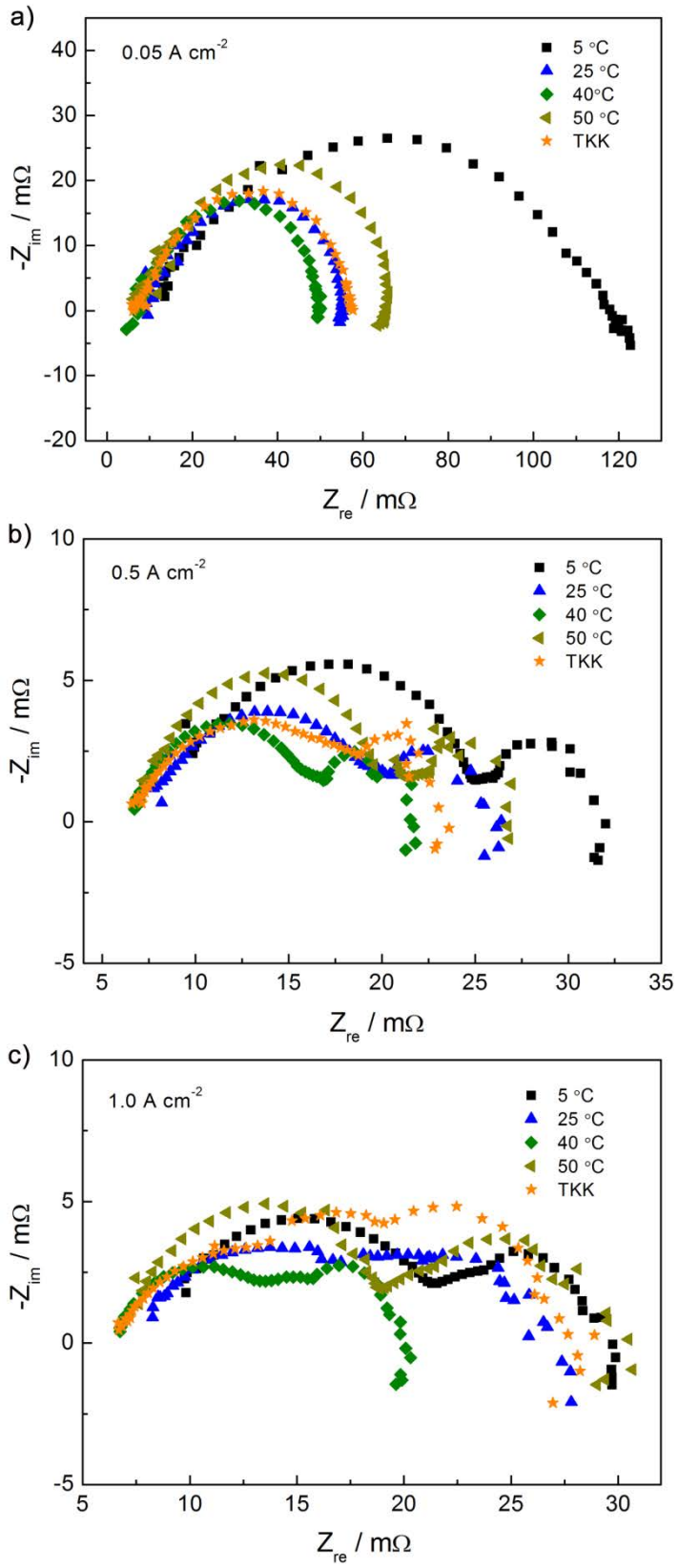

Fig. 4.13 EIS measured at (a) 0.05, (b) 0.5 and (c) 1.0 A cm^{-2} for PtNW GDEs grown at different temperatures.

4.4.3 Electrochemical Surface Area (ECSA)

Cathode cyclic voltammograms (CVs) were recorded for PtNW GDEs grown at 5, 25, 40 and 50 °C as well as for the TKK Pt/C catalyst in a single cell to measure the ECSA of Pt. From the CVs in Fig. 4.14, based on the H-desorption region and the theoretical Pt loading, the calculated ECSAs for PtNW GDEs grown at 5, 25, 40, 50 °C and Pt/C catalyst are 15.04, 12.90, 34.37, 4.91 and 56.87 $m^2 g_{Pt}^{-1}$, respectively.

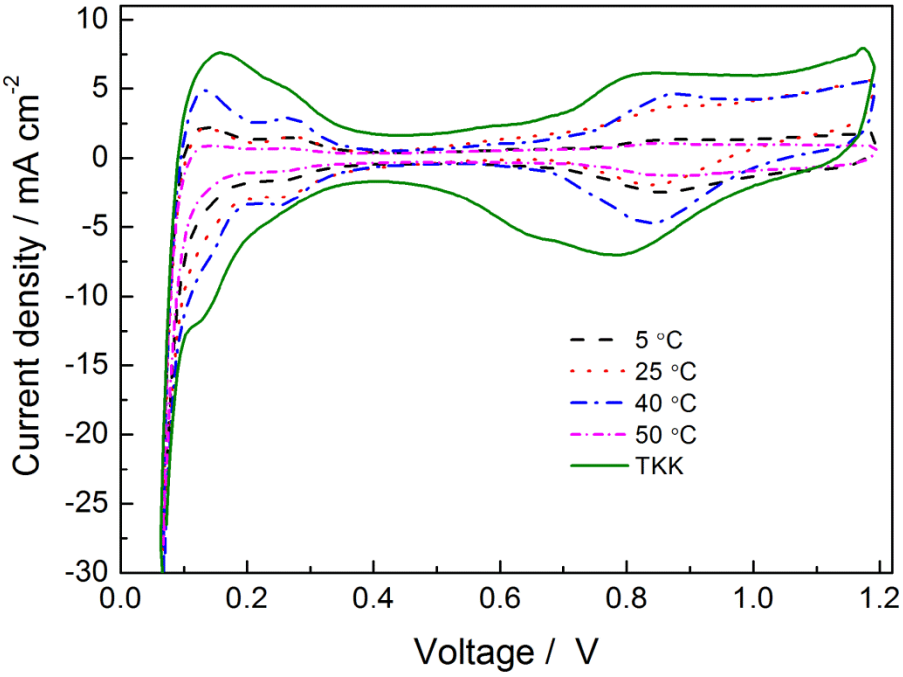

Fig. 4.14 Cathode CVs of PtNW GDEs grown at different temperatures and the one with TKK Pt/C catalyst. The cathode was fed with fully humidified N_2.

TKK Pt/C catalyst exhibits a very large ECSA, owing to the high surface area from its nanoparticle morphology. Despite the heavy aggregation of Pt NWs in PtNW GDE grown at 5 °C, a similar CV was obtained to that at 25 °C. A possible reason is that the very short length of Pt NWs (Fig. 4.5) leads to a relative larger surface area as compared with the longer Pt NWs. At the optimal temperature of 40 °C, uniform Pt NWs covered the whole surface and a better ECSA is achieved as expected. At 50 °C, some Pt nanoparticles grew

directly in the solution rather than on the GDL surface, and all those deposited on the GDL surface also piled together, finally resulting in a very low ECSA.

4.4.4 Durability by Accelerated Degradation Test (ADT)

It could be seen that a temperature of 40 ^{o}C enabled uniform growth of Pt NWs to achieve the highest catalytic activity. To confirm the excellent stability of the single-crystal Pt NWs as reported in the literature [167, 205], an ADT was conducted to check the durability of the as-prepared PtNW GDE of 40 ^{o}C and commercial TKK Pt/C catalyst. The ADT was performed by 2000 potential sweep cycles at 50 mV s^{-1} between 0.6 and 1.2 V (vs. reversible hydrogen electrode (RHE)) in real fuel cell conditions with cathode filling of humidified nitrogen gas. After the ADT test, CVs were scanned again to compare with the initial curves. Fig. 4.15a shows the CVs before and after the durability test. After the ADT, the remained ECSA value of PtNW GDE of 40 ^{o}C and Pt/C is 17.76 and 18.81 m^2 g_{Pt}^{-1}, corresponding to 48% and 67% loss in their ECSA value, respectively, which is summarised in Fig. 4.15b. The lower degradation rate indicates better durability of the PtNW GDE as compared with the nanoparticle one.

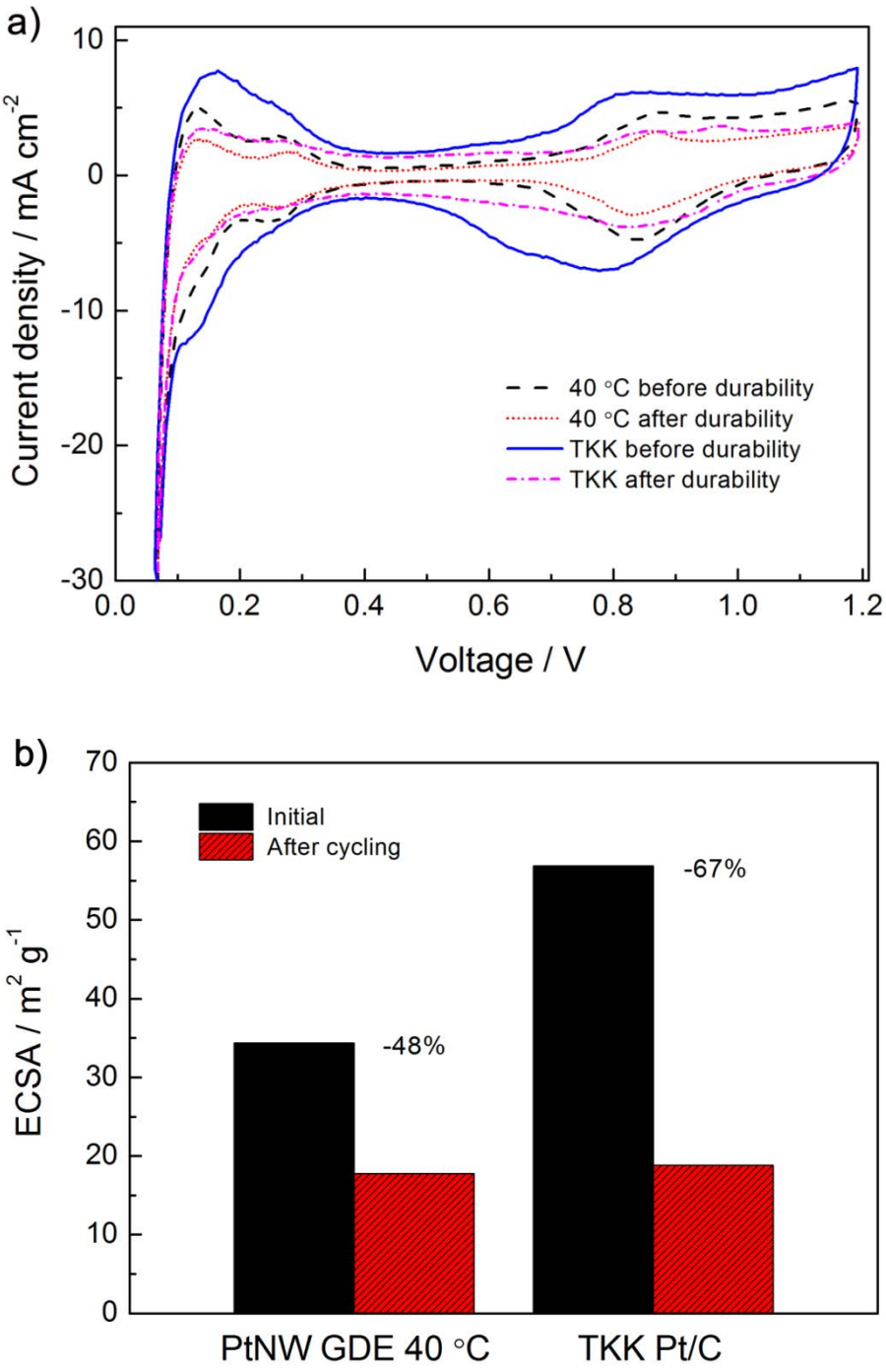

Fig. 4.15 (a) CVs and (b) summary of the ECSAs of PtNW GDE 40 °C and TKK Pt/C before and after the potential cycling. Measurements were taken at T_{cell}=70 °C with fully humidified H_2 and N_2 at 2 bar (stoichiometry s=1.3/2.4).

4.4.5 Catalytic Activity in Oxygen

For a better understanding of the intrinsic catalytic performance of Pt NWs over Pt/C, the catalytic activity of TKK Pt/C and Pt NWs grown at 40 °C was also tested in MEA using H_2/O_2 to minimise the mass transfer polarisations in GDEs. The kinetic catalytic activity was evaluated at 0.9 V from the H_2/O_2 performances after ohmic and H_2 crossover corrections [191, 206]. The resistance-corrected cell voltage was determined via in-situ EIS (evaluated at 1 kHz) vs. current density. Current densities were H_2 crossover corrected to yield the shown effective current density, which is referenced to the process mentioned in section 3.4.5. The original uncorrected and corrected polarisation curves in H_2/O_2 are shown in Fig. 4.16 and the results are summarised in Table 4.1.

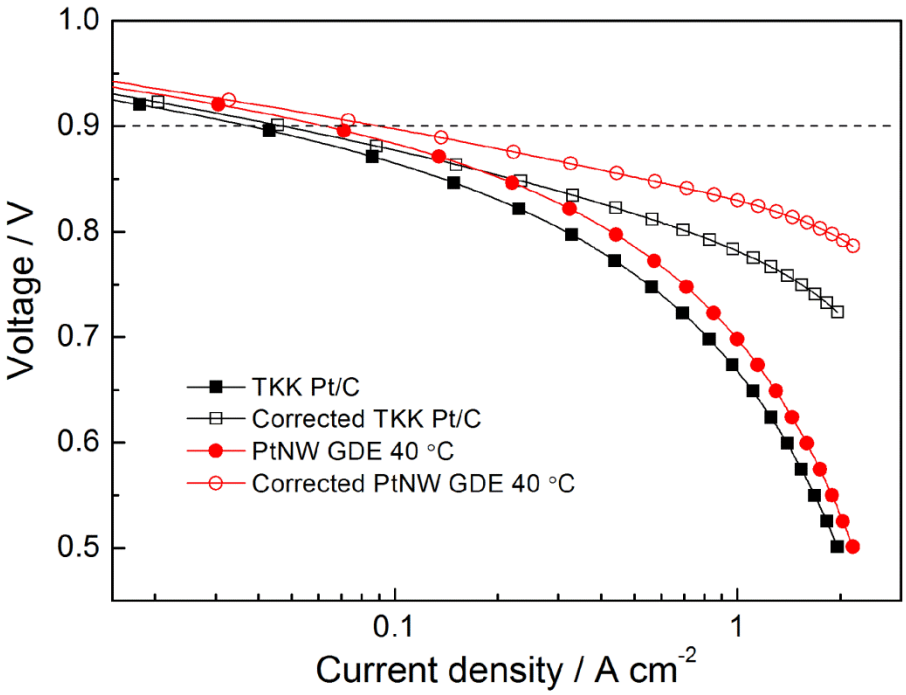

Fig. 4.16 Original uncorrected (solid square and circular symbols) and corrected (empty square and circular symbols) H_2/O_2 performance of the MEAs with the TKK Pt/C and PtNW GDEs. Measurements were taken at 80 °C with fully humidified reactants at 1.5 bar (H_2/O_2 stoichiometric flows of s=2/9.5).

The mass activity (i_m) of PtNW 40 °C is 0.225 A mg_{Pt}^{-1} which is nearly double of 0.118 A mg_{Pt}^{-1} for TKK Pt/C, and more than 3 times higher specific area activity (i_s) is achieved, which agrees with the data reported in the literature [191]. The kinetic activities obtained here are in line with the measured power performance above, further indicating the better catalytic activity of our Pt nanowire catalysts.

Table 4.1 Catalytic performance characteristics of the two MEAs with TKK Pt/C and PtNW 40 °C.

Catalysts	ECSA ($m^2\ g_{Pt}^{-1}$)	i (0.9 V) (mA cm^{-2})	i_m (0.9 V) (A mg_{Pt}^{-1})	i_s (0.9 V) (μA cm_{Pt}^{-2})
TKK Pt/C	56.87	47.29	0.118	207.89
PtNW 40 ℃	34.37	89.85	0.225	653.55

(i_m is mass activity and i_s is specific area activity)

4.5 Growth Mechanism

It can be seen that the growth temperature plays a key role not only for PtNW nanostructures, but also for their behaviour including distribution and aggregation. As we know, in the synthesis of nanostructures by wet chemical process, the nucleation can start in the reaction solution by homogeneous nucleation [207] or on the rough sites at the support surface by heterogeneous nucleation [208]. The heterogeneous nucleation usually needs a lower energy than homogenous nucleation [209], but is subjected to the existing barrier and energy provided for nucleation in the system [210].

In GDL carbon paper, the top layer mainly consists of carbon nanospheres. The surfaces of these carbon nanospheres are inert where a surface modification is usually needed if used

specially as catalyst support [211, 212]. Furthermore, to prevent water flooding in fuel cell operation, GDL carbon paper is usually treated with PTFE to achieve super hydrophobicity. In this case, at a low temperature, the high surface tension of the aqueous reaction solution can not wet the GDL support surface very well, in particular at the centre area for such a large piece [213], thus the active sites provided on the surface for nucleation are very limited. Furthermore, the very low temperature also significantly slows down the crystal growth rate [214]. Hence, the main structures obtained were large aggregates of short Pt nanowires at the edge area and very few Pt nanowires grew in the centre area, as seen in Fig. 4.4. With increase in reaction temperature, the surface tension of water is reduced and the wettability of the support surface is improved [213]. Therefore, in the centre area, the population of the nucleation sites multiplied and more Pt nanowires were obtained, as observed for PtNW GDEs grown at the medium temperature. At an optimal range, e.g. 40 ^{o}C here, uniform Pt NWs were grown on the carbon paper surface, as seen in Fig. 4.8. However, when the temperature reached a very high point, e.g. 50 ^{o}C, the energy provided in the system would be large enough to overcome the barrier for homogeneous nucleation, and nuclei would be formed in solution [215, 216]. It is also known that the crystal growth is very fast at a high temperature [214]. In this case, nanoparticles will be obtained rather than nanowires due to the fast crystal growth rate and the large amount of nuclei formed. This fact has been widely used to synthesise small nanoparticles [57]. Therefore, in our work here, although even more nucleation sites were obtained on the carbon paper surface, a uniform growth of Pt nanowires still could not be achieved. Some of these Pt nanoparticles formed in solution would then partially deposit and pile up on the support surface, as shown in Fig. 4.10d. In the experiment, it was also noticed that the reactant solution became dark at 50 ^{o}C, indicating the direct formation of

Pt nanoparticles in the solution. The thick Pt nanoparticle layer on the GDL will block the oxygen transfer during operation, in addition to the loss of Pt nanoparticles in solution, thus a poor catalyst electrode performance is expected.

Hence, to achieve uniform Pt nanowires with good distribution, surface structure and morphology on the support surface, an optimal temperature is necessary to effectively control the Pt nucleation and crystal growth in the reaction system. In our work here, this was achieved at 40 ^{o}C. A schematic diagram is shown in Fig. 4.17 to explain the growth mechanisms of Pt nanowires on the carbon paper surface at low, moderate and high temperature.

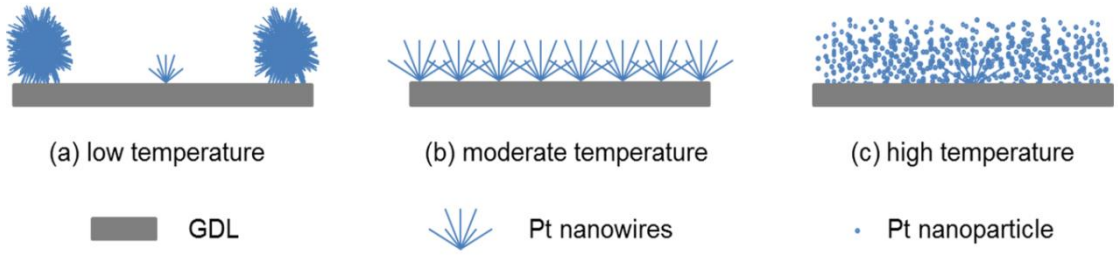

Fig. 4.17 Schematic diagram for Pt nanostructures grown on carbon paper surface at (a) low, (b) moderate and (c) high temperature.

4.6 Conclusions

In this chapter, the effects of the reaction temperature on the growth behaviour of Pt nanowires with large-area 16 cm^2 carbon paper GDL as direct support were discussed. The experimental results indicated that the growth temperature played a key role in this process. At low temperature, the main structures obtained were huge aggregates from short Pt NWs, resulting in a low catalyst utilisation and poor catalytic performance. An increased temperature brought in an improved distribution and longer Pt NWs on the GDL

surface. However, too high reaction temperature resulted in the formation of nanoparticles in solution.

At an optimal temperature of 40 ^{o}C, uniformly distributed PtNW arrays were achieved on the GDL surface with a diameter of ca. 4 nm and length of ca. 10–25 nm. This GDE showed the best catalytic performance in practical fuel cell test. A higher power density of 0.822 W cm^{-2} was obtained at 0.6 V compared with 0.74 W cm^{-2} of the commercial TKK Pt/C catalyst. The in-situ H_2/O_2 testing demonstrated a double mass activity and a three times higher specific activity of Pt NWs over TKK Pt/C, which were 0.225 A mg_{Pt}^{-1} and 653.55 μA cm_{Pt}^{-2}, respectively. The as-prepared PtNW GDE at 40 ^{o}C also exhibited a better durability than the one with Pt/C NPs, demonstrating a 48% and 67% ECSA loss after the durability test, respectively.

Because other nanostructures face the same challenge as here in the synthesis, in particular on various support surfaces, our improved understanding from PtNW GDEs could provide reference for research on novel nanostructures in fuel cells and other catalytic applications.

CHAPTER 5

INTEGRATED CATALYST ELECTRODES BASED ON PdPt NANODENDRITES

5. Integrated Catalyst Electrodes Based on PdPt Nanodendrites

In this chapter, Pd is introduced to develop integrated catalyst electrodes based on 1D PdPt nanostructures. The effects of Pd on the controlled growth and distribution of PdPt nanostructures on the gas diffusion layer (GDL) surface are investigated and the catalytic performance towards oxygen reduction reaction (ORR) is studied under real fuel cell operational conditions. Based on the results from physical characterisation and hydrogen-air fuel cell testing, the structure-property relationship is further discussed and a possible mechanism for the influence of Pd on the in-situ growth process of PdPt bimetallic nanodendrites (NDs) is suggested.

5.1 Introduction

With a cheaper price and similar properties, Pd has been confirmed as a promising candidate [63, 217] to reduce the Pt loading in polymer electrolyte fuel cell (PEFC) electrodes while not compromising the catalytic activity. In addition, the incorporation of Pd can offer desired interactions with Pt to tune both electronic and surface effects, triggering synergistic effects to enhance physical and chemical properties [89, 218]. The reported 1D Pt-Pd bimetallic electrocatalysts with various structures have been summarised in Chapter 2. The synergistic advantages of the bimetallic feature and 1D anisotropic properties can lead to an improved catalysis process [219-221], resulting in improved long-term durability and also superior activity towards the ORR. Some references also indicate that the existence of Pd could play a significant role in the morphology of Pt-Pd bimetallic nanostructures [123, 221]. For example, Xia's group [123] reported that in the presence of Pd, open branched dendrites are formed, whereas only foam-like Pt aggregates are obtained. In this PhD work, moving a step forward from those

pure material investigations, the influence of Pd on the morphology of 1D Pt-Pd bimetallic nanostructures, in particular their behaviour on the real fuel cell performance is further studied.

In this work, inspired by the Pt-nanowire (PtNW) catalyst electrodes and considering the synergistic effect between Pd and Pt, the influence mechanisms of Pd are studied on the morphology, crystal structure and distribution of PdPt bimetallic nanodendrites in-situ grown on 16 cm^2 GDLs [68, 194]. The GDLs with PdPt nanostructures are directly tested as cathodes in H_2/air PEFCs to evaluate the performance. The electrochemical surface area (ECSA) and intrinsic catalytic activities of PdPt bimetallic nanostructures are measured in-situ in PEFCs and their contribution to power performance in real fuel cell operation conditions are discussed in detail in comparison to Pt NWs. Based on the results, the influence mechanisms of Pd on the morphology, distribution and performance of PdPt nanostructured gas diffusion electrodes (GDEs) are proposed at the end of this chapter.

5.2 Distribution and Morphology of PdPt Nanostructures

The as-prepared PdPt GDEs with Pd amounts from 50–0.5 at% were characterised by SEM to investigate the behaviour of PdPt nanostructures on GDL surfaces. TEM analysis was performed to get detailed microstructure information for the PdPt catalysts.

Fig. 5.1 shows SEM images of the distribution of PdPt nanostructures on the carbon paper surface with 50 at% Pd. It can be observed that many aggregates with a size of 100–200 nm are formed. TEM images in Fig. 5.2 display more details of the catalyst aggregates

formed on the carbon surface. The high magnification image (Fig. 5.2d) shows that the formed nanostructures are spherical nanoparticles with an average diameter of ca. 5 nm.

With the decrease of the Pd content to 25 at%, similar aggregates are formed to that of 50 at% Pd and the images are shown in Fig. 5.3. Although the diameter of the aggregates becomes slightly larger (ca. 200–300 nm), the number is evidently decreased. TEM images (Fig. 5.4) show that the product consists of dominant nanoparticles with a small quantity of elongated particles and short dendrites.

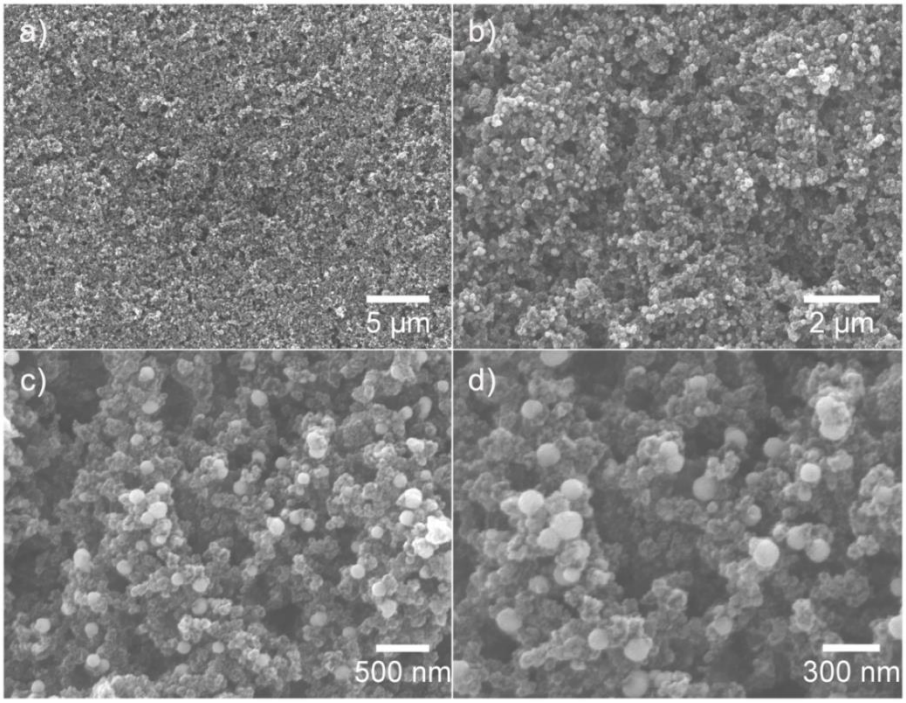

Fig. 5.1 (a-d) SEM images at different magnifications for PdPt nanostructures grown on the GDL surface with 50 at% Pd.

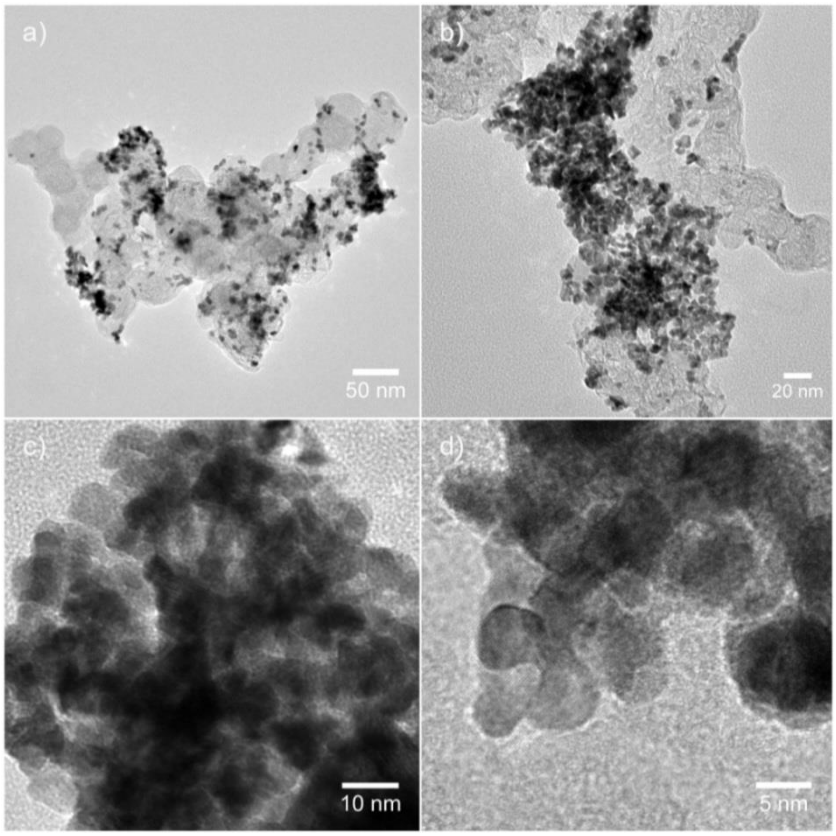

Fig. 5.2 TEM images at different magnifications for PdPt nanostructures with 50 at% Pd.

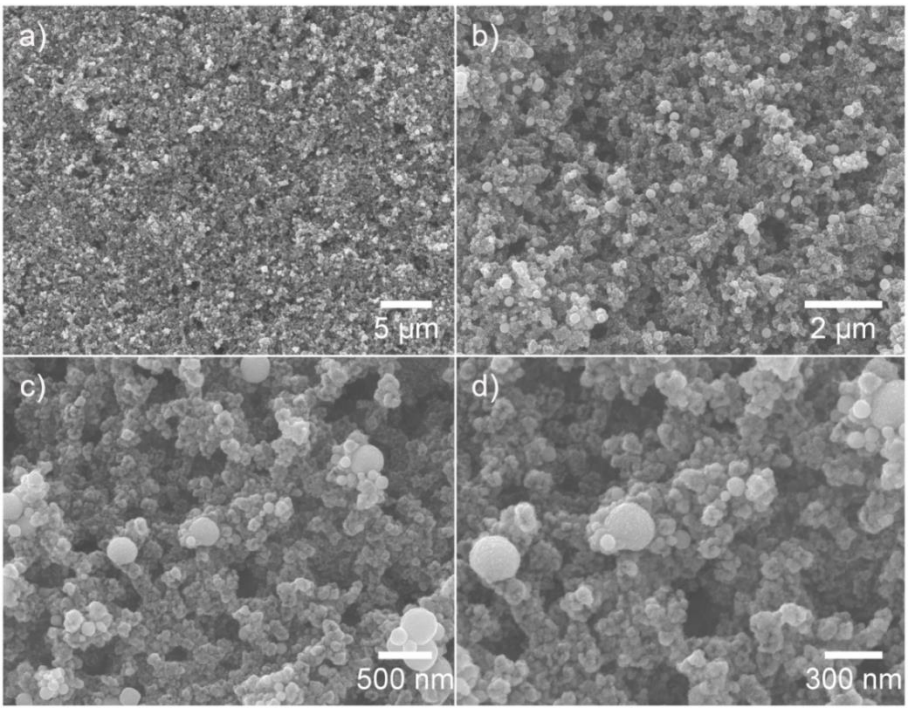

Fig. 5.3 SEM images at different magnifications for PdPt nanostructures grown on the GDL surface with 25 at% Pd.

When further reducing the Pd amount to 10 at%, no large aggregates can be observed from SEM images (Fig. 5.5). TEM images in Fig. 5.6 show a better dispersion of PdPt nanostructures. It also shows that a high yield of nanodendrites is formed and the nanoparticles have disappeared. The dendrite morphology can even be observed at a lower magnification. The branch diameter of such nanodendrites is ca. 4 nm and the length is ca. 5–10 nm (Fig. 5.6b).

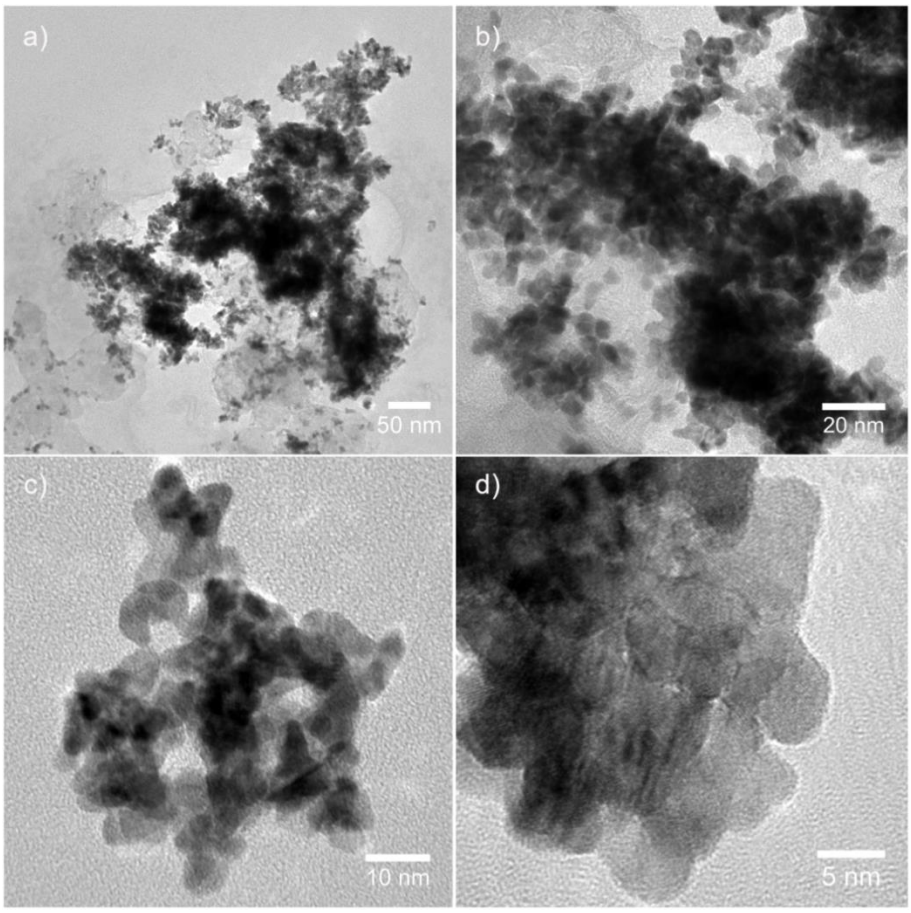

Fig. 5.4 TEM images at different magnifications for PdPt nanostructures with 25 at% Pd.

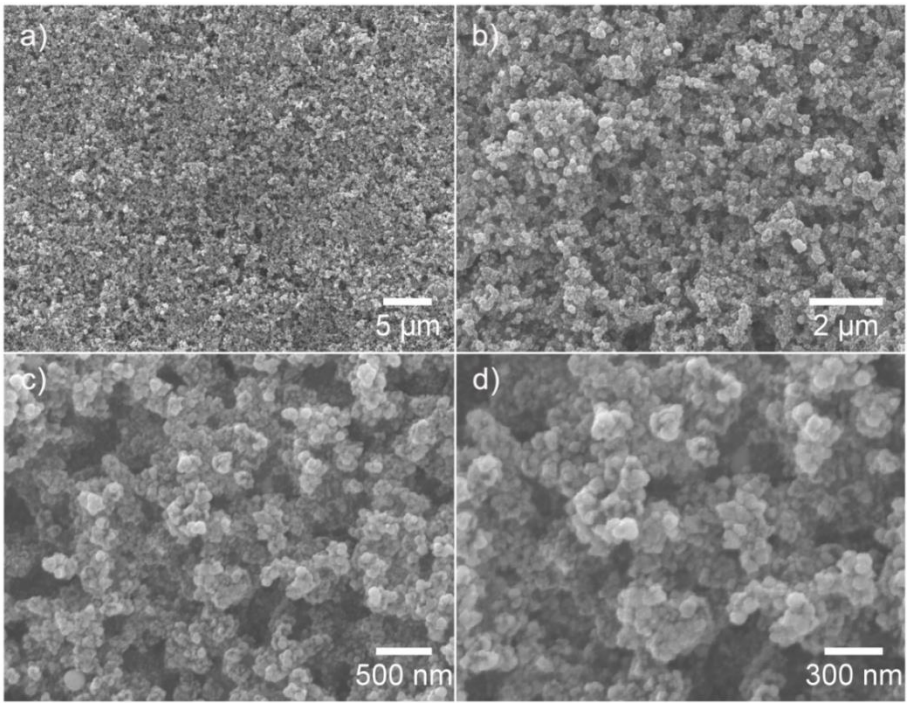

Fig. 5.5 SEM images at different magnifications for PdPt nanostructures grown on the GDL surface with 10 at% Pd.

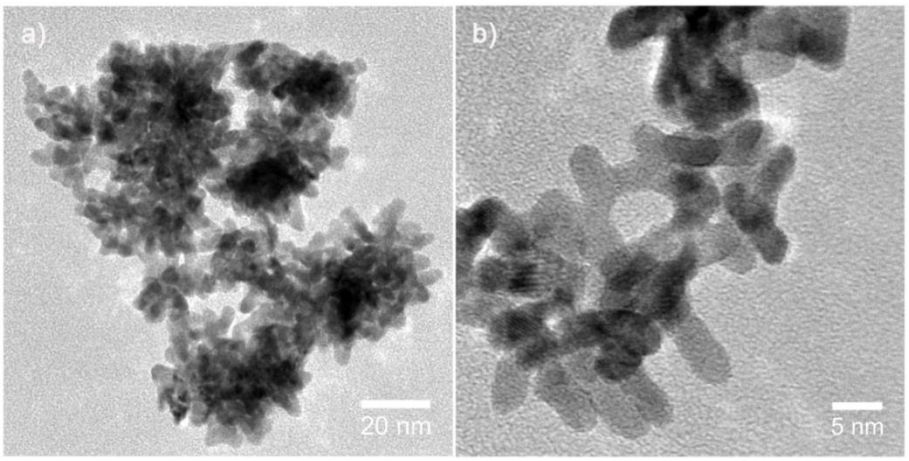

Fig. 5.6 TEM images at different magnifications for PdPt nanostructures with 10 at% Pd.

At a Pd content of 5 at%, uniform PdPt nanostructures are achieved on the GDL surface with very few aggregates (Fig. 5.7). TEM images in Fig. 5.8 show the crystalline nature of PdPt NDs, which is elucidated by the selected-area electron diffraction (SAED) pattern with intense rings assigned to the (111), (200), (220) and (311) planes of the Pt face-

centred cubic (fcc) crystals (inset in Fig. 5.8a). A HR-TEM image shown in Fig. 5.8d displays typical nanodendrites. The inset image indicates a lattice spacing distance of 0.22 nm for one branch of PdPt nanodendrites, which is slightly smaller than 0.23 nm of the {111} lattice spacing of the fcc Pt. This contraction of lattice caused by the addition of Pd is in line with the reported results in literature [222], which indicates the interactions between Pt and Pd atoms in the formation of PdPt NDs.

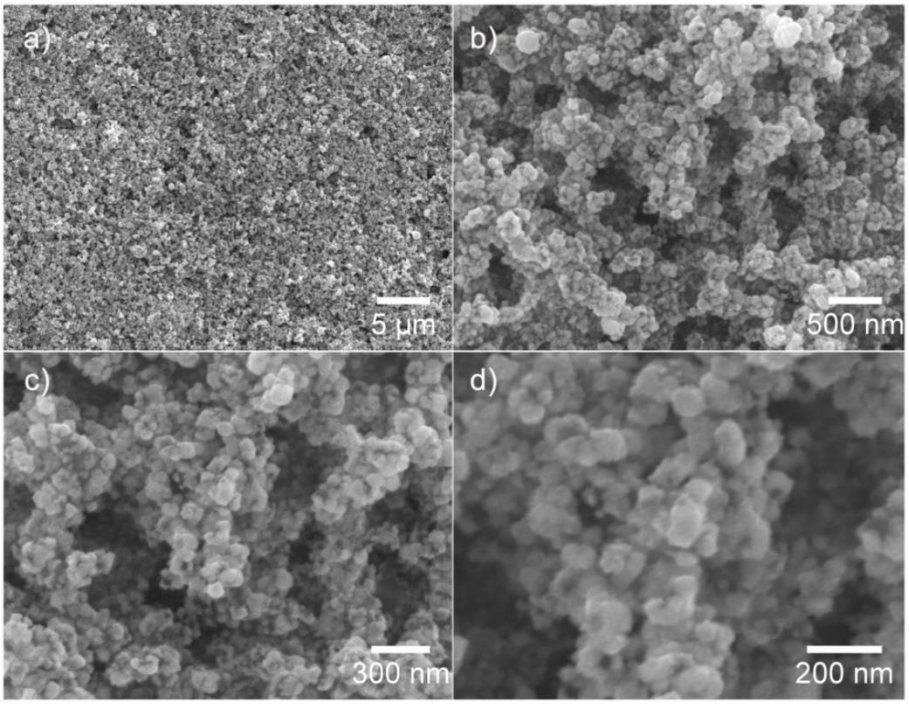

Fig. 5.7 SEM images at different magnifications for PdPt nanostructures grown on the GDL surface with 5 at% Pd.

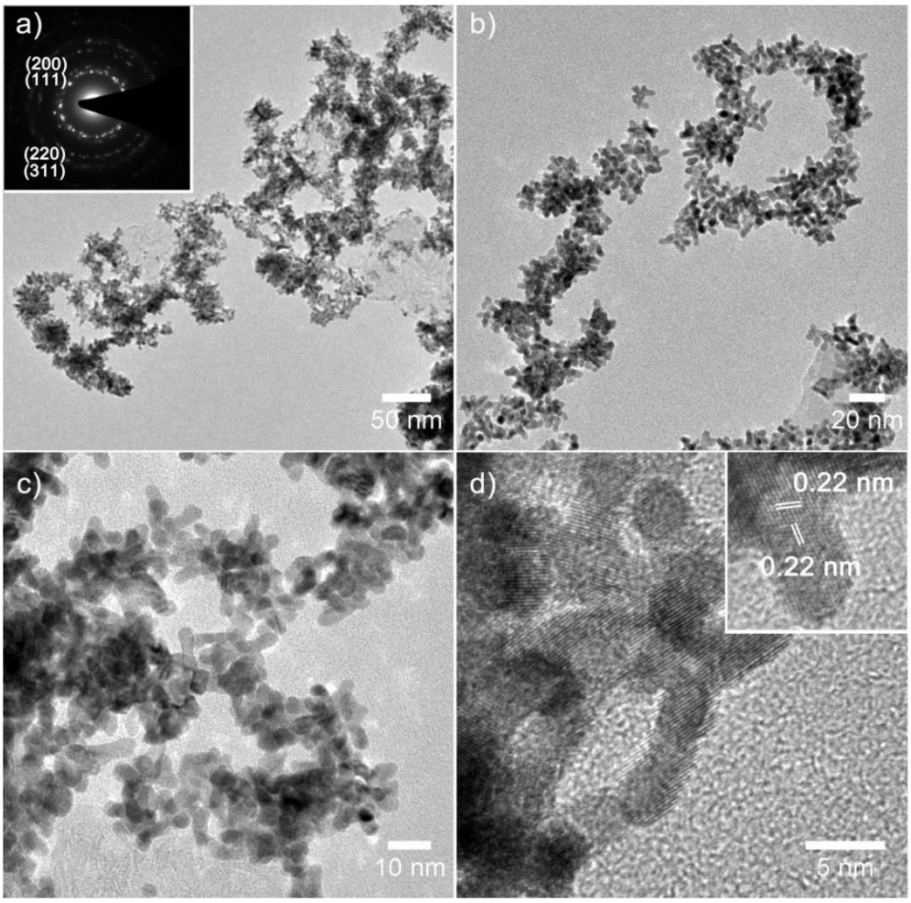

Fig. 5.8 TEM images at different magnifications for PdPt nanodendrites with 5 at% Pd. Inset in a) and d) shows the SAED pattern and HR-TEM image, respectively.

When the Pd content further decreases to 2.5 at% (Fig. 5.9) and even lower to 0.5 at% (Fig. 5.10), the distribution of PdPt nanostructures on GDLs becomes non-uniform again and only a part of each carbon sphere surface is covered by the catalysts.

TEM images in Fig. 5.11 display the dendrite morphology. Compared with PdPt 5 at%, the length of branch increases to 10–20 nm while the diameter has no obvious change. Therefore, in the presence of a high Pd content, nanoparticles are inclined to form and nanodendrites are achieved when the Pd content decreases.

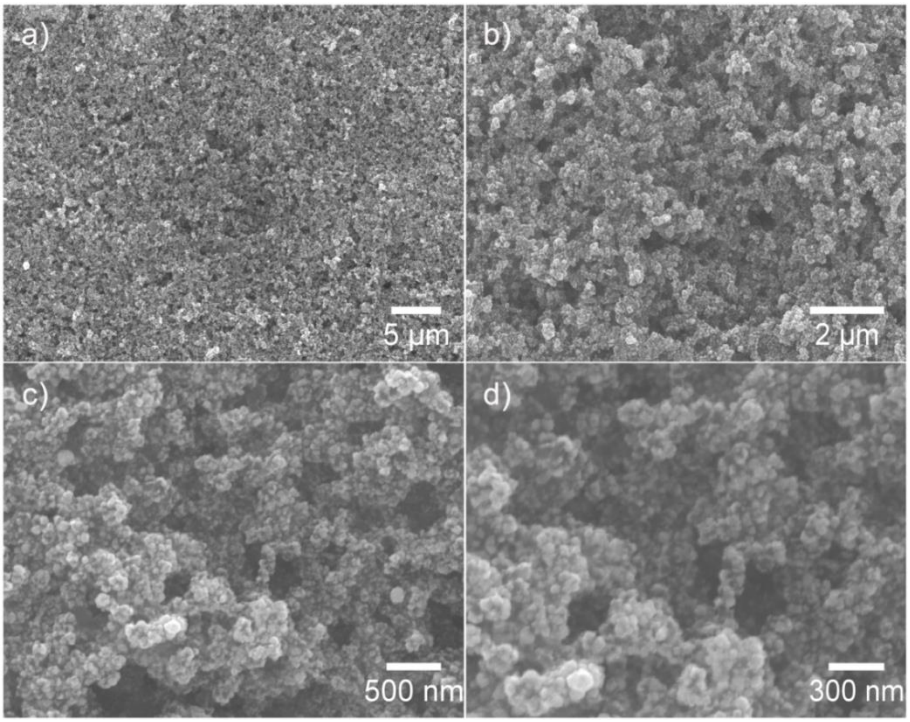

Fig. 5.9 SEM images at different magnifications for PdPt nanostructures grown on the GDL surface with 2.5 at% Pd.

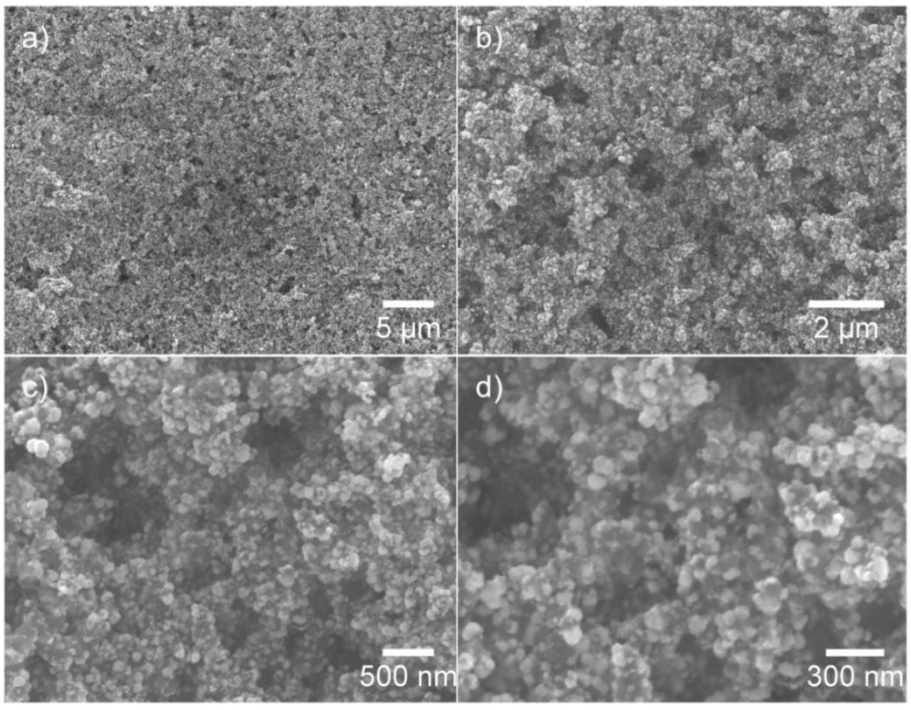

Fig. 5.10 SEM images at different magnifications for PdPt nanostructures grown on the GDL surface with 0.5 at% Pd.

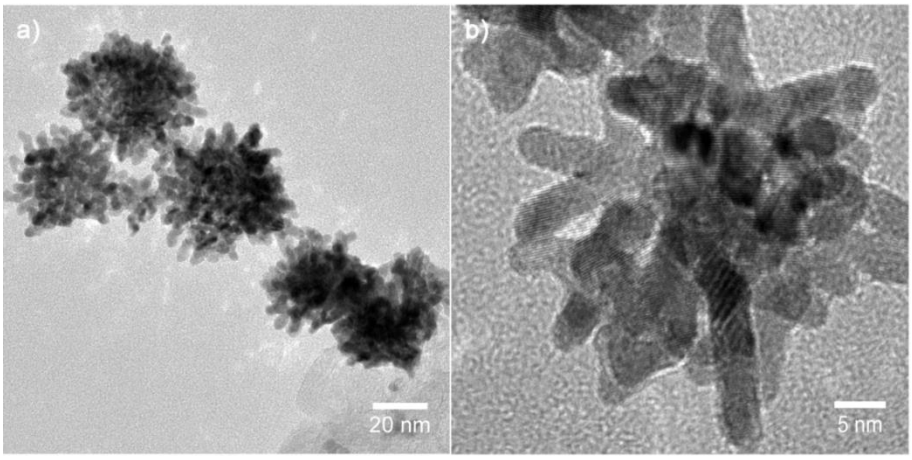

Fig. 5.11 TEM images at different magnifications for PdPt nanostructures with 2.5 at% Pd.

5.3 Performance in Single Cell Testing

In order to understand the catalytic performance in real fuel cell conditions, PdPt GDEs fabricated with different Pd amounts were directly used as cathodes and tested in hydrogen-air PEFCs with an active area of 16 cm^2. The effects of Pd on the catalytic activity and durability were further measured by polarisation curve, EIS, CV, ADT as well as mass and specific area activities. PtNW GDE was also tested under the same testing conditions for comparison with the PdPtND GDEs.

5.3.1 Power Performance in Fuel Cells

Fig. 5.12 shows the polarisation and power density curves of the MEAs with the as-prepared PdPt GDEs. The PdPt GDE with 50 at% Pd shows a very poor performance. With the decrease of the Pd content, a better performance is obtained, reaching the maximum value at 5 at%. Further decrease of the Pd amount results in a decline of the electrode performance but there is no big difference between PdPt 2.5 at% and 0.5 at% GDEs. The performance of PtNW GDE (with the same metal loading of 0.4 mg cm^{-2}) without Pd is also very close to that of the PdPt 2.5 at% and 0.5 at% GDEs. The trend of

the power density at 0.6 V of these GDEs versus Pd content is shown in Fig. 5.12c. PdPtND GDE with 5 at% Pd exhibits the highest power density of 0.73 W cm^{-2} at 0.6 V, better than the 0.64 W cm^{-2} of PtNW GDE. The performance results could be well explained by the distribution and morphology information obtained from SEM and TEM analysis. The large aggregates formed at high Pd loading lead to the poor performance while the non-uniform distribution of PdPt NDs obtained at very low Pd amount also couldn't reach the highest performance.

5.3.2 Electrochemical Impedance Spectroscopy (EIS)

To further understand the behaviour of PdPt nanostructures, EIS measurements were conducted for PdPt GDEs with different compositions as well as for the PtNW GDE, and the results are shown in Fig. 5.13. It can be seen that the PdPtND GDE with 50 at% Pd shows the largest semicircles, followed by the one at 25 at% Pd. PdPt GDEs with medium and low Pd amount together with PtNW GDE show similar semicircles while the smallest semicircles are observed for the GDE with 5 at% Pd, indicating the best ORR catalytic kinetic performance and smallest mass transfer resistance, which is in agreement with polarisation and power density curves shown in Fig. 5.12a and b. Another thing worth noticing is that the PtNW GDE has a larger second semicircle at the high current density, demonstrating that Pd plays a key role in the improvement of catalyst distribution to facilitate the transfer of reactants and products.

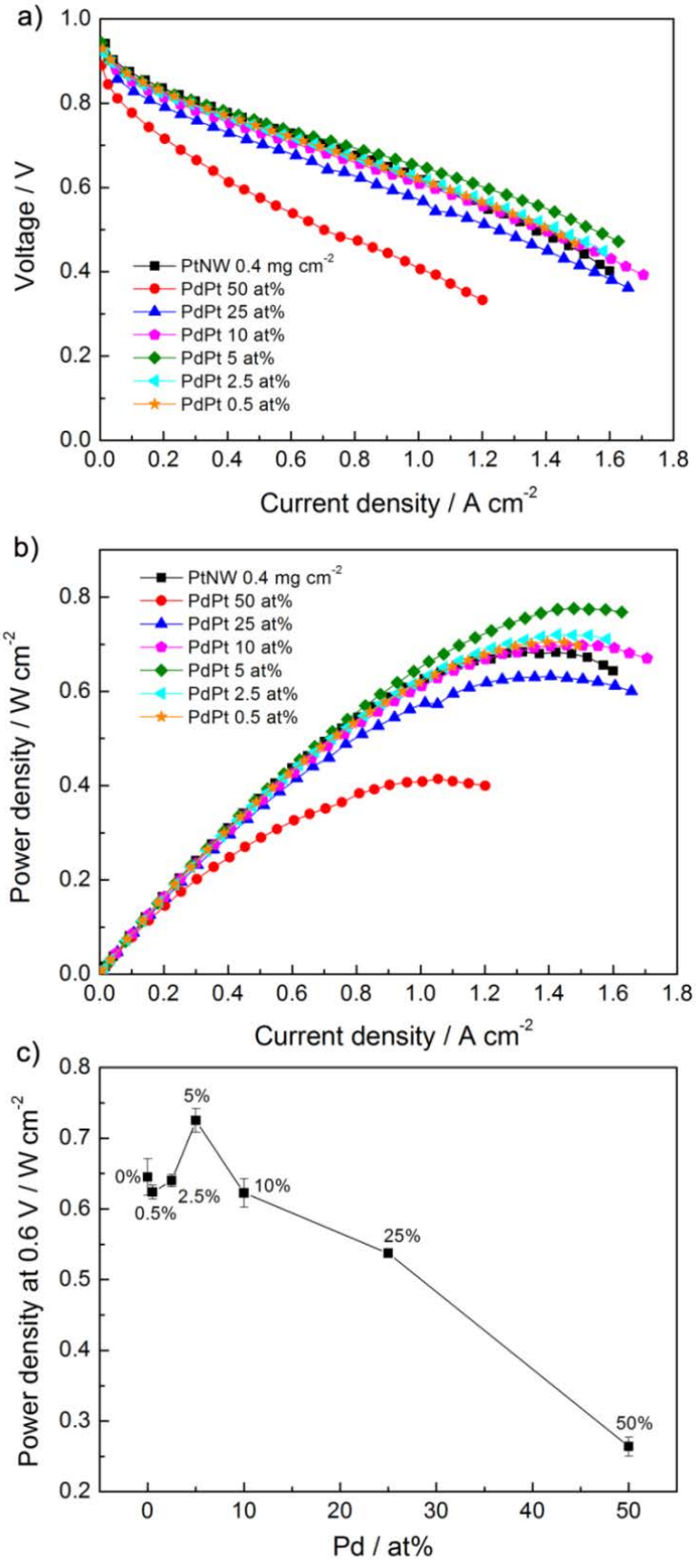

Fig. 5.12 (a) Polarisation curves, (b) power density curves and (c) the trend of the power density at 0.6 V for PdPt GDEs with different Pd amounts and the PtNW GDE.

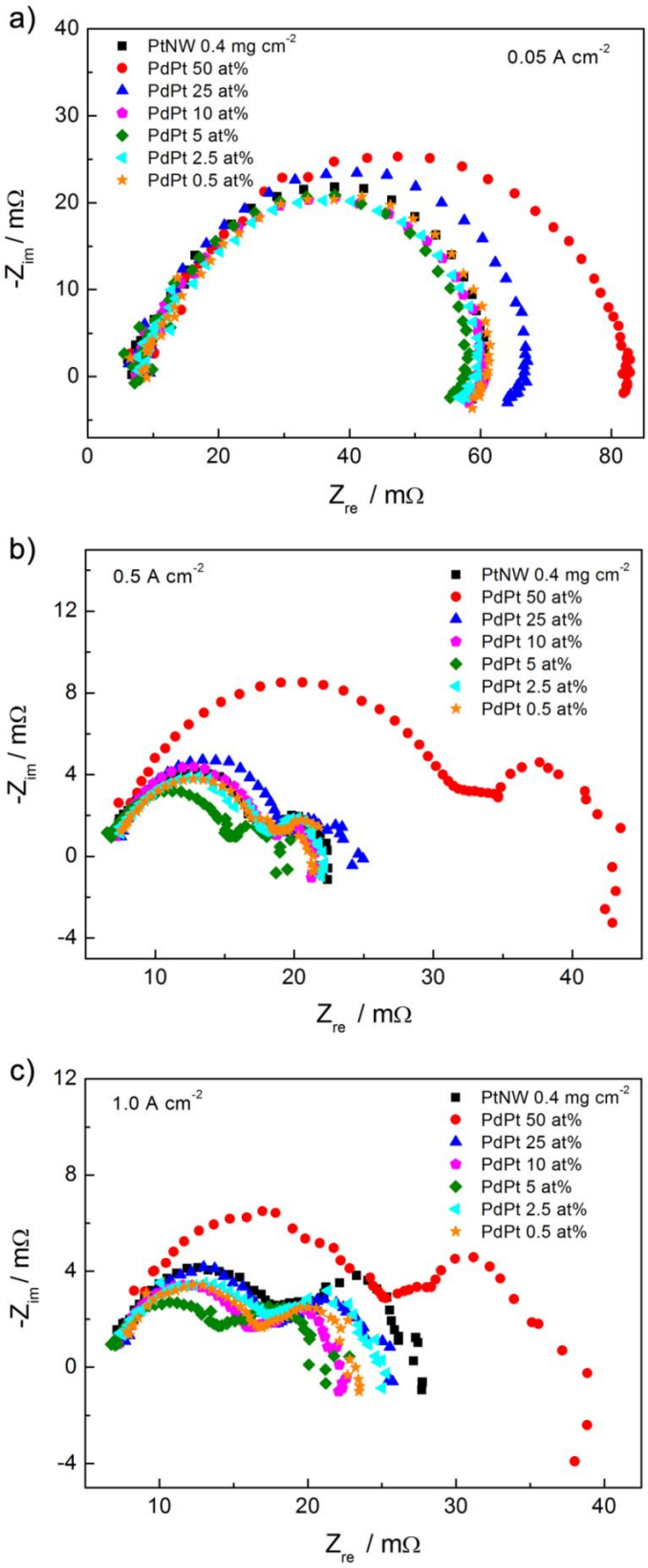

Fig. 5.13 EIS measured at (a) 0.05, (b) 0.5 and (c) 1.0 A cm^{-2} for PdPtND GDEs with various Pd amounts and the PtNW GDE.

5.3.3 Electrochemical Surface Area (ECSA)

Cathode cyclic voltammograms (CVs) were recorded in the single cell for PdPt GDEs with different Pd loadings to measure the ECSA of the catalysts within electrodes. From CVs in Fig. 5.14, based on the total metal amount in the precursor, the ECSAs for PdPt GDEs with the Pd atomic percentage of 50, 25, 10, 5, 2.5, 0.5 and PtNW GDE are 0.49, 7.21, 11.59, 22.40, 18.76, 18.15 and 14.70 $m^2\ g^{-1}$, respectively. It can be seen that the sequence of ECSA matches very well with that of the power performance shown in Fig. 5.12. The smallest ECSA value of PdPt 50 at% GDE can be ascribed to the formation of large nanoparticle aggregates (Fig. 5.1). Larger ECSAs are obtained as the aggregates reduce with the decreased Pd amount (Fig. 5.3 and 5.5). When the composition of Pd is at an optimal amount of 5 at%, uniform PdPt NDs cover the whole surface and a better ECSA is achieved as expected. The ECSAs of PdPt GDEs with 2.5 and 0.5 at% Pd are slightly lower. The long and dense nanodendrite branch and a non-uniform distribution on the GDLs together lead to these slightly lower ECSAs. It also shows that the PdPtND 5 at% GDE has a larger ECSA than that of PtNW GDE, which indicates that PdPtND GDE is more electrochemically accessible due to the particular structure of the bimetallic nanodendrites and their better dispersion on the GDL surface.

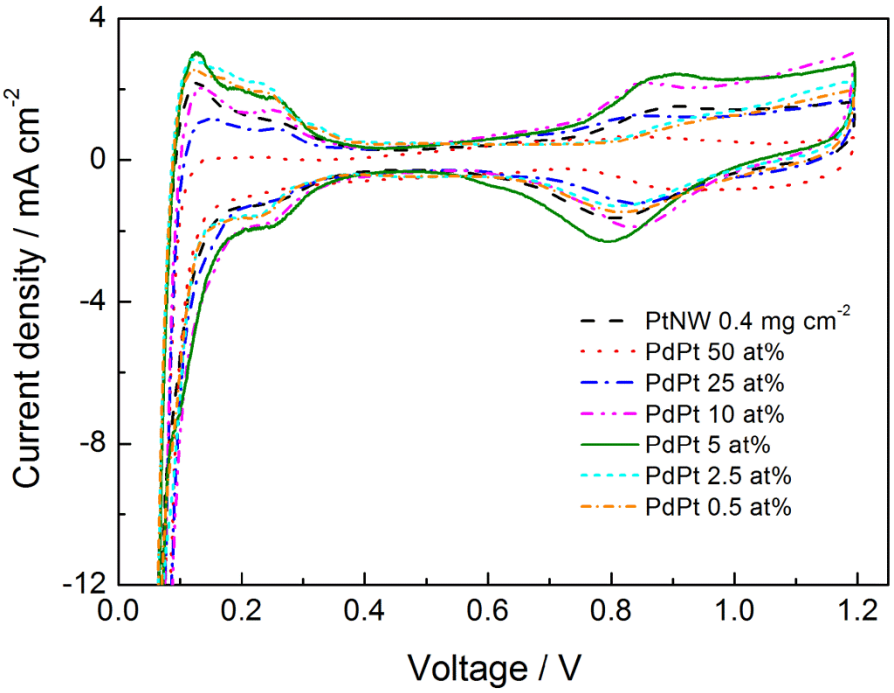

Fig. 5.14 Cathode CVs for PdPt GDEs with different compositions and the one with Pt nanowire catalysts. Measurements were taken at T_{cell}=25 ^{o}C with fully humidified H_2 and N_2 at 0 bar (stoichiometry s=1.3/2.4).

5.3.4 Stability from the Accelerated Degradation Test (ADT)

It can be seen that the MEA with the PdPtND GDE with 5 at% Pd shows a better power performance than that with the PtNW GDE, and this seems to be consistent with the reported synergistic effect for the enhanced catalytic activities of PdPt hybrid structures [223]. To check the durability of the as-prepared PdPt NDs, an ADT was carried out by 3000 potential sweep cycles in the single cell at room temperature. CVs after the ADT test are displayed with the initial curves and compared with those of PtNW GDE in Fig. 5.15a. After the ADT, both GDEs exhibit a big decline of their ECSAs. The remaining values of PdPtND 5 at% and PtNW GDEs, summarised in Fig. 5.15b, are 11.96 and 5.55 m^2 g^{-1}, corresponding to 46.6% and 62.2% loss of their initial ECSA value, respectively. The

enhanced stability of PdPt NDs agrees well with literature [221, 224], which is based on the synergistic effect of Pd and Pt of catalysts during the potential cycling.

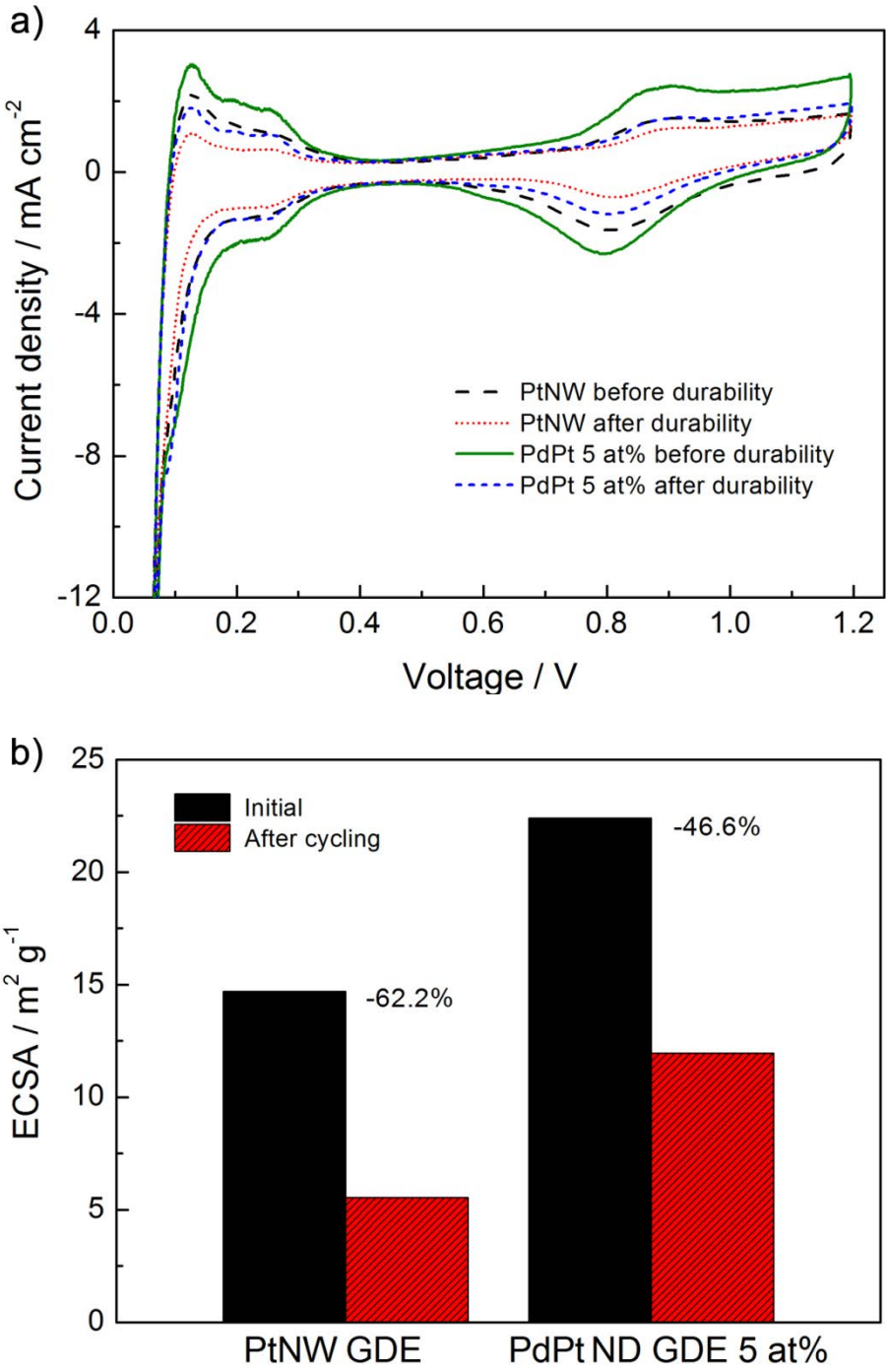

Fig. 5.15 (a) CVs; (b) summary of the ECSAs of PtNW GDE and PdPtND GDE with 5 at% Pd before and after the potential cycling.

5.3.5 Catalytic Activity in Oxygen

To confirm the enhanced effect of Pd to Pt, the intrinsic catalytic activities towards ORR of both GDEs were also measured in practical PEFCs with H_2/O_2 by the standard protocol [191]. Fig. 5.16 shows original polarisation curves in oxygen and the corrected ones considering the H_2-crossover and ohmic resistance losses. Both GDEs display similar polarisation curves despite that the PtNW GDE shows a slightly better performance than that of PdPtND GDE. The kinetic catalytic activities at 0.9 V from the corrected polarisation curves as well as the corresponding mass and specific area activities of Pt NWs and PdPt NDs with 5 at% Pd catalysts are summarised in Table 5.1.

Other than with the reported enhanced catalytic activities by introducing Pd to Pt, a slightly lower mass activity is observed for PdPt bimetallic nanodendrites over Pt nanowires. While most results from literatures are obtained through the ex-situ electrochemical measurement by using rotating disk electrodes in liquid electrolytes, the testing here is conducted in-situ in fuel cells. In fact, this is not the first time that a lower mass activity is observed in practical fuel cells for a heterostructure catalyst. Work from several research groups also demonstrated that 5 nm size Pt catalyst based electrodes only exhibited comparable mass activity as that of 4.9 nm Pt_3Co catalyst based electrodes [225]. On one hand, this indicates the difference in the characterisation of catalytic activities by ex-situ electrochemical measurement in liquid electrolytes and the in-situ fuel cell testing, which has also been pointed out by Gasteiger [191], although the detailed mechanism is still not clear at the moment. Testing fuel cell electrodes under practical operating conditions provides more valuable information for real applications, but it is also more complex compared with pure material research by ex-situ measurements. On the other

hand, the in-situ tests confirm that the higher performance of the PdPtND GDE results from the lower mass transfer losses due to the uniform distribution of PdPt NDs on the GDL surface.

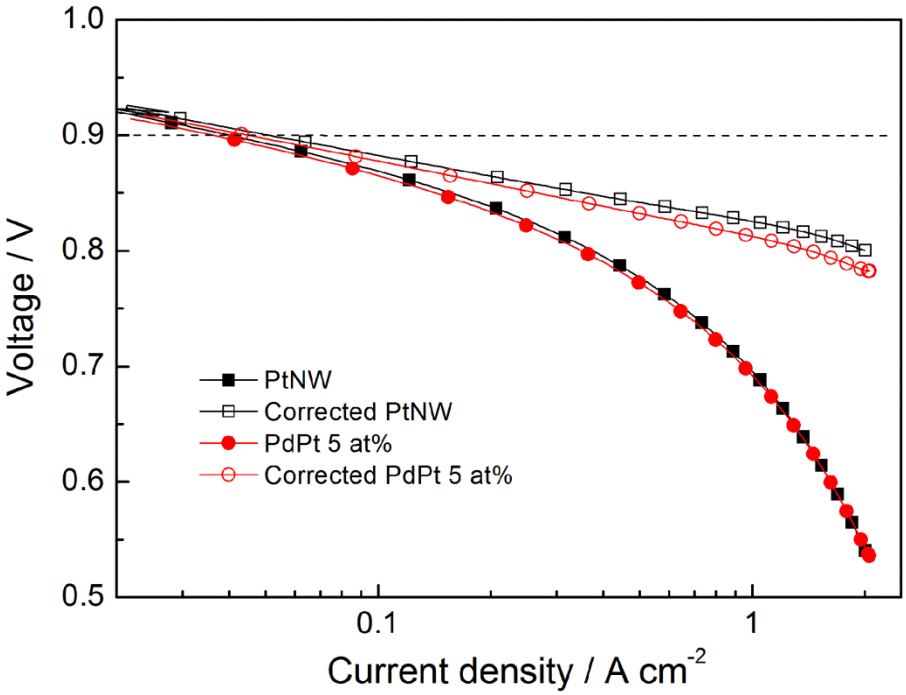

Fig. 5.16 Original uncorrected (solid symbols) and corrected (empty symbols) H_2/O_2 performance of the MEAs with the PtNW and PdPtND 5 at% GDEs.

This is demonstrated by the EIS measurement results shown in Fig. 5.13. The smaller impedance semicircles at the large current density (1.0 A cm^{-2}) reveal the improved mass transfer performance. Therefore, a same conclusion can be reached here as in Chapter 4 that the distribution of catalysts on the GDL is as important as catalysts themselves, which together contributes to the performance in PEFC electrodes.

Table 5.1 Catalytic performance characteristics of the two MEAs with Pt NWs and PdPt 5 at% NDs.

Catalysts	ECSA ($m^2\ g^{-1}$)	i (0.9 V) (mA cm^{-2})	i_m (0.9 V) (A mg^{-1})	i_s (0.9 V) (μA cm^{-2})
Pt NWs	14.70	51.17	0.128	870
PdPt NDs (5 at% Pd)	22.40	44.96	0.112	502

(i_m is mass activity and i_s is specific area activity)

5.4 Structural and Compositional Characterisation of As-Prepared PdPt Nanodendrites

PdPtND GDE with 5 at% Pd which demonstrated the best power performance possessed the nanodendrite morphology and a uniform catalyst dispersion on the GDL. To further check the structure and composition, physical characterisation techniques such as XRD, EDS and XPS were used to analyse the catalyst.

XRD patterns of the GDL 35BC, as well as Pd, Pt and PdPt 5 at% GDEs are presented in Fig. 5.17. The main characteristic peaks of pure Pd and Pt are at very similar positions. However, the intensity of the Pd peaks is much stronger than that of Pt and the width of the Pt peaks is broader than that of their Pd counterparts. PdPt 5 at% NDs show the characteristic peaks of the fcc crystalline Pd and Pt. The peaks at ca. 39.9°, 46.8°, 67.9° and 81.7° are indexed to the (111), (200), (220) and (311) planes, which is in agreement with the SAED results shown in Fig. 5.8a. However, it is very difficult to identify Pt and Pd peaks separately just from XRD pattern due to their very close lattice space. In case of this, the composition of the PdPt 5 at% NDs was analysed by EDS spectroscopy in TEM

mode. The corresponding spectrum (Fig. 5.18) displays C, Pd and Pt elements, confirming the existence of Pd and Pt on the surface of carbon paper. The strong Cu peak comes from the Cu grid. The table inside the figure shows the percentage of the Pd and Pt elements. The obtained Pd atomic percentage of 3.04% is a bit lower than the expected value of 5%.

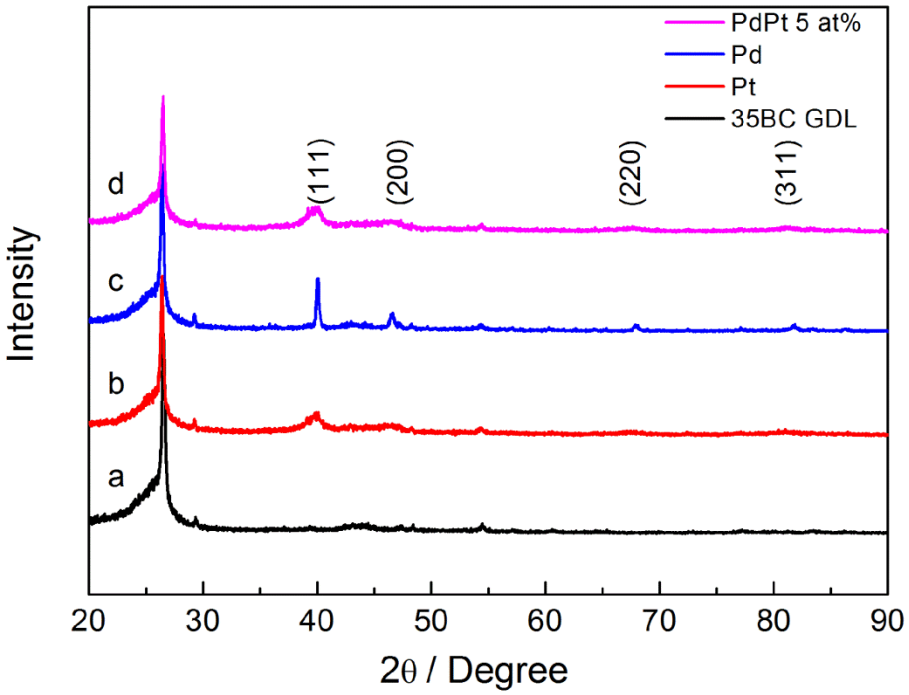

Fig. 5.17 XRD patterns of (a) 35BC GDL; (b) pure Pt on GDL; (c) pure Pd on GDL; and (d) PdPt 5 at% NDs on GDL.

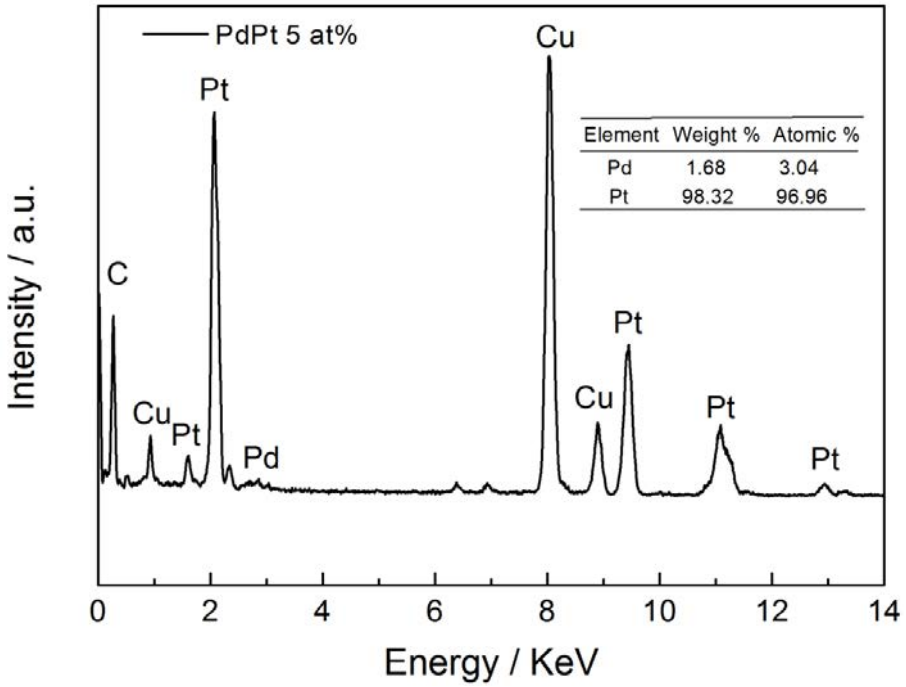

Fig. 5.18 EDS spectrum of PdPt NDs with 5 at% Pd (Cu comes from Cu grid used in TEM analysis).

To estimate the effective metal loading on the GDL surface, TGA analysis was implemented for the pristine 35BC GDL carbon paper and the PdPt GDEs with 5% Pd. The corresponding curves shown in Fig. 5.19 are similar to those of the PtNW GDEs in the previous chapter. Comparing the stable part of the pristine 35BC GDL with that of the PdPt 5% GDE sample, an actual total metal loading of 6.132±0.004 mg is obtained, which is very close to the theoretical target, revealing that almost all of the PdPt NDs were grown on the GDL support.

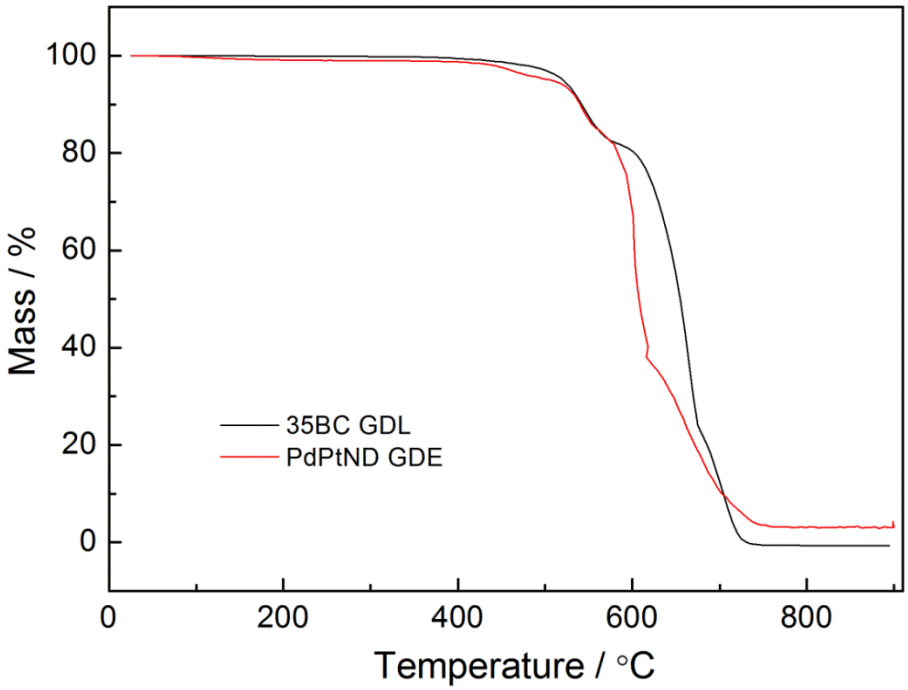

Fig. 5.19 (a) TGA curves of the pristine 35BC GDL and PdPt GDE with 5 at% Pd.

XPS analysis was also conducted to identify the near-surface species involved in the PdPt heterostructures. The XPS survey spectrum of the PdPtND GDE with 5 at% Pd (Fig. 5.20a) shows a strong Pt 4f and Pt 4d signals as well as Pd 3d signal, confirming the existence of Pt and Pd formed on the GDL surface. Fig. 5.20b compares typical peaks of Pt 4d3/2, Pd 3d5/2 and Pd 3d3/2 in PdPt GDEs with various Pd contents. With the decrease of the Pd content, the intensity of Pd 3d peaks becomes weaker while that of the Pt 4d peaks increases. Also, all peaks shift positively in the obtained PdPt GDEs compared with the monometallic Pt (4d3/2 at 331 eV) and Pd (3d5/2 and 3/2 at 335 and 340 eV, respectively), suggesting the Pd-Pt interactions [226] change the atomic structure thus contributing to the synergistic effect in PdPt bimetallic hybrids [227].

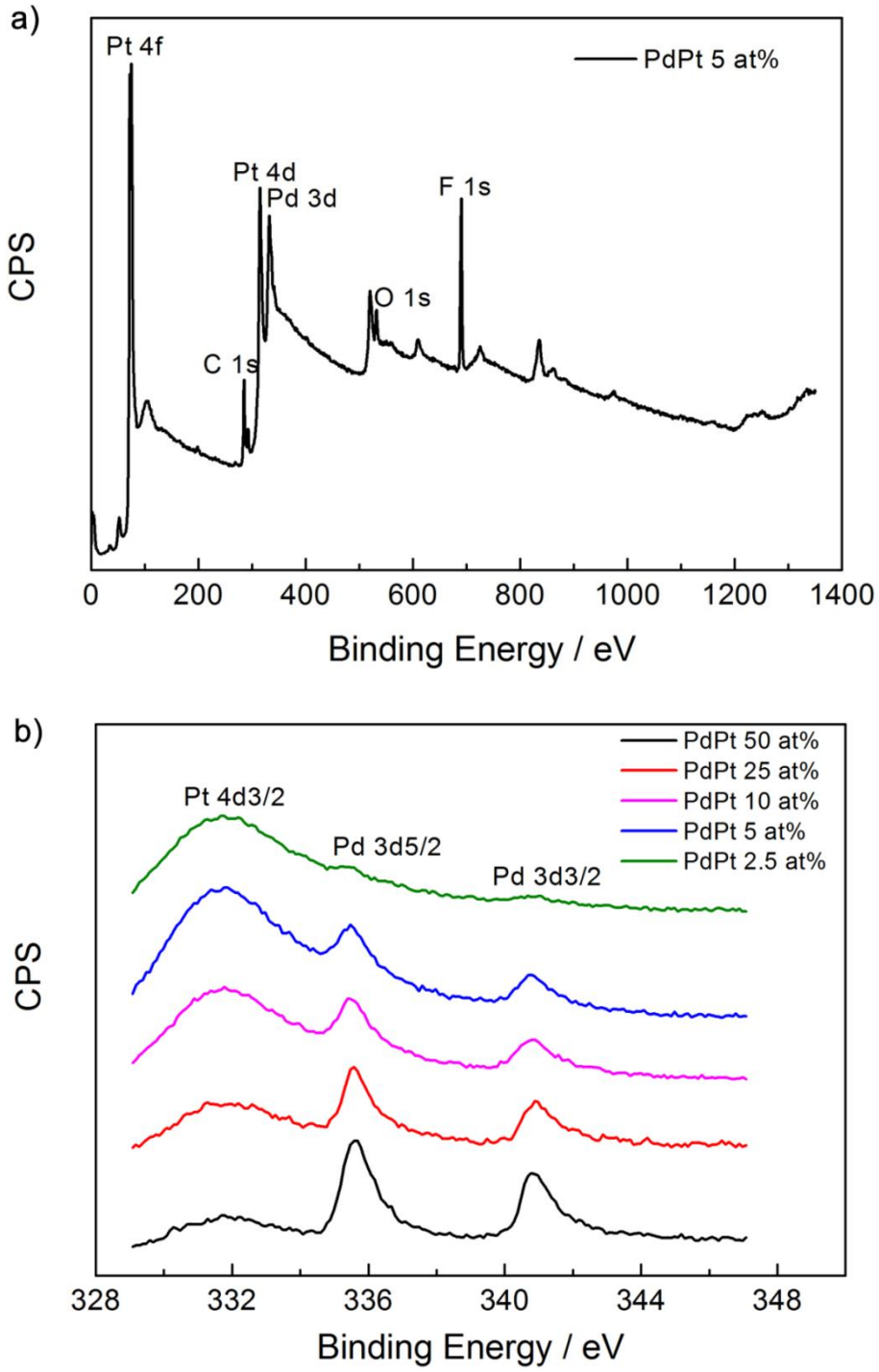

Fig. 5.20 (a) XPS survey of PdPt NDs with 5 at% Pd and (b) XPS spectra of PdPt nanostructures with different Pd amounts in Pd 3d and Pt 4d3/2 region.

5.5 Growth Mechanism of PdPt Nanostructures at Various Pd Amounts

Although plenty of work has been reported on PdPt nanostructures, there really is not a lot of evidences for the growth mechanism. Hence, based on the composition-dependent morphology and distribution of PdPt nanostructures on GDLs, the influence mechanism of Pd on PdPt growth is proposed with the help from the time-dependent experiments. Considering the fact that the standard reduction potential of Pd^{2+}/Pd (0.92 V vs. standard hydrogen electrode (SHE)) is more positive than that of the $PtCl_6^{2-}$/Pt (0.73 V vs. SHE) couple, the reduction of Pd(II) is more preferred than that of Pt(IV) [221]. Therefore, Pd nuclei can form at the very initial stage and then act as seeds to induce the co-reduction and further growth of PdPt nanostructures [124, 228]. Besides, given that Pt has a higher surface energy than Pd [123], it can be inferred that Pt will grow on the Pd surface rather than forming Pt nuclei separately. In this case, at a high Pd percentage, abundant Pd nuclei form rapidly upon the addition of the reductant and serve as multiple nucleation sites for the formation of PdPt NPs. The high supersaturation of Pd atoms greatly lowers the free-energy barrier for heterogeneous nucleation and is responsible for the rapid nucleation rate of Pt with a vanishingly small growth rate [229]. Therefore, the main morphology obtained was nanoparticle-like, as seen in Fig. 5.2. The produced nanoparticles engage in a self-aggregation process to minimise the total surface free energy of the system, thus a lot of aggregates are formed (Fig. 5.1 and Fig. 5.3). This aggregation reduces the contribution of the catalyst to the three-phase boundary (TPB) in the electrodes and leads to a low catalyst utilisation ratio, finally resulting in a poor electrode performance (Fig. 5.12a).

With decrease in Pd content, the nucleation sites provided are reduced, and accordingly, short nanodendrites are formed through the reported particle attachment growth process

[221], which is also consistent with the TEM images in Fig. 5.6. At an optimal Pd amount, the generated Pd seeds are just sufficient in number to accommodate the Pt atoms, making the Pt nucleation and growth rate balance. Thus, uniform PdPt NDs are formed. In this case, the regular catalyst layer is beneficial for the mass transfer to achieve a high catalyst utilisation ratio, thus a better catalytic performance is expected. With a further decrease in Pd and the increase in Pt content, the seed number provided by Pd nuclei becomes fewer and PdPt nanodendrites with longer and dense branches are obtained.

To confirm the above assumptions, PdPt nanostructured GDEs with 25 at% Pd were fabricated through two approaches. One was a one-step approach, during which Pd and Pt precursors were added together while the other was a two-step process, in which Pd was reduced first and after that Pt precursor was added to the mixture. It can be seen in Fig. 5.21a that the performance of the two obtained PdPt GDEs is almost the same, indicating that even when Pd and Pt are added together, Pd is reduced first to act as the nucleation seeds for the further growth of PdPt nanostructures, possessing similar behaviour as that in the two-step method. UV-Vis spectroscopy was also employed to monitor the whole one-step reaction process from 0 to 92 hours. Fig. 5.21b shows the absorption peaks of the Pd and Pt precursor as well as that of the PdPt mixture at different time intervals. It can be seen that only after 2 h reaction, the line of the PdPt mixture almost overlaps with that of the Pt precursor, which implies that Pd is mainly reduced at the initial stage of the reaction. With the on-going of the reaction, the intensity of Pt is gradually reduced and no absorption peak can be observed until 24 h, indicating the whole reaction is nearly completed.

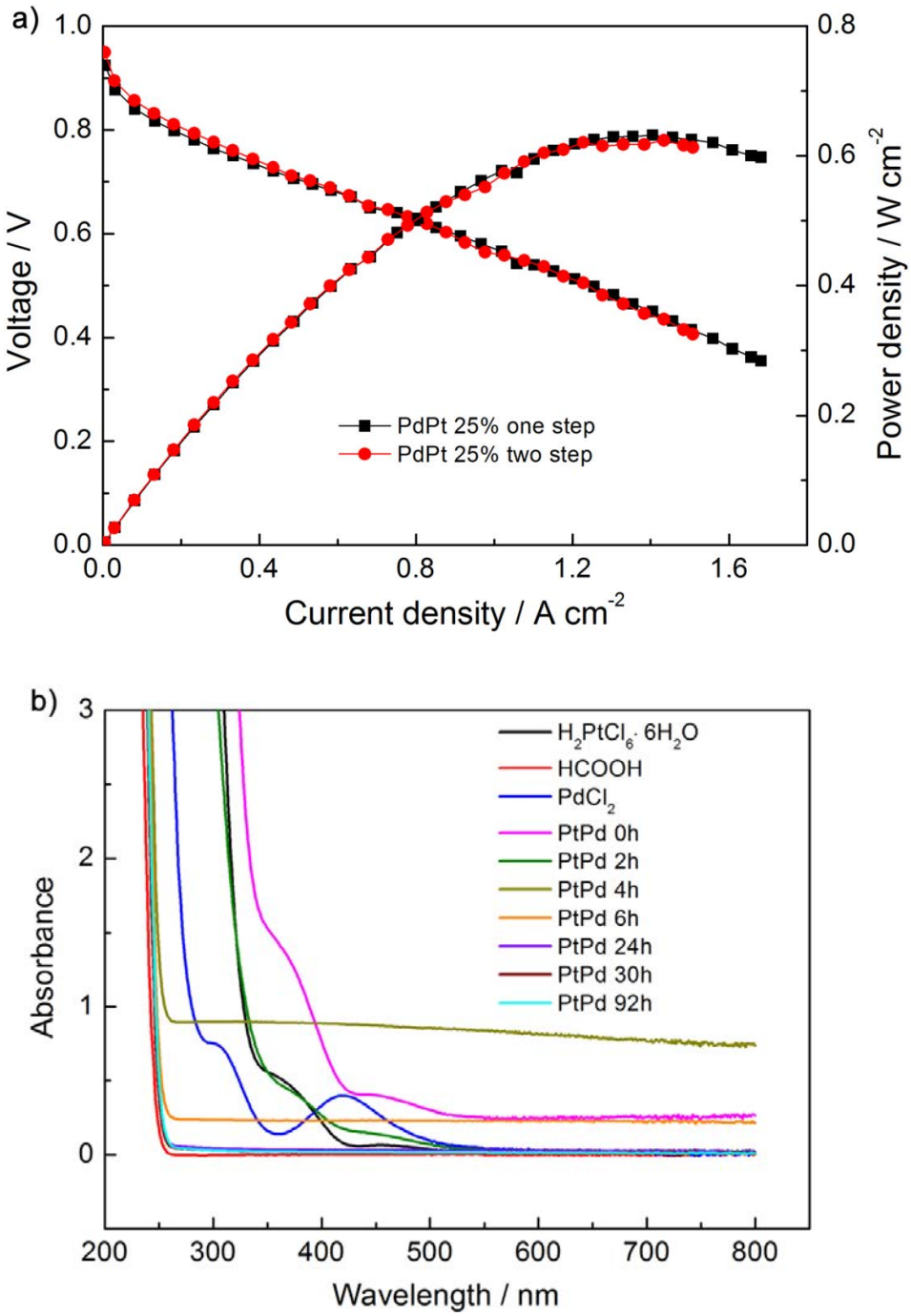

Fig. 5.21 (a) Power performance of PdPt GDEs fabricated by two approaches and (b) UV-Vis spectra of the precursor solution and the mixture of PdPt at different hours.

In order to understand the morphological evolution of PdPt NDs, catalyst nanostructures from PdPt GDEs with 5 at% Pd at various reaction periods were examined by TEM and

EDS. Fig. 5.22-5.25 show PdPt nanostructures with 5 at% Pd that were taken out from the reaction system at 2nd, 5th, 10th and 24th hour, respectively.

Fig. 5.22 shows that after reaction for 2 hours there are only tiny catalyst nanoparticles on carbon spheres. EDS results reveal a high Pd atomic percentage, indicating the preferred reduction of Pd at the initial stage. At the same time, Pt atoms were nucleated on the surface of Pd seeds.

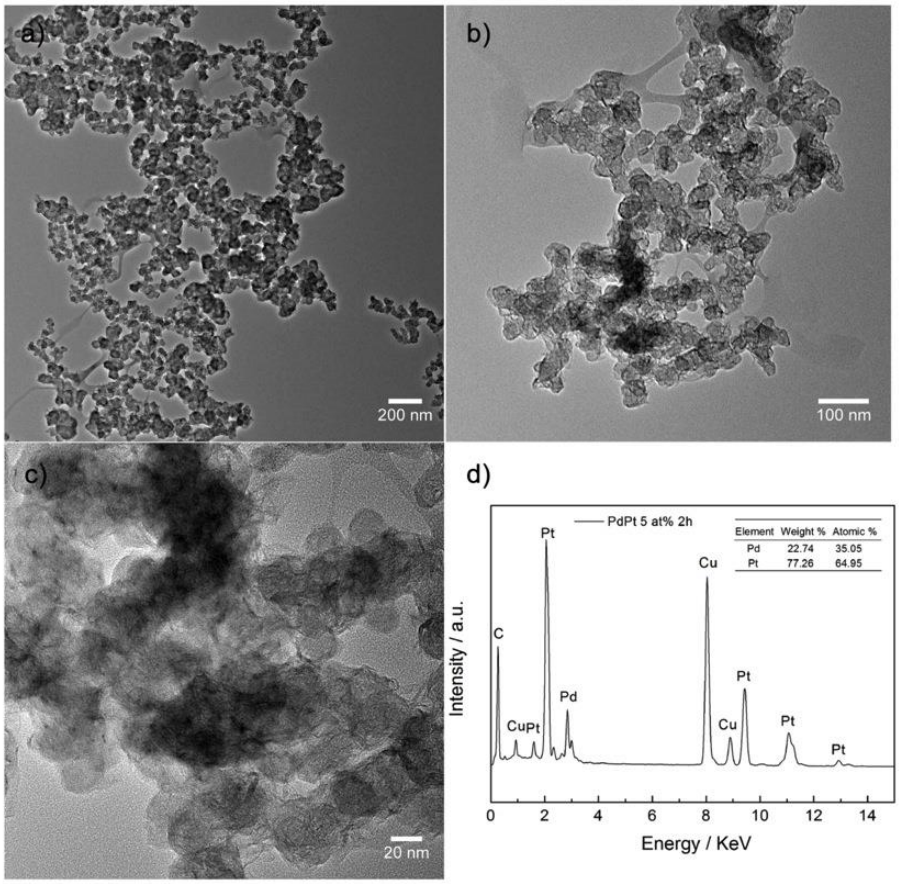

Fig. 5.22 (a-c) TEM images at different magnifications for PdPt nanostructures with 5 at% Pd reacted for 2h and (d) the corresponding EDS spectrum.

As the reaction proceeds to 5h, more PdPt nanostructures can be found on the carbon sphere surface (Fig. 5.23). The high resolution TEM image displays that the nanodendrite

branches start to appear and co-exist with a number of nanoparticles. EDS results also show a decreased Pd content from the initial stage and more Pt was reduced from the precursor solution and deposited on the Pd nanoparticle surface.

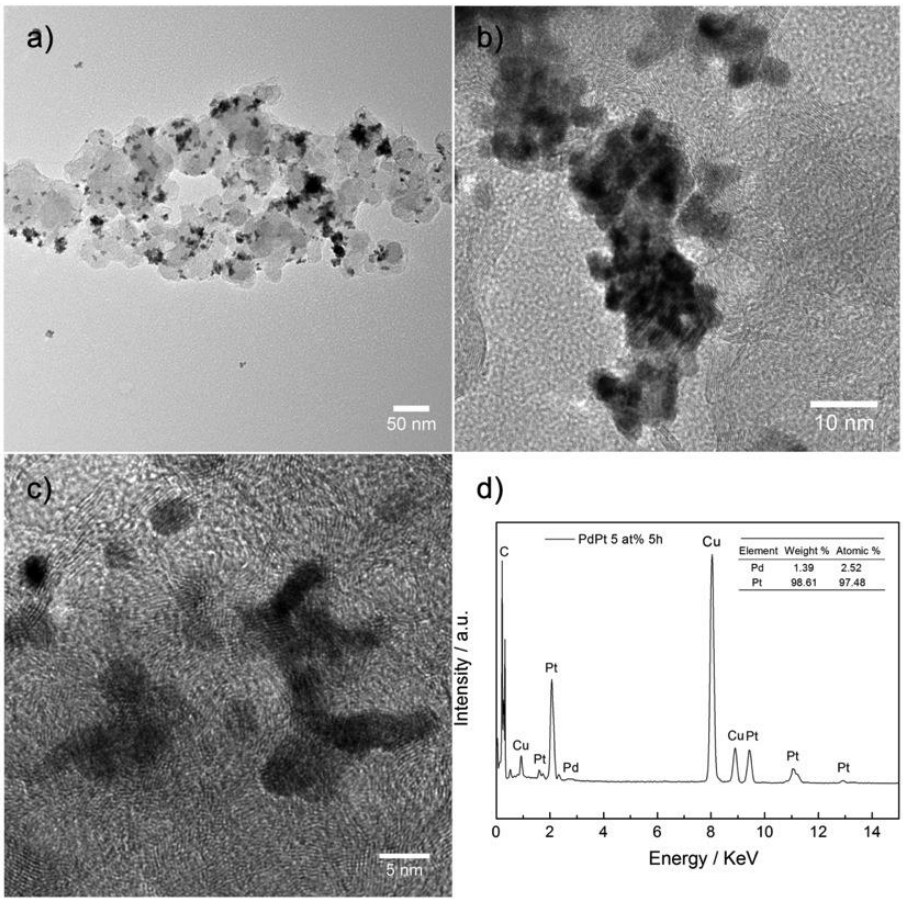

Fig. 5.23 (a-c) TEM images at different magnifications for PdPt nanostructures with 5 at% Pd reacted for 5h and (d) the corresponding EDS spectrum.

In the following time to 10 hours, almost all of the small nanoparticles disappear and PdPt nanostructures evolve into a highly branched dendritic morphology (Fig. 5.24). The atomic percentage of Pd is even lower. When the reaction goes forward to 24h, both of the morphology and atomic percentage do not exhibit any obvious change at this stage (Fig. 5.25), indicating that the reaction has been nearly finished at 10^{th} hour.

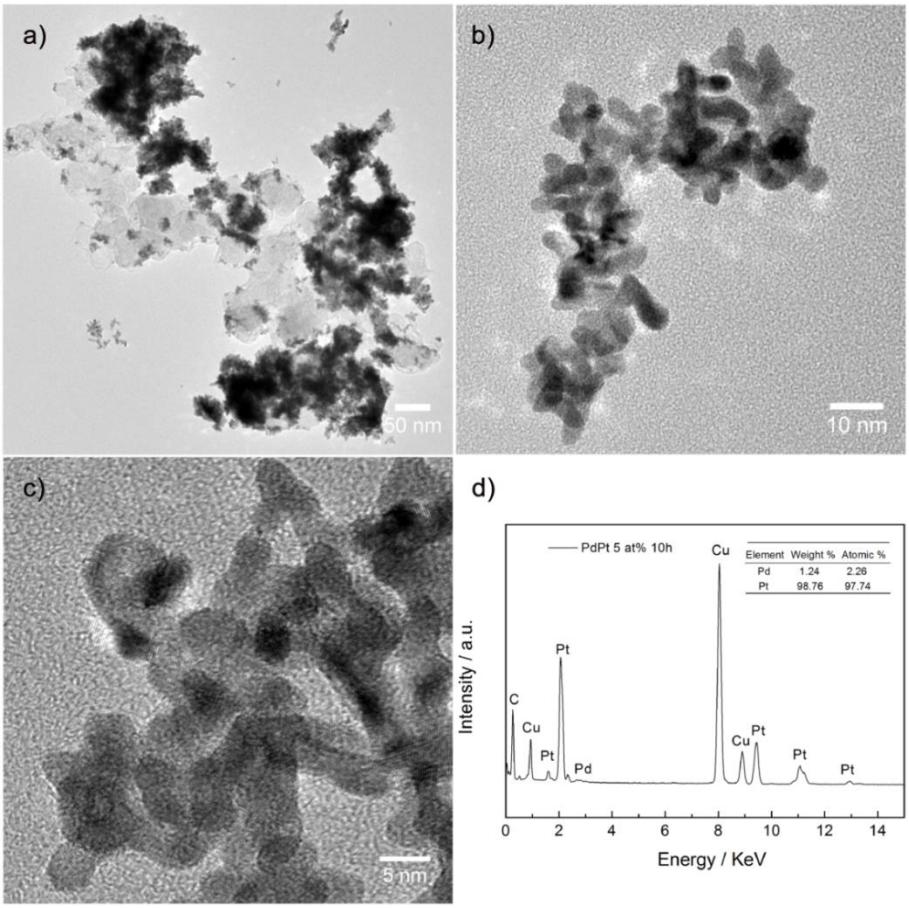

Fig. 5.24 (a-c) TEM images at different magnifications for PdPt nanostructures with 5 at% Pd reacted for 10h and (d) the corresponding EDS spectrum.

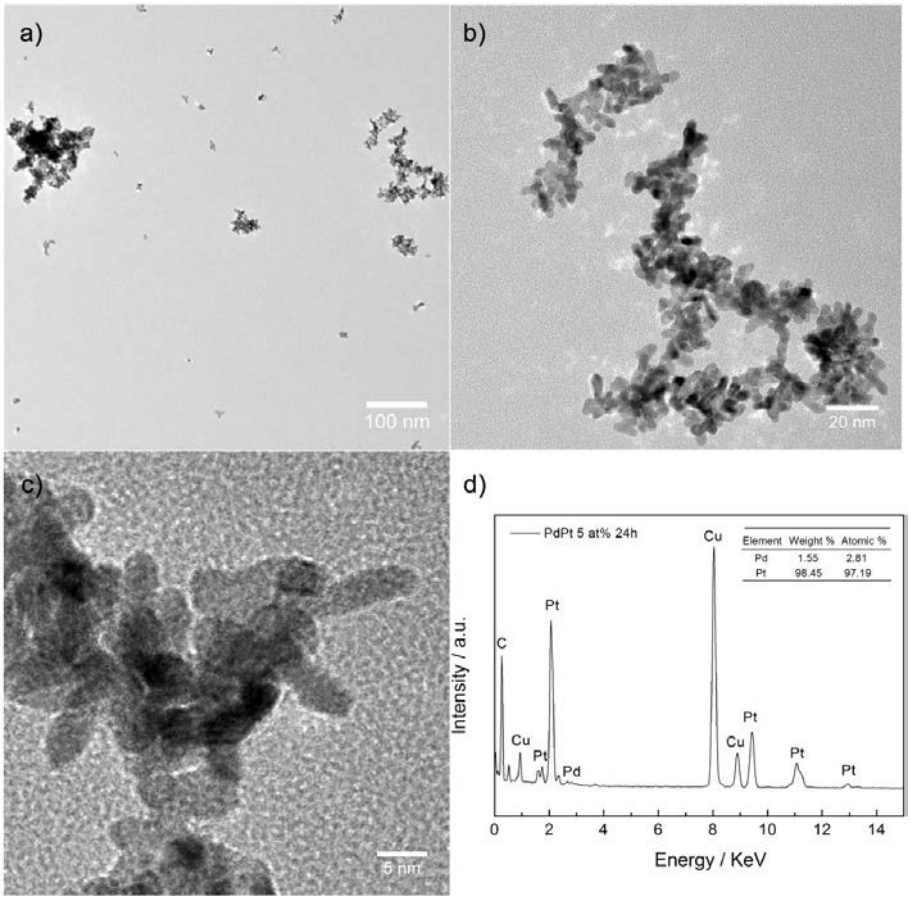

Fig. 5.25 (a-c) TEM images at different magnifications for PdPt nanostructures with 5 at% Pd reacted for 24h and (d) the corresponding EDS spectrum.

Another reason for the different distributions of PdPt nanostructures on the GDL surface is the relative negative standard reduction potential of $PtCl_6^{2-}$/Pt. Because Pt nuclei can't form on the GDL surface as easily as Pd nuclei, only the rough sites of the GDL surface can serve as the main heterogeneous nucleation sites. However, these sites are usually limited in particular on the hydrophobic PTFE coated inert carbon sphere surfaces in the GDL. In the previous chapter it was already demonstrated that on the super hydrophobic GDL surface, the edge area was usually easier to be wetted and provided more nucleation sites than the central region in an aqueous solution [230]. In this case, the population of Pt nuclei may multiply at the edge area while fewer are in the centre; therefore more catalyst

nanostructures are formed and accumulated at the edge of the GDL. In Chapter 4 SEM images of the edge and centre area of a 16 cm^2 PtNW GDE were already shown, from which it can be observed that Pt NWs are densely distributed at the edge but sparsely scattered in the centre. Much more uniform and well covered PdPt nanostructures are observed with PdPtND GDE (Fig. 5.7). As a result, although the mass activity of PtNW GDE is higher than that of the PdPtND 5 at% GDE (Fig. 5.16), the electrode performance is still poorer at a large current density due to the larger mass transfer losses caused by the non-uniform distribution of catalyst nanostructures on the GDL surface.

Fig. 5.26 shows a schematic diagram that summarises the growth mechanism of PdPt nanostructures on the GDL surface at high, medium, optimal and very low Pd amount.

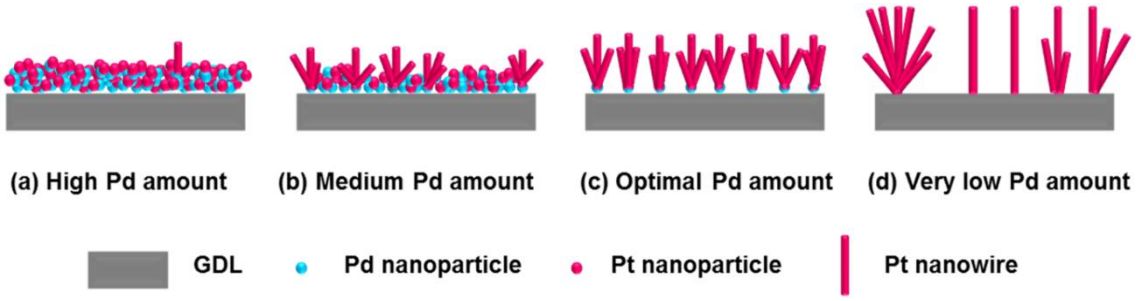

Fig. 5.26 Schematic diagram for PdPt nanostructures grown on carbon paper surface at (a) high, (b) medium, (c) optimal and (d) very low Pd amount.

5.6 Conclusions

It can be concluded that Pd plays a complex role in controlling the structure, morphology and distribution of PdPt nanostructures in-situ grown on the GDL surface, and it is not just working as an alloy or hybrid element for an enhanced durability and activity as reported in pure material research.

At a high Pd content, the main structures obtained were PdPt nanoparticle aggregates, resulting in a low catalyst utilisation and poor catalytic performance. At a moderate Pd content, the obtained mixture of PdPt NPs and NDs delivered an improved performance. However, at very low Pd content, although PdPt NDs with longer branches were produced, the distribution of NDs became non-uniform on the GDL surface. The optimal Pd content is 5 at% which enabled the uniform distribution of PdPt NDs on the GDL surface.

Compared with the PtNW GDE, the PdPtND GDE with 5 at% Pd exhibited unexpected lower mass and specific area activities, though, the literature trends usually suggest improved mass activity with heterostructures. Even like this, the PdPtND GDE with 5 at% Pd achieved a higher power density of 0.73 W cm^{-2} at 0.6 V and a better durability corresponding to 46.6% ECSA loss after the ADT test, which were 0.64 W cm^{-2} and 62.2% for the PtNW GDE, respectively. The lower catalytic activity along with higher in-situ performance and durability demonstrate the complex effect resulting from the intrinsic activity of the catalyst and extrinsic behaviour on the GDL, which will finally together determine the performance of the electrodes.

CHAPTER 6

EVALUATION OF GAS DIFFUSION LAYER (GDL) STRUCTURES FOR PLATINUM NANOWIRE ELECTRODES

6. Evaluation of Gas Diffusion Layer (GDL) Structures for Pt Nanowire Electrodes

Chapters 4 and 5 studied the effects of temperature and hybridizing metal Pd on the controlled growth and distribution of Pt NWs and PdPt NDs on gas diffusion layers (GDLs). This chapter focuses on investigating the influence of GDL structures on the in-situ growth of Pt NWs for the fabrication of gas diffusion electrodes (GDEs). The study is undertaken with the standard and self-painted GDLs, including the carbon loading, carbon composition, carbon treatment and polytetrafluoroethylene (PTFE) loading in the microporous layer (MPL), as well as PTFE in the carbon fibre substrate. Considering the Pt nanowire behaviour on GDLs, e.g. the growth and distribution, as well as the practical testing results within fuel cells, the influence mechanisms will be discussed in detail.

6.1 Introduction

The GDL, consisting of the carbon fibre substrate and MPL, is one of the key components in polymer electrolyte fuel cells (PEFCs). A schematic diagram of the GDL configuration is shown in Fig. 6.1. As a component next to the catalyst layer (CL) in fuel cell construction, the whole GDL serves to provide mechanical strength to support CLs, deliver reactants to and remove produced water from CLs as well as reduce interfacial contact resistance (ICR) with CLs [231-233]. The close relationship between GDLs and CLs makes the characteristics of GDL significant to the performance of CLs, especially when the GDE technique is employed by directly coating catalysts on the surface of GDL [234, 235].

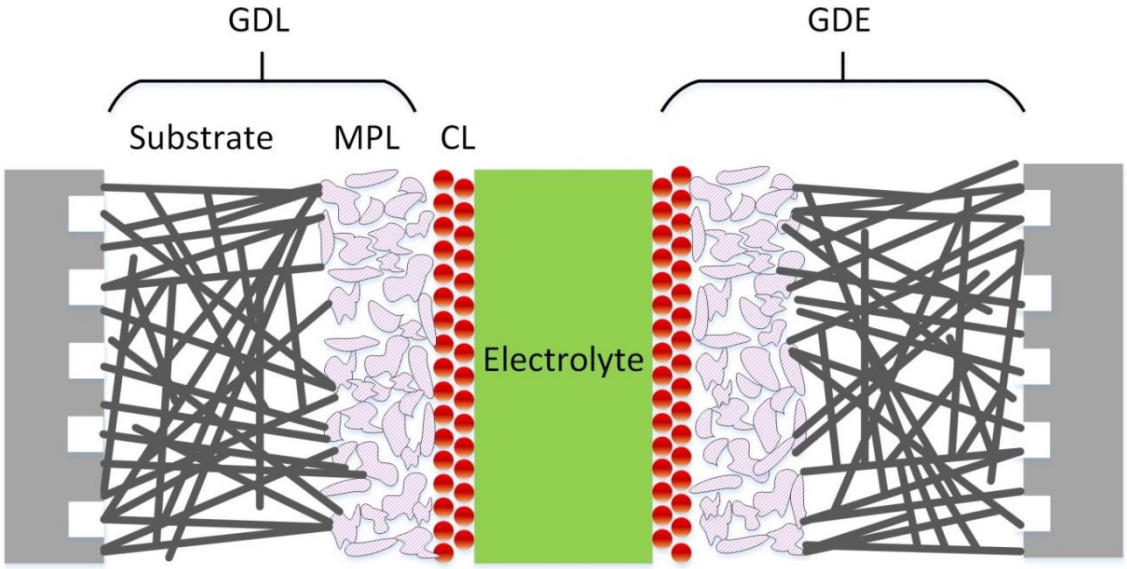

Fig. 6.1 Schematic of the GDL configuration.

Conventional methods for fabricating GDEs use painting [236, 237], spraying [238, 239] or printing [240, 241] catalyst layers on GDLs. The integrated GDE concept refers to Pt nanowire catalysts grown directly on the GDL surface [160-162] by a one-pot wet-chemical process, thus the surface features of the GDL, including the porosity, hydrophobicity, homogeneity, etc. will critically influence the growth and distribution of Pt NWs on the GDL surface and further affect the power performance of produced GDEs.

Using Sigracet® gas diffusion media as the standard GDLs and self-made GDLs with painted MPLs on the 35BA substrate, a systematic study was conducted to understand the influence mechanism of GDL structures on the performance of PtNW GDEs. Considering the crystal nucleation and growth processes of Pt NWs, together with the actual performance of PtNW GDE in the single cell, the carbon loading, carbon composition and carbon treatment in the MPL, as well as the PTFE amount in both of the substrate and MPL were comprehensively investigated.

6.2 Carbon Loadings in Microporous Layers (MPLs)

Surface optical microscopy images of 35BA substrate and the GDLs with self-painted MPLs with Vulcan XC-72R carbon black (CB) at loadings of 1, 3, 4, 4.48 and 5 mg cm^{-2} are shown in Fig. 6.2, where 4.48 mg cm^{-2} is the carbon loading in commercial GDLs as shown in Chapter 3. It can be seen that the plain 35BA substrate (Fig. 6.2a) is made of stacked carbon fibres. With the CB loading of 1 or 3 mg cm^{-2} in the MPL, the substrate is not fully covered and the bottom carbon fibres can still be seen. With a higher CB loading, better coverage is achieved on the substrate surface. There is no obvious difference between the three high CB loadings. Some cracks appear on the dried MPL, which can't be avoided although they can be minimised by a complex painting approach [236].

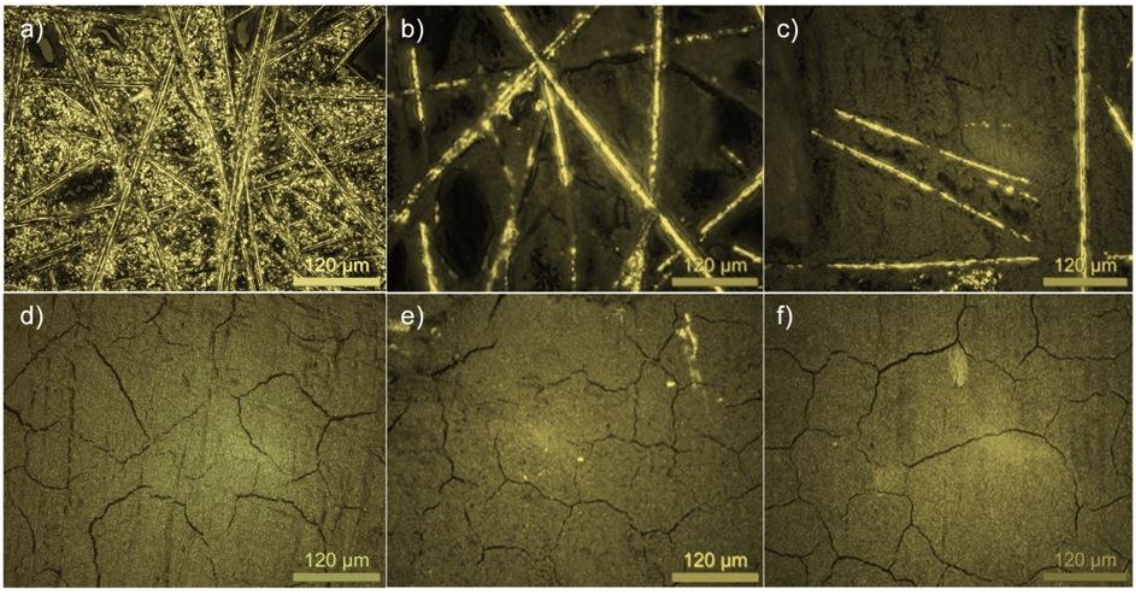

Fig. 6.2 Optical microscopy images of (a) 35BA substrate and the GDLs with self-painted MPLs at the Vulcan XC-72R CB loading of (b) 1, (c) 3, (d) 4, (e) 4.48 and (f) 5 mg cm^{-2}.

The self-made GDLs with various carbon loadings in the MPL were used as supports for in-situ growth Pt NWs. Fig. 6.3 shows SEM images of Pt NWs grown on the self-painted MPL with a carbon loading of 1 mg cm^{-2}. It can be seen that the carbon fibre substrate is

only partially covered by the carbon black, which is quite similar to the optical microscopy image in Fig. 6.2b. Some Pt NWs are directly grown on the carbon fibre surface while others beneath carbon black surface, which will result in a poor contact with the electrolyte membrane in the MEA. The PtNW GDEs with other carbon loadings display very similar surface morphology, and SEM images are shown in Fig. 6.4.

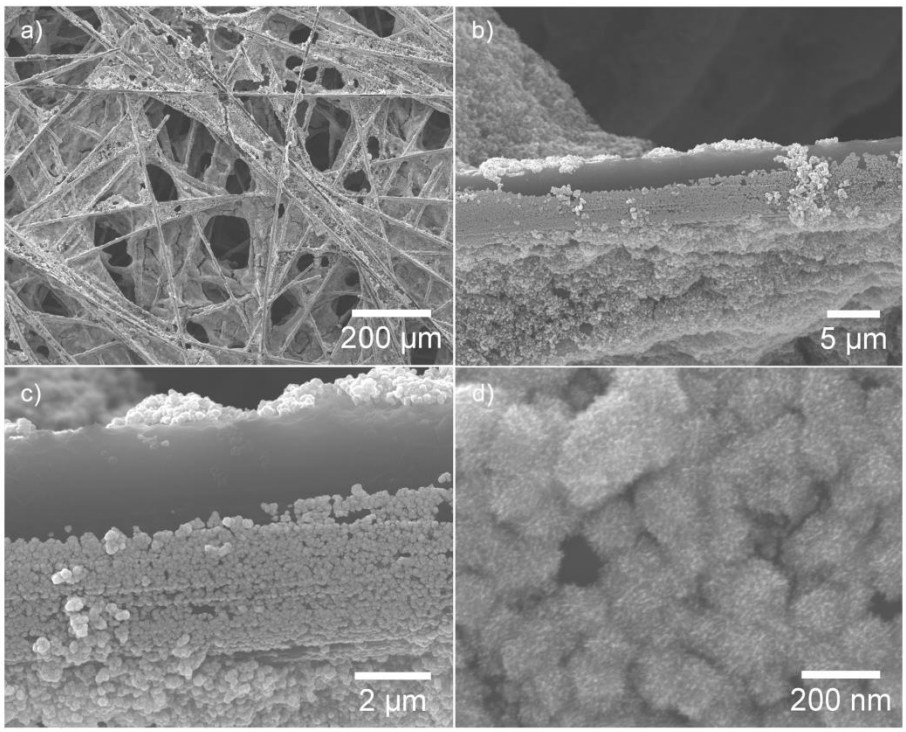

Fig. 6.3 SEM images at different magnifications for Pt NWs grown on the self-painted MPL with carbon loading of 1 mg cm^{-2} (20% PTFE in MPLs based on the total MPL weight).

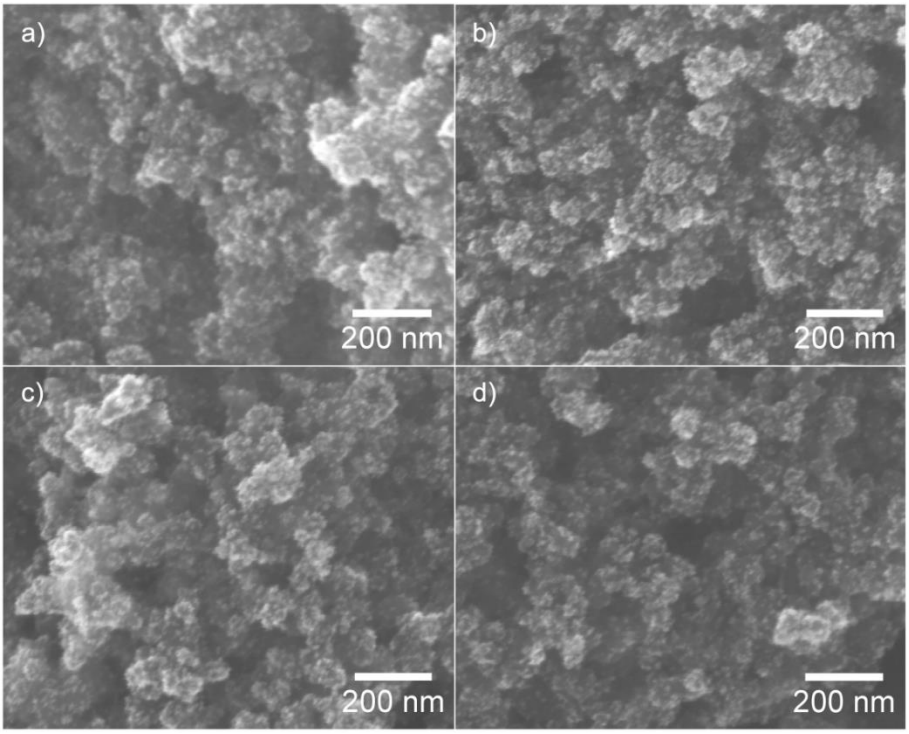

Fig. 6.4 SEM images of Pt NWs grown on the self-painted MPL with carbon loading of (a) 3 (b) 4, (c) 4.48 and (d) 5 mg cm^{-2} (20% PTFE in MPLs based on the total MPL weight).

The catalytic performance of Pt NWs in-situ grown on the GDLs with painted MPLs loaded with various CB amounts was characterised in the single fuel cell and the corresponding results are shown in Fig. 6.5. The results of Pt NWs directly grown on 35BA substrate without the MPL are also included for comparison. Fig. 6.5a shows that the use of MPL results in a significant improvement in the fuel cell performance, which is in line with the results reported in literature [242]. The figure also displays that the performance is highly dependent on the CB loading in the MPLs. With the lower CB amount of 1 and 3 mg cm^{-2}, the performance is low, and this can be ascribed to the poor contact with the polymer electrolyte membrane due to the uneven substrate surface (Fig. 6.2), leading to a large ICR. Furthermore, some Pt NWs may grow in the substrate rather than on the MPL surface because the large pores in the substrate enable the penetration of

reaction solution. There is very little ionic conducting path between substrate and the electrolyte membrane, thus no contribution to the catalytic activity. The performance increases with growing CB loading due to the improved coverage of the substrate surface. At 4 mg cm^{-2}, the current density at 0.6 V reaches 0.77 A cm^{-2}. With further increase of the carbon loading, the power performance decreases at 0.6 V, although a slightly higher power density is observed at the low voltage when CB is 4.48 mg cm^{-2}. Given that the practical fuel cell operation voltage is usually at 0.6–0.65 V, the CB loading of 4 mg cm^{-2} was regarded as the optimal amount and used in the following experiments.

EIS measurements were conducted to help understand the effect of carbon loading on the behaviour of Pt NWs. From Fig. 6.6a, it can be seen that all samples show a very similar impedance, but the samples with the low carbon loadings of 1 and 3 mg cm^{-2} exhibit a much larger ohmic resistance shown by larger start points at a high frequency. Considering the same fuel cell construction is used for all samples except the GDE, this difference can be ascribed to the large ICR between the GDE surface and the polymer electrolyte membrane, in particular the uneven GDL surface with the uncovered carbon fibres at the low carbon loading as shown in Fig. 6.2. Samples with 4, 4.48 and 5 mg cm^{-2} carbon loadings all show a similar ohmic resistance due to the even MPL surface, further confirming that the main contribution to the ohmic resistance in these samples is the ICR. This is also confirmed by EIS at larger current densities of 0.5 A cm^{-2} (Fig. 6.6b) and 1.0 A cm^{-2} (Fig. 6.6c). A slightly lower charge transfer resistance is observed for the sample with a carbon loading of 4 mg cm^{-2} and lower mass transfer resistance for the one with 4.48 mg cm^{-2} at a large current density (Fig. 6.6c), which is in line with polarisation curves shown in Fig. 6.5.

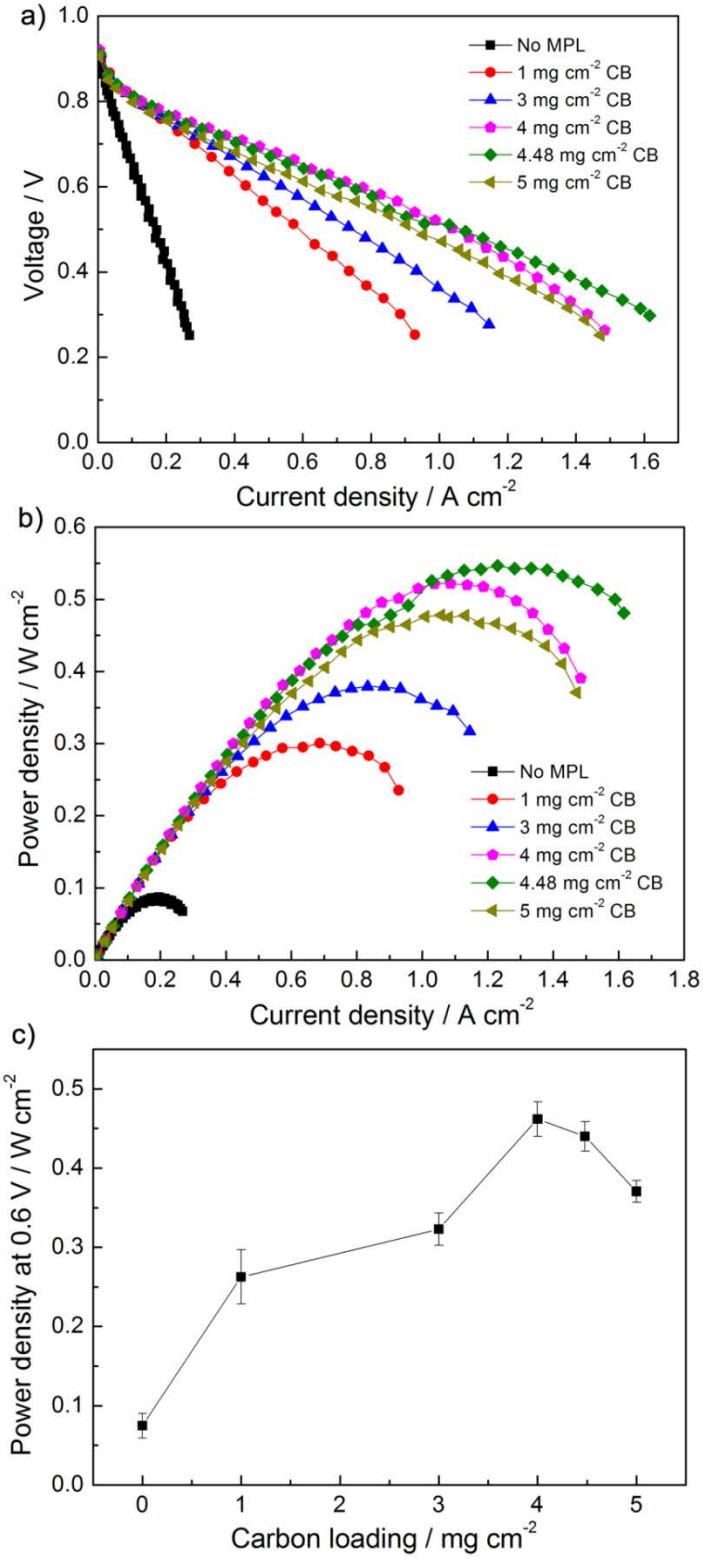

Fig. 6.5 (a) Polarisation curves, (b) power density curves and (c) the trend of the power density at 0.6 V for PtNW GDEs with different CB loadings in the painted MPLs.

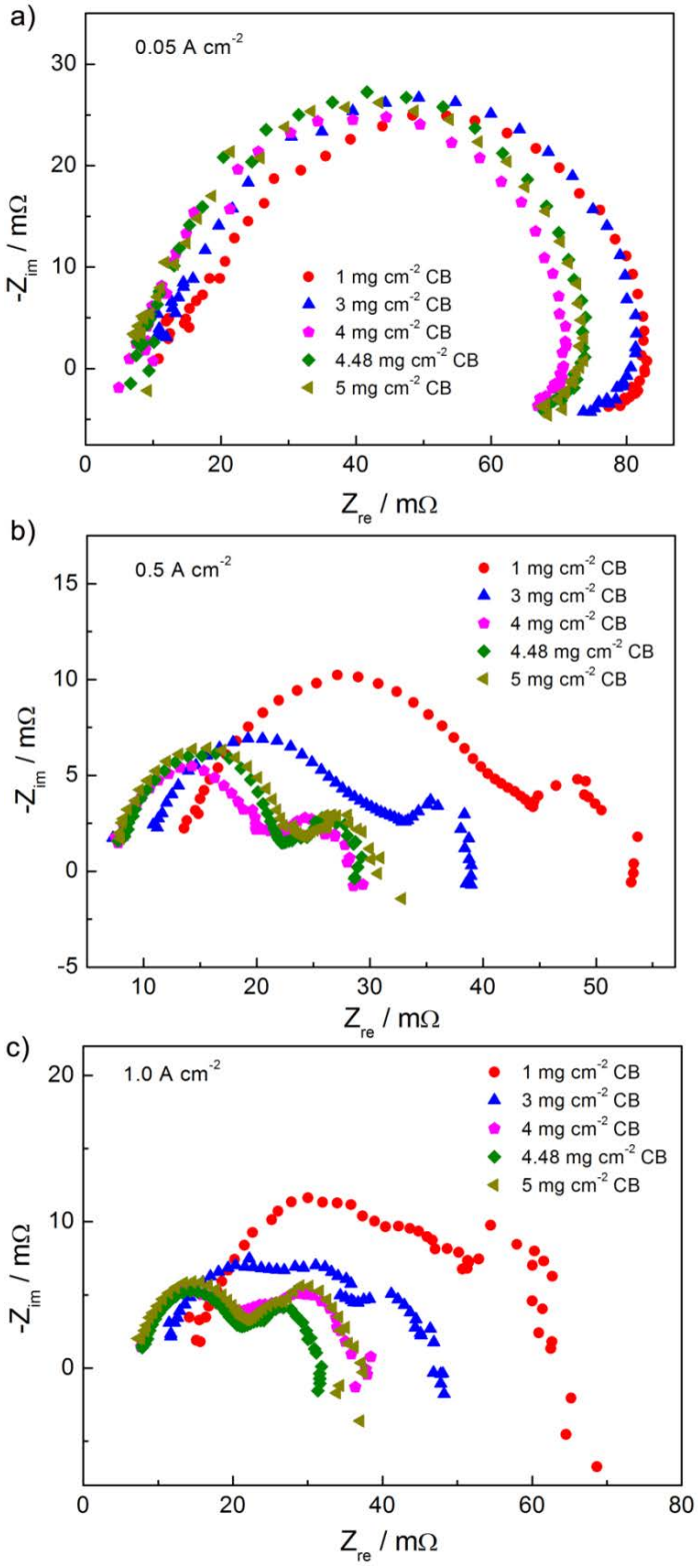

Fig. 6.6 EIS measured at (a) 0.05, (b) 0.5 and (c) 1.0 A cm^{-2} for PtNW GDEs with different CB loadings in the painted MPLs.

6.3 Carbon Compositions in MPLs

With a high specific surface area (ca. 250 m^2/g) [243], Vulcan XC-72R CB is extensively used to fabricate MPLs in commercial GDLs and also as catalyst supports [244]. Acetylene black (AB), with a surface area range of 15 to 70 $m^2\ g^{-1}$, is also commonly used in MPLs to achieve a homogeneous surface [245]. The mixture of CB and AB with various compositions has been used to control the surface properties of MPLs such as specific surface area, porosity and electrical conductivity [246, 247], and this was also investigated in this work to evaluate their influence on in-situ grown Pt NWs. TEM images of CB and AB presented in Fig. 6.7 demonstrate that CB has a spherical shape with an average diameter of ca. 50 nm (Fig. 6.7a, b) and AB consists of graphitic flakes with irregular shape (Fig. 6.7c, d). According to the literature, CB has a microporous structure and thus a large specific surface area [244] while the smooth and inert surface of AB results in a lower specific surface [245]. In this work, the irregular surface of CB particles can provide more nucleation sites for Pt than the smooth AB surface. The mixture of CB and AB with different compositions may change the external surface and internal pore structures in the MPL, influencing the growth and distribution of Pt NWs on the GDL surface. Therefore, with the optimum carbon loading of 4 mg cm^{-2}, the carbon composition in the MPL with different CB and AB ratios will be further investigated.

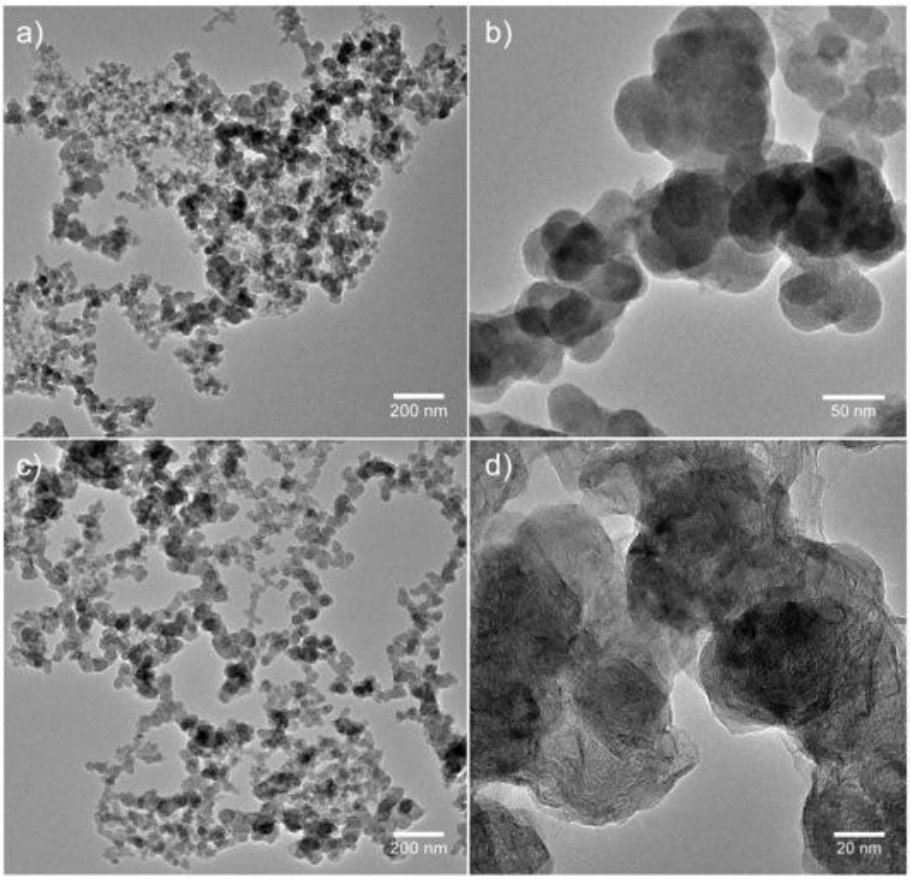

Fig. 6.7 TEM images of (a, b) carbon black and (c, d) acetylene black.

Figs. 6.8 to 6.12 show SEM images of Pt NWs grown on the self-painted MPLs with different carbon compositions. It can be seen that Pt NWs are sparsely distributed on the surface of the MPL with pure AB due to the inert surface (Fig. 6.8). Adding 25% CB in the MPL makes the surface preferable for Pt nanowire growth as more of them are observed on the surface but with obvious agglomeration (Fig. 6.9). It improves with the increase of CB (Fig. 6.10 and 6.11). But when pure CB is used, the number of Pt NWs on the surface decreases and some of them even grow into the carbon surface in the pores (Fig. 6.12) due to the large amount of nucleation sites on the active CB surface.

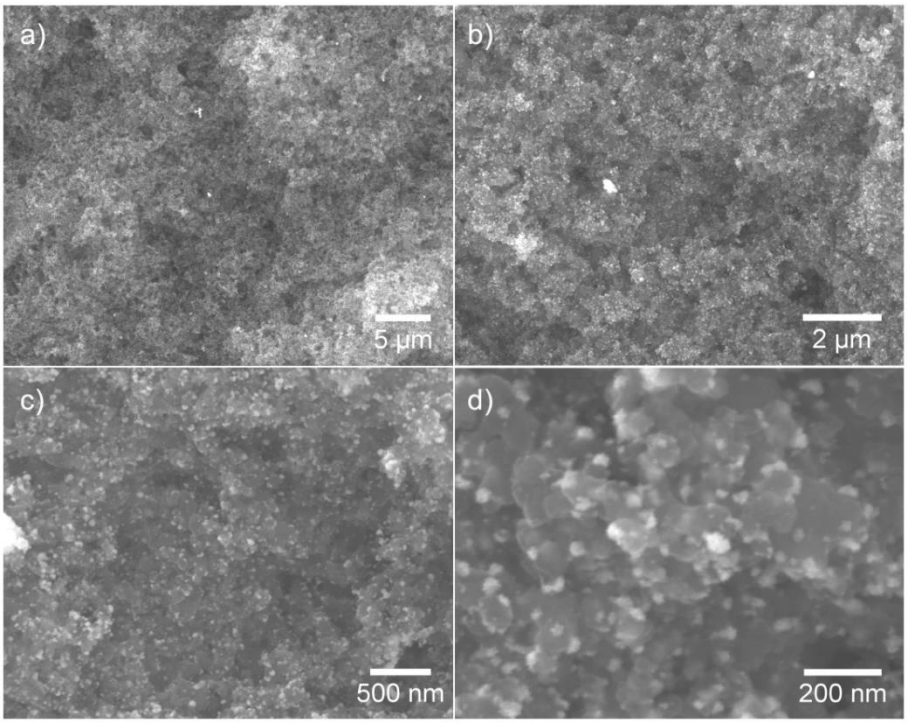

Fig. 6.8 SEM images at different magnifications for Pt NWs grown on the self-painted MPL with pure AB.

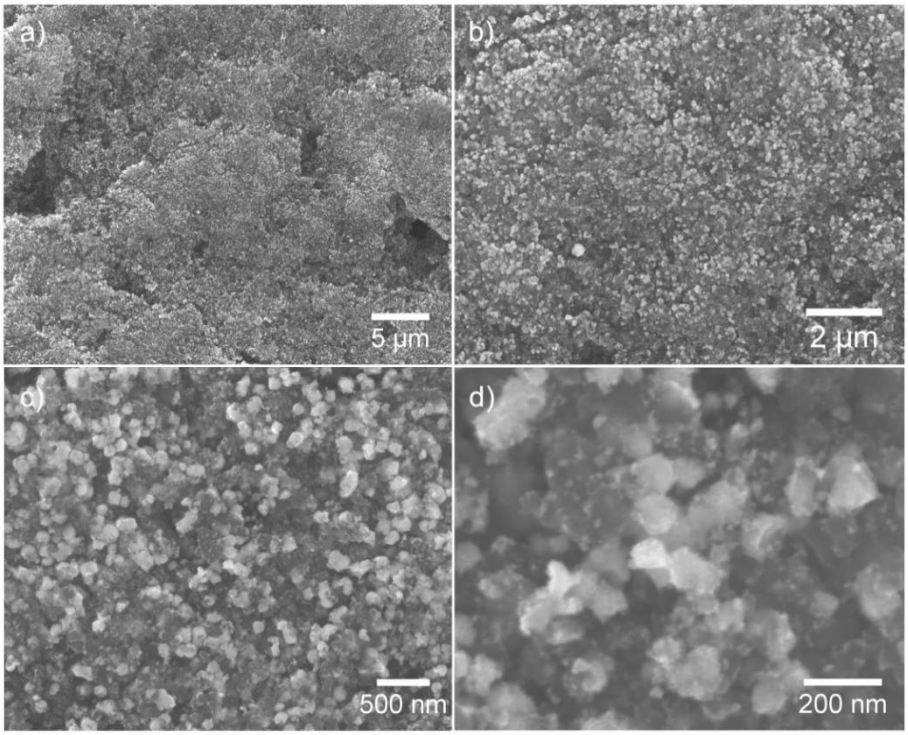

Fig. 6.9 SEM images at different magnifications for Pt NWs grown on the self-painted MPL with CB 25% and AB 75%.

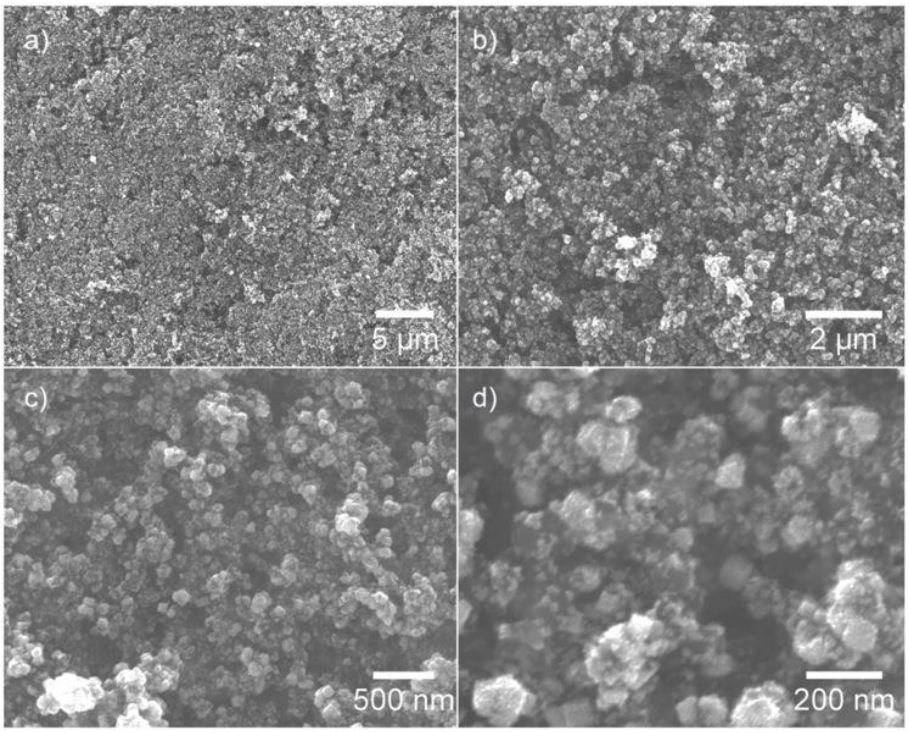

Fig. 6.10 SEM images at different magnifications for Pt NWs grown on the self-painted MPL with CB 50% and AB 50%.

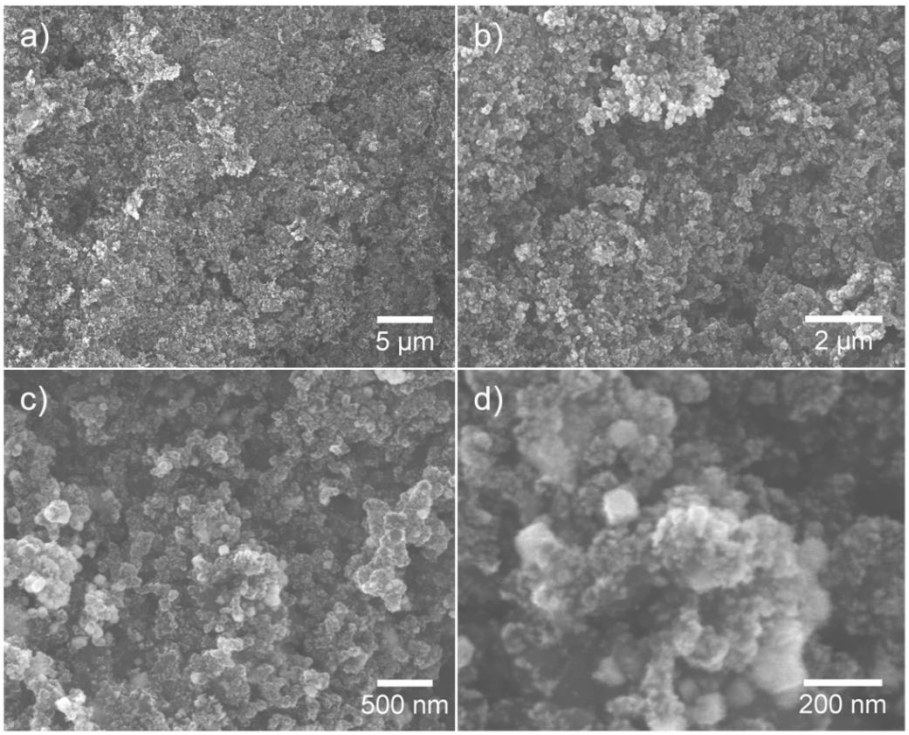

Fig. 6.11 SEM images at different magnifications for Pt NWs grown on the self-painted MPL with CB 75% and AB 25%.

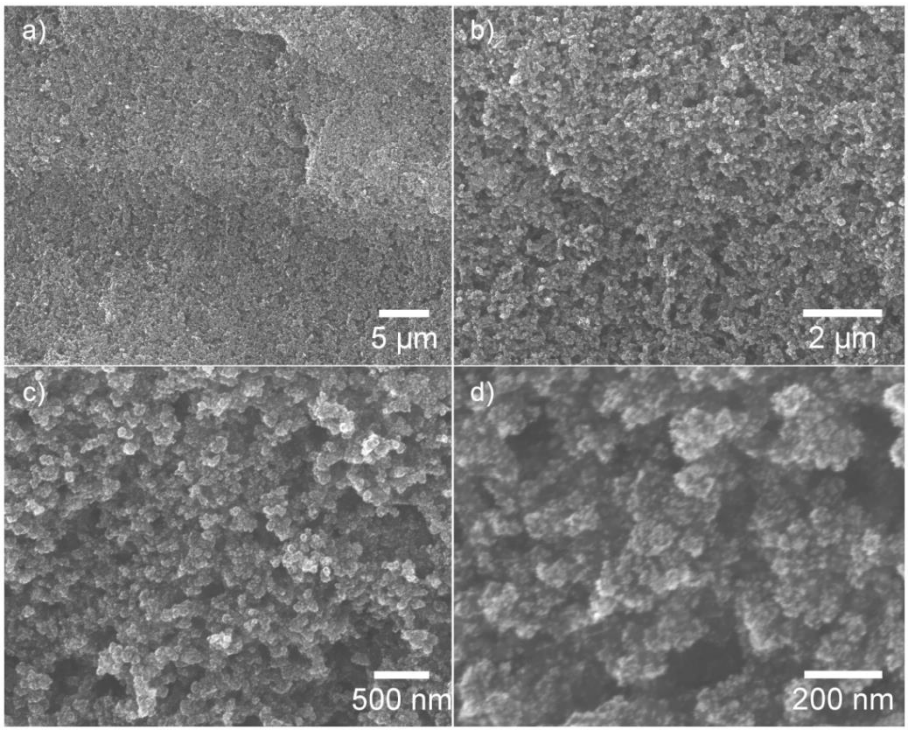

Fig. 6.12 SEM images at different magnifications for Pt NWs grown on the self-painted MPL with pure CB.

The in-situ performance of PtNW GDEs from painted GDLs with different carbon compositions in the MPLs is shown in Fig 6.13 with the cases of MPLs made from pure AB and CB. PtNW GDE with pure AB in the MPL exhibits the poorest performance. With the addition of CB the performance is gradually improved and achieves the highest value with CB 50%+AB 50% (Fig. 6.13c). At a higher CB amount, the performance slightly declines but no big difference is observed with the CB amount between 60–100%.

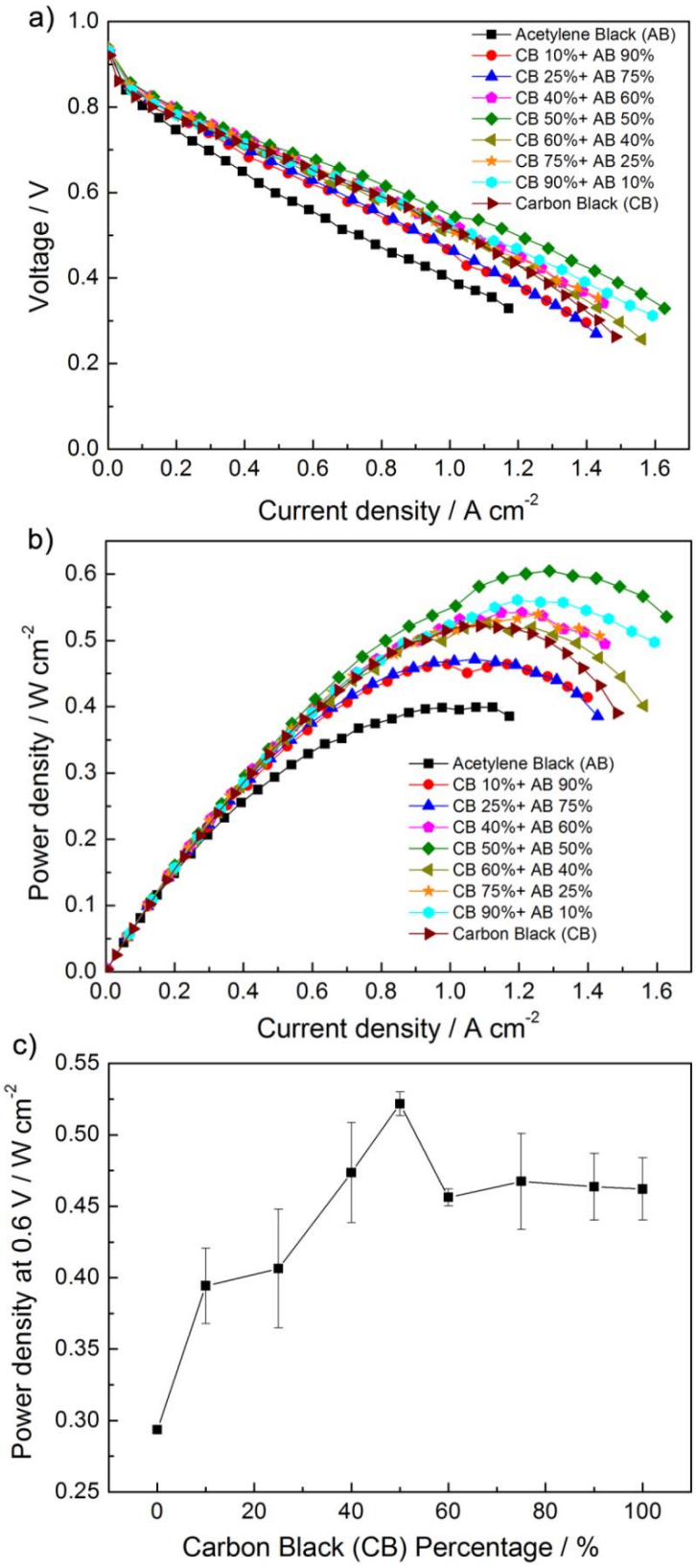

Fig. 6.13 (a) Polarisation curves, (b) power density curves and (c) the trend of the power density at 0.6 V for PtNW GDEs with different carbon compositions in the painted MPLs.

EIS measurement results at three current densities of 0.05, 0.5 and 1.0 A cm^{-2} are shown in Fig. 6.14. At the low current density (Fig. 6.14a), the PtNW GDE with pure AB in the MPL shows the largest resistance while the smallest value is observed for the one with CB 50%+AB 50%. Three other GDEs show a similar impedance to each other. At the medium and high current densities (Fig. 6.14b and c), the change trend of the impedance with the carbon composition generally agrees with that of the polarisation curves (Fig. 6.13a), with the smallest charge and mass transfer resistances observed for the sample with CB 50% and AB 50% and the largest of that for the one with pure AB.

The possible reason for the different behaviour of Pt NWs on the MPL surface can be ascribed to the various surface structures of the MPLs. When the pure AB is used, the inert surface provides few sites for the nucleation of Pt thus sparsely distributed PtNW agglomerates are formed. With the increase of the CB amount, more nucleation sites are provided for more Pt NWs growth, thus a better distribution is obtained and achieves the highest performance at the optimum composition. Further increasing the CB amount results in a much loose MPL and some Pt NWs may grow into the internal surface of the pores in MPL, which has very little contribution to the power performance as there is not enough ionic conduction path to the polymer electrolyte membrane, resulting in a lower catalyst utilisation. Therefore, the carbon composition in the MPL can influence the growth of Pt NWs and further affects the fuel cell performance.

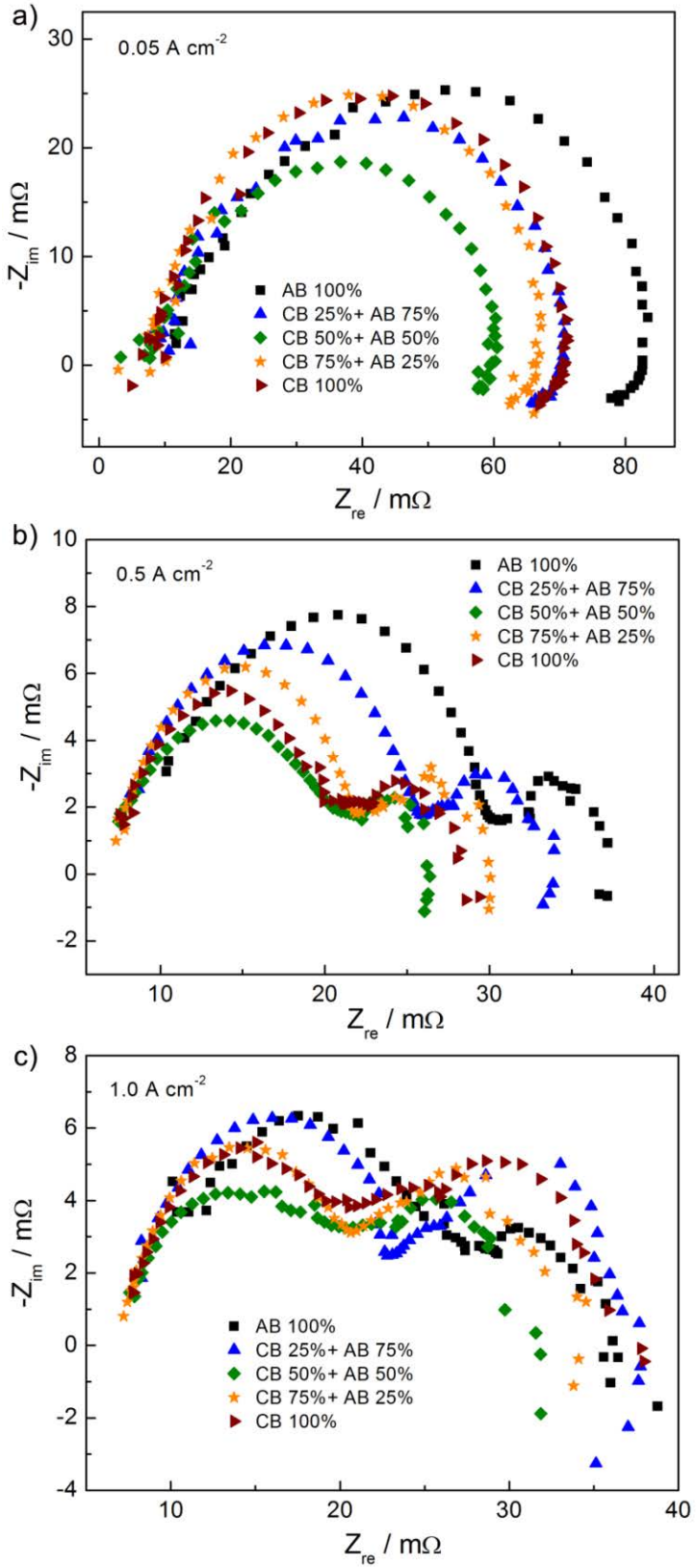

Fig. 6.14 EIS measured at (a) 0.05, (b) 0.5 and (c) 1.0 A cm^{-2} for PtNW GDEs with different carbon compositions in the painted MPLs.

6.4 Carbon Treatment for MPLs

It is reported that acid treatment of carbon samples may change their porosity structure, surface functional group and the hydrophobic/hydrophilic characteristics [248]. As these features may influence the surface structure and wettability of the GDL and further affect the wet-chemical growth and distribution of Pt NWs, a further study will be conducted to investigate the effect of carbon treatment for the MPL on the behaviour of Pt NWs.

Fig. 6.15 shows TEM images of the nitric acid treated CB (Fig. 6.15a, b) and AB (Fig. 6.15c, d). Compared with the original CB (Fig. 6.7a, b), after treatment the shape of CB is still spherical but the diameter is slightly reduced, now below 40 nm. The irregular shape of the acid treated AB is very similar to that of the original AB (Fig. 6.7c, d).

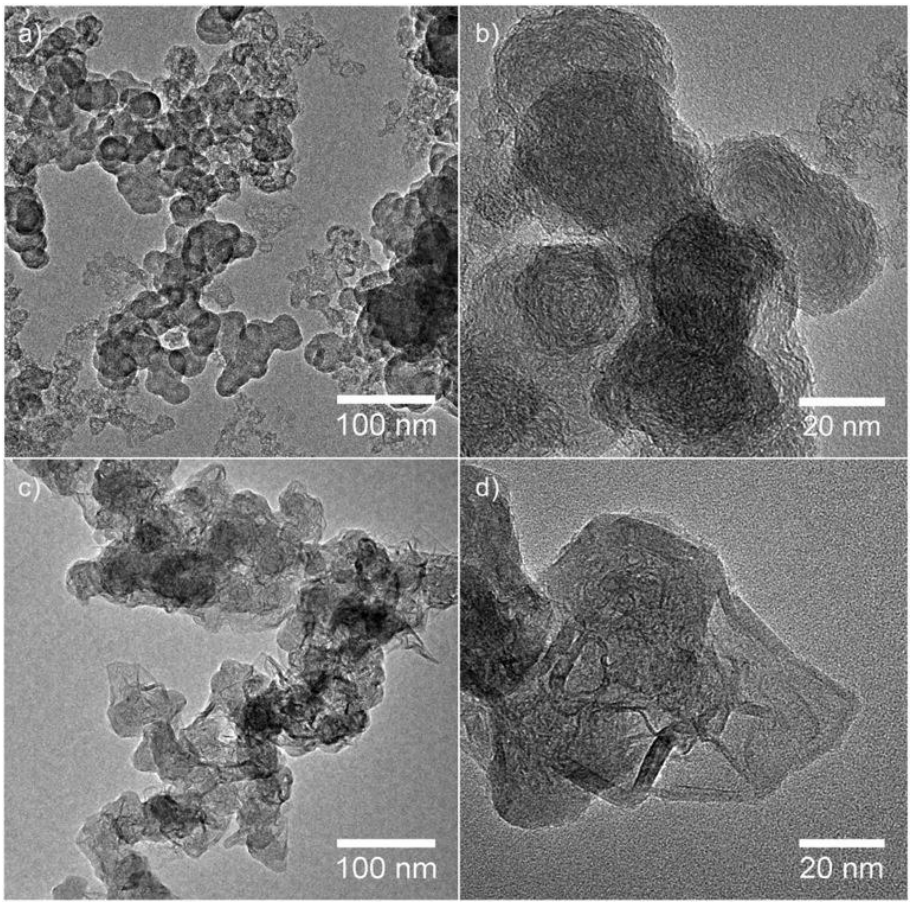

Fig. 6.15 TEM images of nitric acid treated (a, b) carbon black and (c, d) acetylene black.

However, due to the etching by nitric acid, some graphene-like sheets appear, which has also been reported in literature [249].

Fig. 6.16 shows polarisation and power density curves, as well as the comparison of power densities at 0.6 V for the PtNW GDEs with MPLs with different carbon treatments. Compared with the original pure AB and CB, the performance of acid treated AB improves while that of acid treated CB decreases. The possible reason is that after the acid treatment the specific surface areas of the two carbon blacks are changed, which was proven by other researchers' work: for CB, the surface area reduces after oxidant treatment and the nucleation sites significantly decrease [250]; in contrast, the surface area of acid treated AB increases due to the etched surface and the exposure of graphene-like sheets [249]. The performance is quite similar for the four cases of CB 50%+HNO_3 treated AB 50%, HNO_3 treated both CB 50% and AB 50%, CB 50%+AB 50%, and HNO_3 treated pure AB, but the former two show a slightly higher power density at 0.6 V. Given that the improvement of PtNW GDEs with acid treated carbon is not remarkable and the process of carbon treatment is time-consuming and environmental unfriendly, CB 50%+AB 50% was thus regarded as the optimum carbon composition and used in the following work.

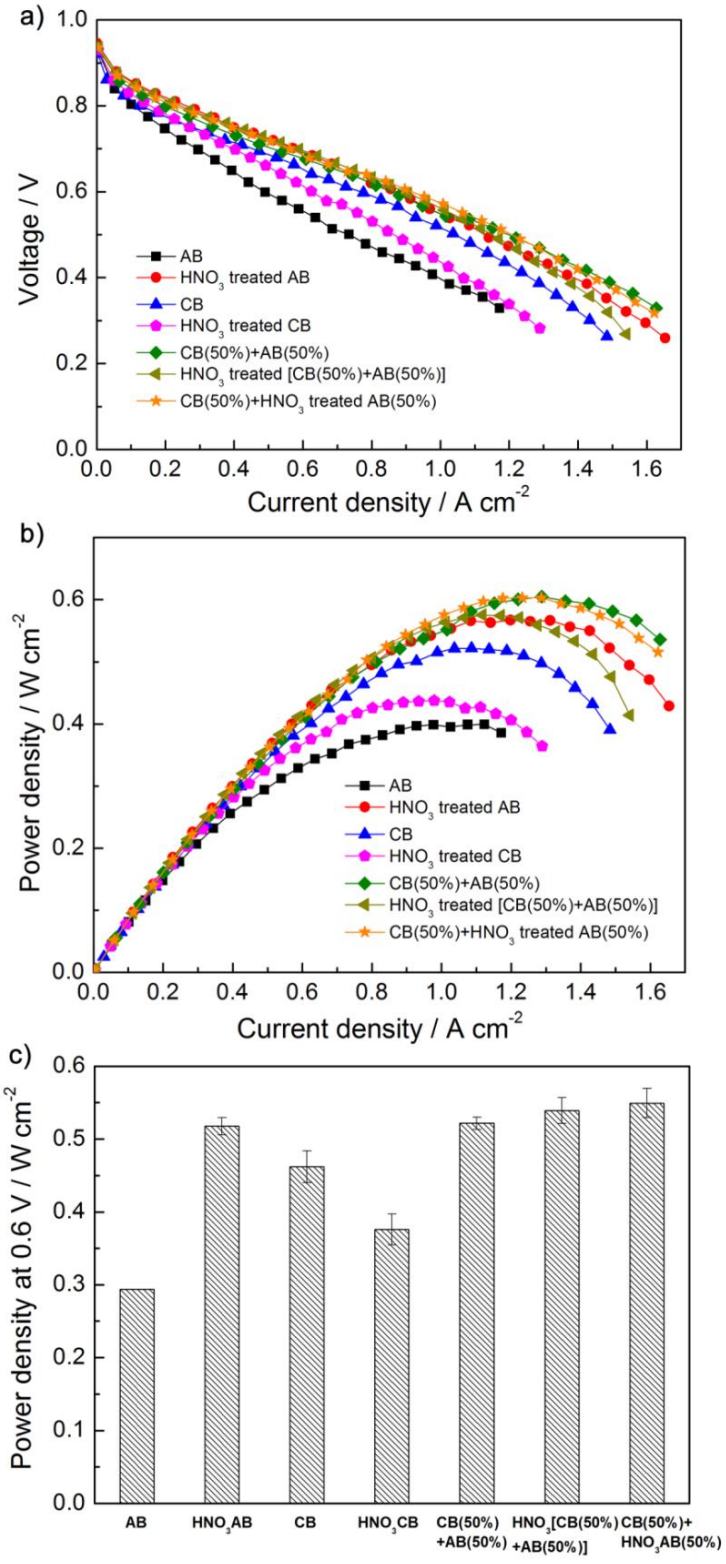

Fig. 6.16 (a) Polarisation curves, (b) power density curves and (c) the trend of the power density at 0.6 V for the PtNW GDEs with different carbon treatment situations in the painted MPLs.

EIS measurement results are shown in Fig. 6.17. At 0.05 A cm^{-2} (Fig. 6.17a), the resistance of the treated AB greatly decreases in terms of original AB while no obvious change is observed between CB and the acid treated CB. The resistance of original CB 50%+AB 50% is slightly smaller than that of the other carbon combinations. At a current density of 0.5 A cm^{-2} (Fig. 6.17b), there is an obvious resistance difference between CB and acid treated CB, and the original CB 50%+AB 50% still possesses the smallest charge and mass transfer resistances. At 1.0 A cm^{-2} (Fig. 6.17c), the impedances of original and treated AB become similar. However, the acid treated CB exhibits the largest impedance and the possible reason is that after surface functionalisation the limited nucleation sites at surface lead to an agglomeration of Pt NWs, which can block the diffusion of oxygen to catalytic sites on nanowire surfaces, resulting in a large mass transfer resistance. Although the resistance of original CB 50%+AB 50% is larger than that of original CB 50%+HNO_3 treated AB 50%, the difference is very small.

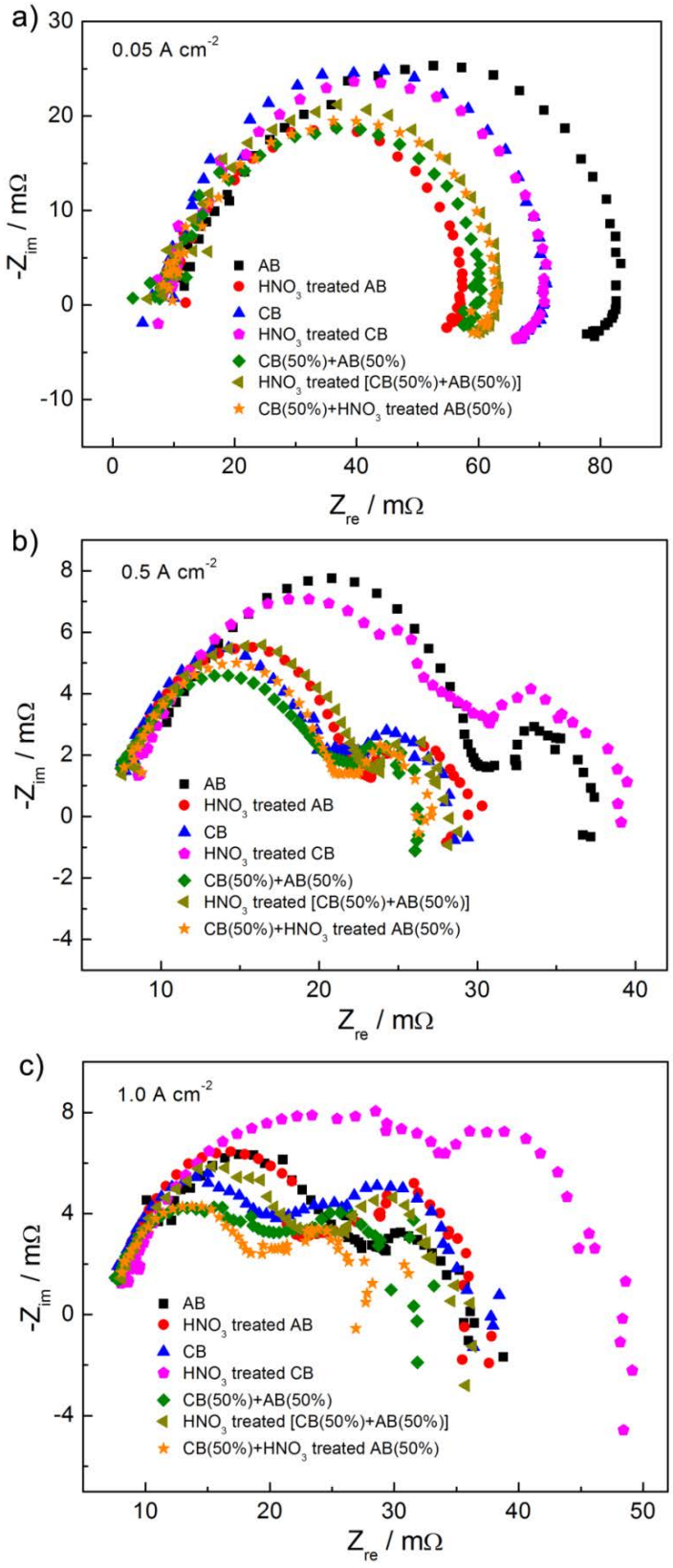

Fig. 6.17 EIS measured at (a) 0.05, (b) 0.5 and (c) 1.0 A cm^{-2} for PtNW GDEs with different carbon treatment situations in the painted MPLs.

6.5 PTFE Loading in GDLs

To avoid water flooding in fuel cell operation, both the substrate and MPL are usually treated with PTFE to achieve super-hydrophobicity. This feature will significantly affect the GDL porosity and also the surface wettability [180]. As PtNW GDEs are fabricated by in-situ growing Pt NWs on the GDL surface through a wet-chemical process, the hydrophobicity feature of the GDL could affect the nucleation and growth of Pt NWs, inevitably influencing the final PEFC performance.

6.5.1 PTFE Loading in the Substrate

Standard GDLs from Sigracet® are chosen to investigate the effect of the PTFE loading in the substrate. Table 6.1 shows the information of the PTFE loading in the commercial GDLs which have different PTFE loadings in the substrates with the standard Sigracet® MPL. Surface optical images of the standard 35BC, 35CC and 35DC GDLs show a very similar MPL surface (Fig. 6.18).

Table 6.1 PTFE loading in standard GDLs from Sigracet®.

Sigracet® GDLs	PTFE loading in the substrate (%)	PTFE loading in the MPL (%)
35BC	5	20
35CC	10	20
35DC	20	20

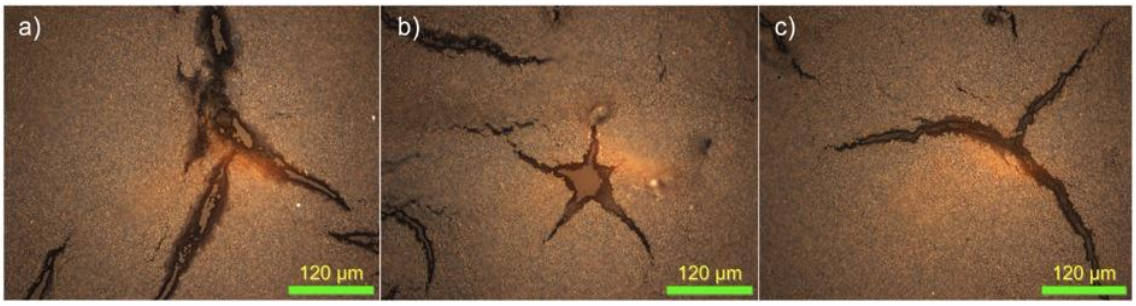

Fig. 6.18 Surface images of the commercial (a) 35BC, (b) 35CC and (c) 35DC GDLs.

The power performance of PtNW GDEs with various PTFE loadings in the carbon fibre substrate of GDLs is shown in Fig. 6.19. The polarisation and power density curves for three samples almost overlap with each other and the only difference comes from the 35DC GDL, which has a slight decline at high current density. This is caused by the large mass transfer resistance resulting from partially blocked pores at the high PTFE loading. The EIS results (Fig. 6.20) obtained at three different current densities show similar diameters of semicircles, indicating that the charge and mass transfer resistances are nearly the same at three situations. This is in agreement with the power performance results shown in Fig. 6.19. Therefore, it can be concluded that the PTFE amount in the substrate shows little effect on the growth of Pt NWs.

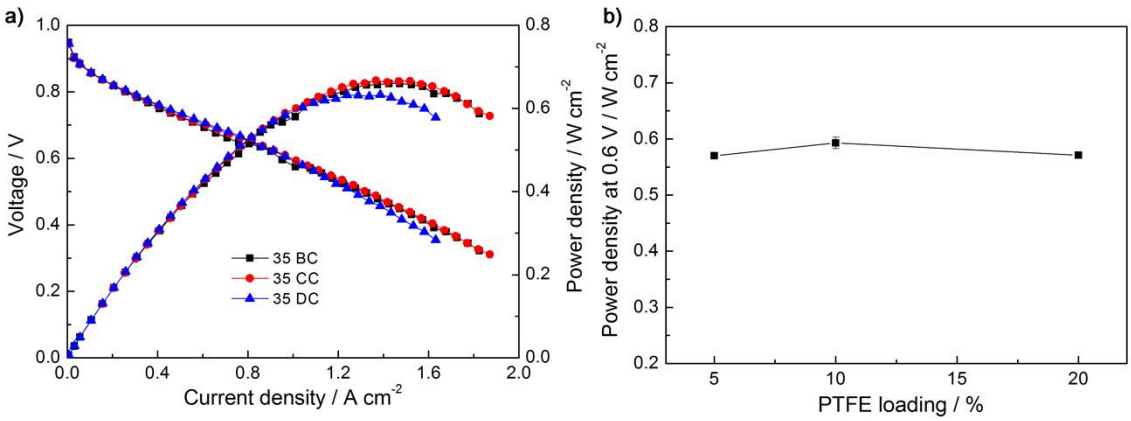

Fig. 6.19 (a) Polarisation and power density curves and (b) the trend of the power density at 0.6 V for the PtNW GDEs with different PTFE loadings in the substrate of the commercial GDLs.

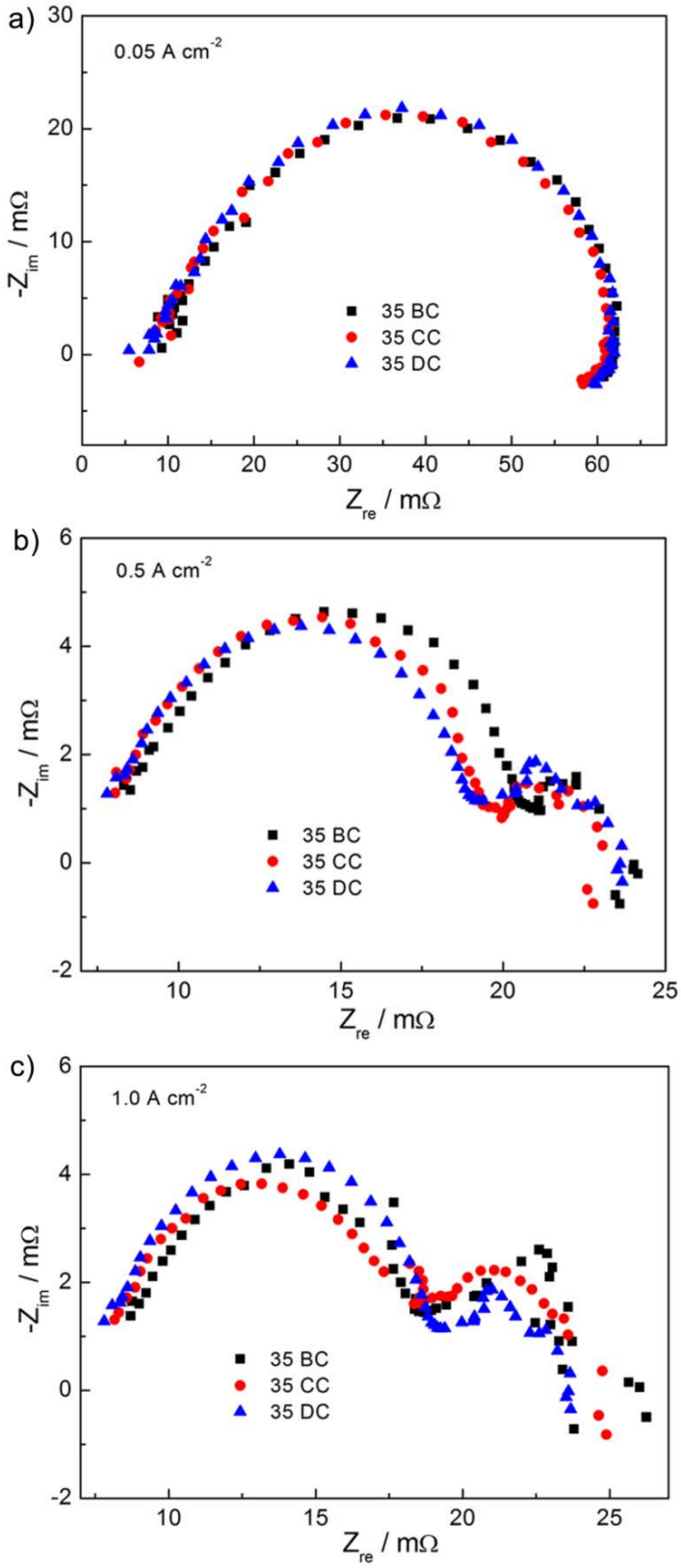

Fig. 6.20 EIS measured at (a) 0.05, (b) 0.5 and (c) 1.0 A cm^{-2} for the PtNW GDEs with different PTFE loadings in the substrate of commercial GDLs.

6.5.2 PTFE Loading in the MPL

To evaluate the effect of the PTFE loading in the MPL, GDLs with different PTFE amounts in the MPL but with the same substrate were studied. As this kind of GDLs couldn't be obtained commercially, MPLs were self-painted on 35BA substrates in the lab. Based on the optimal carbon loading of 4 mg cm^{-2} and the composition of CB 50%+AB 50%, carbon inks were prepared with different PTFE loadings of 5, 10, 15, 20, 25, 30 and 40% with respect to the total MPL weight. The detailed information of the self-made GDLs is shown in Table. 6.2.

Table 6.2 PTFE loading in the self-made GDLs.

Self-made GDLs	PTFE loading in the substrate (%)	PTFE loading in the MPL (%)
35BA+MPL1	5	5
35BA+MPL2	5	10
35BA+MPL3	5	15
35BA+MPL4	5	20
35BA+MPL5	5	25
35BA+MPL6	5	30
35BA+MPL7	5	40

The hydrophobicity of the self-made GDLs was analysed by measuring the water contact angle through a drop shape analyser. The measured water contact angles for all samples are in the range of 165.3º to 166.8º, indicating that the painted GDLs with various PTFE loadings have a very similar superhydrophobic surface.

The morphology and distribution of Pt NWs grown on the GDLs with the self-painted MPLs with 5, 20 and 40% PTFE, corresponding to the low, medium and high PTFE amount, were analysed by SEM. Fig. 6.21 and 6.22 show SEM images of the centre and edge area of a PtNW GDE with 5% PTFE in the painted MPL. Pt NWs have a denser

distribution and longer length at the edge area, which is possibly due to the preferable nucleation and growth processes on the rough sites of the GDL surface. At the medium and high PTFE amount of 20% (Fig. 6.23) and 40% (Fig. 6.25), the distribution of Pt NWs in the centre area becomes non-uniform and tends to aggregate to form superstructures, and some parts of the surface are not covered by Pt nanowires. As for the edge area, the density of 20% PTFE (Fig. 6.24) is still heavy while that of 40% PTFE (Fig. 6.26) has a similar coverage density to the centre. Furthermore, the length of Pt NWs has shortened with increase in PTFE amount. This is because the high PTFE loading covers more surface area of the GDL thus presents a hurdle for the surface nucleation and finally growing into dense Pt NW agglomerates.

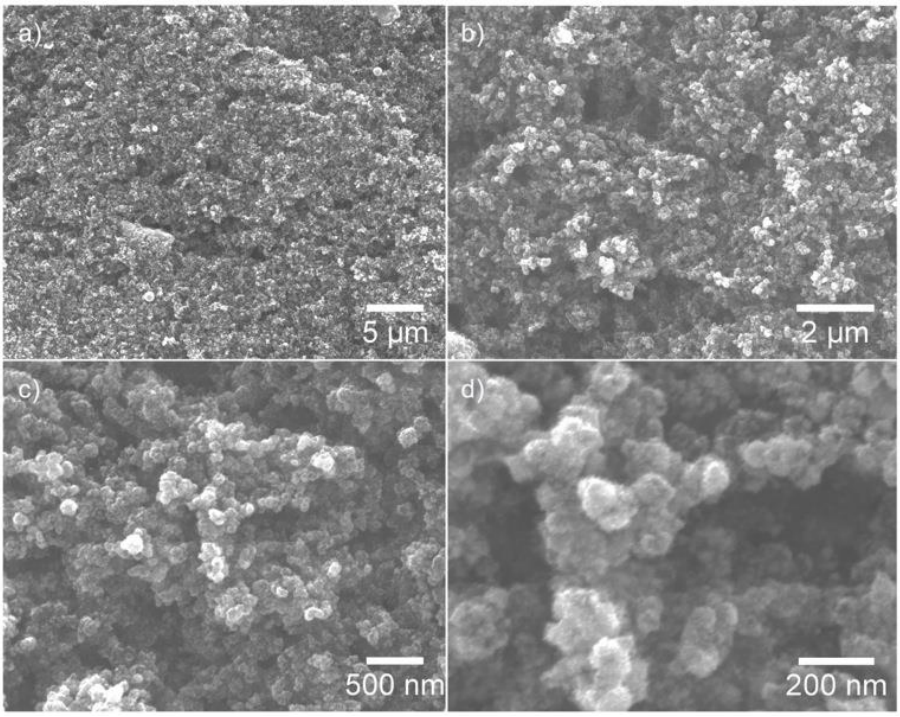

Fig. 6.21 SEM images at different magnifications for the centre area of the PtNW GDE with 5% PTFE in the painted MPL.

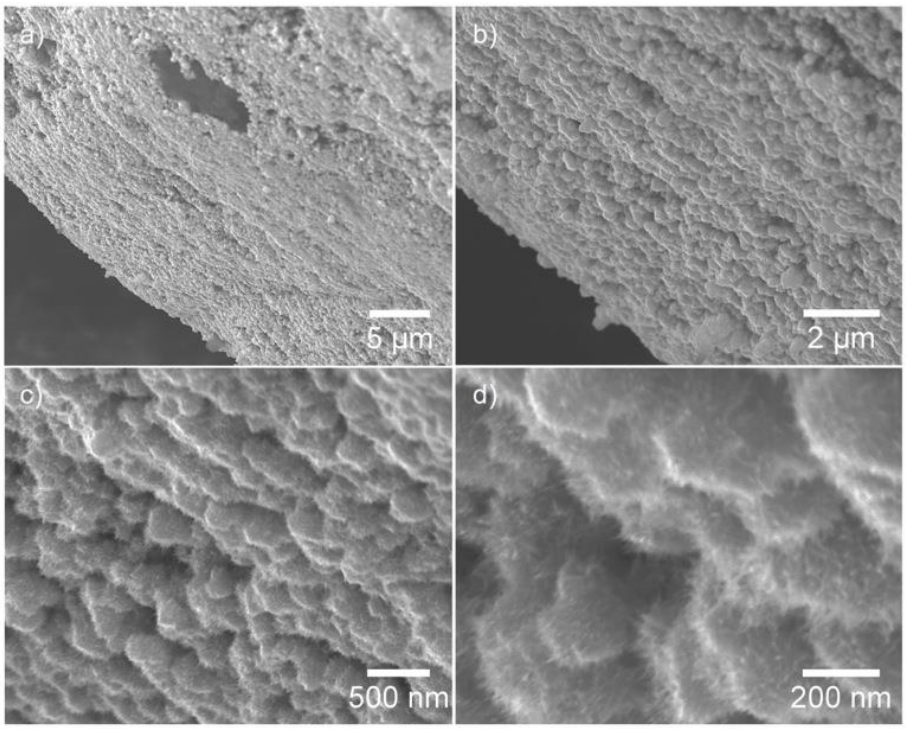

Fig. 6.22 SEM images at different magnifications for the edge area of the PtNW GDE with 5% PTFE in the painted MPL.

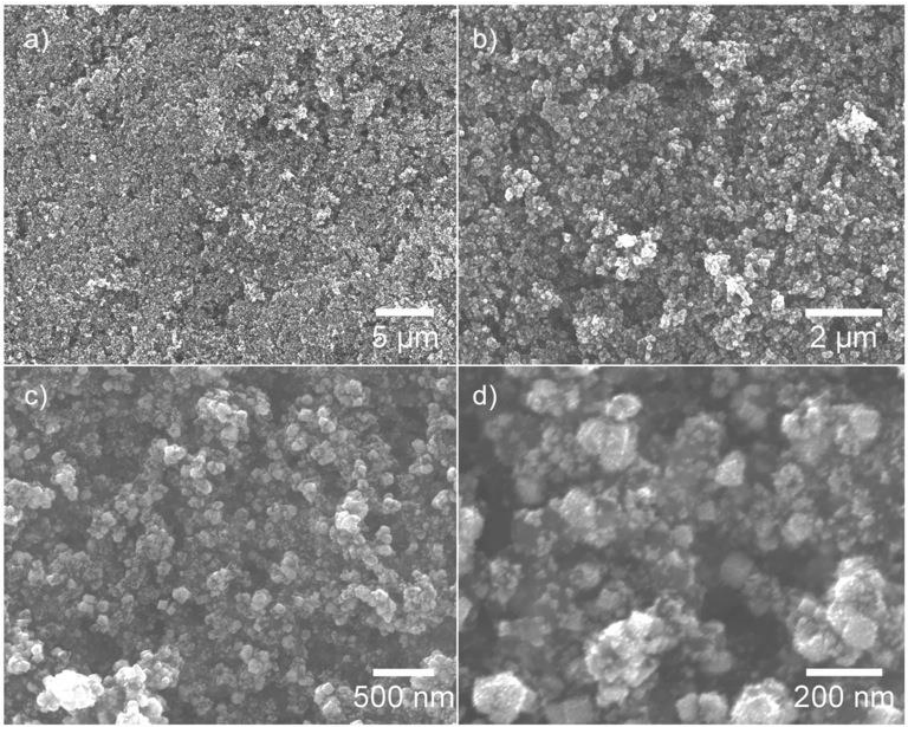

Fig. 6.23 SEM images at different magnifications for the centre area of the PtNW GDE with 20% PTFE in the painted MPL.

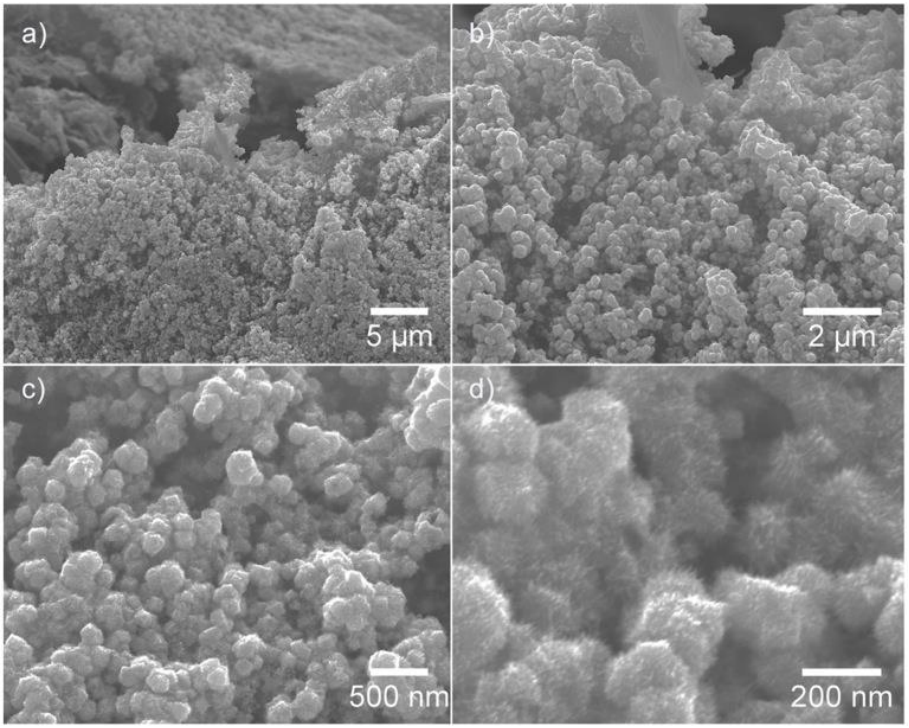

Fig. 6.24 SEM images at different magnifications for the edge area of the PtNW GDE with 20% PTFE in the painted MPL.

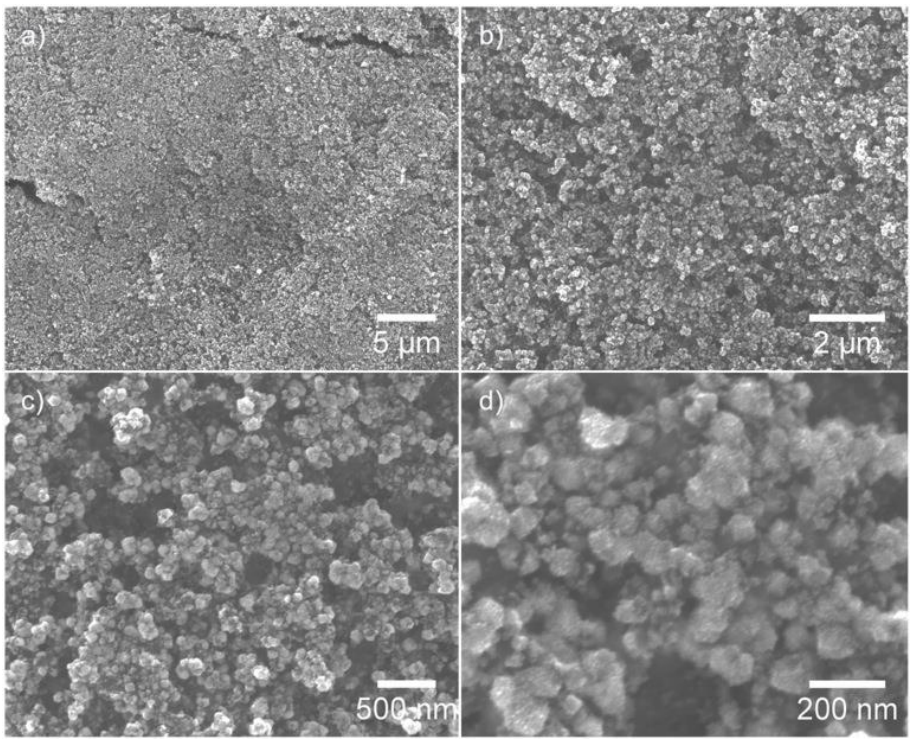

Fig. 6.25 SEM images at different magnifications for the centre area of the PtNW GDE with 40% PTFE in the painted MPL.

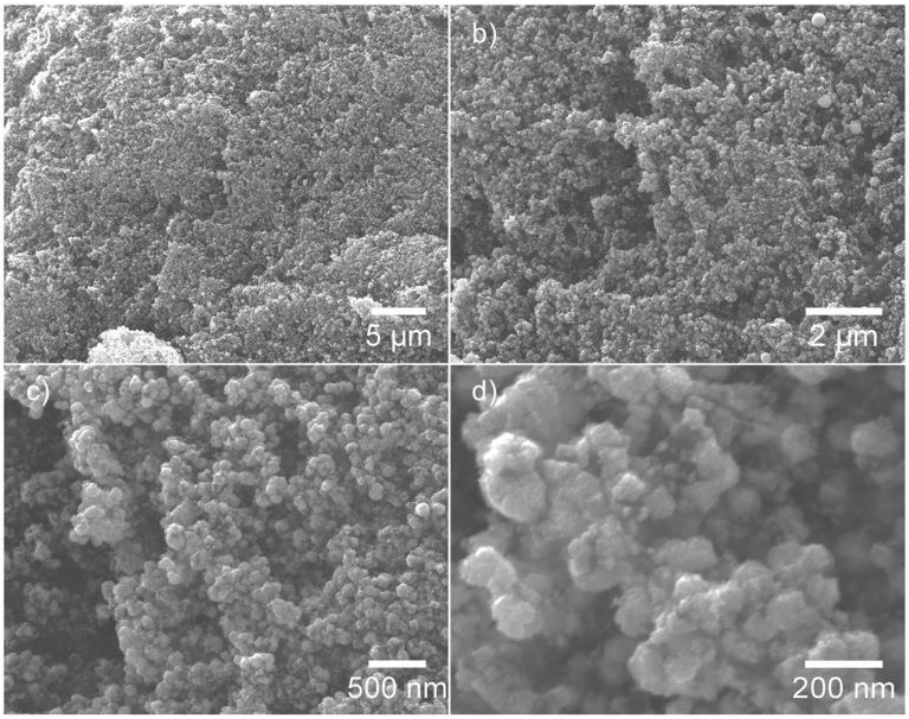

Fig. 6.26 SEM images at different magnifications for the edge area of the PtNW GDE with 40% PTFE in the painted MPL.

The in-situ performance of the PtNW GDEs grown on the painted MPLs with various PTFE loadings from 5 to 40% was tested in a single fuel cell and the results are shown in Fig. 6.27. Generally, the performance decreases with increase in PTFE amount and the largest power density is achieved with 5% PTFE in the MPL. A similar trend is observed for EIS measurement results at all three current densities in Fig. 6.28. The sample with 5% PTFE exhibits the smallest charge and mass transfer resistances. On one hand this can be attributed to the uniform distribution of Pt NWs on the carbon surface at low PTFE loading and the increasing agglomeration at higher PTFE amounts. On the other hand, at a high PTFE loading, the polymer in the pores partially reduces the porosity of the MPL, resulting in a large mass transfer loss [251].

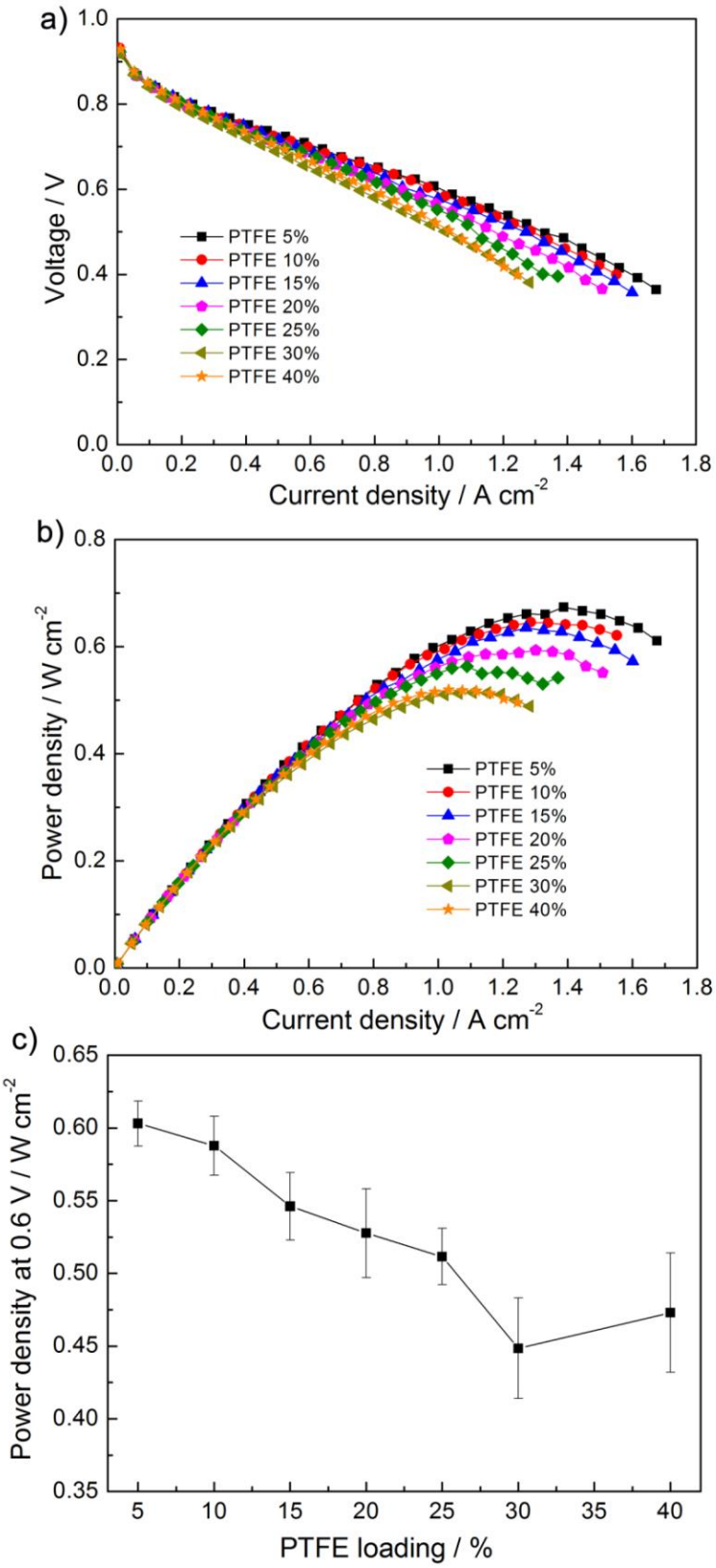

Fig. 6.27 (a) Polarisation curves, (b) power density curves and (c) the trend of the power density at 0.6 V for the PtNW GDEs with different PTFE loadings in self-painted MPLs.

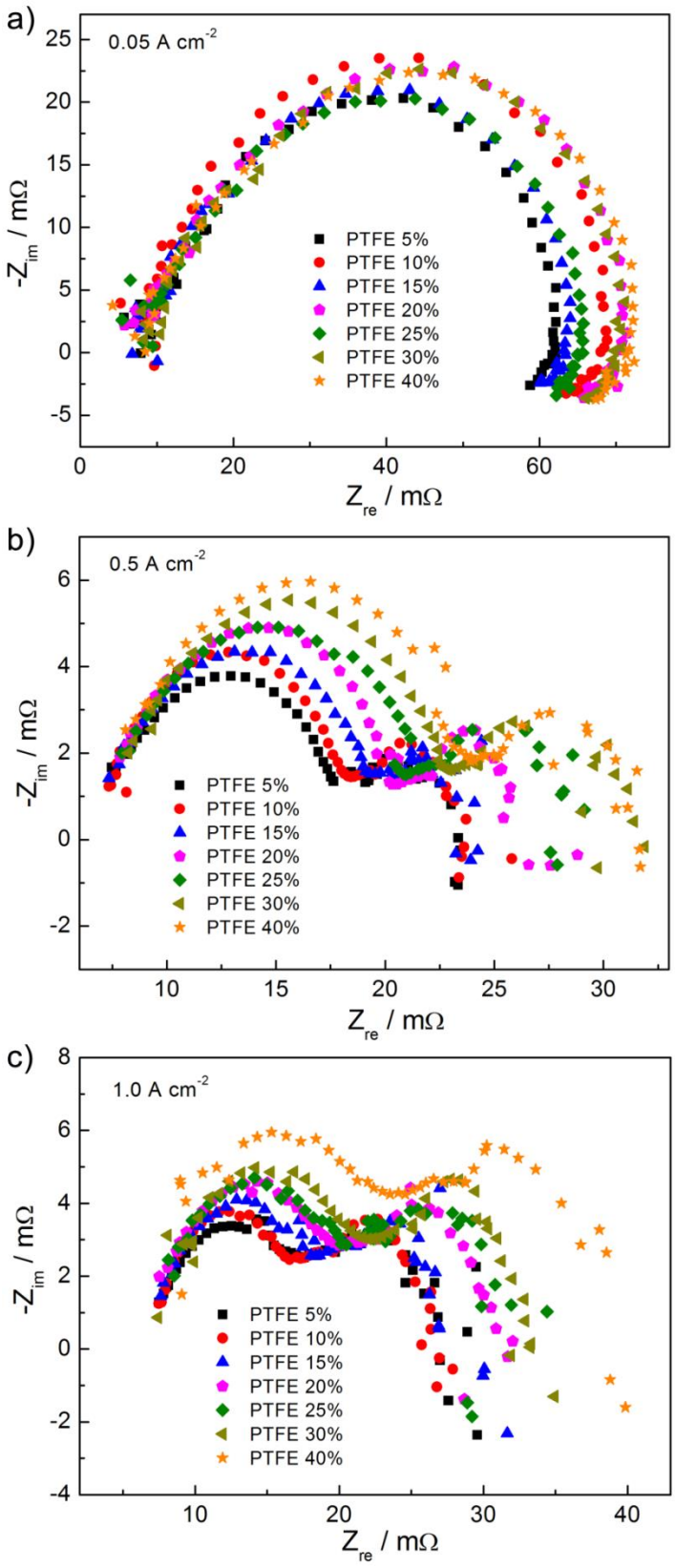

Fig. 6.28 EIS measured at (a) 0.05, (b) 0.5 and (c) 1.0 A cm^{-2} for the PtNW GDEs with different PTFE loadings in the self-painted MPLs.

Cathode cyclic voltammograms (CVs) were recorded in the single cell to compare the electrochemical surface area (ECSA) of the PtNW GDEs with different PTFE loadings in MPLs. According to CV curves in Fig. 6.29a and the Pt precursor, the calculated ECSAs for PtNW GDEs with the PTFE loading of 5, 10, 15, 20, 25, 30 and 40% are 19.65, 19.35, 18.25, 18.17, 18.61, 18.25, 16.13 $m^2 g^{-1}$, respectively. A summary of the ECSAs with the PTFE loading is shown in Fig. 6.29b. It can be seen that the ECSA value slowly decreases with increase in PTFE amount, but the values are still very close to each other except the value of 40% which is slightly lower. Considering the SEM analysis results (Fig. 6.21-6.26), it can be concluded that with the increase in PTFE amount, the catalyst utilisation slowly becomes poorer and thus a smaller ECSA value is obtained, finally resulting in an increased charge transfer loss and a lower catalytic activity (Fig. 6.28).

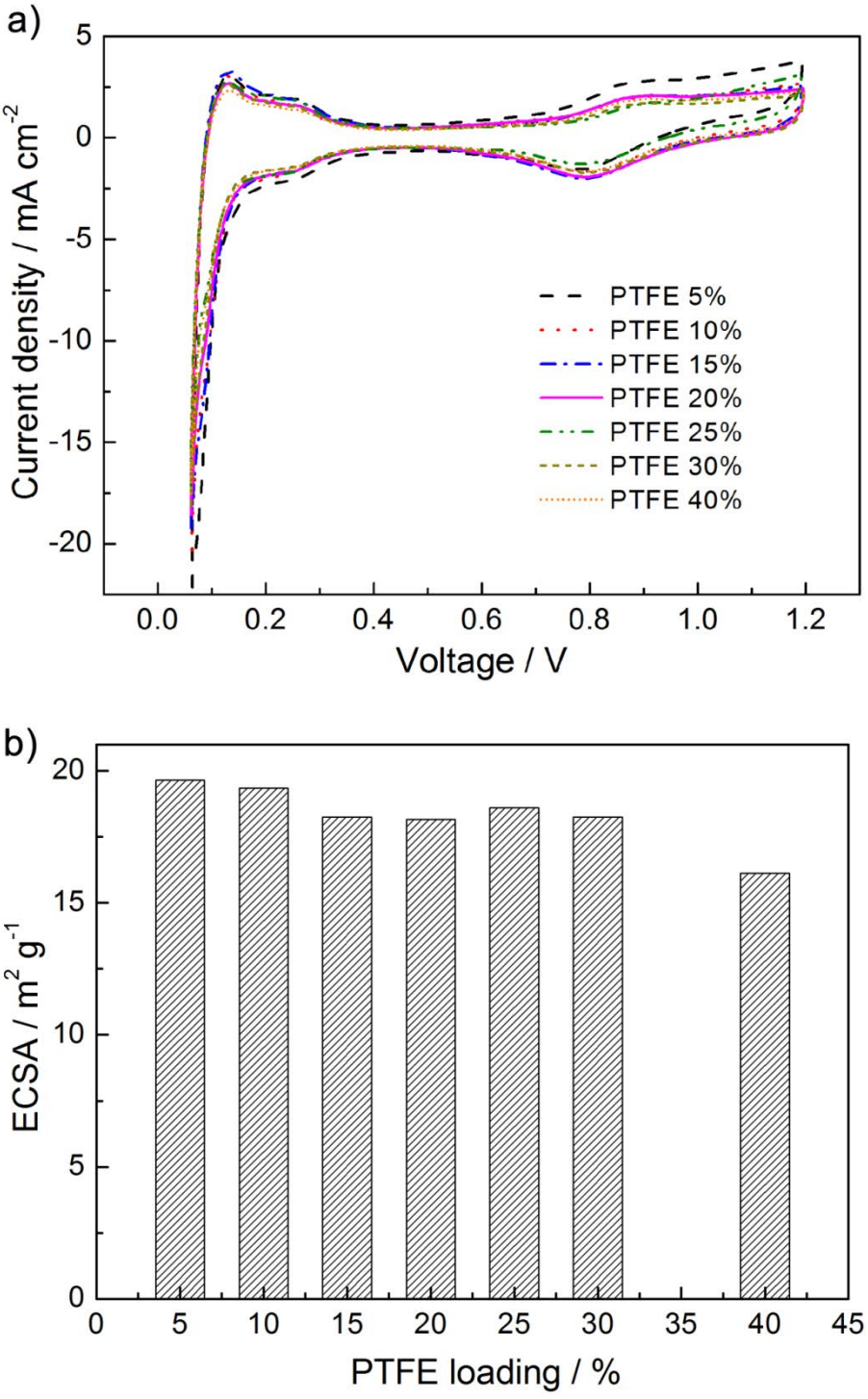

Fig. 6.29 (a) Cathode CVs and (b) summary of ECSAs for the PtNW GDEs with different PTFE loadings in the MPLs.

The above test results demonstrate the influence of the amount of PTFE in the MPL on the in-situ performance. To further check the possible role in water flooding during the fuel cell testing, in particular at a lower PTFE loading, e.g. 5%, PtNW GDEs with the painted MPLs at low, medium and high PTFE amounts were tested as cathodes by soaking at 0.6 V over a period of ca. 24h. Fig. 6.30 indicates that during this period the performance of PtNW GDEs is generally stable for the MPLs with low and medium PTFE loadings, but an obvious decrease can be observed with the PTFE loading of 40%.

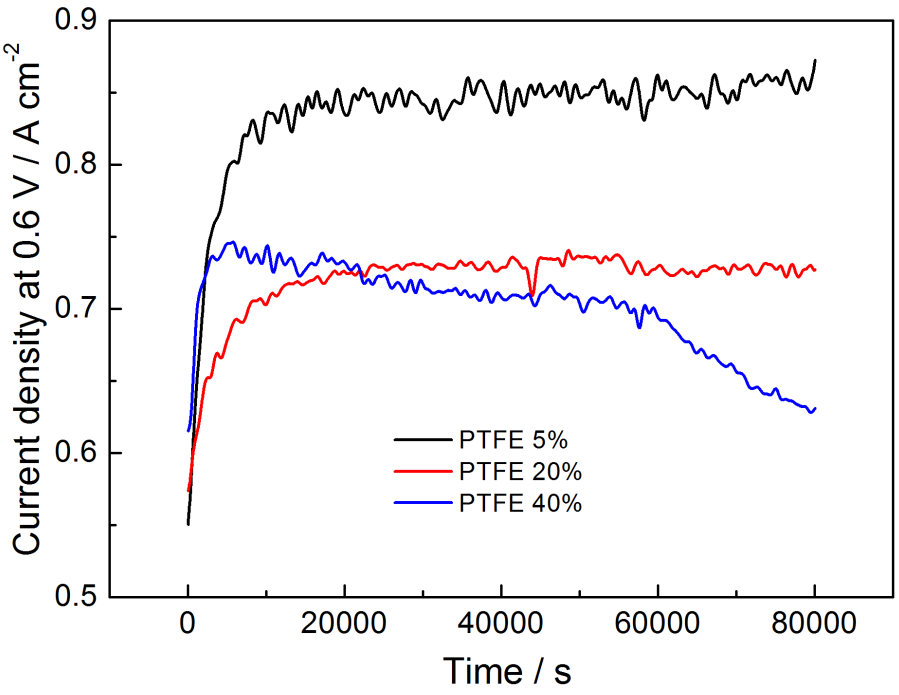

Fig. 6.30 Continuous operation test at 0.6 V for PtNW GDEs with painted MPLs at the low, medium and high PTFE amounts. Measurements were taken at T_{cell}=70 °C with fully humidified H_2 and air at 2 bar (stoichiometry s=1.3/2.4).

Although further investigation is needed to clarify the mechanism, one possible reason is that the high PTFE loading results in limited nucleation sites with agglomerated Pt NWs on the surface, which could not have a good contact with the coated Nafion ionomer,

finally resulting in a fast interface degradation in the operation. Hence, it can be deduced that a PTFE loading below 20% in the MPL doesn't result in water flooding in the continuous operation of fuel cells. Nevertheless, the low loading of 5% again shows the best performance.

6.6 Conclusions

In this study, the GDL structures such as carbon loading, carbon composition, carbon treatment and PTFE loading were systematically investigated to understand their effects on the performance of PtNW GDEs. The results demonstrate that, to achieve a high performance GDE, it is critical to control the amount of nucleation sites on the MPL surface for the production of uniform Pt NWs with a balanced mass transport loss, but the PTFE loading in the substrate exhibited very limited influence.

The obtained optimum carbon loading in the MPL is 4 mg cm^{-2}, as a higher carbon loading results in a very thick MPL and a smaller carbon amount could not cover the surface very effectively. Regarding the carbon composition in the MPL, the mixture of CB 50% and AB 50% provided a suitable porosity and a reasonable number of surface nucleation sites for the growth of Pt NWs to achieve a high power performance PtNW GDE. The higher CB amount made Pt NWs to grow into the inner pore surface between the active CB spheres while the higher AB content resulted in agglomerates and sparse distribution of Pt NWs owing to the inert surface properties. After nitric acid treatment, the performance of treated CB and AB changed opposite to each other compared with the original situation. Under the optimum carbon composition, the performance only slightly improved over that from the mixture of CB 50% and AB 50%. Furthermore, the PTFE amount within the

MPL needs to be kept at a low level, e.g. 5%, to enable effective nucleation sites on the surface while still preventing water flooding during fuel cell operation.

CHAPTER 7

CONCLUSIONS AND PERSPECTIVE

7. Conclusions and Perspective

7.1 Conclusions

In this thesis, the in-situ growing process of one-dimensional (1D) Pt-based nanostructures on gas diffusion layers (GDLs) was systematically studied to help understand the structure-property relationship of the gas diffusion electrodes (GDEs). The crystal nucleation and growth, coupled with the distribution of the produced nanostructures were investigated based on the corresponding GDE performance in polymer electrolyte fuel cells (PEFCs). The influence of the in-situ growing temperature, the hybridizing Pd metal and the structures of the GDL itself were comprehensively investigated for a further understanding of the in-situ nanowire growing process.

Effects of Growth Temperature. The in-situ growing temperature not only tuned the phase formation kinetics of Pt nanostructures but also affected the wettability of the GDL surface by the reaction solution, thus influencing the morphology and distribution of Pt nanostructures. At a low temperature, e.g. 5 or 15 ^{o}C, the high surface tension of the aqueous reaction solution resulted in a poor contact with the GDL surface, providing very limited nucleation sites, in addition to the slow crystal growth rate. Only large dense aggregates of Pt nanowires were formed at the rough edge area, resulting in a low catalyst utilisation and poor catalytic performance. At a medium temperature, the reduced surface tension of water enabled multiple nucleation sites in the centre area, resulting in an improved distribution of Pt NWs on the GDL surface. Further increasing the temperature to a very high value allowed to overcome the homogeneous nucleation barrier and a large amount of nuclei were directly formed in the solution at a fast crystal growth rate, thus nanoparticles were produced rather than nanowires.

The optimal temperature was achieved at 40 ^{o}C, at which uniform Pt nanowire arrays were obtained on the GDL surface. A high catalytic performance was demonstrated in the hydrogen/air fuel cells with the power density of 0.822 W cm^{-2} at 0.6 V. Double the mass activity and three times higher specific area activity over the reference TKK Pt/C GDE was achieved, although a smaller ECSA was observed due to the 1D nanowire morphology. The accelerated degradation test (ADT) with 2000 potential cycles confirmed a better durability. After the ADT, the PtNW GDE and TKK Pt/C GDE retained 52% and 33% of their initial ECSA, respectively.

Effects of Hybridizing Pd. The introduced Pd not only served as growing seed for the growth of PdPt nanostructures but could also tune their morphology and distribution on the GDL surface. At the high Pd content, e.g. 50 at%, the abundant Pd nuclei served as multiple nucleation sites for the formation of PdPt nanoparticles (NPs) and gradually shaped into aggregates due to the high surface energy, resulting in a low catalyst utilisation ratio and poor catalytic performance. At the medium Pd content, the reduced nucleation sites enabled the formation of a mixture of PdPt NPs and nanodendrites (NDs), and the formed aggregates were gradually reduced, delivering an improved performance. Further decreasing the Pd amount made the nucleation process mainly happen on the rough sites of the GDL edge area due to the low number of Pd seeds, and the produced dense PdPt NDs on the edge area contributed to a non-uniform distribution, leading to a decline in performance.

The optimum Pd atomic percentage was achieved at 5 at%, at which the generated Pd seeds were just sufficient to accommodate Pt atoms and able to balance the nucleation and

growth rate, resulting in a uniform distribution of PdPt NDs on the GDL surface. The high power performance of PdPtND GDE with 5 at% Pd was demonstrated by the current density of 1.21 A cm^{-2} and power density of 0.73 W cm^{-2} at 0.6 V, respectively, which was higher than that of the PtNW GDE prepared under the same conditions. This improved performance was attributed to the larger ECSA and the synergistic effect between both metals. A better durability was also demonstrated. After 3000 potential cycles in the ADT, the ECSA losses of PdPtND and PtNW GDEs were 46.6% and 62.2%, respectively. However, slightly lower mass and specific area activities were observed for PdPtND. Considering the better performance in H_2/air in-situ tests and the lower mass activities in H_2/O_2 in-situ tests, it can be concluded that the final performance of electrodes is determined by the combined effects from both the intrinsic catalytic activity of catalysts and the extrinsic GDE structure.

Effects of GDL Structure. The surface structures of GDLs such as porosity, homogeneity, hydrophobicity, etc. determined by carbon loading, carbon composition, carbon treatment and PTFE loading influenced the in-situ growth process of Pt NWs and further affected the final performance of the PtNW GDE. The study indicated that an optimal amount of nucleation sites on the MPL surface in the GDL was critical for the controlled growth of uniform Pt NWs with a balanced mass transport loss to achieve a high performance GDE, but the substrate in the GDL exhibited very limited influence. The high carbon loading led to very thick MPLs, while the low carbon amount resulted in incompletely covered substrate surfaces, finally causing a poor contact between the electrolyte membrane and the Pt NWs grown beneath the MPL, thus a large interfacial contact resistance and poor performance were obtained.

The carbon black type used in the MPL showed influence on the Pt NW growth. When pure acetylene black (AB) was used, due to the inert surface, Pt NWs were sparsely distributed on the surface. With the increase of the share of carbon black (CB), more Pt NWs were grown on the surface because more nucleation sites were provided. When pure CB was employed, a large amount of active sites enabled a full coverage of the entire GDL surface, even on the inner pore surface in the MPL, resulting in a lower catalyst utilisation ratio and thus a poorer performance. After acid treatment, the surface area of AB increased while that of CB decreased, but the opposite change of their surface areas only slightly improved the performance under the optimum carbon composition.

As for the PTFE amount, the loading in the substrate didn't have a large effect on the growth of Pt NWs. On the contratry, a low PTFE loading in the MPL enabled uniform distribution of Pt NWs and could still prevent water flooding while a high loading amount resulted in the aggregation of Pt NWs on the hydrophobic GDL surface combined with reduced performance.

The optimum MPL structure achieved in this work occured at the carbon loading of 4 mg cm^{-2} with the carbon composition of CB 50%+AB 50% and the PTFE loading of 5%, which provided a suitable substrate coverage, reasonable surface nucleation sites and satisfying hydrophobicity for the growth of Pt NWs. With this optimum structure, Pt NWs uniformly covered the whole GDL surface with less aggregation and showed a better contact with the electrolyte membrane, leading to a better power performance.

The experimental results from the investigation of the growth temperature, and hybridizing Pd, together with the structures of the GDL, demonstrate that the controlled nucleation and growth processes are significant for the in-situ employment of one-dimensional Pt-based nanostructures. The final performance in single fuel cells is not only affected by the intrinsic activities of catalysts but also influenced by their extrinsic behaviour on the GDL. This further demonstrates the important role of the electrode structure in the optimisation of PEFC performance.

7.2 Perspective

Based on the present results, some suggestions and perspectives are proposed for further improvement:

- This is only the fundamental study of integrated GDEs with 1D Pt-based nanostructures. Although a better durability was achieved by the ADT in single fuel cells, to meet the requirements for practical applications, a long-term life time test, in particular in PEFC stacks, is necessary to further confirm the potential of this kind of GDEs.
- This work demonstrated the lower intrinsic mass activity of PtPd nanodendrites as compared with pure Pt nanowires in PEFCs. Although a similar result has also been reported for the lower intrinsic mass activity of the PtCo nanostructures over the pure Pt nanostructures in practical PEFCs [225], further work is required to evaluate the activities of other alloys and hybrid Pt nanostructures in practical fuel cells. This could also further help to clarify the different catalytic mechanisms measured by electrochemical approaches and in-situ fuel cell tests, helping to reduce the gap in

catalytic activity evaluation between the liquid electrolyte measurement and the practical PEFC testing.

- In this work only PtNW and PdPtND GDEs were fabricated and tested in the PEFC single cell. Expanding the strategies described here to exploit approaches to produce Pt-transition metals and even non-precious metal based GDEs is significant for the further reduction of Pt loading in PEFC electrodes.
- As for self-painted MPLs, besides the water contact angle test for the hydrophobicity information, other physical properties of GDLs such as the thickness, roughness, pore size, bulk density, permeability, etc. also need to be studied for the understanding of the effects on the Pt nanowire growth and fuel cell testing results.

References

[1] C.S. Song, Fuel processing for low-temperature and high-temperature fuel cells - Challenges, and opportunities for sustainable development in the 21st century, *Catalysis Today* 77 **(2002)** 17-49.

[2] M. Winter, R.J. Brodd, What are batteries, fuel cells, and supercapacitors?, *Chemical Reviews* 104 **(2004)** 4245-4269.

[3] M. Dadvar, E. Afshari, Analysis of design parameters in anodic recirculation system based on ejector technology for PEM fuel cells: A new approach in designing, *International Journal of Hydrogen Energy* 39 **(2014)** 12061-12073.

[4] F. Barbir, PEM fuel cells: theory and practice, Elsevier, London, 2005.

[5] K. Kordesch, G. Simader, Fuel cells and their applications, VCH, Weinheim ; New York, 1996.

[6] O.Z. Sharaf, M.F. Orhan, An overview of fuel cell technology: Fundamentals and applications, *Renewable & Sustainable Energy Reviews* 32 **(2014)** 810-853.

[7] S. Srinivasan, Fuel cells: from fundamentals to applications, Springer; New York, 2006.

[8] A. Jayakumar, S.P. Sethu, M. Ramos, J. Robertson, A. Al-Jumaily, A technical review on gas diffusion, mechanism and medium of PEM fuel cell, *Ionics* 21 **(2015)** 1-18.

[9] O. Savadogo, Emerging membranes for electrochemical systems - Part II. High temperature composite membranes for polymer electrolyte fuel cell (PEFC) applications, *Journal of Power Sources* 127 **(2004)** 135-161.

[10] J. Zhang, PEM fuel cell electrocatalysts and catalyst layers: fundamentals and applications, Springer, London, 2008.

[11] I. Katsounaros, S. Cherevko, A.R. Zeradjanin, K.J.J. Mayrhofer, Oxygen electrochemistry as a cornerstone for sustainable energy conversion, *Angewandte Chemie-International Edition* 53 **(2014)** 102-121.

[12] I. Bar-On, R. Kirchain, R. Roth, Technical cost analysis for PEM fuel cells, *Journal of Power Sources* 109 **(2002)** 71-75.

[13] C. Houchins, G.J. Kleen, J.S. Spendelow, J. Kopasz, D. Peterson, N.L. Garland, D.L. Ho, J. Marcinkoski, K.E. Martin, R. Tyler, D.C. Papageorgopoulos, U.S. DOE progress towards developing low-cost, high performance, durable polymer electrolyte membranes for fuel cell applications, *Membranes* 2 **(2012)** 855-878.

[14] H.A. Gasteiger, J.E. Panels, S.G. Yan, Dependence of PEM fuel cell performance on catalyst loading, *Journal of Power Sources* 127 **(2004)** 162-171.

[15] M.K. Debe, Electrocatalyst approaches and challenges for automotive fuel cells, *Nature* 486 **(2012)** 43-51.

[16] N. Yousfi-Steiner, P. Mocoteguy, D. Candusso, D. Hissel, A review on polymer electrolyte membrane fuel cell catalyst degradation and starvation issues: Causes, consequences and diagnostic for mitigation, *Journal of Power Sources* 194 **(2009)** 130-145.

[17] P.J. Ferreira, G.J. la O', Y. Shao-Horn, D. Morgan, R. Makharia, S. Kocha, H.A. Gasteiger, Instability of Pt/C electrocatalysts in proton exchange membrane fuel cells - A mechanistic investigation, *Journal of the Electrochemical Society* 152 **(2005)** A2256-A2271.

[18] Y. Shao-Horn, W.C. Sheng, S. Chen, P.J. Ferreira, E.F. Holby, D. Morgan, Instability of supported platinum nanoparticles in low-temperature fuel cells, *Topics in Catalysis* 46 **(2007)** 285-305.

[19] E.F. Holby, W.C. Sheng, Y. Shao-Horn, D. Morgan, Pt nanoparticle stability in PEM fuel cells: influence of particle size distribution and crossover hydrogen, *Energy & Environmental Science* 2 **(2009)** 865-871.

[20] P.A. Thiel, M. Shen, D.J. Liu, J.W. Evans, Coarsening of two-dimensional nanoclusters on metal surfaces, *Journal of Physical Chemistry C* 113 **(2009)** 5047-5067.

[21] N. Alonso-Vante, Platinum and non-platinum nanomaterials for the molecular oxygen reduction reaction, *Chemphyschem* 11 **(2010)** 2732-2744.

[22] J. Greeley, I.E.L. Stephens, A.S. Bondarenko, T.P. Johansson, H.A. Hansen, T.F. Jaramillo, J. Rossmeisl, I. Chorkendorff, J.K. Norskov, Alloys of platinum and early transition metals as oxygen reduction electrocatalysts, *Nature Chemistry* 1 **(2009)** 552-556.

[23] S.J. Guo, S. Zhang, S.H. Sun, Tuning nanoparticle catalysis for the oxygen reduction reaction, *Angewandte Chemie-International Edition* 52 **(2013)** 8526-8544.

[24] V. Stamenkovic, B.S. Mun, K.J.J. Mayrhofer, P.N. Ross, N.M. Markovic, J. Rossmeisl, J. Greeley, J.K. Norskov, Changing the activity of electrocatalysts for oxygen reduction by tuning the surface electronic structure, *Angewandte Chemie-International Edition* 45 **(2006)** 2897-2901.

[25] J.K. Norskov, J. Rossmeisl, A. Logadottir, L. Lindqvist, J.R. Kitchin, T. Bligaard, H. Jonsson, Origin of the overpotential for oxygen reduction at a fuel-cell cathode, *Journal of Physical Chemistry B* 108 **(2004)** 17886-17892.

[26] K. Jiang, H.X. Zhang, S.Z. Zou, W.B. Cai, Electrocatalysis of formic acid on palladium and platinum surfaces: from fundamental mechanisms to fuel cell applications, *Physical Chemistry Chemical Physics* 16 **(2014)** 20360-20376.

[27] Y. Liu, T.G. Kelly, J.G.G. Chen, W.E. Mustain, Metal carbides as alternative electrocatalyst supports, *ACS Catalysis* 3 **(2013)** 1184-1194.

[28] C.N.R. Rao, A.K. Cheetham, Science and technology of nanomaterials: current status and future prospects, *Journal of Materials Chemistry* 11 **(2001)** 2887-2894.

[29] Y.N. Xia, P.D. Yang, Y.G. Sun, Y.Y. Wu, B. Mayers, B. Gates, Y.D. Yin, F. Kim, Y.Q. Yan, One-dimensional nanostructures: Synthesis, characterization, and applications, *Advanced Materials* 15 **(2003)** 353-389.

[30] J.Y. Chen, B.J. Wiley, Y.N. Xia, One-dimensional nanostructures of metals: Large-scale synthesis and some potential applications, *Langmuir* 23 **(2007)** 4120-4129.

[31] J.T. Hu, T.W. Odom, C.M. Lieber, Chemistry and physics in one dimension: Synthesis and properties of nanowires and nanotubes, *Accounts of Chemical Research* 32 **(1999)** 435-445.

[32] S.V.N.T. Kuchibhatla, A.S. Karakoti, D. Bera, S. Seal, One dimensional nanostructured materials, *Progress in Materials Science* 52 **(2007)** 699-913.

[33] Y.S. Zhao, H.B. Fu, A.D. Peng, Y. Ma, D.B. Xiao, J.N. Yao, Low-dimensional nanomaterials based on small organic molecules: Preparation and optoelectronic properties, *Advanced Materials* 20 **(2008)** 2859-2876.

[34] L.X. Yi, Y.Y. Liu, N.L. Yang, Z.Y. Tang, H.J. Zhao, G.H. Ma, Z.G. Su, D. Wang, One dimensional $CuInS_2$-ZnS heterostructured nanomaterials as low-cost and high-performance counter electrodes of dye-sensitized solar cells, *Energy & Environmental Science* 6 **(2013)** 835-840.

[35] N. Chopra, V.G. Gavalas, B.J. Hinds, L.G. Bachas, Functional one-dimensional nanomaterials: Applications in nanoscale biosensors, *Analytical Letters* 40 **(2007)** 2067-2096.

[36] C.Y. Cha, S.R. Shin, N. Annabi, M.R. Dokmeci, A. Khademhosseini, Carbon-based nanomaterials: multifunctional materials for biomedical engineering, *ACS Nano* 7 **(2013)** 2891-2897.

[37] S.K. Kamarudin, N. Hashim, Materials, morphologies and structures of MEAs in DMFCs, *Renewable & Sustainable Energy Reviews* 16 **(2012)** 2494-2515.

[38] S. Zhang, Y.Y. Shao, G.P. Yin, Y.H. Lin, Recent progress in nanostructured electrocatalysts for PEM fuel cells, *Journal of Materials Chemistry A* 1 **(2013)** 4631-4641.

[39] Y.H. Bing, H.S. Liu, L. Zhang, D. Ghosh, J.J. Zhang, Nanostructured Pt-alloy electrocatalysts for PEM fuel cell oxygen reduction reaction, *Chemical Society Reviews* 39 **(2010)** 2184-2202.

[40] P.J. Ferreira, G.J. la O', Y. Shao-Horn, D. Morgan, R. Makharia, S. Kocha, H.A. Gasteiger, Instability of Pt/C electrocatalysts in proton exchange membrane fuel cells: A mechanistic investigation, *Journal of the Electrochemical Society* 152 **(2005)** A2256-A2271.

[41] S.H. Sun, G.X. Zhang, D.S. Geng, Y.G. Chen, R.Y. Li, M. Cai, X.L. Sun, A highly durable platinum nanocatalyst for proton exchange membrane fuel cells: multiarmed starlike nanowire single crystal, *Angewandte Chemie-International Edition* 50 **(2011)** 422-426.

[42] L. Cademartiri, G.A. Ozin, Ultrathin nanowires - A materials chemistry perspective, *Advanced Materials* 21 **(2009)** 1013-1020.

[43] J.T. Zhang, C.M. Li, Nanoporous metals: fabrication strategies and advanced electrochemical applications in catalysis, sensing and energy systems, *Chemical Society Reviews* 41 **(2012)** 7016-7031.

[44] C. Koenigsmann, W.-p. Zhou, R.R. Adzic, E. Sutter, S.S. Wong, Size-dependent enhancement of electrocatalytic performance in relatively defect-free, processed ultrathin platinum nanowires, *Nano Letters* 10 **(2010)** 2806-2811.

[45] C. Koenigsmann, S.S. Wong, One-dimensional noble metal electrocatalysts: a promising structural paradigm for direct methanol fuel cells, *Energy & Environmental Science* 4 **(2011)** 1161-1176.

[46] B.Y. Xia, W.T. Ng, H.B. Wu, X. Wang, X.W. Lou, Self-supported interconnected Pt nanoassemblies as highly stable electrocatalysts for low-temperature fuel cells, *Angewandte Chemie-International Edition* 51 **(2012)** 7213-7216.

[47] W.C. Choi, S.I. Woo, Bimetallic Pt-Ru nanowire network for anode material in a direct-methanol fuel cell, *Journal of Power Sources* 124 **(2003)** 420-425.

[48] I.S. Park, J.H. Choi, Y.E. Sung, Synthesis of 3 nm Pt nanowire using MCM-41 and electrocatalytic activity in methanol electro-oxidation, *Electrochemical and Solid State Letters* 11 **(2008)** B71-B75.

[49] G.Y. Zhao, C.L. Xu, D.J. Guo, H. Li, H.L. Li, Template preparation of Pt nanowire array electrode on Ti/Si substrate for methanol electro-oxidation, *Applied Surface Science* 253 **(2007)** 3242-3246.

[50] L.X. Ding, G.R. Li, Z.L. Wang, Z.Q. Liu, H. Liu, Y.X. Tong, Porous Ni@Pt core-shell nanotube array electrocatalyst with high activity and stability for methanol oxidation, *Chemistry-A European Journal* 18 **(2012)** 8386-8391.

[51] S.M. Choi, J.H. Kim, J.Y. Jung, E.Y. Yoon, W.B. Kim, Pt nanowires prepared via a polymer template method: Its promise toward high Pt-loaded electrocatalysts for methanol oxidation, *Electrochimica Acta* 53 **(2008)** 5804-5811.

[52] Y. Lee, J. Kim, D.S. Yun, Y.S. Nam, Y. Shao-Horn, A.M. Belcher, Virus-templated Au and Au-Pt core-shell nanowires and their electrocatalytic activities for fuel cell applications, *Energy & Environmental Science* 5 **(2012)** 8328-8334.

[53] X.F. Lu, C. Wang, Y. Wei, One-dimensional composite nanomaterials: synthesis by electrospinning and their applications, *Small* 5 **(2009)** 2349-2370.

[54] E.P. Lee, Z.M. Peng, W. Chen, S.W. Chen, H. Yang, Y.N. Xia, Electrocatalytic properties of Pt nanowires supported on Pt and W Gauzes, *ACS Nano* 2 **(2008)** 2167-2173.

[55] S. Du, Pt-based nanowires as electrocatalysts in proton exchange fuel cells, *International Journal of Low-Carbon Technologies* 7 **(2012)** 44-54.

[56] M.E. Scofield, H.Q. Liu, S.S. Wong, A concise guide to sustainable PEMFCs: recent advances in improving both oxygen reduction catalysts and proton exchange membranes, *Chemical Society Reviews* 44 **(2015)** 5836-5860.

[57] J.Y. Chen, T. Herricks, M. Geissler, Y.N. Xia, Single-crystal nanowires of platinum can be synthesized by controlling the reaction rate of a polyol process, *Journal of the American Chemical Society* 126 **(2004)** 10854-10855.

[58] W.X. Du, D. Su, Q. Wang, A.I. Frenkel, X.W. Teng, Promotional effects of bismuth on the formation of platinum-bismuth nanowires network and the electrocatalytic activity toward ethanol oxidation, *Crystal Growth & Design* 11 **(2011)** 594-599.

[59] Z.Y. Zhang, M.J. Li, Z.L. Wu, W.Z. Li, Ultra-thin PtFe-nanowires as durable electrocatalysts for fuel cells, *Nanotechnology* 22 **(2011)**.

[60] A.C. Chen, P. Holt-Hindle, Platinum-based nanostructured materials: synthesis, properties, and applications, *Chemical Reviews* 110 **(2010)** 3767-3804.

[61] K.D. Gilroy, P. Farzinpour, A. Sundar, R.A. Hughes, S. Neretina, Sacrificial templates for galvanic replacement reactions: design criteria for the synthesis of pure Pt nanoshells with a smooth surface morphology, *Chemistry of Materials* 26 **(2014)** 3340-3347.

[62] Y. Liu, D.G. Li, S.S. Sun, Pt-based composite nanoparticles for magnetic, catalytic, and biomedical applications, *Journal of Materials Chemistry* 21 **(2011)** 12579-12587.

[63] H. Zhang, M.S. Jin, Y.N. Xia, Enhancing the catalytic and electrocatalytic properties of Pt-based catalysts by forming bimetallic nanocrystals with Pd, *Chemical Society Reviews* 41 **(2012)** 8035-8049.

[64] M.L. Calegaro, H.B. Suffredini, S.A.S. Machado, L.A. Avaca, Preparation, characterization and utilization of a new electrocatalyst for ethanol oxidation obtained by the sol-gel method, *Journal of Power Sources* 156 **(2006)** 300-305.

[65] S. Bharathi, N. Fishelson, O. Lev, Direct synthesis and characterization of gold and other noble metal nanodispersions in sol-gel-derived organically modified silicates, *Langmuir* 15 **(1999)** 1929-1937.

[66] M.R. Gao, J. Jiang, S.H. Yu, Solution-based synthesis and design of late transition metal chalcogenide materials for oxygen reduction reaction (ORR), *Small* 8 **(2012)** 13-27.

[67] S. Sun, D. Yang, G. Zhang, E. Sacher, J.P. Dodelet, Synthesis and characterization of platinum nanowire-carbon nanotube heterostructures, *Chemistry of Materials* 19 **(2007)** 6376-6378.

[68] S.H. Sun, D.Q. Yang, D. Villers, G.X. Zhang, E. Sacher, J.P. Dodelet, Template- and surfactant-free room temperature synthesis of self-assembled 3D Pt nanoflowers from single-crystal nanowires, *Advanced Materials* 20 **(2008)** 571-574.

[69] S. Sun, G. Zhang, D. Geng, Y. Chen, R. Li, M. Cai, X. Sun, A highly durable platinum nanocatalyst for proton exchange membrane fuel cells: multiarmed starlike nanowire single crystal, *Angewandte Chemie* 123 **(2011)** 442-446.

[70] S. Sun, G. Zhang, D. Geng, Y. Chen, M.N. Banis, R. Li, M. Cai, X. Sun, Direct growth of single-crystal Pt nanowires on Sn@CNT nanocable: 3D electrodes for highly active electrocatalysts, *Chemistry – A European Journal* 16 **(2010)** 829-835.

[71] Y. Xu, B. Zhang, Recent advances in porous Pt-based nanostructures: synthesis and electrochemical applications, *Chemical Society Reviews* 43 **(2014)** 2439-2450.

[72] Q. Xiao, M. Cai, M. Balogh, M. Tessema, Y. Lu, Symmetric growth of Pt ultrathin nanowires from dumbbell nuclei for use as oxygen reduction catalysts, *Nano Research* 5 **(2012)** 145-151.

[73] L.Y. Ruan, E.B. Zhu, Y. Chen, Z.Y. Lin, X.Q. Huang, X.F. Duan, Y. Huang, Biomimetic synthesis of an ultrathin platinum nanowire network with a high twin density for enhanced electrocatalytic activity and durability, *Angewandte Chemie-International Edition* 52 **(2013)** 12577-12581.

[74] A.B. Papandrew, R.W. Atkinson, G.A. Goenaga, S.S. Kocha, J.W. Zack, B.S. Pivovar, T.A. Zawodzinski, Oxygen reduction activity of vapor-grown platinum nanotubes, *Journal of the Electrochemical Society* 160 **(2013)** F848-F852.

[75] S.M. Alia, G. Zhang, D. Kisailus, D. Li, S. Gu, K. Jensen, Y. Yan, Porous platinum nanotubes for oxygen reduction and methanol oxidation reactions, *Advanced Functional Materials* 20 **(2010)** 3742-3746.

[76] S. Ci, J. Zou, G. Zeng, S. Luo, Z. Wen, Single crystalline Pt nanotubes with superior electrocatalytic stability, *Journal of Materials Chemistry* 22 **(2012)** 16732-16737.

[77] G. Zhang, S. Sun, M. Cai, Y. Zhang, R. Li, X. Sun, Porous dendritic platinum nanotubes with extremely high activity and stability for oxygen reduction reaction, *Scientific Reports* 3 **(2013)** 1526.

[78] S.M. Alia, K. Jensen, C. Contreras, F. Garzon, B. Pivovar, Y. Yan, Platinum coated copper nanowires and Platinum nanotubes as oxygen reduction electrocatalysts, *ACS Catalysis* 3 **(2013)** 358-362.

[79] W.J. Khudhayer, N.N. Kariuki, X.P. Wang, D.J. Myers, A.U. Shaikh, T. Karabacak, Oxygen reduction reaction electrocatalytic activity of glancing angle deposited Platinum nanorod arrays, *Journal of the Electrochemical Society* 158 **(2011)** B1029-B1041.

[80] J. Xu, G. Fu, Y. Tang, Y. Zhou, Y. Chen, T. Lu, One-pot synthesis of three-dimensional platinum nanochain networks as stable and active electrocatalysts for oxygen reduction reactions, *Journal of Materials Chemistry* 22 **(2012)** 13585-13590.

[81] G. Fu, X. Jiang, M. Gong, Y. Chen, Y. Tang, J. Lin, T. Lu, Highly branched platinum nanolance assemblies by polyallylamine functionalization as superior active, stable, and alcohol-tolerant oxygen reduction electrocatalysts, *Nanoscale* 6 **(2014)** 8226-8234.

[82] T.T.H. Van, C.J. Pan, J. Rick, W.N. Su, B.J. Hwang, Nanostructured $Ti_{0.7}Mo_{0.3}O_2$ support enhances electron transfer to Pt: high-performance catalyst for oxygen

reduction reaction, *Journal of the American Chemical Society* 133 **(2011)** 11716-11724.

[83] W. Shimizu, K. Okada, Y. Fujita, S. Zhao, Y. Murakami, Platinum nanowire network with silica nanoparticle spacers for use as an oxygen reduction catalyst, *Journal of Power Sources* 205 **(2012)** 24-31.

[84] V.T.T. Ho, N.G. Nguyen, C.J. Pan, J.H. Cheng, J. Rick, W.N. Su, J.F. Lee, H.S. Sheu, B.J. Hwang, Advanced nanoelectrocatalyst for methanol oxidation and oxygen reduction reaction, fabricated as one-dimensional pt nanowires on nanostructured robust $Ti_{0.7}Ru_{0.3}O_2$ support, *Nano Energy* 1 **(2012)** 687-695.

[85] R. Wu, Y. Xue, X. Qian, H. Liu, K. Zhou, S.H. Chan, J.N. Tey, J. Wei, B. Zhu, Y. Huang, Pt nanodendrites anchored on bamboo-shaped carbon nanofiber arrays as highly efficient electrocatalyst for oxygen reduction reaction, *International Journal of Hydrogen Energy* 38 **(2013)** 16677-16684.

[86] S.C. Sahu, A.K. Samantara, B. Satpati, S. Bhattacharjee, B.K. Jena, A facile approach for in situ synthesis of graphene-branched-Pt hybrid nanostructures with excellent electrochemical performance, *Nanoscale* 5 **(2013)** 11265-11274.

[87] R. Wang, D.C. Higgins, M.A. Hoque, D. Lee, F. Hassan, Z. Chen, Controlled growth of Platinum nanowire arrays on sulfur doped graphene as high performance electrocatalyst, *Scientific Reports* 3 **(2013)** 2431.

[88] J.N. Tiwari, K.C. Kemp, K. Nath, R.N. Tiwari, H.-G. Nam, K.S. Kim, Interconnected Pt-nanodendrite/DNA/reduced-graphene-oxide hybrid showing remarkable oxygen reduction activity and stability, *ACS Nano* 7 **(2013)** 9223-9231.

[89] W.T. Yu, M.D. Porosoff, J.G.G. Chen, Review of Pt-based bimetallic catalysis: from model surfaces to supported catalysts, *Chemical Reviews* 112 **(2012)** 5780-5817.

[90] C. Koenigsmann, M.E. Scofield, H. Liu, S.S. Wong, Designing enhanced one-dimensional electrocatalysts for the oxygen reduction reaction: probing size- and composition-dependent electrocatalytic behavior in noble metal nanowires, *The Journal of Physical Chemistry Letters* 3 **(2012)** 3385-3398.

[91] R. Carrera-Cerritos, V. Baglio, A.S. Aricò, J. Ledesma-García, M.F. Sgroi, D. Pullini, A.J. Pruna, D.B. Mataix, R. Fuentes-Ramírez, L.G. Arriaga, Improved Pd electro-catalysis for oxygen reduction reaction in direct methanol fuel cell by reduced graphene oxide, *Applied Catalysis B: Environmental* 144 **(2014)** 554-560.

[92] Z. Zhang, L. Xin, K. Sun, W. Li, Pd–Ni electrocatalysts for efficient ethanol oxidation reaction in alkaline electrolyte, *International Journal of Hydrogen Energy* 36 **(2011)** 12686-12697.

[93] Z. Zhu, Y. Zhai, C. Zhu, Z. Wang, S. Dong, Bimetallic alloy nanowires and nanosponges: A comparative study of peroxidase mimetics and as enhanced catalysts for oxygen reduction reaction, *Electrochemistry Communications* 36 **(2013)** 22-25.

[94] Y.Z. Lu, Y.Y. Jiang, W. Chen, PtPd porous nanorods with enhanced electrocatalytic activity and durability for oxygen reduction reaction, *Nano Energy* 2 **(2013)** 836-844.

[95] T.H. Yeh, C.W. Liu, H.S. Chen, K.W. Wang, Preparation of carbon-supported PtM (M = Au, Pd, or Cu) nanorods and their application in oxygen reduction reaction, *Electrochemistry Communications* 31 **(2013)** 125-128.

[96] Y.C. Tseng, H.S. Chen, C.W. Liu, T.H. Yeh, K.W. Wang, The effect of alloying on the oxygen reduction reaction activity of carbon-supported PtCu and PtPd nanorods, *Journal of Materials Chemistry A* 2 **(2014)** 4270-4275.

[97] I.E.L. Stephens, A.S. Bondarenko, U. Gronbjerg, J. Rossmeisl, I. Chorkendorff, Understanding the electrocatalysis of oxygen reduction on platinum and its alloys, *Energy & Environmental Science* 5 **(2012)** 6744-6762.

[98] Z. Duan, G. Wang, A first principles study of oxygen reduction reaction on a Pt(111) surface modified by a subsurface transition metal M (M = Ni, Co, or Fe), *Physical Chemistry Chemical Physics* 13 **(2011)** 20178-20187.

[99] J.I. Shui, C. Chen, J.C.M. Li, Evolution of nanoporous Pt-Fe alloy nanowires by dealloying and their catalytic property for oxygen reduction reaction, *Advanced Functional Materials* 21 **(2011)** 3357-3362.

[100] Z. Zhang, M. Li, Z. Wu, W. Li, Ultra-thin PtFe-nanowires as durable electrocatalysts for fuel cells, *Nanotechnology* 22 **(2011)** 015602.

[101] S.J. Guo, D.G. Li, H.Y. Zhu, S. Zhang, N.M. Markovic, V.R. Stamenkovic, S.H. Sun, FePt and CoPt nanowires as efficient catalysts for the oxygen reduction reaction, *Angewandte Chemie-International Edition* 52 **(2013)** 3465-3468.

[102] N.N. Kariuki, W.J. Khudhayer, T. Karabacak, D.J. Myers, GLAD Pt-Ni alloy nanorods for oxygen reduction reaction, *ACS Catalysis* 3 **(2013)** 3123-3132.

[103] X.F. Lu, M. McKiernan, Z.M. Peng, E.P. Lee, H. Yang, Y.N. Xia, Noble-metal nanotubes prepared via a galvanic replacement reaction between Cu nanowires and aqueous $HAuCl_4$, H_2PtCl_6, or Na_2PdCl_4, *Science of Advanced Materials* 2 **(2010)** 413-420.

[104] L. Su, S. Shrestha, Z. Zhang, W. Mustain, Y. Lei, Platinum–copper nanotube electrocatalyst with enhanced activity and durability for oxygen reduction reactions, *Journal of Materials Chemistry A* 1 **(2013)** 12293-12301.

[105] M. Mohl, D. Dobo, A. Kukovecz, Z. Konya, K. Kordas, J. Wei, R. Vajtai, P.M. Ajayan, Formation of CuPd and CuPt bimetallic nanotubes by galvanic replacement reaction, *The Journal of Physical Chemistry C* 115 **(2011)** 9403-9409.

[106] C.H. Cui, H.H. Li, X.J. Liu, M.R. Gao, S.H. Yu, Surface composition and lattice ordering-controlled activity and durability of CuPt electrocatalysts for oxygen reduction reaction, *ACS Catalysis* 2 **(2012)** 916-924.

[107] S.W. Chou, J.J. Shyue, C.H. Chien, C.C. Chen, Y.Y. Chen, P.T. Chou, Surfactant-directed synthesis of ternary nanostructures: nanocubes, polyhedrons, octahedrons, and nanowires of PtNiFe. their shape-dependent oxygen reduction activity, *Chemistry of Materials* 24 **(2012)** 2527-2533.

[108] H. Zhu, S. Zhang, S. Guo, D. Su, S. Sun, Synthetic control of FePtM nanorods (M = Cu, Ni) to enhance the oxygen reduction reaction, *Journal of the American Chemical Society* 135 **(2013)** 7130-7133.

[109] L.C. Liu, G. Samjeske, S. Takao, K. Nagasawa, Y. Lwasawa, Fabrication of PtCu and PtNiCu multi-nanorods with enhanced catalytic oxygen reduction activities, *Journal of Power Sources* 253 **(2014)** 1-8.

[110] H.H. Li, C.H. Cui, S. Zhao, H.B. Yao, M.R. Gao, F.J. Fan, S.H. Yu, Mixed-PtPd-shell PtPdCu nanoparticle nanotubes templated from copper nanowires as efficient and highly durable electrocatalysts, *Advanced Energy Materials* 2 **(2012)** 1182-1187.

[111] L. Liu, E. Pippel, Low-platinum-content quaternary PtCuCoNi nanotubes with markedly enhanced oxygen reduction activity, *Angewandte Chemie International Edition* 50 **(2011)** 2729-2733.

[112] X. Liu, D. Wang, Y. Li, Synthesis and catalytic properties of bimetallic nanomaterials with various architectures, *Nano Today* 7 **(2012)** 448-466.

[113] M. Oezaslan, F. Hasché, P. Strasser, Pt-based core–shell catalyst architectures for oxygen fuel cell electrodes, *The Journal of Physical Chemistry Letters* 4 **(2013)** 3273-3291.

[114] H. Yang, Platinum-based electrocatalysts with core–shell nanostructures, *Angewandte Chemie International Edition* 50 **(2011)** 2674-2676.

[115] S.J. Hwang, S.J. Yoo, J. Shin, Y.H. Cho, J.H. Jang, E. Cho, Y.E. Sung, S.W. Nam, T.H. Lim, S.C. Lee, S.K. Kim, Supported core@shell electrocatalysts for fuel cells: close encounter with reality, *Scientific Reports* 3 **(2013)** 1309.

[116] C. Koenigsmann, A.C. Santulli, K. Gong, M.B. Vukmirovic, W.-p. Zhou, E. Sutter, S.S. Wong, R.R. Adzic, Enhanced electrocatalytic performance of processed, ultrathin, supported Pd–Pt core–shell nanowire catalysts for the oxygen reduction reaction, *Journal of the American Chemical Society* 133 **(2011)** 9783-9795.

[117] M.A. Bromley, C. Boxall, Photocatalytically initiated electroless deposition of macroporous metal films onto insulating substrates, *Electrochemistry Communications* 23 **(2012)** 87-89.

[118] H. Naohara, Y. Okamoto, N. Toshima, Preparation and electrocatalytic activity of palladium–platinum core–shell nanoalloys protected by a perfluorinated sulfonic acid ionomer, *Journal of Power Sources* 196 **(2011)** 7510-7513.

[119] S.M. Alia, K.O. Jensen, B.S. Pivovar, Y. Yan, Platinum-coated palladium nanotubes as oxygen reduction reaction electrocatalysts, *ACS Catalysis* 2 **(2012)** 858-863.

[120] C.W. Liu, Y.C. Wei, C.C. Liu, K.W. Wang, Pt-Au core/shell nanorods: preparation and applications as electrocatalysts for fuel cells, *Journal of Materials Chemistry* 22 **(2012)** 4641-4644.

[121] S. Guo, S. Zhang, D. Su, S. Sun, Seed-mediated synthesis of core/shell FePtM/FePt (M = Pd, Au) nanowires and their electrocatalysis for oxygen reduction reaction, *Journal of the American Chemical Society* 135 **(2013)** 13879-13884.

[122] Y.M. Tan, J.M. Fan, G.X. Chen, N.F. Zheng, Q.J. Xie, Au/Pt and Au/Pt_3Ni nanowires as self-supported electrocatalysts with high activity and durability for oxygen reduction, *Chemical Communications* 47 **(2011)** 11624-11626.

[123] B. Lim, M. Jiang, T. Yu, P.C. Camargo, Y. Xia, Nucleation and growth mechanisms for Pd-Pt bimetallic nanodendrites and their electrocatalytic properties, *Nano Research* 3 **(2010)** 69-80.

[124] S. Ghosh, S. Mondal, C. Retna Raj, Carbon nanotube-supported dendritic Pt-on-Pd nanostructures: growth mechanism and electrocatalytic activity towards oxygen reduction reaction, *Journal of Materials Chemistry A* 2 **(2014)** 2233-2239.

[125] H.B. Liao, Y.L. Hou, Liquid-phase templateless synthesis of Pt-on-$Pd_{0.85}Bi_{0.15}$ nanowires and PtPdBi porous nanoparticles with superior electrocatalytic activity, *Chemistry of Materials* 25 **(2013)** 457-465.

[126] C. Koenigsmann, A.C. Santulli, E. Sutter, S.S. Wong, Ambient surfactantless synthesis, growth mechanism, and size-dependent electrocatalytic behavior of high-quality, single crystalline palladium nanowires, *ACS Nano* 5 **(2011)** 7471-7487.

[127] X. Teng, W.-Q. Han, W. Ku, M. Hücker, Synthesis of ultrathin palladium and platinum nanowires and a study of their magnetic properties, *Angewandte Chemie* 120 **(2008)** 2085-2088.

[128] S.M. Alia, K. Duong, T. Liu, K. Jensen, Y. Yan, Palladium and gold nanotubes as oxygen reduction reaction and alcohol oxidation reaction catalysts in base, *ChemSusChem* **(2014)** 1739-1744.

[129] F.J. Yu, W.Z. Zhou, R.M. Bellabarba, R.P. Tooze, One-step synthesis and shape-control of CuPd nanowire networks, *Nanoscale* 6 **(2014)** 1093-1098.

[130] Z. Zhang, K.L. More, K. Sun, Z. Wu, W. Li, Preparation and characterization of PdFe nanoleaves as electrocatalysts for oxygen reduction reaction, *Chemistry of Materials* 23 **(2011)** 1570-1577.

[131] W. Sun, A. Hsu, R.R. Chen, Palladium-coated manganese dioxide catalysts for oxygen reduction reaction in alkaline media, *Journal of Power Sources* 196 **(2011)** 4491-4498.

[132] X.R. Li, X.L. Li, M.C. Xu, J.J. Xu, H.Y. Chen, Gold nanodendrities on graphene oxide nanosheets for oxygen reduction reaction, *Journal of Materials Chemistry A* 2 **(2014)** 1697-1703.

[133] C. Koenigsmann, E. Sutter, T.A. Chiesa, R.R. Adzic, S.S. Wong, Highly enhanced electrocatalytic oxygen reduction performance observed in bimetallic palladium-based nanowires prepared under ambient, surfactantless conditions, *Nano Letters* 12 **(2012)** 2013-2020.

[134] C. Koenigsmann, E. Sutter, R.R. Adzic, S.S. Wong, Size- and composition-dependent enhancement of electrocatalytic oxygen reduction performance in

ultrathin palladium–gold ($Pd_{1-x}Au_x$) Nanowires, *The Journal of Physical Chemistry C* 116 **(2012)** 15297-15306.

[135] A. Cha, J.H. Shim, A. Jo, S.C. Lee, Y. Lee, C. Lee, Facile synthesis of AuPd nanochain networks on carbon supports and their application as electrocatalysts for oxygen reduction reaction, *Electroanalysis* 26 **(2014)** 723-731.

[136] Z.L. Gengtao Fu, Yu Chen, Jun Lin, Yawen Tang, Tianhong Lu, Synthesis and electrocatalytic activity of Au@Pd core-shell nanothorns for the oxygen reduction reaction, *Nano Research* 7 **(2014)** 1205-1214.

[137] N. Wang, X. Cao, Q. Chen, G. Lin, Ag Nanobelts: synthesis, morphological evolution, and their use as electrocatalysts for oxygen reduction, *Chemistry – A European Journal* 18 **(2012)** 6049-6054.

[138] Y.Z. Lu, Y.C. Wang, W. Chen, Silver nanorods for oxygen reduction: Strong effects of protecting ligand on the electrocatalytic activity, *Journal of Power Sources* 196 **(2011)** 3033-3038.

[139] B. Kim, Y. Choi, S.Y. Cho, Y.S. Yun, H.-J. Jin, Silver nanowire catalysts on carbon nanotubes-incorporated bacterial cellulose membrane electrodes for oxygen reduction reaction, *Journal of Nanoscience and Nanotechnology* 13 **(2013)** 7454-7458.

[140] D. Yu, J. Yao, L. Qiu, Y. Wu, L. Li, Y. Feng, Q. Liu, D. Li, H. Wang, The synergetic effect of N-doped graphene and silver nanowires for high electrocatalytic performance in the oxygen reduction reaction, *RSC Advances* 3 **(2013)** 11552-11555.

[141] M. Han, S. Liu, L. Zhang, C. Zhang, W. Tu, Z. Dai, J. Bao, Synthesis of octopus-tentacle-like Cu nanowire-Ag nanocrystals heterostructures and their enhanced

electrocatalytic performance for oxygen reduction reaction, *ACS Applied Materials & Interfaces* 4 **(2012)** 6654-6660.

[142] J.H. Shim, J. Yang, S.J. Kim, C. Lee, Y. Lee, One dimensional Ag/Au/AgCl nanocomposites stemmed from Ag nanowires for electrocatalysis of oxygen reduction, *Journal of Materials Chemistry* 22 **(2012)** 15285-15290.

[143] Z. Wen, S. Ci, F. Zhang, X. Feng, S. Cui, S. Mao, S. Luo, Z. He, J. Chen, Nitrogen-enriched core-shell structured Fe/Fe_3C-C nanorods as advanced electrocatalysts for oxygen reduction reaction, *Advanced Materials* 24 **(2012)** 1399-1404.

[144] S. Liu, Z. Zhang, J. Bao, Y. Lan, W. Tu, M. Han, Z. Dai, Controllable synthesis of tetragonal and cubic phase Cu_2Se nanowires assembled by small nanocubes and their electrocatalytic performance for oxygen reduction reaction, *The Journal of Physical Chemistry C* 117 **(2013)** 15164-15173.

[145] Z. Yang, X.M. Zhou, H.G. Nie, Z. Yao, S.M. Huang, Facile construction of manganese oxide doped carbon nanotube catalysts with high activity for oxygen reduction reaction and investigations into the origin of their activity enhancement, *ACS Applied Materials & Interfaces* 3 **(2011)** 2601-2606.

[146] J.S. Lee, G.S. Park, H.I. Lee, S.T. Kim, R.G. Cao, M.L. Liu, J. Cho, Ketjenblack carbon supported amorphous manganese oxides nanowires as highly efficient electrocatalyst for oxygen reduction reaction in alkaline solutions, *Nano Letters* 11 **(2011)** 5362-5366.

[147] T.N. Lambert, D.J. Davis, W. Lu, S.J. Limmer, P.G. Kotula, A. Thuli, M. Hungate, G.D. Ruan, Z. Jin, J.M. Tour, Graphene-Ni-alpha-MnO_2 and -Cu-alpha-MnO_2 nanowire blends as highly active non-precious metal catalysts for the oxygen reduction reaction, *Chemical Communications* 48 **(2012)** 7931-7933.

[148] J. Du, Y.D. Pan, T.R. Zhang, X.P. Han, F.Y. Cheng, J. Chen, Facile solvothermal synthesis of $CaMn_2O_4$ nanorods for electrochemical oxygen reduction, *Journal of Materials Chemistry* 22 **(2012)** 15812-15818.

[149] C. Jin, F.L. Lu, X.C. Cao, Z.R. Yang, R.Z. Yang, Facile synthesis and excellent electrochemical properties of $NiCo_2O_4$ spinel nanowire arrays as a bifunctional catalyst for the oxygen reduction and evolution reaction, *Journal of Materials Chemistry A* 1 **(2013)** 12170-12177.

[150] T. Fujigaya, T. Uchinoumi, K. Kaneko, N. Nakashima, Design and synthesis of nitrogen-containing calcined polymer/carbon nanotube hybrids that act as a platinum-free oxygen reduction fuel cell catalyst, *Chemical Communications* 47 **(2011)** 6843-6845.

[151] G. Tuci, C. Zafferoni, P. D'Ambrosio, S. Caporali, M. Ceppatelli, A. Rossin, T. Tsoufis, M. Innocenti, G. Giambastiani, Tailoring carbon nanotube N-dopants while designing metal-free electrocatalysts for the oxygen reduction reaction in alkaline medium, *ACS Catalysis* 3 **(2013)** 2108-2111.

[152] A. Zhao, J. Masa, W. Schuhmann, W. Xia, Activation and stabilization of nitrogen-doped carbon nanotubes as electrocatalysts in the oxygen reduction reaction at strongly alkaline conditions, *The Journal of Physical Chemistry C* 117 **(2013)** 24283-24291.

[153] B. Li, Z. Yan, D.C. Higgins, D. Yang, Z. Chen, J. Ma, Carbon-supported Pt nanowire as novel cathode catalysts for proton exchange membrane fuel cells, *Journal of Power Sources* 262 **(2014)** 488-493.

[154] M.-T. Sung, M.-H. Chang, M.-H. Ho, Investigation of cathode electrocatalysts composed of electrospun Pt nanowires and Pt/C for proton exchange membrane fuel cells, *Journal of Power Sources* 249 **(2014)** 320-326.

[155] B. Li, D.C. Higgins, Q.F. Xiao, D.J. Yang, C.M. Zhng, M. Cai, Z.W. Chen, J.X. Ma, The durability of carbon supported Pt nanowire as novel cathode catalyst for a 1.5 kW PEMFC stack, *Applied Catalysis B-Environmental* 162 **(2015)** 133-140.

[156] W.H. Lee, H. Kim, Electrocatalytic activity and durability study of carbon supported Pt nanodendrites in polymer electrolyte membrane fuel cells, *International Journal of Hydrogen Energy* 38 **(2013)** 7126-7132.

[157] S. Sui, X.L. Zhuo, K.H. Su, X.Y. Yao, J.L. Zhang, S.F. Du, K. Kendall, In situ grown nanoscale platinum on carbon powder as catalyst layer in proton exchange membrane fuel cells (PEMFCs), *Journal of Energy Chemistry* 22 **(2013)** 477-483.

[158] S. Holdcroft, Fuel cell catalyst layers: A polymer science perspective, *Chemistry of Materials* 26 **(2014)** 381-393.

[159] M.K. Debe, Nanostructured thin film electrocatalysts for PEM fuel cells - A tutorial on the fundamental characteristics and practical properties of NSTF Catalysts, *Tutorials on Electrocatalysis in Low Temperature Fuel Cells* 45 **(2012)** 47-68.

[160] S.F. Du, A facile route for polymer electrolyte membrane fuel cell electrodes with in situ grown Pt nanowires, *Journal of Power Sources* 195 **(2010)** 289-292.

[161] S.F. Du, B. Millington, B.G. Pollet, The effect of Nafion ionomer loading coated on gas diffusion electrodes with in-situ grown Pt nanowires and their durability in proton exchange membrane fuel cells, *International Journal of Hydrogen Energy* 36 **(2011)** 4386-4393.

[162] S.F. Du, B.G. Pollee, Catalyst loading for Pt-nanowire thin film electrodes in PEFCs, *International Journal of Hydrogen Energy* 37 **(2012)** 17892-17898.

[163] S.F. Du, K.J. Lin, S.K. Malladi, Y.X. Lu, S.H. Sun, Q. Xu, R. Steinberger-Wilckens, H.S. Dong, Plasma nitriding induced growth of Pt-nanowire arrays as high performance electrocatalysts for fuel cells, *Scientific Reports* 4 **(2014)** 6439.

[164] X.Y. Yao, K.H. Su, S. Sui, L.W. Mao, A. He, J.L. Zhang, S.F. Du, A novel catalyst layer with carbon matrix for Pt nanowire growth in proton exchange membrane fuel cells (PEMFCs), *International Journal of Hydrogen Energy* 38 **(2013)** 12374-12378.

[165] K. Su, S. Sui, X. Yao, Z. Wei, J. Zhang, S. Du, Controlling Pt loading and carbon matrix thickness for a high performance Pt-nanowire catalyst layer in PEMFCs, *International Journal of Hydrogen Energy* 39 **(2014)** 3397-3403.

[166] Z. Wei, K. Su, S. Sui, A. He, S. Du, High performance polymer electrolyte membrane fuel cells (PEMFCs) with gradient Pt nanowire cathodes prepared by decal transfer method, *International Journal of Hydrogen Energy* 40 **(2015)** 3068-3074.

[167] H.W. Liang, X.A. Cao, F. Zhou, C.H. Cui, W.J. Zhang, S.H. Yu, A free-standing Pt-nanowire membrane as a highly stable electrocatalyst for the oxygen reduction reaction, *Advanced Materials* 23 **(2011)** 1467-1471.

[168] G. Fu, X. Jiang, M. Gong, Y. Chen, Y. Tang, J. Lin, T. Lu, Highly branched platinum nanolance assemblies by polyallylamine functionalization as superior active, stable, and alcohol-tolerant oxygen reduction electrocatalysts, *Nanoscale* 6 **(2014)** 8226-8234.

[169] Y. Li, Q. Wu, S. Jiao, C. Xu, L. Wang, Single Pt nanowire electrode: preparation, electrochemistry, and electrocatalysis, *Analytical Chemistry* 85 **(2013)** 4135-4140.

[170] S.J. Percival, B. Zhang, Electrocatalytic reduction of oxygen at single platinum nanowires, *Journal of Physical Chemistry C* 117 **(2013)** 13928-13935.

[171] G.T. Fu, K. Wu, J. Lin, Y.W. Tang, Y. Chen, Y.M. Zhou, T.H. Lu, One-pot water-based synthesis of Pt-Pd alloy nanoflowers and their superior electrocatalytic activity for the oxygen reduction reaction and remarkable methanol-tolerant ability in acid media, *Journal of Physical Chemistry C* 117 **(2013)** 9826-9834.

[172] D.J. Guo, S.K. Cui, D. Cheng, P. Zhang, L. Jiang, C.C. Zhang, One-pot synthesis of PtNi alloy nanoflowers supported on multi-walled carbon nanotubes with superior electrocatalytic activity for the oxygen reduction, *Journal of Power Sources* 255 **(2014)** 157-162.

[173] K. Gong, J. Park, D. Su, R.R. Adzic, Metalizing carbon nanotubes with Pd–Pt core–shell nanowires enhances electrocatalytic activity and stability in the oxygen reduction reaction, *Journal of Solid State Electrochemistry* 18 **(2013)** 1171-1179.

[174] S.H. Chun, H.A. Choi, M. Kang, M. Koh, N.S. Lee, S.C. Lee, M. Lee, Y. Lee, C. Lee, M.H. Kim, Highly efficient electrochemical responses on single crystalline ruthenium–vanadium mixed metal oxide nanowires, *ACS Applied Materials & Interfaces* 5 **(2013)** 8401-8406.

[175] A. El-Kharouf, T.J. Mason, D.J.L. Brett, B.G. Pollet, Ex-situ characterisation of gas diffusion layers for proton exchange membrane fuel cells, *Journal of Power Sources* 218 **(2012)** 393-404.

[176] S. Park, J.W. Lee, B.N. Popov, A review of gas diffusion layer in PEM fuel cells: Materials and designs, *International Journal of Hydrogen Energy* 37 **(2012)** 5850-5865.

[177] J.S. Preston, R.S. Fu, U. Pasaogullari, D.S. Hussey, D.L. Jacobson, Consideration of the role of micro-porous layer on liquid water distribution in polymer electrolyte fuel cells, *Journal of the Electrochemical Society* 158 **(2011)** B239-B246.

[178] C. Chan, N. Zamel, X.G. Li, J. Shen, Experimental measurement of effective diffusion coefficient of gas diffusion layer/microporous layer in PEM fuel cells, *Electrochimica Acta* 65 **(2012)** 13-21.

[179] T. Kitahara, H. Nakajima, K. Mori, Hydrophilic and hydrophobic double microporous layer coated gas diffusion layer for enhancing performance of polymer electrolyte fuel cells under no-humidification at the cathode, *Journal of Power Sources* 199 **(2012)** 29-36.

[180] Z. Fishman, A. Bazylak, Heterogeneous through-plane porosity distributions for treated PEMFC GDLs I. PTFE effect, *Journal of the Electrochemical Society* 158 **(2011)** B841-B845.

[181] www.sglgroup.com

[182] S. Park, J.W. Lee, B.N. Popov, Effect of carbon loading in microporous layer on PEM fuel cell performance, *Journal of Power Sources* 163 **(2006)** 357-363.

[183] M.Y. Jing, L.H. Jiang, S.L. Wang, F.N. Jing, G.Q. Sun, Application of FTIR in direct methanol fuel cells - Quantitative analysis of PTFE in gas diffusion layers, *International Journal of Hydrogen Energy* 38 **(2013)** 7957-7963.

[184] S. Park, J.W. Lee, B.N. Popov, Effect of PTFE content in microporous layer on water management in PEM fuel cells, *Journal of Power Sources* 177 **(2008)** 457-463.

[185] I. Kruusenberg, N. Alexeyeva, K. Tammeveski, J. Kozlova, L. Matisen, V. Sammelselg, J. Solla-Gullon, J.M. Feliu, Effect of purification of carbon nanotubes on their electrocatalytic properties for oxygen reduction in acid solution, *Carbon* 49 **(2011)** 4031-4039.

[186] H.H. Chen, M.H. Chang, Effect of cathode microporous layer composition on proton exchange membrane fuel cell performance under different air inlet relative humidity, *Journal of Power Sources* 232 **(2013)** 306-309.

[187] D.P. Zhan, J. Velmurugan, M.V. Mirkin, Adsorption/desorption of hydrogen on Pt nanoelectrodes: evidence of surface diffusion and spillover, *Journal of the American Chemical Society* 131 **(2009)** 14756-14760.

[188] Y. Garsany, O.A. Baturina, K.E. Swider-Lyons, S.S. Kocha, Experimental methods for quantifying the activity of platinum electrocatalysts for the oxygen reduction reaction, *Analytical Chemistry* 82 **(2010)** 6321-6328.

[189] T.J. Schmidt, H.A. Gasteiger, G.D. Stab, P.M. Urban, D.M. Kolb, R.J. Behm, Characterization of high-surface area electrocatalysts using a rotating disk electrode configuration, *Journal of the Electrochemical Society* 145 **(1998)** 2354-2358.

[190] Y.Y. Shao, G.P. Yin, Y.Z. Gao, Understanding and approaches for the durability issues of Pt-based catalysts for PEM fuel cell, *Journal of Power Sources* 171 **(2007)** 558-566.

[191] H.A. Gasteiger, S.S. Kocha, B. Sompalli, F.T. Wagner, Activity benchmarks and requirements for Pt, Pt-alloy, and non-Pt oxygen reduction catalysts for PEMFCs, *Applied Catalysis B-Environmental* 56 **(2005)** 9-35.

[192] A. Mallik, PhD thesis, National Institute of Technology, India, 2010.

[193] J.H. ter Horst, D. Bedeaux, S. Kjelstrup, The role of temperature in nucleation processes, *The Journal of Chemical Physics* 134 **(2011)** 1-11.

[194] S.H. Sun, F. Jaouen, J.P. Dodelet, Controlled growth of Pt nanowires on carbon nanospheres and their enhanced performance as electrocatalysts in PEM fuel cells, *Advanced Materials* 20 **(2008)** 3900-3904.

[195] X. Wang, J. Zhuang, Q. Peng, Y.D. Li, A general strategy for nanocrystal synthesis, *Nature* 437 **(2005)** 121-124.

[196] E.P. Lee, Z.M. Peng, D.M. Cate, H. Yang, C.T. Campbell, Y.N. Xia, Growing Pt nanowires as a densely packed array on metal gauze, *Journal of the American Chemical Society* 129 **(2007)** 10634-10635.

[197] J.Y. Chen, B. Lim, E.P. Lee, Y.N. Xia, Shape-controlled synthesis of platinum nanocrystals for catalytic and electrocatalytic applications, *Nano Today* 4 **(2009)** 81-95.

[198] Y.Y. Liu, X.Q. Chen, J.H. Xin, Can superhydrophobic surfaces repel hot water?, *Journal of Materials Chemistry* 19 **(2009)** 5602-5611.

[199] A.L.N. Pinheiro, A. Oliveira-Neto, E.C. de Souza, J. Perez, V.A. Paganin, E.A. Ticianelli, E.R. Gonzalez, Electrocatalysis on noble metal and noble metal alloys dispersed on high surface area carbon, *Journal of New Materials for Electrochemical Systems* 6 **(2003)** 1-8.

[200] S.C. Yu, X.J. Li, S. Liu, J.K. Hao, Z.G. Shao, B.L. Yi, Study on hydrophobicity loss of the gas diffusion layer in PEMFCs by electrochemical oxidation, *RSC Advances* 4 **(2014)** 3852-3856.

[201] R. Carrera-Cerritos, V. Baglio, A.S. Arico, J. Ledesma-Garcia, M.F. Sgroi, D. Pullini, A.J. Pruna, D.B. Mataix, R. Fuentes-Ramirez, L.G. Arriaga, Improved Pd electro-catalysis for oxygen reduction reaction in direct methanol fuel cell by reduced graphene oxide, *Applied Catalysis B-Environmental* 144 **(2014)** 554-560.

[202] O.A. Baturina, S.R. Aubuchon, K.J. Wynne, Thermal stability in air of Pt/C catalysts and PEM fuel cell catalyst layers, *Chemistry of Materials* 18 **(2006)** 1498-1504.

[203] H.J. Huang, H.Q. Chen, D.P. Sun, X. Wang, Graphene nanoplate-Pt composite as a high performance electrocatalyst for direct methanol fuel cells, *Journal of Power Sources* 204 **(2012)** 46-52.

[204] L.H. Qiu, Y.J. Peng, B.Q. Liu, B.C. Lin, Y. Peng, M.J. Malik, F. Yan, Polypyrrole nanotube-supported gold nanoparticles: An efficient electrocatalyst for oxygen reduction and catalytic reduction of 4-nitrophenol, *Applied Catalysis A-General* 413 **(2012)** 230-237.

[205] Z.W. Chen, M. Waje, W.Z. Li, Y.S. Yan, Supportless Pt and PtPd nanotubes as electrocatalysts for oxygen-reduction reactions, *Angewandte Chemie-International Edition* 46 **(2007)** 4060-4063.

[206] S.S. Kocha, Principles of MEA preparation, in: W. Vielstich, A. Lamm, H. Gasteiger (Eds.), Handbook of fuel cells-fundamentals, technology and applications 3 **(2003)** 538.

[207] D. Kashchiev, G.M. van Rosmalen, Review: Nucleation in solutions revisited, *Crystal Research and Technology* 38 **(2003)** 555-574.

[208] D.J. Srolovitz, G.S. Grest, M.P. Anderson, A.D. Rollett, Computer simulation of recrystallization—II. Heterogeneous nucleation and growth, *Acta Metallurgica* 36 **(1988)** 2115-2128.

[209] S. Puri, V.K. Wadhawan, Kinetics of phase transitions, CRC Press, Boca Raton, 2009.

[210] X.Y. Liu, Heterogeneous nucleation or homogeneous nucleation?, *The Journal of Chemical Physics* 112 **(2000)** 9949-9955.

[211] P. Serp, M. Corrias, P. Kalck, Carbon nanotubes and nanofibers in catalysis, *Applied Catalysis A-General* 253 **(2003)** 337-358.

[212] P. Trogadas, T.F. Fuller, P. Strasser, Carbon as catalyst and support for electrochemical energy conversion, *Carbon* 75 **(2014)** 5-42.

[213] K.Q. Li, X.R. Zeng, H.Q. Li, X.J. Lai, C.X. Ye, H. Xie, Study on the wetting behavior and theoretical models of polydimethylsiloxane/silica coating, *Applied Surface Science* 279 **(2013)** 458-463.

[214] O. Song, Z.J. Zhang, Shape control and associated magnetic properties of spinel cobalt ferrite nanocrystals, *Journal of the American Chemical Society* 126 **(2004)** 6164-6168.

[215] M.V. Massa, K. Dalnoki-Veress, Homogeneous crystallization of poly(ethylene oxide) confined to droplets: The dependence of the crystal nucleation rate on length scale and temperature, *Physical Review Letters* 92 **(2004)** 255509.

[216] D.W. Oxtoby, Homogeneous nucleation - theory and experiment, *Journal of Physics-Condensed Matter* 4 **(1992)** 7627-7650.

[217] Y.J. Deng, N. Tian, Z.Y. Zhou, R. Huang, Z.L. Liu, J. Xiao, S.G. Sun, Alloy tetrahexahedral Pd-Pt catalysts: enhancing significantly the catalytic activity by synergy effect of high-index facets and electronic structure, *Chemical Science* 3 **(2012)** 1157-1161.

[218] C. Koenigsmann, S.S. Wong, Tailoring chemical composition to achieve enhanced methanol oxidation reaction and methanol-tolerant oxygen reduction reaction performance in palladium-based nanowire systems, *ACS Catalysis* 3 **(2013)** 2031-2040.

[219] C. Zhu, S. Guo, S. Dong, PdM (M = Pt, Au) Bimetallic alloy nanowires with enhanced electrocatalytic activity for electro-oxidation of small molecules, *Advanced Materials* 24 **(2012)** 2326-2331.

[220] S.J. Guo, S.J. Dong, E.K. Wang, Ultralong Pt-on-Pd bimetallic nanowires with nanoporous surface: nanodendritic structure for enhanced electrocatalytic activity, *Chemical Communications* 46 **(2010)** 1869-1871.

[221] J.J. Lv, J.N. Zheng, S.S. Li, L.L. Chen, A.J. Wang, J.J. Feng, Facile synthesis of Pt–Pd nanodendrites and their superior electrocatalytic activity, *Journal of Materials Chemistry A* 2 **(2014)** 4384-4390.

[222] Y. Kim, Y. Noh, E.J. Lim, S. Lee, S.M. Choi, W.B. Kim, Star-shaped Pd@Pt core-shell catalysts supported on reduced graphene oxide with superior electrocatalytic performance, *Journal of Materials Chemistry A* 2 **(2014)** 6976-6986.

[223] L.X. Ding, C.L. Liang, H. Xu, A.L. Wang, Y.X. Tong, G.R. Li, Porous hollow nanorod arrays composed of alternating Pt and Pd nanocrystals with superior electrocatalytic activity and durability for methanol oxidation, *Advanced Materials Interfaces* **(2014)** 1400005.

[224] C. Koenigsmann, A.C. Santulli, K.P. Gong, M.B. Vukmirovic, W.P. Zhou, E. Sutter, S.S. Wong, R.R. Adzic, Enhanced Electrocatalytic Performance of processed, ultrathin, supported Pd-Pt core-shell nanowire catalysts for the oxygen reduction reaction, *Journal of the American Chemical Society* 133 **(2011)** 9783-9795.

[225] M. Gummalla, S.C. Ball, D.A. Condit, S. Rasouli, K. Yu, P.J. Ferreira, D.J. Myers, Z.W. Yang, Effect of Particle Size and Operating Conditions on Pt_3Co PEMFC Cathode Catalyst Durability, *Catalysts* 5 **(2015)** 926-948.

[226] C.Z. Zhu, S.J. Guo, S.J. Dong, PdM (M = Pt, Au) bimetallic alloy nanowires with enhanced electrocatalytic activity for electro-oxidation of small molecules, *Advanced Materials* 24 **(2012)** 2326-2331.

[227] S. Du, Y. Lu, R. Steinberger-Wilckens, PtPd nanowire arrays supported on reduced graphene oxide as advanced electrocatalysts for methanol oxidation, *Carbon* 79 **(2014)** 346-353.

[228] X. Chen, Z. Cai, X. Chen, M. Oyama, Green synthesis of graphene–PtPd alloy nanoparticles with high electrocatalytic performance for ethanol oxidation, *Journal of Materials Chemistry A* 2 **(2014)** 315.

[229] A. Cacciuto, S. Auer, D. Frenkel, Onset of heterogeneous crystal nucleation in colloidal suspensions, *Nature* 428 **(2004)** 404-406.

[230] Y.X. Lu, S.F. Du, R. Steinberger-Wilckens, Temperature-controlled growth of single-crystal Pt nanowire arrays for high performance catalyst electrodes in polymer electrolyte fuel cells, *Applied Catalysis B-Environmental* 164 **(2015)** 389-395.

[231] A. Rofaiel, J.S. Ellis, P.R. Challa, A. Bazylak, Heterogeneous through-plane distributions of polytetrafluoroethylene in polymer electrolyte membrane fuel cell gas diffusion layers, *Journal of Power Sources* 201 **(2012)** 219-225.

[232] A. Arvay, E. Yli-Rantala, C.H. Liu, X.H. Peng, P. Koski, L. Cindrella, P. Kauranen, P.M. Wilde, A.M. Kannan, Characterization techniques for gas diffusion layers for proton exchange membrane fuel cells - A review, *Journal of Power Sources* 213 **(2012)** 317-337.

[233] N N. Parikh, J.S. Allen, R.S. Yassar, Microstructure of gas diffusion layers for PEM fuel cells, *Fuel Cells* 12 **(2012)** 382-390.

[234] C. Lau, E.R. Adkins, R.P. Ramasamy, H.R. Luckarift, G.R. Johnson, P. Atanassov, Design of carbon nanotube-based gas-diffusion cathode for O_2 reduction by multicopper oxidases, *Advanced Energy Materials* 2 **(2012)** 162-168.

[235] H. Su, T.C. Jao, S. Pasupathi, B.J. Bladergroen, V. Linkov, B.G. Pollet, A novel dual catalyst layer structured gas diffusion electrode for enhanced performance of high temperature proton exchange membrane fuel cell, *Journal of Power Sources* 246 **(2014)** 63-67.

[236] B. Millington, S.F. Du, B.G. Pollet, The effect of materials on proton exchange membrane fuel cell electrode performance, *Journal of Power Sources* 196 **(2011)** 9013-9017.

[237] H.R. Jhong, F.R. Brushett, P.J.A. Kenis, The effects of catalyst layer deposition methodology on electrode performance, *Advanced Energy Materials* 3 **(2013)** 589-599.

[238] L. Wang, S.G. Advani, A.K. Prasad, Membrane electrode assembly with enhanced membrane/electrode interface for proton exchange membrane fuel cells, *Journal of Physical Chemistry C* 117 **(2013)** 945-948.

[239] B. Millington, V. Whipple, B.G. Pollet, A novel method for preparing proton exchange membrane fuel cell electrodes by the ultrasonic-spray technique, *Journal of Power Sources* 196 **(2011)** 8500-8508.

[240] D.S. Hwang, C.H. Park, S.C. Yi, Y.M. Lee, Optimal catalyst layer structure of polymer electrolyte membrane fuel cell, *International Journal of Hydrogen Energy* 36 **(2011)** 9876-9885.

[241] C. Bois, A. Blayo, D. Chaussy, R. Vincent, A.G. Mercier, C. Nayoze, Catalyst layers for PEMFC manufactured by flexography printing process: performances and structure, *Fuel Cells* 12 **(2012)** 199-211.

[242] N. Zamel, J. Becker, A. Wiegmann, Estimating the thermal conductivity and diffusion coefficient of the microporous layer of polymer electrolyte membrane fuel cells, *Journal of Power Sources* 207 **(2012)** 70-80.

[243] E. Passalacqua, G. Squadrito, F. Lufrano, A. Patti, L. Giorgi, Effects of the diffusion layer characteristics on the performance of polymer electrolyte fuel cell electrodes, *Journal of Applied Electrochemistry* 31 **(2001)** 449-454.

[244] Y. Xiao, M.L. Dou, J.L. Yuan, M. Hou, W. Song, B. Sunden, Fabrication process simulation of a PEM fuel cell catalyst layer and its microscopic structure characteristics, *Journal of the Electrochemical Society* 159 **(2012)** B308-B314.

[245] T. Kitahara, H. Nakajima, K. Okamura, Gas diffusion layers coated with a microporous layer containing hydrophilic carbon nanotubes for performance

enhancement of polymer electrolyte fuel cells under both low and high humidity conditions, *Journal of Power Sources* 283 **(2015)** 115-124.

[246] X.L. Wang, H.M. Zhang, J.L. Zhang, H.F. Xu, X.B. Zhu, J. Chen, B.L. Yi, A bi-functional micro-porous layer with composite carbon black for PEM fuel cells, *Journal of Power Sources* 162 **(2006)** 474-479.

[247] X.L. Wang, H.M. Zhang, J.L. Zhang, H.F. Xu, Z.Q. Tian, J. Chen, H.X. Zhong, Y.M. Liang, B.L. Yi, Micro-porous layer with composite carbon black for PEM fuel cells, *Electrochimica Acta* 51 **(2006)** 4909-4915.

[248] K. Kamegawa, K. Nishikubo, M. Kodama, Y. Adachi, H. Yoshida, Oxidative degradation of carbon blacks with nitric acid - II. Formation of water-soluble polynuclear aromatic compounds, *Carbon* 40 **(2002)** 1447-1455.

[249] X.L. Chen, W.S. Li, C.L. Tan, W. Li, Y.Z. Wu, Improvement in electrochemical capacitance of carbon materials by nitric acid treatment, *Journal of Power Sources* 184 **(2008)** 668-674.

[250] M. Carmo, M. Linardi, J.G.R. Poco, Characterization of nitric acid functionalized carbon black and its evaluation as electrocatalyst support for direct methanol fuel cell applications, *Applied Catalysis A-General* 355 **(2009)** 132-138.

[251] H.Y. Du, C.H. Wang, H.C. Hsu, S.T. Chang, S.C. Yen, L.C. Chen, B. Viswanathan, K.H. Chen, High performance of catalysts supported by directly grown PTFE-free micro-porous CNT layer in a proton exchange membrane fuel cell, *Journal of Materials Chemistry* 21 **(2011)** 2512-2516.